ROTATED HALF-MODE SUBSTRATE INTEGRATED WAVEGUIDE AND OTHER PLANAR INTEGRATED STRUCTURES

A Thesis submitted to the
University of Kent for the degree
of Doctor of Philosophy
in the subject of Electronic Engineering

by

Andrew J Farrall

2015

Dedication

To all of my family –
for being patient with me during this journey.

Especially for my parents Sheila and Derrick.

But most of all to my wife Lorrie;
for the support and encouragement
for the help with proof reading
and for letting me off all those jobs at the time,
which I now have to do….

Without her blessing this would not have been possible.

Abstract

High data rate communication channels are becoming more and more integrated into our increasingly technological society. Substrate Integrated Waveguides (SIW) are one planar solution available to the microwave engineer, offering a low-loss and low dispersion means of propagating these high speed, high bandwidth signals.

In this thesis, a brief synopsis of SIW structures and components is presented covering the basic waveguide propagating modes and cut-off frequencies. The main analysis techniques associated with SIWs including full wave electromagnetic modelling methods are overviewed, and the associated loss mechanisms of conduction, dielectric and radiation defined, leading to the design rules and guidelines on how best to mitigate them.

SIW antennas as both leaky-wave and radiating slots are discussed and an example of a single and dual resonating slot antenna design is presented, along with a detailed review of a novel switch beam antenna developed for use within the current WiFi bands.

The Slot SIW (or SSIW), which has a small longitudinal gap in one of the main conducting surfaces, allows easy integration of lumped elements or active devices, enabling the waveguide to be loaded with impedances or to be shorted. When the slot is shorted, the waveguide reverts back to the full SIW mode, and when partially loaded an intermediate state results. This is discussed, and the SSIW analysed with the transverse resonance technique, leading to the development of a travelling wave attenuator with the SSIW being periodically loaded with pin diodes. The application of the pin diodes required the use of a capacitive overlay, a development of flexi circuit design to allow capacitive coupling of impedances to connect to the waveguide. The overlay concept is extended further, to form novel passive bandpass filters, with the introduction of *virtual vias.*

A limitation of the SSIW is that the majority of the field resides within the dielectric; this allows only a limited interaction with the field at the slot. The rotated Half Mode SIW (rHMSIW), a new variant of the SIW family, places the maximum of the electric field directly on the top dielectric surface, allowing for direct interaction. The waveguide width *a* is now defined by the dielectric thickness, allowing for the waveguide height *b* to be adjustable, in normal SIWs this is the other way round; the dielectric thickness fixing the waveguide height and the waveguide width being adjustable. The rHMSIW is characterised with regard to the height and width ratios *b/a* and the dielectric exposed width (which is adjustable). These parameters effect the modal cut-off frequency, this is investigated and a new equation describing the fundamental mode cut-off frequency is empirically derived. Finally a test coupon which spans the Ku band is designed and measured, which required the development of a novel waveguide transition.

Acknowledgements

Many thanks to my supervisor Dr Paul Young for the support and guidance throughout the entire PhD.

For the funding that supported this research project from ESPRC and the Rogers Corporation University support program for the PTFE laminate samples, plus the business support from Total Access Research and Design Limited.

The help and support from all my friends and colleagues at the School of Engineering and Digital arts, University of Kent, especially the front office and workshop, was much appreciated - helping me balance being an Associate Lecturer as well as a research student.

Not forgetting the other '*mature*' students who were on similar journeys; Paul '*textbook*' Taylor, Mark '*eager*' Esdale and '*mad*' Mike Gillham. Thanks for all the encouragement and coffee break chats!

Andy '*faffing*' Farrall

July 2015

Contents:

List of Publications

Location	Date	Authors	Title	Reference
IEEE Electronics Letters (Volume40-Issue16)	Aug 2004	Farrall / Young	Integrated Waveguide Slot Antennas	[1]
IEEE 2004 High Frequency Postgraduate Student Colloquium	Sep 2004	Farrall / Young	Substrate Integrated Rectangular Waveguides	[2]
APSYM2012 Conference	Dec 2012	Young / Farrall	Travelling Wave Attenuator	
LAPC2013 Conference	Nov 2013	Farrall / Young	Rotated Half-Mode SIW	[3]
LAPC2013 Conference	Nov 2013	Lindo / Anju / Aanandan / Farrall / Young (IEEE as Farrel, A.J.)	HMSIW without Via	[4]
IEEE Microwave & Wireless Components Letters	Jan 2014	Xu / Farrall / Young	Analysis of Loaded Substrate Loaded Integrated Waveguides and Attenuators	[5]
Journal of Physics: Conference Series	Apr 2014	R. Nag / A.J. Farrall, P.R. Young / R.F. Xu	Modelling of loaded substrate integrated waveguides	
LAPC2014 Conference	Nov 2014	Farrall / Young	Microstrip to Rotated Half-Mode Substrate Integrate Waveguide Planar Transition	[6]
IEEE Transactions on Antennas and Propagation - Communication	May 2015	Farrall / Wu / Young	Substrate Integrated Waveguide Switched Beam Antenna	[7]
IEEE Transactions on Antennas and Propagation	Re-submitted Sep 2015	Ming-Tao Zhang / Steven Gao / Yong-Chang Jiao / Ji-Xiang Wan / Bu-Ning Tian, Chun-Bang Wu / Andrew-John Farrall	Novel Reconfigurable Reflectarrays with Single-bit Phase Resolution for Ku-Band Satellite Antenna	

References

[1] A. J. Farrall and P. R. Young, "Integrated waveguide slot antennas," *Electronics Letters*, vol. 40, pp. 974-975, 2004.

[2] A. J. Farrall and P. R. Young, "High frequency postgraduate student colloquium, 2004; substrate integrated rectangular waveguides," in 2004, pp. 133-to 138.

[3] A. J. Farrall and P. R. Young, "Rotated half-mode substrate integrated waveguide," in *Antennas and Propagation Conference (LAPC), 2013 Loughborough*, 2013, pp. 514-517.

[4] A. O. Lindo, P. M. Anju, C. K. Aanandan, A. J. Farrall and P. R. Young, "Half mode substrate integrated waveguide without via," in *Antennas and Propagation Conference (LAPC), 2013 Loughborough*, 2013, pp. 131-134.

[5] Ruo Feng Xu, A. J. Farrall and P. R. Young, "Analysis of Loaded Substrate Integrated Waveguides and Attenuators," *Microwave and Wireless Components Letters, IEEE*, vol. 24, pp. 62-64, 2014.

[6] A. J. Farrall and P. R. Young. Microstrip to rotated half-mode substrate integrate waveguide planar transition. Presented at Antennas and Propagation Conference (LAPC), 2014 Loughborough. 2014, . DOI: 10.1109/LAPC.2014.6996332.

[7] L. Wu, A. J. Farrall and P. R. Young, "Substrate Integrated Waveguide Switched Beam Antennas," *Antennas and Propagation, IEEE Transactions On*, vol. 63 Issue 5, pp. 2301-2305, 2015.

Abbreviation	Full Description
AC	Alternating Current
ACA	adaptive cross-approximation
ADC	analogue-to-digital conversion
ADSL	Asymmetric Digital Subscriber Line
AR	axial ratio
AV	audio / video
AWGN	Additive White Gaussian Noise
BEM	Boundary Element Method
BER	bit error rate
BFACP	Balanced-Fed Aperture Coupled Patch
BI-RME	Boundary Integral-Resonant Mode Expansion
BW	Band-width
CAD	Computer Aided Design
CAE	Computer Aided Engineering
CAM	Computer Aided Manufacturing
CMOS	complementary metal oxide semiconductor
CPS	coplanar stripline
CPW	coplanar waveguide
CSIW	Corrugated Substrate Integrated Waveguide
CSRR	Complimentary Split Ring Resonator
CST	Computer Simulation Technology
DAS	Dual Antenna System
DC	Direct Current
DCA	Direct Chip Attach
DOA	Direction of Arrival
DRC	Discontinuity Radiation Concept
EBG	Electromagnetic Band-Gap
EDGE	Enhanced Data Rates for GSM Evolution
EIRP	Equivalent Isotropic Radiated Power
ECMSA	Electromagnetic Coupling Micro-Strip patch Antenna
ENIG	Electroless NickelImersion Gold
ENZ	Epsilon Near Zero
EPSRC	Engineering and Physical Sciences Research Council
HASL	Hot Air Solder Level
HSAS	Hybrid Smart Antenna System
FDFD	Finite-Difference Frequency Domain
FHMSIW	Folded Half-Mode Substrate Integrated Waveguide
FPA	Folded Patch Antenna
FSIW	Folded Substrate Integrated Waveguide
GPIB	General Purpose Information Bus
GPRS	General Packet Radio Service
GSM	Global System for Mobile communication
HASL	Hot Air Solder Level
HDMI	high-definition multimedia interface
HFSS	High Frequency Structural Simulator
HMLWA	Half Mode Leaky Wave Antenna
HMSIW	Half Mode Substrate Integrated Waveguide

HPBW	Half Power Beam Width
IEEE	Institute of Electrical and Electronic Engineers
LAPC	Loughborough Antenna and Propagation Conference
LMDS	Local Multipoint Distribution System
LOS	Line of Sight
LTCC	Low temp co-fired ceramics
LWA	Leaky Wave Antenna
MAA	Microstrip Antenna Array
MAC	Media Access Control
MAFA	Multilayer Antenna-Filter Antenna
MCM	Multiple chip modules
MCOF	Microwave chip on flex
MEMS	Micro Electro Mechanical Systems
MLWA	Microstrip Leaky-Wave Antenna
MoL	Method of Lines
MoM	Method of Moments
MSK	Minimum Shift Keying
MWGA	Microstrip Wire Grid Array
NEC	Numerical Electromagnetics Code
NLOS	non-Line of Sight
PADS	Personal Automated Design System
PIN	p-i-n junction
PLWA	Planar Leaky Wave Antenna
PSU	Power Supply Unit
PTFE	Polytetrafluoroethylene
PWW	Post Wall Waveguide (SIW equivalent)
RADAR	Radio Detection and Ranging
RF	Radio Frequency
rHMSIW	Rotated Half-Mode SIW
RIM	Radiating Integrated Module
RIS	Reactive Impedance Surface
RISW	Ridge Substrate Integrated Waveguide
RSISW	Ridge Substrate Integrated Slab Waveguide
RSIW	Rectangular Substrate Integrated Waveguide
S	Scattering
SAS	Smart Antenna System
SDMA	Space Division Multiple Access
SIC	Substrate Integrated Cavity
SICL	Substrate Integrated Coaxial Line
SIHC	Substrate Integrated Hybrid Circuit
SiP	System in Package
SIR	signal-to-interference
SIRW	Substrate Integrated Rectangular Waveguide
SISW	Substrate Integrated Slab Waveguide
SIW	Substrate Integrated Waveguide
SMA	Sub-Miniature version A
SNR	signal-to-noise ratio
SOLT	Short Open Line Through
SoC	System on Chip

SoS	System on Substrate
SSIW	Slot Substrate Integrated Waveguide
TA	Transmit Array
TE	Transverse Electric
TEM	Transverse Electro-Magnetic
TM	Transverse Magnetic
UEP	Unequal Error Protection
UWB	Ultra WideBand
VNA	Vector Network Analyser
VSWR	Voltage Standing Wave Ratio
WiGig	Wireless Gigabit Alliance Group
WLAN	wireless local area network
WPAN	wireless personal area network
WVAN	wireless video area network

Variable	Description	Units
α	attenuation constant	Nepers per meter
β	phase constant	radians per meter
γ	propagation constant	Nepers per meter
ε_r	relative permittivity	$\mathbb{R}$
ε_{eff}	effective permittivity	Fm^{-1}
θ	phase offset	rad
λ	wavelength	m
λ_c	cut-off wavelength	m
λ_g	guided wavelength	m
λ_m	wavelength in medium	m
ρ	electric charge density	C/m^3
σ	conductivity	siemens m^{-1}
v_m	velocity in a medium	ms^{-1}
ω	angular frequency	rad s^{-1}
a	waveguide width	m
a_{eff}	effective waveguide width	m
a_{HM}	half mode waveguide width	m
$\boldsymbol{B}$	magnetic flux density	Teslas or $Webers/m^2$
B	susceptance	siemens
b	waveguide height	m
b_{eff}	effective waveguide height	m
C	capacitance	F
C_e	minimum copper clearance	m
C_w	rHMSIW top copper width	m
$\boldsymbol{D}$	electric flux density	C/m^2
D	SIW via diameter	m
D_w	rHMSIW dielectric width	m
$\boldsymbol{E}$	electric field intensity	V/m
f	frequency	Hz
f_c	cut-off frequency	Hz
f_{cl}	leaky wave cut-off frequency	Hz
f_0	resonant or centre frequency	Hz
G_a	antenna gain	dBi
g	shunt conductance	siemens
$\boldsymbol{H}$	magnetic field intensity	A/m
h	laminate thickness	m
$\boldsymbol{J}$	electric current density	A/m^2
k	wave number	m^{-1}
k_o	wave number in freespace	m^{-1}
k_c	cut-off wave number	m^{-1}
L	inductance	H
L_C	cable loss	dB
L_s	SIW slot length	m
L_1	SSIW main section width	m
L_2	SSIW shunt section width	m
P_R	received power	dB
P_T	transmitted power	dB
P_v	via pitch in SIW wall	m
R	resistance	Ω
VL	virtual via shunt length	m
VLo	virtual via pad length	m
VW	virtual via shunt width	m
VWx	virtual via width extension	m
VWo	virtual via pad width	m

W	via wall pitch (waveguide width)	m
W_{eff}	effective via wall pitch (waveguide width)	m
W_{gL}	waveguide length	m
w	slot width	m
X	reactance	Ω
x	SIW slot displacement	m
Y	admittance	S (siemens)
Z	impedance	Ω

1 Introduction

1.1 Historic Perspective

Electronic communication has developed over the last century from the analysis of a physical phenomenon into a global communication network that pervades every aspect of our modern lives. From simple remote controls to high definition media streaming on a mobile phone, from text messages to on-line shopping over the internet, the propagation of electromagnetic waves (Fig. 1.1) in the form of signals and data has become a cornerstone of our modern community. It is useful periodically to reflect on how far we have come in such a short time.

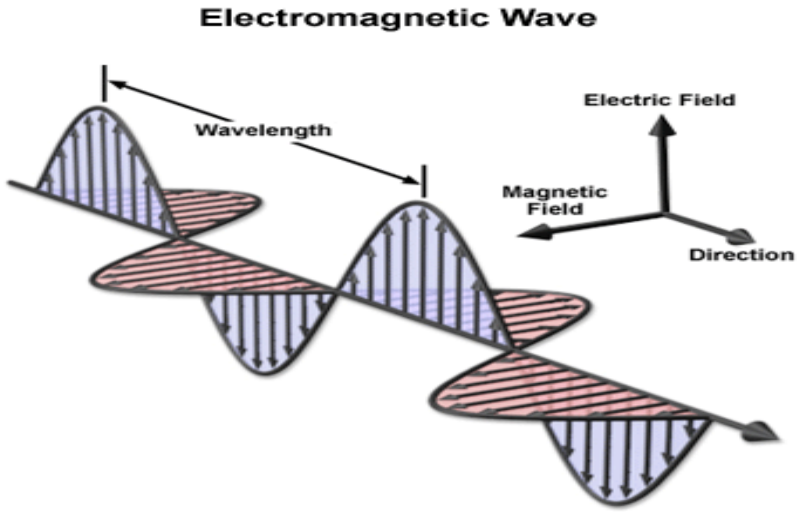

Fig 1.1 Electromagnetic Wave (diagram from nationalmaglab.org)

Our real understanding of electromagnetics begins with James Clerk Maxwell and his equations. Maxwell published in 1873 his *"A Treatise on Electricity and Magnetism"* a result of ten years work to try and unify these two phenomena. By adding a term to describe 'the displacement current' to existing equations, Maxwell predicated the existence of electromagnetic waves that travel at the speed of light, which in turn led to the insight that light itself must be electromagnetic [1]. Many people have commented on Maxwell's work, as an example; Albert Einstein (in "*The Evolution of Physics"*) wrote *'The formulation of these equations is the most important event in physics since Newton's time'.*

Unfortunately Maxwell died (aged 48 in 1879) before he could experimentally confirm his predictions, and it was Heinrich Hertz, a former pupil of Hermann von Hemlholtz, who first verified them in 1888. Indeed it is Hertz who is accredited [2] with publishing the first antenna book "*Electric Waves: Being Researches on the Propagation of Electric Action with Finite Velocity*

Through Space" in 1893 [3]. Hertz managed to generate and receive electromagnetic waves and performed experiments with diffraction, reflection, refraction and polarization. Hertz died in 1894 aged just under 37.

Maxwell in his treatise of 1873 expressed his equations in terms of '*quarternions*' and used twenty equations to describe the behaviour of electric and magnetic fields. It was Oliver Heaviside and Heinrich Hertz who in 1884 combined Maxwell's twenty equations, using vector calculus, and simplified them into four sets; the basis of those used today. We now call these four equations; Gauss's law for electric fields, Gauss's law for magnetic fields, Faraday's law and Ampere-Maxwell's law [4], shown here in differential form:

$$\boldsymbol{\nabla} \cdot \boldsymbol{D} = \rho$$

{the electric field produced by electric charge diverges from positive charge and converges on negative charge, $\boldsymbol{D}$ electric flux density (C/m^2), ρ electric charge density (C/m^3)}

$$\boldsymbol{\nabla} \cdot \boldsymbol{B} = 0$$

{the divergence of the magnetic field at any point is zero, $\boldsymbol{B}$ magnetic flux density (Teslas or Webers/m^2)}

$$\boldsymbol{\nabla} \times \boldsymbol{E} = -\frac{\partial \boldsymbol{B}}{\partial t}$$

{a circulating electric field is produced by a magnetic field that changes with time, $\boldsymbol{E}$ electric field intensity (V/m)}

$$\boldsymbol{\nabla} \times \boldsymbol{H} = \boldsymbol{J} + \frac{\partial \boldsymbol{D}}{\partial t}$$

{a circulating magnetic field is produced by an electric current and by an electric field that changes with time, $\boldsymbol{H}$ magnetic field intensity (A/m), $\boldsymbol{J}$ electric current density (A/m^2)

As is often the case with good ideas and technologies, things start slowly and progress exponentially; in 1901 Guglielmo Marconi, with a team of colleagues successfully demonstrated trans-Atlantic wireless telegraphy. Then in 1916 engineers and scientists at Naval Research Laboratory, Virginia, transmitted the first practical amplitude-modulated (AM) radio signal. During the 1930's radio communications and broadcasting spread, British developed RADAR

(radio detection and ranging) and World War II became the first main conflict fought with electronics [5]. WWII caused a massive leap forward in the field of electromagnetic and antennas and post-war this developed knowledge fed a global expansion, founded on the classic 28 volume *Radiation Laboratory Series* of books, a collaboration of notable work from researchers working at MIT [6].

It is not possible to cover the complete history of microwaves and antennas in this document; however it was felt that a key summary would be beneficial in setting the scene for later work. At the start of the 19th century the first detectors had been created, notably Jagadish Chandra Bose's "bolometer' which according to papers published in 1897 was used up to 60GHz in experiments! [1, 7]. Lord Rayleigh in the same year published a landmark treatise on the theory of transmission of electromagnetic waves [8] where he proposed the removal of the centre conductor of a coaxial transmission line, thus paving the way for hollow waveguides. In 1906 Henry Harrison Chase Dunwoody became the first to patent a rectifying detector, and in the same year Greenleaf Whittier Pickard patented the first silicon based detector. Pickard would go one to make advances in crystal based detectors.

There was a move from spark signals to continuous wave, as the broadband noise caused by spark transmissions caused too much interference. This was typified by the documented failure of 'live commentary coverage' of the 1901 Americas Cup Yacht Race, involving Marconi, Pickard and Lee de Forest. Progress was made with Reginald Fessenden making the first AM broadcast over Christmas in 1906, then leading to Valdemar Poulson running a 1 megawatt continuous wave transmitter just after WWI.

Edward Howard Armstrong in 1917 patented a superhetrodyne demodulator, which he ended up selling the rights to RCA, who using this technology became the leader in the radio market, its shares growing massively throughout the 1920's as the market itself grew beyond all expectation; until the crash in 1929. A direct comparison with the "dot com" bubble of the 1990's, it would seem. But rapid growth in the radio market also caused problems with limited spectrum availability. Commercial, government and amateur radio interests all vied for the 'best' frequencies, which at the time were deemed just below the megahertz range. As a by-product of this the 'radio hams' were pushed up to using 1.5 MHz (sub 200m wavelengths), these 'short waves' produced unexpected benefits and stimulated research into microwaves during the 1930's.

As frequencies increased, so did the realisation that the losses in cables also increased, leading to knowledge that the greatest loss was in the centre conductor. This prompted investigation into removing the centre conductor, giving rise to waveguides in 1936 (individually credited to George C Southworth of Bell Labs and Wilmer Marrow of MIT), building on the previous work by Rayleigh. Waveguides were a key piece of the puzzle for radar, with the British deploying the first ever system in 1937. The original system used 22 MHz signals but by the end of the war 55 MHz was being used and 200 MHz was in development. Microwave at this time referred to frequencies of 1 GHz and higher [1].

Russell Varian invented "the klystron" in 1937, offering the first opportunity for 'pulsing' waves, which led to the reflector klystron shortly after, and then in 1940 the first cavity magnetron producing 500W of pulsed power at 3GHz, attributed to Henry A H Boot and John T Randall. By 1945 100kW pulses at 10 GHz were being produced and 24 GHz magnetrons were in development. Commercial and military radio clearly advanced, with two way FM radio available in 1941, and 1943 seeing the first 'walkie-talkie'.

Post-war, towards the end of the decade, saw the first mobile radio mast launched in St Louis, Missouri. A six channel FDD (frequency division duplexing) system based at 150 MHz. Then in the 1950's the first 'microwave' ovens were produced, credited to Percy Spencer (of Ratheon) using a 900 MHz magnetron, and in 1957 the space-race began with the launch of Sputnik and satellite microwave communications technology commenced. Also in this decade (1957) due to the improvement in microwave components the first measurements in cosmic background radiation were made.

Improvements in solid state transistors during the 1950's and 1960's saw the decline in vacuum tube components and the creation of gallium arsenide devices, which gave superior mobility of electrons. Towards the end of this era the first commercial cellular system was introduced as a payphone on a train (running between New York City and Washington DC). In the 1970's, Motorola filed the first cellular patent and Bell Systems were granted the first trial licence by the FCC for a trial mobile phone service.

However, it was during this period that the early stages of the internet was formed, four US universities were linked on the ARPA (Advanced Research Projects Agency), and additional nodes were quickly added. In 1972, the first email was sent, and the following year the TCP/IP (Transmission Control Protocol / Internet Protocol) was introduced; later becoming the standard in

the early 1980's. Domain names start to be used and a connection system based around 56 kb/s is introduced, but it is too slow for many applications especially running multimedia.

The 1980's saw growth of the analogue mobile phone industry, and then an explosion in the 1990's as the 2G digital systems were introduced, based initially on 900 MHz spectrum, and later as well on 1800 MHz. Microwave technology development up until this point had been the province of the military and aeronautic industries, but since the development of mobile phones and personal computers has very much been driven by commercial product development. The 2G systems brought in digital encryption, more efficient spectrum use and introduced data services for mobile users, but suffered from range issues and limited data rates. Stepping stones on the path of development in the early 2000's were dubbed 2.5G (GPRS) and 2.75G (EDGE). The General Packet Radio Service offered bundling data packets together, improving efficiency but not necessarily speed of service, however the Enhanced Data Rates for GSM Evolution produced the faster data rates the system required (kbps).

Broadband for internet users is launched around the second millennium allowing access rates of 512 kbps, quickly rising to connection speeds of up to 1 Mbps with improved variants such as ADSL (asymmetric digital subscriber line) broadband. The mid 1990's saw ~ 45 million users on the internet, by 2006 there were over 100 million websites online. With the use of fibre links to improve broadband speed, data rates of 1 Gbps become possible for some, but not all users. Average home broadband speed for UK at the time of writing is just under 20 Mbps, but increasing at a rate of ~10% per year.

Through the first decade of the 21st century, mobile communications grew rapidly as a third generation (3G), offering improved reliability and faster data rates (typically Mbps), by using spread spectrum technology and improvements in technology and coding. Then into a fourth (4G) with even higher data rates (100s Mbps), offering a truly mobile broadband service capable of full audio video (AV) media streaming, including high definition content.

Data rates will be pushed further as the next mobile communications standards (5G) are expected to reach the market towards the end of this decade. With communications at very high frequencies (30 to 300 GHz) in the millimetre wave band, significantly higher data bandwidths will be achievable (Gbps). However, as communication frequencies increase to enable the higher data rates demanded, it becomes more difficult to deliver services from a system architecture view point, which will necessitate more complex software algorithms as well as higher specification radio and

antenna hardware. This means the implications for new technology will be significant due to the extremely small wavelengths being used, leading to further integrated devices (such as chip on board, embedded antenna and microwave components). Also associated with the higher frequencies, are increased losses, with particular frequencies having specific propagation problems (such as 60 GHz and oxygen absorption).

The next generation communication systems, wireless and directly connected, will no doubt deliver the faster data rates required by the modern user, however more than ever microwave engineering will be a central part of the new technology providing efficient and high bandwidth connectivity.

1.2 Millimetre-wave Communications

To support these new demands, global legislation being considered is to create an unlicensed area of the spectrum around the E band (see Table 1.1), predominantly for use in high data rate wireless networks. The fact that oxygen has an absorption peak in this frequency (see Fig. 1.2), limits the range of high data rate distance transmissions, which is why this part of the spectrum has remained relatively 'commercially clear' [9]. The legislation will cover both indoor networks and outside point-to-point communication.

Applications under development include wireless video area networks (WVANs), which will be able to stream uncompressed audio and video up to 1080p resolution (24 bit colour at 60 Hz refresh rate). Ranges of up to 10m for the highest AV resolutions are possible using smart antenna technology to enable non-line of sight operation (NLOS). NLOS is only possible at these frequencies and data rates, by using wireless protocols that enables directional connections; by dynamically steering the transmitter antenna beam whilst focussing the receiver antenna in the required direction. This optimises the line of sight link, but also allows the use of reflections and other indirect paths to form NLOS paths.

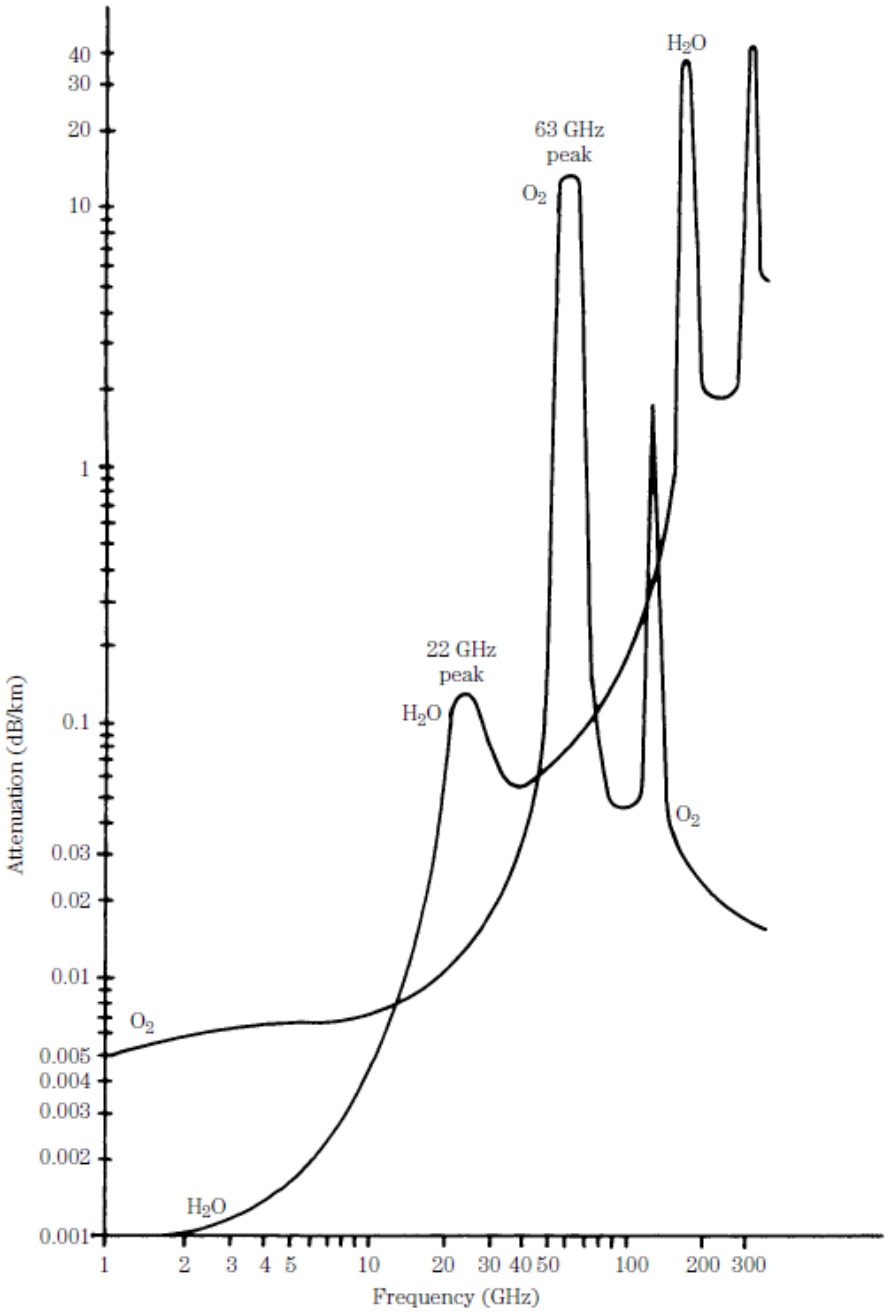

Figure 1.2: Atmospheric absorption of wireless signals at millimetre frequencies [5]

Other applications include: ‘sync and go’ file transfer (large gigabit data), wireless docking stations and wireless gigabit Ethernet [10]. Specific elements of these applications include wireless gaming and cable replacement for high definition video. In addition there are point to point applications being developed, including mobile communications ‘backhaul’ systems, some of which are now commercially available.

Frequency bands are repeatedly referred to within this document, a summary is shown in table 1.1 for reference.

BAND	f_{start} (GHz)	λ_{start} (cm)	f_{stop} (GHz)	λ_{stop} (cm)	f_{centre} (GHz)	λ_{centre} (cm)
L	1.0	29.98	2.0	14.99	1.5	19.99
S	2.0	14.99	4.0	7.49	3.0	9.99
C	4.0	7.49	8.0	3.75	6.0	5.00
X	8.0	3.75	12.0	2.50	10.0	3.00
Ku	12.0	2.50	18.0	1.67	15.0	2.00
K	18.0	1.67	26.0	1.15	22.0	1.36
Ka	26.0	1.15	40.0	0.75	33.0	0.91
U	40.0	0.75	60.0	0.50	50.0	0.60
V	50.0	6.00	75.0	4.00	62.5	4.80
E	60.0	5.00	90.0	3.33	75.0	4.00
W	75.0	4.00	110.0	2.73	92.5	3.24
F	90.0	3.33	140.0	2.14	115.0	2.61
D	110.0	2.73	170.0	1.76	140.0	2.14

Table 1.1. Frequency bands and wavelengths (in freespace)

521-2002 - IEEE Standard Letter Designations for Radar-Frequency Bands

1.3 60 GHz Legislation

Current Wi-Fi systems are based around 2.4 GHz and 5 GHz with data rates around 300 Mbps up to 750 Mbps, which is already limiting certain applications and will restrict the proposed Gbps data rates proposed for the future. Hence a revision (or possible revolution) to the WiFi market was required. The goal of allocating a common frequency spectrum globally is an ongoing challenge, and the key groups involved in the specification development for 60 GHz band are;

- WirelessHD Group (www.wirelesshd.org),
- Silicon Image (www.siliconimage.com)
    - acquired SiBeam the original WirelessHD founders in May 2011.

- Wi-Fi Alliance (http://www.wi-fi.org/)
    - Sometimes referred to as Gi-Fi (Gigabit Wireless)
    - Wireless Gigabit Alliance Group (WiGig http://wirelessgigabitalliance.org/)
        - Subsumed by Wi-Fi Alliance in March 2013.
- IEEE Groups
    - 802.11ac
        - http://www.ieee802.org/11/Reports/tgac_update.htm
        - completed in Sept 2013
    - 802.11.ad http://www.ieee802.org/11/Reports/tgad_update.htm
    - 802.15.3c WPAN mmWave alternative PHY
        - http://www.ieee802.org/15/pub/TG3c.html
- ECMA International
    - ECMA-387, "High Rate 60 GHz PHY MAC and HDMI PALS" (2nd Edition December 2010)
    - http://www.ecma-international.org/publications/standards/Ecma-387.htm

The main difference between WiGig and WirelessHD, is the wish to incorporate the existing 2.4 and 5 GHz Wi-Fi bands. A common description worth adopting is the term 'microwave bands' to refer to the 6 to 40 GHz bands, the term 'millimetre-wave' (sometimes abbreviated to mm-wave) refers to the frequency range 30 to 300 GHz.

High data rate wireless transmissions require large bandwidth, but the current EM spectrum is crowded with little room, hence partly the restricted Wi-Fi bandwidths. There is bandwidth available in the V and W Bands which have previously not been utilised. The 60 GHz band covers various frequencies globally between 57 and 66 GHz. Short range (<10m) communications at these frequencies can deliver 4 Gb/s (up to 20 Gb/s in specifications), and at longer distances (few hundred meters) rates of 1 Gb/s.

There are higher frequency bands in the 70 and 80 GHz regions globally available, 71 to 76 GHz and 81 to 86 GHz (within the E Band). With 5 GHz bandwidth very high data rates (6 Gb/s) can be delivered, and greater distances (1 Gb/s over several kilometres) than that of the 60 GHz band.

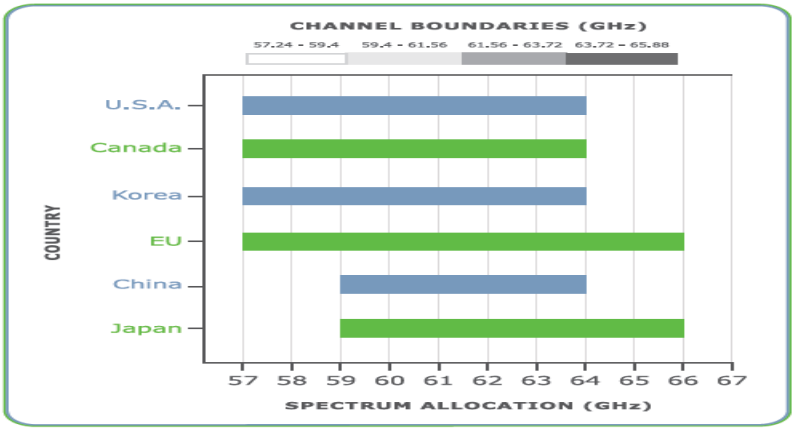

Fig. 1.3: Proposed Worldwide spectrum availability in 60 GHz Band
(from original WiGig reference white paper)

Some allocation is also available in the 90 GHz region, although at the moment this is not global. The current frequency allocation for the main countries involved is shown in Fig. 1.3, the legislation is not completely finalised and there are global variations still being discussed.
In addition to the frequency allocation there is a range of other legislation for each country, including maximum transmit power and highest EIRP (Equivalent Isotropically Radiated Power).

Parameter	United States	Canada	Pt-Pt Europe	Europe	Japan	Australia		New Zealand
in / out door	Both	Both	Both	Both	Both	Indoor	Outdoor	Both
Frequency	57 to	57 to	64 to	57 to	59 to	57 to	59 to	59 to
	65 GHz	65 GHz	66 GHz	66 GHz	66 GHz	66 GHz	63 GHz	64 GHz
Max Tx Power	27dBm	27dBm	35 dBm	10 dBm	10 dBm	13 dBm	13 dBm	27dBm
Max EIRP (av)	40 dBm	40 dBm	85 dBm	55 dBm	57 dBm	43 dBm	51.8 dBm	40 dBm
(peak)	43 dBm	43 dBm						43 dBm

Table 1.2: Technical Specifications for Unlicensed 60 GHz Bands in Different Countries [9]

The European 64 to 66 GHz band has the highest output power and EIRP, targeting longer distance point-to-point applications. The United States allocation has the lowest EIRP limits predominating shorter distance higher data rate applications, even though transmit power allocation for US is high.

1.4 Practicalities of 60 GHz fabrication & measurement

In addition to the propagation losses (which include atmospheric gas attenuation, precipitation attenuation, scattering effects and diffraction) NLOS propagation causing multipath fading may be significant, plus other factors including shadowing and noise. All this creates very high demands on

the associated hardware, in order to create a communications channel performance that is useable. The transmitting and receiving antennas must be of significant gain, as due to the legislation the problem may not be simply overcome by increasing the transmission power.

From Table 1.2, the European specification for unlicensed 60 GHz band, 57 to 64 GHz (BW of 7 GHz), for high data rate, over short distance, as an internal band, the maximum transmit power is 10 dBm (10 mW) and a maximum EIRP 55 dBm, then leaves a target antenna gain = 55 dBm – 10 dBm (P_T) + 10 dB (cable losses L_C) = 55 dBi. This will only be met by an antenna array which has additional features such as beam steering capabilities. There is little or no room for loss within the hardware architecture and noise must be minimised as in all microwave systems.

At 60 GHz the freespace wavelength is 5 mm, and if travelling in a dielectric reduces even further (by factor of $\varepsilon_r^{-1/2}$), for $\varepsilon_r = 2.2$ the wavelength in medium (λ_m) is ~3.4 mm. These wavelengths are of the order of the physical package dimensions utilised requiring extreme care and attention to physical layout and part interfacing. Due to these high constraints and high losses, solutions integrating systems directly onto an integrated chip (SiP – system in package, of SoC – system on chip, SoS – system on substrate), for example [11]. Fig 1.4 shows an Imec 60 GHz transceiver with BGA contacts for assembly into a larger system / PCB. The chipset consists of a receiver and a transmitter chip, and these are based on a direct conversion architecture combined with an on-chip phased-array architecture using four antennas. Millimetre-wave (mm-wave) integrated circuits face additional difficulties in circuit design, layout, and measurement, as compared to lower frequency. The parasitic effects are so much accentuated at these frequencies that the circuit may fail to operate correctly just as a result of layout problems.

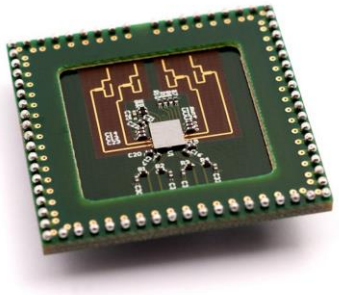

Fig. 1.4 Imec transceiver 60GHz multi-Gbit chipset
http://www.siliconsemiconductor.net

Calibration and measurements at mm-wave frequencies are also problematic, system artefacts can seriously effect the results and spurious wave modes may be excited and propagate. Higher frequencies (such as E band 60-90 GHz) require specialist techniques such as thick film photoimaging [12, 13] as at mm-wave frequencies traditional waveguide structures become difficult and expensive to manufacture to high tolerance machining requirements.

1.5 SIW use for 60 GHz

These higher data rate and high bandwidth signals require a low loss and low dispersion transmission path within hardware architectures, and SIWs are capable of meeting these requirements. At lower frequencies, common planar transmissions are microstrip and coplanar waveguides, however, at higher frequencies (>30 GHz) increasing transmission and radiation losses make them inefficient [14]. Substrate Integrated Waveguides (SIW), generally utilise vias to form the waveguide side walls and the top and bottom metal surfaces of laminates, however, it is also possible to form the waveguide walls with plated slots , bandgap structures and by using conductive printing. SIWs behave similar to traditional rectangular waveguides; hence offering a low loss and shielded transmission method with high Q factor, high power handling capability and low insertion loss.

SIWs will discussed in further depth in Chapter 2, but it is worth mentioning a few examples demonstrated at higher frequencies. A 60 GHz multi-chip module receiver using SIWs, SIW filter and SIW antenna; on a single multilayer substrate has been demonstrated [15, 16]. SIW Butler matrices have been demonstrated at 60 GHz [17], and also combined directly with a switched beam SIW slot antenna [18]. LTCC 60 GHz antenna array with SIW feed and resonant cavity for bandwidth enhancement has been demonstrated [19], as well as a wideband 60 GHz SIW Slot antenna array with SIW feed network [20]. High gain planar antenna array [21] also with a SIW feed network and multi-slot SIW antenna elements has been presented.

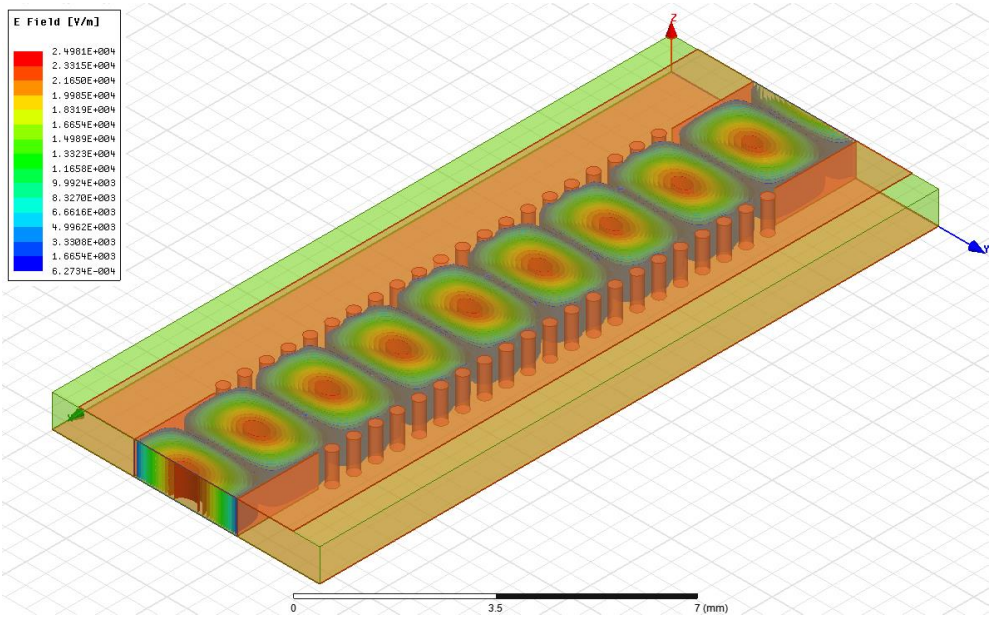

Fig. 1.5 linear electric field plot of rectangular SIW at 70 GHz

SIW has been demonstrated and utilized in frequencies ranging from 3 to 90 GHz, with a limited implementation over 100 GHz, Fig.1.5 is a simple SIW representation at 70 GHz. At lower frequencies (below 3 GHz) the size of the SIW structures becomes large and costly in the terms of PCB ‘real estate’. Also, at the lower frequencies the benefits of SIW over microstrip and CPW are not as great due to the lower associated loss. However, as SIWs are a function of wavelength they scale with frequency, and at very high frequencies, fabrication tolerances become restrictive and costly. Within this demonstrated range, and certainly around the 60 GHz band, the wavelength, tolerances and cost factors create an opportune area for SIW use.

1.6 Thesis Overview

The size of SIWs architectures are directly related to the frequency of operation and the associated wavelength means that SIWs are an important transmission option for high frequency (60 GHz) mm-waves; due to the low loss, low radiation, and easy integration. Directly developing SIW structures and components at mm-wave frequencies is complex and costly, as SIW structures are frequency scalable, a pragmatic approach has been to use lower frequencies to demonstrate new approaches. In this thesis, the substrate integrated waveguide (SIW) is discussed and then applied to several different applications at various frequencies.

Chapter 2 reviews the SIW, looking at the propagating modes, how they are described and the associated cut-off frequencies below which these modes will not function. The main analysis techniques associated with SIWs are briefly overviewed including full wave electromagnetic modelling methods. Loss mechanisms associated with SIWs; conduction, dielectric and radiation are defined, leading to design rules and guidelines on how best to mitigate them. The last part of the chapter summaries the key SIW structures and components, identifying the benefits and limitations of each.

Chapter 3 investigates the use of SIW as an antenna, both as a leaky-wave and radiating slot. An early research example of a single and dual slot antenna design is presented, along with a detailed review of a novel switch beam antenna developed for use within the current WiFi bands. The switched beam antenna has variants for 2, 4 and 6 directions, each of which utilises only a single SIW - with 2 or 4 slot apertures (plus a central reflector for the 4 and 6 direction designs). This was a joint research project, however the material included here has not been published in its entirety before.

Chapter 4 investigates one of the known SIW variants, the Slot SIW (or SSIW); this has a small longitudinal gap along one of the main conducting surfaces (usually the top). The waveguide is split forcing the main propagating mode away from the traditional full SIW mode. The slot allows easy integration of lumped elements or active devices, enabling the waveguide to be loaded with impedances or to be shorted. When the slot is shorted, the waveguide reverts back to the full SIW mode, and when partially loaded an intermediate state results. This is discussed, and the SSIW analysed with the transverse resonance technique (overviewed in chapter 2), leading to the development of a travelling wave attenuator with the SSIW being periodically loaded with pin diodes. The application of the pin diodes required the use of a capacitive overlay, a development of

flexi circuit design to allow capacitive coupling of impedances to connect to the waveguide. The overlay concept is extended further, to form novel passive bandpass filters, and the introduction of *virtual vias.*

A limitation of the SSIW is that the majority of the field resides within the dielectric, this allows only a limited interaction with the field at the slot. Chapter 5 introduces the rotated Half Mode SIW (rHMSIW), a new variant of the SIW family. The rHMSIW places the maximum of the electric field directly on the top dielectric surface, allowing for direct interaction, and control of the amount of dielectric exposed. As a subsequence of this, the waveguide width *a* is now defined by the dielectric thickness, allowing for the waveguide height *b* to be adjustable. In normal SIWs this is the other way round, the dielectric thickness fixing the waveguide height and the waveguide width being adjustable. The rHMSIW is characterised with regard to the height and width ratios *b/a,* and the dielectric exposed width. These parameters effect the modal cut-off frequency, this is investigated and a new equation describing the fundamental mode cut-off frequency is empirically derived. Finally a test coupon which spans the Ku band is designed and measured, which required the development of a novel waveguide transition.

Chapter 6 concludes the work presented and highlights areas of future work being considered.

1.7 References

[1] T. H. Lee, *Planar Microwave Engineering: A Practical Guide to Theory, Measurement, and Circuits.* Cambridge University Press, 2004.

[2] W. Stutzman. Bibliography for antennas: A list of every english-language antenna book ever written. *Antennas and Propagation Magazine, IEEE 50(4),* pp. 128-143. 2008.

[3] H. Hertz, *Electric Waves.* Dover Publications Inc., 1893 (original).

[4] S. Ramo, T. Van Duzer, J. R. Whinnery and Theodore Van Duzer, *Fields and Waves in Communication Electronics.* New York: Wiley, 1994.

[5] J. J. Carr, *Practical Antenna Handbook (TAB/ Mastering Electronics Series) 639785328544.* McGraw-Hill Professional, 2001.

[6] D. M. Pozar, *Microwave Engineering.* New York: Wiley, 1998.

[7] D. T. Emerson, "The work of Jagadis Chandra Bose: 100 years of millimeter-wave research," *Microwave Theory and Techniques, IEEE Transactions On,* vol. 45, pp. 2267-2273, 1997.

[8] K. S. Packard, "The Origin of Waveguides: A Case of Multiple Rediscovery," *Microwave Theory and Techniques, IEEE Transactions On,* vol. 32, pp. 961-969, 1984.

[9] J. Wells, *Multigigabit Microwave and Millimeter-Wave Wireless Communications.* Artech House Publishers, 2010.

[10] S. Yong, P. Xia and A. L. Garcia, *60GHz Technology for Gbps WLAN and WPAN: From Theory to Practice.* Wiley, 2011.

[11] Inchan Ju, Youngmin Kim, Sanghyo Lee, Sangsub Song, Jangsoo Lee, Changyul Cheon, Kwang-Seok Seo and Youngwoo Kwon. V-band beam-steering ASK transmitter and receiver using BCB-based system-on-package technology on silicon mother board. *Microwave and Wireless Components Letters, IEEE 21(11),* pp. 619-621. 2011.

[12] M. S. Aftanasar, P. R. Young and I. D. Robertson, "Rectangular waveguide filters using photoimageable thick-film processing," in *Microwave Conference, 2002. 32nd European,* 2002, pp. 1-4.

[13] M. S. Aftanasar, P. R. Young, I. D. Robertson, J. Minalgiene and S. Lucyszyn, "Photoimageable thick-film millimetre-wave metal-pipe rectangular waveguides," *Electronics Letters*, vol. 37, pp. 1122-1123, 2001.

[14] M. Bozzi, A. Georgiadis and K. Wu. Review of substrate-integrated waveguide circuits and antennas. *Microwaves, Antennas & Propagation, IET 5(8),* pp. 909-920. 2011.

[15] K. K. Samanta, D. Stephens and I. D. Robertson, "Design and performance of a 60-GHz multi-chip module receiver employing substrate integrated waveguides," *Microwaves, Antennas & Propagation, IET*, vol. 1, pp. 961-967, 2007.

[16] I. D. Robertson and K. K. Samanta. Multilayer thick-film photoimageable technology for 60 GHz system-in-package. Presented at Microwave Conference, 2008. APMC 2008. Asia-Pacific. 2008, . DOI: 10.1109/APMC.2008.4958263.

[17] Chih-Jung Chen and Tah-Hsiung Chu, "Design of a 60-GHz Substrate Integrated Waveguide Butler Matrix—A Systematic Approach," *Microwave Theory and Techniques, IEEE Transactions On*, vol. 58, pp. 1724-1733, 2010.

[18] Fan Fan He, Ke Wu, Wei Hong, Liang Han and Xiao-Ping Chen. Low-cost 60-GHz smart antenna receiver subsystem based on substrate integrated waveguide technology. *Microwave Theory and Techniques, IEEE Transactions On 60(4),* pp. 1156-1165. 2012.

[19] Junfeng Xu, Zhi Ning Chen, Xianming Qing and Wei Hong, "Bandwidth Enhancement for a 60 GHz Substrate Integrated Waveguide Fed Cavity Array Antenna on LTCC," *Antennas and Propagation, IEEE Transactions On*, vol. 59, pp. 826-832, 2011.

[20] M. Ohira, A. Miura and M. Ueba. 60-GHz wideband substrate-integrated-waveguide slot array using closely spaced elements for planar multisector antenna. *Antennas and Propagation, IEEE Transactions On 58(3),* pp. 993-998. 2010.

[21] Xiao-Ping Chen, Ke Wu, Liang Han and Fanfan He. Low-cost high gain planar antenna array for 60-GHz band applications. *Antennas and Propagation, IEEE Transactions On 58(6),* pp. 2126-2129. 2010.

2 Substrate Integrated Waveguides

In this chapter SIWs are reviewed with respect to propagation modes, analysis techniques, loss mechanisms and design guidelines. The range of SIW structures is discussed and an example of a SIW coupler is shown.

Waveguides are not deemed pure transmission lines, as they are single conductors (not the two required for a true transmission line) as such they will not support TEM waves. Waveguides however, do propagate a higher order of modes either transverse magnetic (TM – no magnetic field in direction of propagation) or transverse electric (TE - no electric field in direction of propagation). Waveguides have two main problems for propagating these higher modes, the first is that each mode (TE and TM) has a limited bandwidth in which it will propagate, and a cut-off frequency below which these higher order modes will not work. The other, is that these modes are dispersive, and that the phase velocity is dependent on the frequency.

The traditional 'box' waveguide offers the capability of transmitting high power electromagnetic energy, but it is bulky and expensive. Coaxial line is an alternative medium with high bandwidth, but it is difficult to fabricate complex microwave components using coaxial lines. Stripline, microstrip, slotline, CPW (coplanar waveguide), amongst others have provided a planar form of transmission line since the 1950s [1]. Offering low loss and low cost transmission lines with easy formation of other microwave devices, such as passive components, interconnects and antennas. Planar technologies offer compact, low profile and light weight components capable of being easily fabricated at relatively low cost. However, some printed components may exhibit significant losses due to radiation leakage and close coupling and have limited power handling capability, this becomes more critical as the relative dimensions of the printed structures becomes closer to the wavelength of interest (typically in the millimetre wave region).

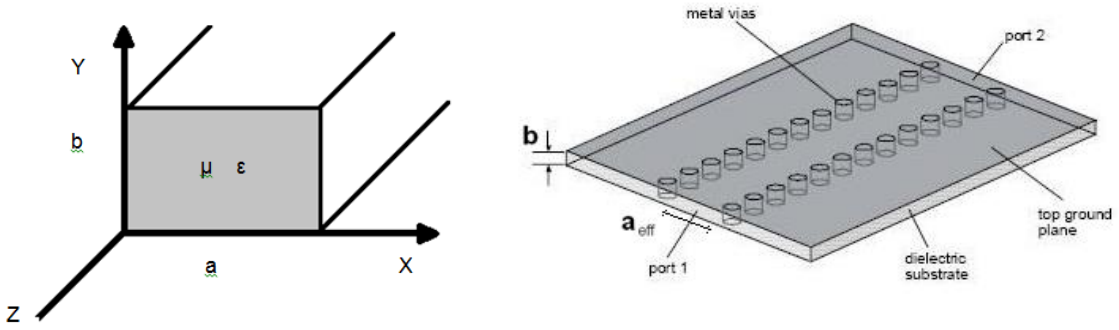

Fig.2.1 Rectangular waveguide and SIW comparison

Shielded propagation in planar form with low loss, good quality factor and high power handling is possible, and substrate integrated waveguides have performed this role for many years. Rectangular SIW [2, 3] were first conceived in the 1990's, with detailed development using via holes (or posts) to form the waveguide side walls (Fig. 2.1), and the top and bottom copper surfaces of the printed circuit board (PCB) laminate to form the roof and floor of the waveguide undertaken in the early 2000's [4-7]. SIWs offer a low loss, low cost, shielded and compact microwave transmission method with easy device integration within the planar technology tool set. The ability to integrate a complete system, including passive and active components, antennas and even chipsets to produce system in package (SiP) [8] is a significant advantage. An example planar configuration is shown in Fig. 2.2.

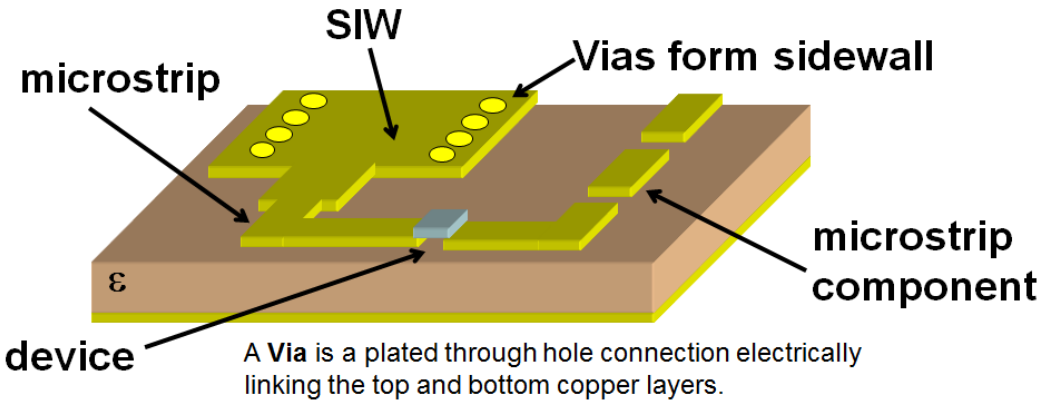

Fig. 2.2 substrate integrated system

Variations of SIW include Folded SIW (FSIW) [9], where the waveguide physical size is reduced, bandwidth is increased but losses are moderately increased. Also there are half-mode variants (HMSIW) [10, 11] which increase the bandwidth and can also have a reduced size, and if designed correctly will match the losses (or possibly reduce) those of regular SIWs [11]. A combination of the folded and half-mode version is also possible (FHMSIW) gaining the benefits of both, as well as the negatives and an increase in complexity. Slab SIW (SISW) offer to increase the bandwidth, and applying a central ridge to the waveguide (SIRW) [12] can increase the bandwidth even further.

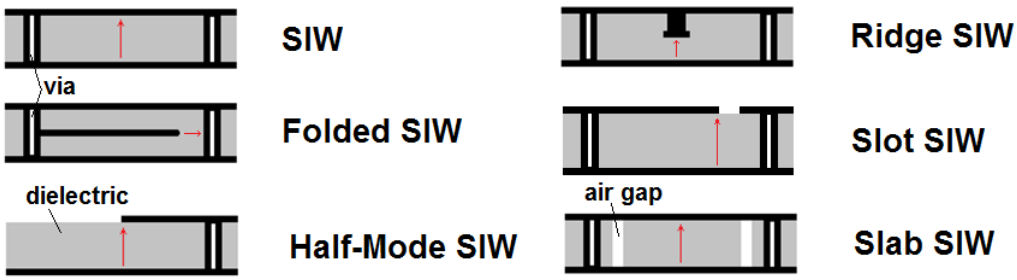

Fig. 2.3 substrate integrated waveguide variants

A combination of the Slab and Ridge versions is also possible, termed the Ridge Substrate Integrated Slab Waveguide (RSISW)[13]. Lastly there is also Slot SIW (SSIW) [14, 15] which allows formation of several devices including travelling wave attenuators and leaky antennas. SSIWs will be discussed further in chapter 4. Outlines of the main SIW structures are shown in Fig. 2.3, with the location of the electric field maximum indicated by a red arrow, and are discussed in more detail in section 2.7.

2.1 Wave equations

Some background is required to describe the movement (or propagation) of waves through transmission lines or waveguides. The time harmonic wave, which varies with time and distance is described by $e^{(j\omega t-\gamma z)}$, where z is the direction of propagation. For plane waves in a lossy medium, consideration needs to be given to both conduction and dielectric losses. Thus we define a complex propagation constant as:

$$\gamma = \alpha + j\beta \qquad \text{(Eq.2.1)}$$

Where α = Attenuation Constant (Nepers per meter) (real part of γ)

β = Phase Constant (radians per meter) (imaginary part of γ)

γ describes the degree of attenuation and the phase and group velocities. The fields in the wave must satisfy both the boundary conditions and the wave equation, which is derived from Maxwell's equations (see chapter 1). Assuming there is no net charge density in the dielectric and that any conduction currents are included with permittivity then $k^2 = \omega^2\mu\varepsilon$ will be complex. Where *k* is a constant of the medium for a particular angular frequency (ω) and is called the *wave number*.

The wave equations, which reduce to the Helmholtz equations for phasor fields [16] are:

$$\nabla^2\boldsymbol{E} = -k^2\boldsymbol{E} \text{ and } \nabla^2\boldsymbol{H} = -k^2\boldsymbol{H} \qquad \text{(Eq.2.2)}$$

The Laplacian (Nabla or del operator squared term) may be split such that:

$$\nabla^2\boldsymbol{E} = \nabla_t^2\boldsymbol{E} + \frac{\partial^2\boldsymbol{E}}{\partial z^2} \qquad \text{(Eq.2.3)}$$

The first term is the Laplacian in the transverse plane, and the last term is derivatives in the axial direction, along with the propagation function $e^{-\gamma z}$,

$$\frac{\partial^2 \boldsymbol{E}}{\partial z^2} = \gamma^2 \boldsymbol{E} \qquad \text{(Eq.2.4)}$$

The wave equations travelling in the +z direction are then:

$$\nabla_t^2 \boldsymbol{E} = -(\gamma^2 + k^2)\boldsymbol{E} \qquad \text{(Eq.2.5)}$$

$$\nabla_t^2 \boldsymbol{H} = -(\gamma^2 + k^2)\boldsymbol{H} \qquad \text{(Eq.2.6)}$$

These equations must be satisfied in the dielectric regions of the waveguides. In a loss-less medium, ε and μ are real numbers, then k is real. Solutions to the above equations for a basic propagating plane wave may then be found.

2.2 SIW waveguide modes and propagation

TEM propagation is a mode of wave energy movement where the electric and magnetic field lines are restricted to directions perpendicular (transverse) to the direction of propagation. Traditional hollow rectangular waveguides, as described in [17] are able to propagate TE and TM modes, but not TEM; due to there being only one conductor present. The cut-off frequencies for the TE and TM modes are calculated from $f_c = \frac{c}{2\pi\sqrt{\varepsilon_r}}\sqrt{\left(\frac{m\pi}{a}\right)^2 + \left(\frac{n\pi}{b}\right)^2}$, this is the frequency below which the specified mode will not propagate (derivation to follow). However the Fundamental Mode for rectangular waveguides, which is the first propagating mode is defined with *m = 1* and *n = 0*, and conventionally with waveguide width greater than height ($a>b$) is termed $TE_{1,0}$ **.**

In free-space (deemed air or a vacuum) EM waves travel at the speed of light and the frequency and wavelength are reciprocals ($c = f\lambda$). However, when the EM wave is travelling in a lossless medium it is slowed by the effect of the dielectric, this changes the wavelength of the EM wave. Hence in a medium (or dielectric):

$\lambda_m = \frac{v_m}{f}$, where $v_m = \frac{1}{\sqrt{\mu_0 \mu_r \varepsilon_0 \varepsilon_r}} = \frac{c}{\sqrt{\varepsilon_r}}$ if μ_r=*1* as $c = \frac{1}{\sqrt{\mu_0 \varepsilon_0}}$

In addition, when an EM wave is 'channelled' within a waveguide, the wavelength also changes, as it is a direct function of the waveguide parameters. For TEM waves $\lambda_g = \frac{2\pi}{K}$, and for TE and TM

waves $\lambda_g = \frac{2\pi}{\beta}$. Where k_0 is 'free-space' wave number, k is the wave number, and k_c 'cut-off' wave number for mode being considered.

$$k_o = \frac{\omega}{c} = \frac{2\pi f}{c} \text{ in medium } k = \frac{\omega}{v_m} = \frac{\omega\sqrt{\varepsilon_r}}{c} = k_0\sqrt{\varepsilon_r} \quad \text{(Eq.2.7)}$$

$$\text{and } k_c = \sqrt{\left(\frac{m\pi}{a}\right)^2 + \left(\frac{n\pi}{b}\right)^2} \quad \text{(Eq.2.8)}$$

$$\text{phase constant } \beta = \sqrt{\varepsilon_r k_0^2 - k_c^2} \quad \text{(Eq.2.9)}$$

(also known as phase change constant or coefficient)

Note: the effective relative permittivity is defined as: $\varepsilon_{reff} = \left(\frac{\beta}{k_0}\right)^2$ (Eq.2.10)

Using λ_c and rearranging to obtain the cut-off frequency f_c we obtain:

$$f_c = \frac{v_m}{2\pi} k_c \quad \text{(Eq.2.11)}$$

Then using $v_m = \frac{c}{\sqrt{\varepsilon_r}}$ and the above value for k_c :

$$f_c = \frac{c}{2\pi\sqrt{\varepsilon_r}} \sqrt{\left(\frac{m\pi}{a}\right)^2 + \left(\frac{n\pi}{b}\right)^2} \quad \text{(Eq.2.12)}$$

Now if we consider the standard (rectangular) SIW with waveguide width a_{eff} and height b_{eff}, the fundamental mode $TE_{1,0}$ cut-off frequency, with $m = 1$ and $n = 0$ is then:

$f_{c(1,0)} = \frac{c}{2\pi\sqrt{\varepsilon_r}} \sqrt{\left(\frac{\pi}{a_{eff}}\right)^2 + 0}$ which simplifies to

$$f_{c(1,0)} = \frac{c}{2a_{eff}\sqrt{\varepsilon_r}} \quad \text{(Eq.2.13)}$$

Which in a normal rectangular waveguide would give $a_{eff} = a$

$$\text{now } k_c = \pi / a_{eff} \quad \text{(Eq.2.14)}$$

Finally for HMSIW with the waveguide width $a_{eff} = 2a_{HM}$ the $TE_{1,0}$ cut-off mode becomes:

$$f_{c(1,0)} = \frac{c}{4a_{HM}\sqrt{\varepsilon_r}} \quad \text{(Eq.2.15)}$$

The $TE_{1,0}$ mode for half-mode waveguides is sometimes referred to as $TE_{1/2,0}$ to differentiate between half and full waveguide structures, this convention will be adopted in this work.

Due to the breaks in the via walls SIWs do not support TM modes [2], but have a similar fundamental $TE_{1,0}$ mode, where the electric current density runs vertically on the via side walls. The propagating modes for SIWs are sometimes referred to as $TE_{n,0}$ modes, where n = 1, 2,..

As shown in Fig. 2.3 the electric field is vertical within the SIW, with a maximum defined by its symmetry, which for the standard SIW is the centre of the waveguide. PCB laminates are generally relatively thin, so for SIWs the *a/b* ratio is much higher, sometimes as high as 20:1. However, the main issue the reduced height causes is a reduction in the impedance the propagating wave encounters within the waveguide (compared to lower *a/b* ratios), due to an increased capacitance per unit length.

The SIW cut-off frequency (f_c) for $TE_{1,0}$ mode is fixed by the waveguide width, and its operation bandwidth is limited to one octave bandwidth, so from f_c to $2f_c$. The $TE_{2,0}$ begins at $2f_c$ which is its mode cut-off frequency. Variants of the SIW structures may extend operational bandwidth by pushing the cut-off frequency of the next mode beyond that of one octave. An example of SIW modes are shown in Fig. 2.4 and 2.5 for a RSIW (rectangular SIW), designed for operation with a cut-off of 10 GHz for the $TE_{1,0}$ mode ($a_{eff} = 4.7$ *mm),* when the frequency exceeds twice this frequency the propagation mode changes to the next higher order mode that of $TE_{2,0}$. Fig. 2.5 shows two electric field maximums across the width of the waveguide, the plot also shows some leakage radiation as the waveguide is now beyond its design parameters, a smaller via pitch (and via diameter) would resolve this leakage problem. The leakage in Fig. 2.5 is not uniform due to numerical error within the simulation, in part due to the solution frequency being set for the fundamental mode shown in Fig. 2.4.

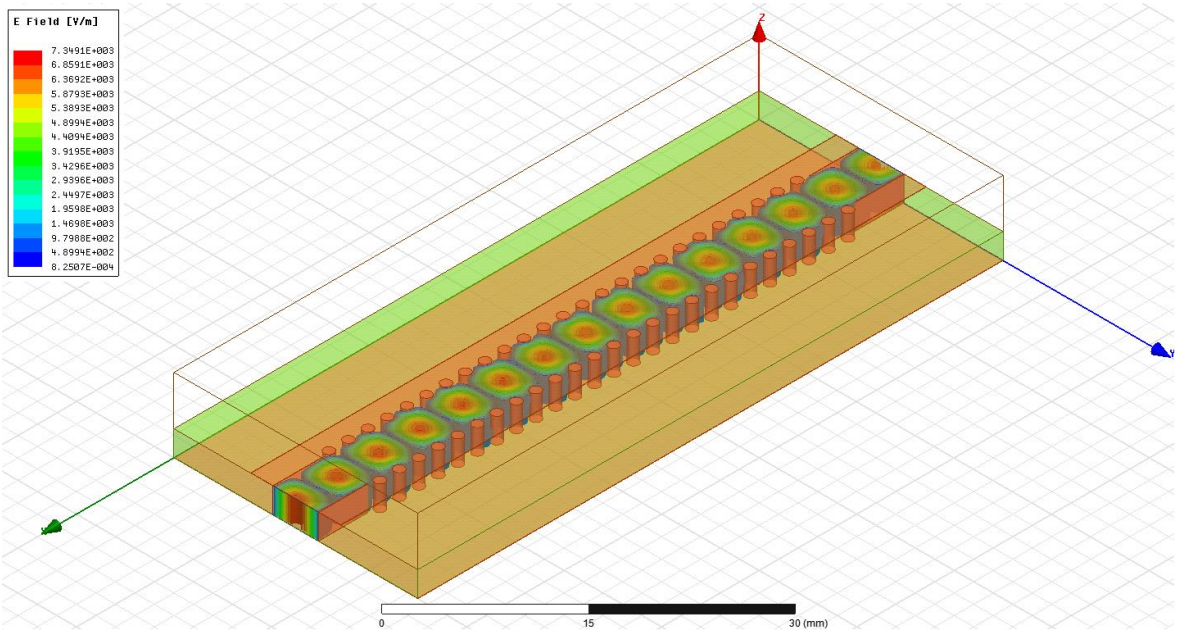

Fig. 2.4. TE_{10} mode in SIW Waveguide (6010 material 15 GHz) – electric field plot

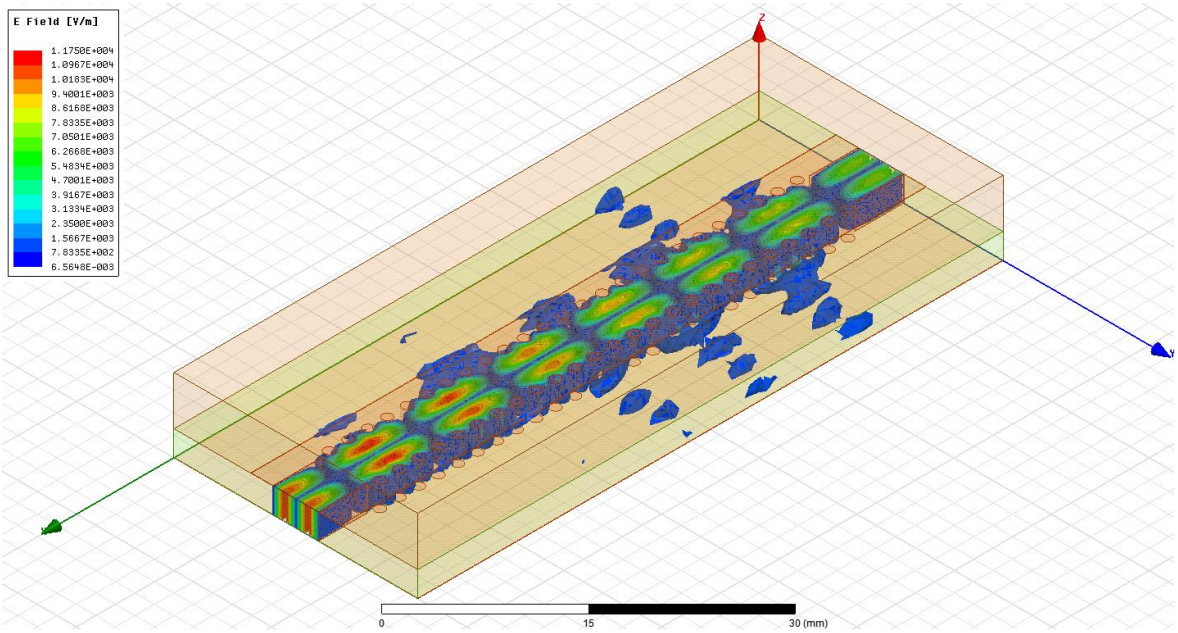

Fig. 2.5. TE_{20} mode in SIW Waveguide (6010 material 21 GHz) – electric field plot

2.3 SIW Analysis Techniques

There are a number of different techniques available for analysing integrated waveguides, these are outlined in brief with comments on the advantages and disadvantages

2.3.1 Equivalent rectangular waveguide

SIW modes exhibit similar characteristics to conventional rectangular waveguide modes [18-20]. The SIW may be modelled using rectangular waveguide theory with the equivalent waveguide width and allowance for the dielectric within the SIW structure. The equivalent width formula is detailed in section 2.6. The impedance of SIW structures may vary slightly along the direction of propagation due to the intersections of the via wall segments.

2.3.2 Full wave EM modelling

Full wave electromagnetic modelling provides a more detailed analysis of SIW structures. Splitting the waveguide into cells can provide more accurate characterization of the SIW to achieve the curves of propagation and attenuation constants.

Full structural analysis with all components may also be performed, depending on the geometries investigated. Simplification techniques for large models are also possible, such as using lines of

symmetry to create perfect magnetic boundaries to halve the computational model, also depending on the model structure the via walls mat be replaced by perfect electrical boundaries to reduce simulation complexity. The analysis techniques for modelling of SIW interconnects may be characterised as outlined in the following sections [1, 21, 22].

2.3.2.1 Eigen value problem

The scattering matrix is a representation of network modelling that encompasses direct measurement techniques and includes the concepts of incident, reflected and transmitted waves. The scattering matrix provides a complete description of the network as seen at each of its ports. Complex networks may be modelled with a number N ports equating to an *n by n* matrix [1], however SIWs are generally considered as a two port network and modelled by a *2 by 2* matrix. The scattering matrix relates the voltage waves incident on the ports (V^-) to those reflected from the ports (V^+). The scattering matrix may be measured or calculated depending on the structures complexity and network analysis techniques available. Once the scattering parameters of a network are known, conversion to other matrix parameters, such as admittance, impedance and ABCD, may be performed. A two port scattering matrix is defined as:

$$\begin{bmatrix} V_1^- \\ V_2^- \end{bmatrix} = \begin{bmatrix} s_{11} & s_{12} \\ s_{21} & s_{22} \end{bmatrix} \begin{bmatrix} V_1^+ \\ V_2^+ \end{bmatrix} \qquad \text{(Eq.2.16)}$$

An equivalent ABCD matrix would be:

$$\begin{bmatrix} V_1 \\ I_1 \end{bmatrix} = \begin{bmatrix} A & B \\ C & D \end{bmatrix} \begin{bmatrix} V_2 \\ I_2 \end{bmatrix}, where\ [T] = \begin{bmatrix} A & B \\ C & D \end{bmatrix} \qquad \text{(Eq.2.17)}$$

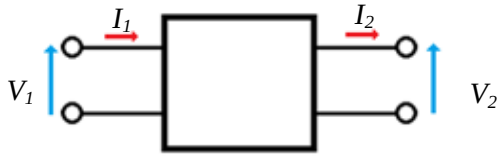

Fig. 2.6 SIW two port network.

Characterising the SIW unit cell as a two port network (or circuit) allows transformation matrices to be developed. Either the scattering matrixes or the more frequently used ABCD matrix. As the SIW is an H-plane structure ($TE_{n,0}$ modes only) rectangular waveguide modes need only be considered at each port. The ABCD matrix relates the modal voltages and the inward modal currents of the rectangular waveguide modes at the ports.

$$\begin{bmatrix} V_1 \\ I_1 \end{bmatrix} = \begin{bmatrix} A & B \\ C & D \end{bmatrix} \times \begin{bmatrix} V_2 \\ -I_2 \end{bmatrix} = e^{\gamma s} \begin{bmatrix} V_2 \\ -I_2 \end{bmatrix} \qquad \text{(Eq.2.18)}$$

From the ABCD two port matrix the periodicity of the EM fields at the SIW ports may be found (by applying Floquet-Bloch theorem). Defining the complex propagation constant (γ) at a frequency for the length of the analysed cell, this in turn leads to the eigenvalue matrix for which the eigensolutions (solved for each frequency of interest) giving the dispersion curves of the SIW modes. The i^{th} eigenvalue gives complex propagation constant γ_i of the i^{th} SIW mode, where $\alpha_i = Re(\gamma_i)$ and $\beta_i = Im(\gamma_i)$. The cut-off frequency f_c of the SIW dominant mode is defined where $\alpha = \beta$, alternatively in the lossless case where $\alpha = \beta = 0$, which can be used to determine the required SIW required width a_{eff}. For a propagating mode β needs to be greater than α and will therefore be real, at the cut-off frequency (when $\beta = 0$) there will be no propagation, the below cut-off when $\alpha > \beta$ there will be no propagation but an evanescent mode will occur; an evanescent mode, is one which exhibits an exponential decay.

An alternative method to obtain the eigenvalues for the mode spectrum of an SIW is using the Numerical Multimode calibration technique [23]. Here, characterisation of two different lengths of SIW leads to a generalised transition matrix.

The finite-difference frequency-domain (FDFD) method has scope for increased geometry and substrate material flexibility. This method gives the propagation constants directly for the specified frequency. Alternatively for a specified value of β the complex frequency may be calculated.

The method of lines (MoL) also provides a solution of the eigenvalues to obtain the propagation constants for SIWs [24]. With MoL the SIW structure is handled analytically in one direction and via segmentation in the other. MoL yields a matrix eigenvalue equation of the form equal to γBx , where γ is the complex propagation constant and x is related to the electric field components.

2.3.2.2 Integral equation techniques

The Method of Moments (MoM), is efficient for solving SIW due to its simple geometry, homogeneous medium and vertical field configuration and is more computationally efficient than finite-element and finite difference methods. The periodic structure of SIW enables it to be broken into cell based analysis with periodic boundaries, or simplified further using symmetry along the centre of the waveguide using a perfect magnetic wall. The current density J_p flowing along the surface of the metal post (or via), generates an associated electric field which may be expressed using Green's function:

$$\int_{S_p} \underline{G}(r,r').J_p(r')dS' = 0 \qquad \text{(Eq.2.19)}$$

Where S_p denotes the boundary of the metal post,

2.3.2.3 Surface impedance concept

With this method the rows of vias are represented as complex impedance walls and the propagation and attenuation constants are obtained by the transverse resonance technique [25]. Within the SIW the fundamental mode is represented as two plane waves (developed from rectangular waveguide theory [26]), propagating at an angle $\pm\theta$ w.r.t. the longitudinal direction. With k as the wavenumber at the operation frequency, the longitudinal component gives the propagation constant $\beta = kcos\theta$. At the cut-off frequency (f_c), for lossless waveguides $\beta=0$, meaning that at f_c the two waves propagate in opposite directions and $\theta = \pm 90°$. For lossy waveguides cut-off frequency is characterised by $\alpha = \beta$.

In the lossless case, at f_c two plane waves are 90° to the rows of vias, and are subject to a complex reflection coefficient (S_{11}). Which may be found in a number of ways including full wave MoM, simplifications may be made to the vias reducing to them to thin wires or square posts.

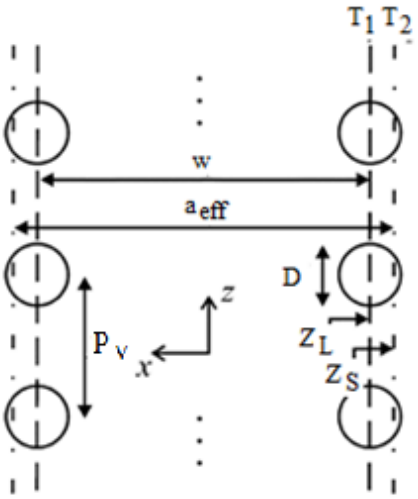

Fig. 2.7 Top view of an SIW with concept of impedance walls (modified from [25])
(*w* denotes via row pitch, a_{eff} shifted *effective* plane pitch, Δa is difference between them)

Starting with a trial value of f_c, a normalised impedance Z_L as seen by the plane wave at T_1 (on via row pitch donated *w* here) may be calculated from: $Z_L = \frac{1+S_{11}}{1-S_{11}}$. The via rows may be represented by a solid metal wall with surface impedance Z_s (on a shifted plane T_2). Impedance Z_L can then be transformed to surface impedance $Z_S = R_S(1+j)$, referred to the T_2 plane. Both R_s and separation Δa may be calculated from:

$$Z_L = r + jx = \frac{Z_s + jA}{1 + jZ_s A} \qquad \text{(Eq.2.20)}$$

Where r and x are real and Imaginary parts of Z_L and $A = tan(k_c \Delta a)$, $k_c = 2\pi/\lambda_c$ the complex wave number of the plane wave at cut-off.

The real and imaginary parts of above equation lead to two equations:

$$r = R_s[1 + A(r + x)] \qquad \text{(Eq.2.21)}$$
$$R_s(rA - xA - 1) = A - x \qquad \text{(Eq.2.22)}$$

By obtaining R_s from Eq.2.21 and substituting it into Eq.2.22, the resultant quadratic equation is obtained:

$$A^2(r + x) + A(1 - r^2 - x^2) + (r - x) = 0 \qquad \text{(Eq.2.23)}$$

Whose solutions yields the values of A, which then leads to plane separation Δa (from $A = tan(k_c \Delta a)$), leading to value of R_s from Eq.2.21.
In the case of lossless structures $a_{eff} = \lambda_c/2$. In the case of lossy structures, transverse resonance condition must be imposed, which is the summation of the impedances seen looking into both sides of the SIW structure must be zero, which resolves to:

$$a_{eff} = \frac{2}{k_c}\sqrt{Re\{cot^{-1}[R_s(1-j)]\}^2 - Im\{cot^{-1}[R_s(1-j)]\}^2} \qquad \text{(Eq.2.24)}$$

The process is reiterated, starting from the initial value of f_c until the condition on effective width a_{eff} is met. The calculation of the complete dispersion diagram of the SIW structure is then obtained by varying θ for both plane waves [21, 25].

Note: The transverse resonance condition is utilised further in section 4.3.1.

2.3.2.4 Finite difference time domain method

The FDTD method is a modelling algorithm based on the direct numerical solution of Maxwell's equations in the differential time-domain form. The important feature of the FDTD method is that broad-band frequency information can be provided in a single-pass simulation. It is a popular and flexible numerical technique applied to the full-wave modelling of SIW components. It suffers from extended computation time and large memory use, so is not overtly

efficient, especially when calculating the circuit parameters (e.g. scattering matrix). This may be offset by using a TL calibration technique (thru-line) [27]. The analysis domain is subdivided into sections similar to: input line, device under test and output line. With the aim to determine the transfer matrix T_D, expressed in the form:

$$T_D = T_{IN} T_{DUT} T_{OUT} \qquad \text{(Eq.2.25)}$$

The thru matric $T_T = T_{IN} T_{OUT}$, which leads to line connect of a straight SIW section of equal length to the DUT, giving the matrix:

$$T_L = T_{IN} T_{SIW} T_{OUT} \qquad \text{(Eq.2.26)}$$

With manipulation of three matrices and solution of eigenvalue problems, it leads to the transmission matric T_{DUT} as required [21, 27]. Note that care should be taken with the surrounding boundary conditions to take into account possible radiation effects. Perfectly matched layers which do not reflect at the interface should be considered and utilised if deemed appropriate. Care should also be given to the length of the in and out transitions, and long enough for the correct propagation mode to establish, also with the SIW and DUT sections.

2.3.2.5 Method of moments

MoM, sometimes known as boundary element method (BEM), is an efficient boundary integral solver based on using a small surface / volume ratio. The structures are broken into sections by a constructed ‘mesh’. The smaller the mesh the greater the accuracy, but the larger the amount of calculations (hence more memory and time required). At each mesh boundary the integral equations are solved by defining the boundary conditions for the adjacent mesh cell, where cells are often tetrahedral in shape. ANSYS HFSS is used as the primary EM field solver in this research, its integral equation solver (HFSS-IE) uses the method of moments (MoM) technique to solve for the sources or currents on the surfaces of conducting and dielectric objects in open regions. HFSS-IE is effective for radiation and scattering studies mostly conducting structures. Adaptive refinement is used to generate the optimum mesh, and the solver uses the adaptive cross-approximation (ACA) method in conjunction with an iterative matrix solver to reduce memory and complexity requirements.

2.3.2.6 Boundary integral resonant mode expansion method

The BI-RME method is a hybrid integral / modal technique, developed for the modelling of classical waveguide components. Originally applied to the modelling of SIW components in the lossless case. Under the assumption of negligible radiation loss, the components can be laterally closed by fictitious metal walls without modifying their physical behaviour. The BI-RME method allows characterizing SIW components through their generalized admittance matrix *Y* expressed in the form of a pole expansion in the frequency domain, relating modal currents and voltages of the port modes. The *ij-th* entry of matrix *Y* is given by:

$$Y_{ij}(\omega) = \frac{A_{ij}}{j\omega} + j\omega B_{ij} + j\omega^3 \sum_{m=1}^{M} \frac{C_{im}C_{jm}}{\omega_m^2(\omega_m^2 - \omega^2)} \qquad \text{(Eq.2.27)}$$

where *i* and *j* refer to the port modes, and *M* is the number of resonances of the cavity obtained by short circuiting the ports of the building block. The terms A_{ij} and B_{ij} are related to the low-frequency behaviour of the admittance matrix, ω_m is the resonance angular frequency of the *m-th* mode of the cavity obtained by short circuiting the ports, and C_{im} is related to the coupling between the *i-th* port mode and the *m-th* cavity mode. The quantities A_{ij} , B_{ij} , C_{im} and ω_m are frequency independent and are calculated efficiently by the BI-RME method. Once these quantities are known, the admittance parameters of the SIW component can be computed at any frequency. The major advantage of the BI-RME method is the possibility to determine in one shot the wideband expression of the frequency response of the SIW component, thus avoiding repeated frequency-by-frequency electromagnetic analyses [21, 28, 29].

2.3.3 Equivalent circuit models of SIW discontinuities

There are a number of discontinuities that may be introduced into an SIW structure, such as: inductive vias (or posts), width step changes (increase and decease), iris windows, bends and junctions (e.g. T-junction), shorts, shunts, slots, and opens. The use of equivalent circuit models is an important design tool for SIW circuits; it provides initial design information that then should be optimized to achieve the best performance. However, modelling of complete and complex waveguide circuits is time consuming, segmentation helps significantly; especially if there are duplicate sections. Each segment (or section) is characterised for scattering or admittance matrices then combined to determine the frequency response of the entire circuit. A further efficiency is obtained, if the segments are derived from equivalent circuits rather than full-wave analysis. The

detailed description of equivalent models will not be investigated in detail here, as there a number of sources for SIW readily available [2, 21, 29, 30].

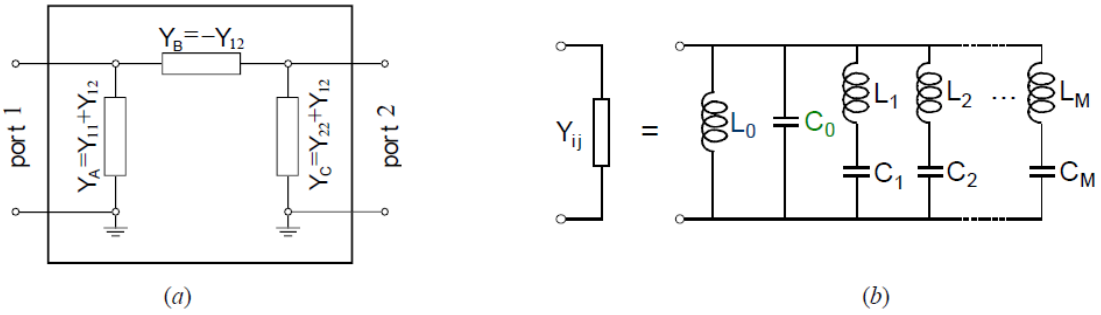

Fig. 2.8 Equivalent circuit model from for lossless two port SIW component (a) π-type (b) admittance circuit model [30]

Two examples are shown in Fig 2.8 for an SIW component, as two port lossless circuit models, an admittance π-type lumped circuit model and by a network of capacitors and inductors. From the BI-RME method [Eq.2.27], the lumped elements can be analytically obtained.

$$L_{0,ij} = \frac{1}{A_{ij}} \quad , \qquad C_{0,ij} = B_{ij} - \sum_{m=1}^{M} \frac{C_{im}C_{jm}}{\omega_m^2} \quad , \qquad L_{m,ij} = \frac{1}{C_{im}C_{jm}} \quad , \qquad C_{m,ij} = \frac{C_{im}C_{jm}}{\omega_m^2}$$

The model can be extended to lossy circuits by using a similar approach, by adding a resistor in parallel to L_0 and C_0, and replacing the *LC*-resonators with *RLC*-resonators [28].

2.4 Losses in SIW

Energy propagation has the unavoidable consideration that transmission mediums are not perfect, by which we refer to *perfect* being that all energy injected into the transmission line reaches the end; this is termed lossless, as in no loss of energy. There are several loss mechanisms associated with SIWs that need to be considered when designing them into microwave circuits. Conductor and dielectric losses are also associated with metallic rectangular dielectric filled waveguides, however breaking the solid side walls into vias adds an additional loss mechanism associated with the periodic placement, finite energy will leek between the gaps leading to radiation loss.

The losses may be added together to give the total attenuation constant for the SIW, where α_C is the attenuation constant due to conduction losses, α_D is the attenuation constant due to dielectric losses and α_R is the attenuation constant due to radiation losses, hence:

$$\alpha_{Total} = \alpha_C + \alpha_D + \alpha_R \qquad \text{(Eq.2.28)}$$

Conduction loss is a measure of the power dissipated in the conductor as the wave energy passes through the waveguide. From established theory [26] the conduction loss for a rectangular waveguide of width a_{eff}, height h, metal conductivity σ_c, filled with dielectric of relative permittivity ε_r and SIW cut-off f_c at frequency f is given by:

$$\alpha_C = \frac{\sqrt{\pi f \varepsilon_0 \varepsilon_r}}{h\sqrt{\sigma_c}} \frac{1+2(f_c/f)^2 h/a_{eff}}{\sqrt{1-(f_c/f)^2}} \qquad \text{(Eq.2.29)}$$

It is worth noting that α_C is proportional to the inverse of dielectric thickness, so increasing h (up to the limit to maintain a/b ratio) will reduce conductor loss, also varying the via diameter (D) and via spacing (P_v) has little overall effect on α_C [21].

The dielectric loss is linked to the loss tangent (Tan δ) of the associated dielectric. Similar to conduction loss, from established theory [21] for the fundamental mode of an SIW structure:

$$\alpha_D = \frac{\pi f \sqrt{\varepsilon_r}}{c\sqrt{1-(f_c/f)^2}} Tan\delta \qquad \text{(Eq.2.30)}$$

Where c is the speed of light and as before f_c is the SIW cut-off frequency. With α_D directly proportional to the square root of the relative permittivity multiplied by the loss tangent careful choice of appropriate material properties is essential.

The radiation loss from the periodic via gaps, will be reduced if the via pitch is decreased or the via diameter is increased, but practical considerations for fabrication tolerances need to be considered. There is a condition for optimum spacing to minimise the radiation loss which leads to the pragmatic design rule of:

$$P_v/D = 2 \qquad \text{(Eq.2.31)}$$

Where P_v is the longitudinal via pitch in the side wall and D is the via diameter, it has been shown however that a ratio of less than 2.5 will result in negligible radiation loss [21, 25, 31].
For a given frequency, a waveguide will be the most efficient transmission line when compared with coaxial line (~10x dB greater loss than waveguide) or MMICs transmission lines, microstrip or coplanar waveguide (~10x dB greater loss than coax), stripline is slightly higher than coax. The different loss mechanisms behave differently over frequency, metal loss is proportional to the square root of frequency, the dielectric loss is proportional to frequency and the dielectric conduction loss is constant over frequency.

2.5 SIW Synopsis

The concept of substrate integrated waveguides was introduced in 1994 where the structure was identified within a Japanese patent [3], but it is the work of Ke Wu and his group in Montreal that laid the true foundations [2, 6, 18, 24, 25, 31-33]. Prof. Wu is attributed to several hundred papers associated with SIW, the earliest being in 2002. The University of Kent, School of Engineering, Microwave and Wireless Communications group has also been active in this area from 2003 and published several related articles [7, 9, 34-39].

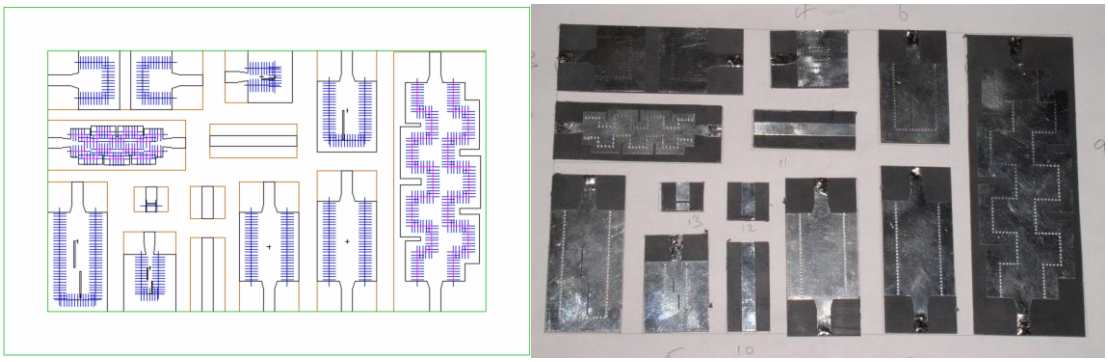

Fig. 2.9 Range of SIW planar components (CAD data and fabricated structures)

The study of SIW components and structures has been developed as a field of microwave knowledge over the past two decades and is still expanding. An example of the range is shown in Fig 2.9 which includes waveguides, transitions, filters, antennas and calibration components [7]. To achieve correct operation, which covers wave propagation mechanisms, leakage characteristics and dispersion losses, a number of key design requirements are required. A correctly designed SIW will provide a good transmission channel, with low loss, allowing for integration with other circuit components.

For decades rectangular waveguides (RWG) have been used as a means of low loss guidance of microwave signals. RWGs are immune from radiation losses and have excellent isolation. Furthermore, there is a wealth of design methodologies and components available to the microwave engineer. Unfortunately, due to their three-dimensional nature, RWGs can be difficult to manufacture and integrate with planar circuitry at millimetre-wave frequencies, which is essential for complete systems.

Novel techniques have been presented for the fabrication of waveguides relying on conventional microwave integrated circuit fabrication. Uchimura et al. [40] used laminate technology to form a dielectric-filled waveguide using multilayer laminated substrates. More recently multilayer low

temperature co-fired ceramic (LTCC) has been used [41]. In both these techniques vias are used to form the sidewall of the guides with metallisation on the top and bottom substrates to form the top and bottom waveguide walls. Single layer alternatives have also been produced [6]. In [42] a two dimensional lattice of plated via holes are used to form the sidewalls of a RWG using microwave laminates. Upper millimetre-wave structures have also been produced using thick-film technology [43] where trenches are etched in a photoimageable dielectric and then screen-printed with conductive paste. All of these techniques have the advantage of easy integration with planar circuitry and comparatively simple and cheap manufacture based on existing fabrication techniques. Furthermore, since the waveguides are dielectric filled both the broad wall dimension and the guided wavelength is reduced by a factor of $\varepsilon_r^{-1/2}$, where ε_r is the dielectric constant of the material. This allows highly integrated structures to be formed using high dielectric constant substrates. Several devices have been proposed using the various types of fabrication including filters [32, 44, 45] and low loss transitions to microstrip [6, 43] and CPW planar guides [4].

2.6 SIW design rules summary

The relationship between the dielectric material (its properties such as dielectric constant and loss tangent along with its thickness) and the metalized holes (vias) diameter and spacing to form the waveguide wall form design guidelines for standard SIWs, and have been developed over a number of years. A design process is outlined highlighting the key criteria that should be met to achieve successful operation.

The first key element for an integrated waveguide is the choice of the substrate itself. The material selection for dielectric constant (ε_r) and dielectric loss (or loss tangent *Tan* δ) needs to be appropriate for the frequency range required and fabrication process to be used. Special attention needs to be considered when the guided wavelength starts becoming close to the physical layout dimensions. For microwave frequencies use of PTFE laminates offers a range of dielectric constants with low dielectric losses. Thickness of copper along with surface roughness need to be considered, plus requirements for strength and rigidity, as PTFE on its own is easily deformed and damaged.

To define the via wall parameters, primarily the via diameter (D) and the via spacing (P_v), need to consider the amount, if any, of leakage is to be allowed. Design rules for the via size and spacing [2, 21, 25] defined that the number of vias per wavelength should be less than 20, and that at the centre operating bandwidth the via pitch should be:

$$P_v < 0.35 \times \lambda_c. \qquad \text{(Eq.2.32)}$$

This leads to the via pitch design rule:

$$0.05 < \frac{P_v}{\lambda_c} < 0.25 \qquad \text{(Eq.2.33)}$$

And the limit via pitch to via diameter is: $\frac{P_v}{D} \leq 1.2$, which leads to the via diameter design rule target:

$$\frac{P_v}{D} = 2 \qquad \text{(Eq.2.34)}$$

With the material chosen and the via wall defined, the value of the cut-off frequency needs to be decided from the operational requirements. Then the effective width of the SIW may be determined from:

$$a_{eff} = \frac{c}{2\pi f_{c(1,0)}\sqrt{\varepsilon_r}} \qquad \text{(Eq.2.35)}$$

This is a rearrangement of the equation in section 2.2.

With the effective width of the SIW now defined, the pitch between the via walls needs to be calculated. The via diameter and pitch effect the position of the reflecting electric wall, a popular calculation from [18] provides the via wall pitch value (*W):*

$$W = a_{eff} + D^2/(0.95 \times P_v) \qquad \text{(Eq.2.36)}$$

Where *W* is the transverse via pitch width (between via walls), *D* is the via diameter and P_v is the via longitudinal pitch (in the via walls).

It is worth noting that there are other formulae developed to describe the effective width of SIW. The two main equations are shown here and are compared in Fig. 2.10 , which shows that the discrepancies between the two equations are relatively small for small waveguide widths, and negligible for larger widths, hence the reason for using the first equation in this work.

$$W_{eff} = W - D^2/(0.95 \times P_v) \text{ [18]} \qquad \text{(Eq.2.37)}$$

$$W_{eff} = W - 1.08 \times (D^2/P_v) + 0.1 \times (D^2/W) \text{ [31]} \qquad \text{(Eq.2.38)}$$

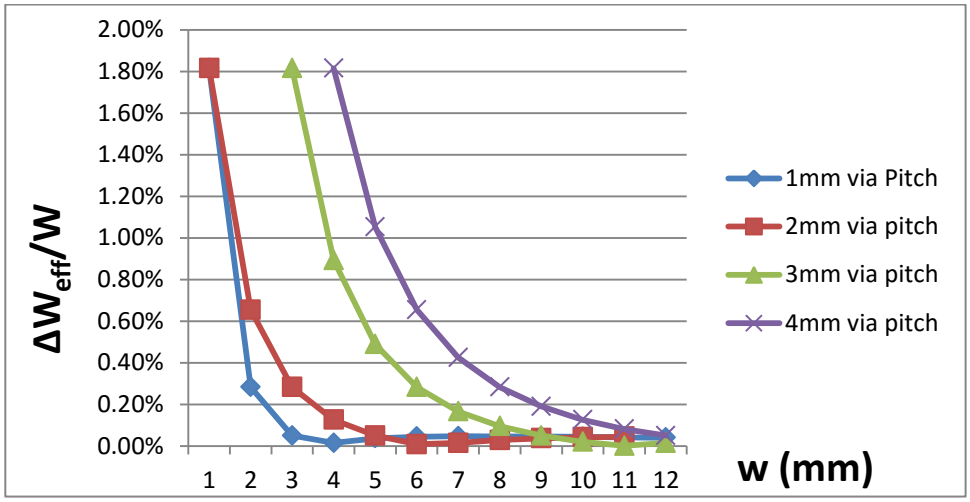

Fig. 2.10. SIW effective width formulae comparison

There are specific design rules for the individual SIW structures, but these are the general SIW rules for the waveguide width and via walls. A single row via wall, if designed correctly for the frequency of operation should be sufficient to contain the wave. However, multiple rows may be used to form the via wall, example configurations are shown in Fig. 2.11 [7].

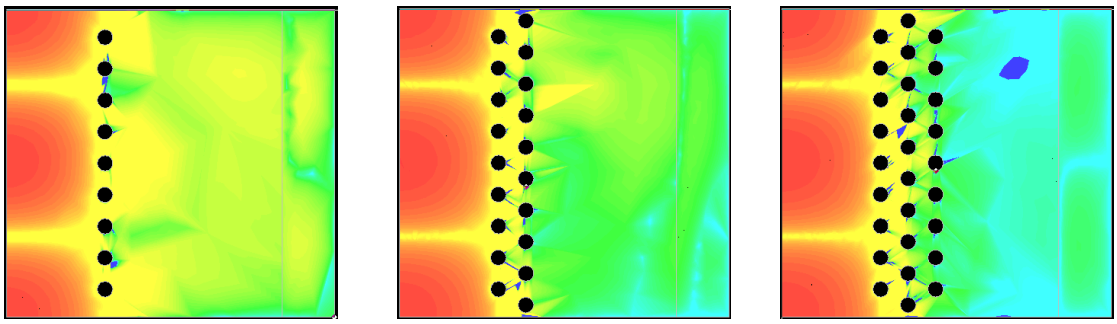

Fig. 2.11 HFSS Simulations for X band, with RT duroid 5880 1, 2 and 3 rows of vias (electric field logarithmic plot, red maximum, dark blue minimum)

At higher frequencies there will be a physical limit for the use of vias due to fabrication limits. For conventional PCB fabrication a minimum via diameter of D=0.2 mm, gives a via pitch P_v=*0.4 mm*, then from (Eq.2.32) $1.14 < \lambda_c$, which in freespace is a centre frequency of ~260 GHz, but in a dielectric of ε_r=10.2 is a centre frequency of ~80 GHz. Cost implications and fabrication limits would mean that these walls could only be quite short. Alternatively, the via wall may be replaced with a plated slot [46], or by an alternative structure altogether (See Fig.2.12)

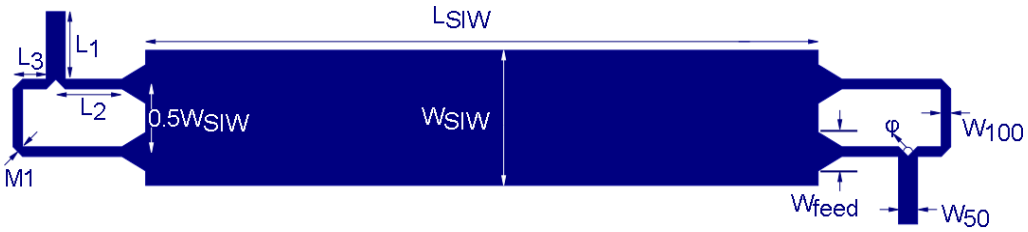

Fig. 2.12 Half-mode SIW without vias [38]

In Fig.212 instead of using a single HMSIW, two of them are placed side by side without vias, facing opposite each other. At the interface, the electric field is forced to be zero by applying 180° phase excitation at the centre of each section.

2.7 SIW Structures and Components

There are several variations of SIW that improve certain aspects of performance that require mentioning. By introducing impedance discontinuities into the waveguide filters may be formed or by removing vias from a wall adjoining two SIWs cross coupling may be achieved. SIW structures instead of transporting wave energy may be used as focussing cavities to create oscillators or increase bandwidth responses for aperture antennas. By adding apertures into the top and bottom surfaces, controlled radiation is achieved and slot antennas or leaky wave antennas are able to be formed. These are discussed in various levels of depth, further information if required is provided in these general summarises [2, 21].

The Folded SIW (FSIW or SIFW) [9, 15] (Fig.2.13) enables the size to be reduced by adding additional layers, i.e. its physical real estate on the PCB, but this adds complexity and thus cost. Measured against a comparative SIW the non-radiative losses are increased due to the large amplitude of the electric field in the gap region, as a consequence loss becomes larger for smaller gaps and less for larger ones (but this increases the physical size).

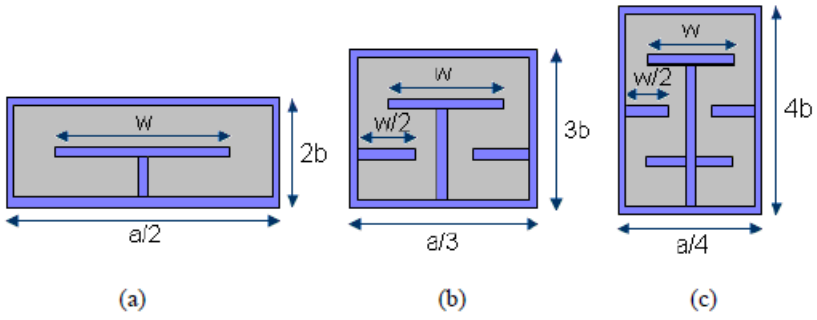

Fig.2.13 FSIW (a) two layers (b) three layers (c) four layers [15]

By adding additional periodic holes into the SIW a bandgap structure can be produced to form Substrate Integrated Slab Waveguide (SISW) [47] which can also increase the operating bandwidth up to 40% [2]. As in traditional box waveguide, adding a central focal point into the waveguide to form Ridge SIW [13, 48] (Fig.2.14) can increase the bandwidth by up to 70%, but this also adds complexity and hence cost.

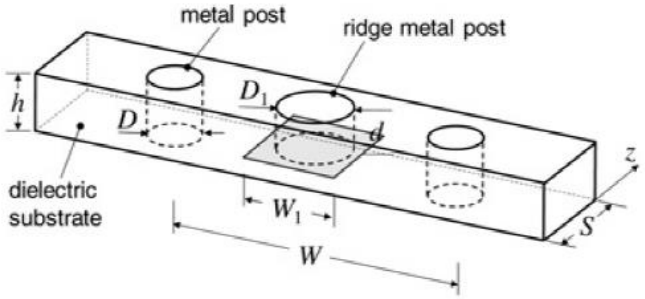

Fig.2.14 Ridge SIW cross-section [13]

The Half-Mode SIW (HMSIW) [10, 11, 38, 49] (Fig.2.15) enables an increase in the one octave bandwidth by extending the operation of the mode $TE_{1/2,0}$ to $TE_{3/2,0}$ as well as reducing the physical size of the waveguide and eliminating one of the via walls. The HMSIW is based on the idea of forming a virtual magnetic wall for the fundamental mode at the symmetrical centre along the line of propagation. Removing half of the waveguide leaves the field practically unchanged. The width of the HMSIW may be calculated by simply reducing the standard SIW width calculation by half. It should be noted that a more accurate design should take into account the effect of the fringing fields which will effect the waveguide width and alter the cut-off frequency. Losses in HMSIW are comparable to SIW, apart from a small frequency band just above cut-off frequency, here the open side of the HMSIW behaves like a slot with uniform field distribution and radiation loss is significant [11]. Half-mode SIWs will be discussed further in chapter 5.

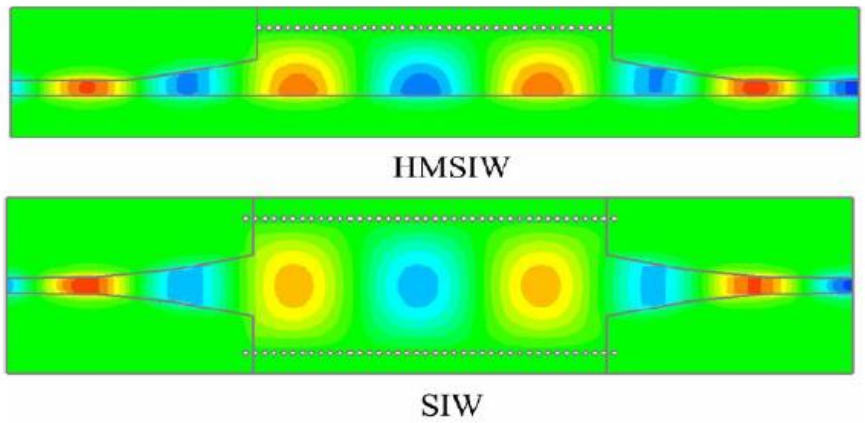

Fig.2.15. HMSIW and SIW field comparison. [10]

Slot SIW (SSIW) have a small gap on one of the larger conducting surfaces, breaking the SIW into two sections, a main waveguide section which acts similar to that of a HMSIW and a shunt waveguide section. The propagation characteristics for SSIW are overall similar to HMSIW, but they also offer additional features such as easier integration with other microwave structures and the option of shifting the cut-off frequency by shorting the gap. SSIWs are discussed in more depth in chapter 4, where there are used in a novel travelling wave attenuator application and as a basis for a new type of waveguide filters.

A few transitions for SIWs have been developed, with probably the most common being the microstrip-to-SIW (See Fig 2.16.a) also used with SSIW in chapter 4. The taper transition from microstrip-to-SIW graduates the change to reduce discontinuity impact, its simple geometry and ease of fabrication as well the ability to achieve a good impedance match are the main benefits for the microstrip-to-SIW transition, in addition it does not limit the bandwidth of the SIW itself.

Coplanar waveguide has also been used for CPW-to-SIW transitions, particularly on thick substrates where microstrip is not feasible. The most common CPW-to-SIW uses 90° bends of each slot within the SIW [2, 4] (Fig. 2.16.b), cavities may be added around the bends for high permittivity substrates, or a stub can be added to the CPW line to improve the match. An alternative transition developed for grounded CPW is shown in Fig.2.16.c, where a current probe is used to feed the SIW. The main problem for CPW-to-SIW transitions is that they limit the bandwidth of the SIW operation.

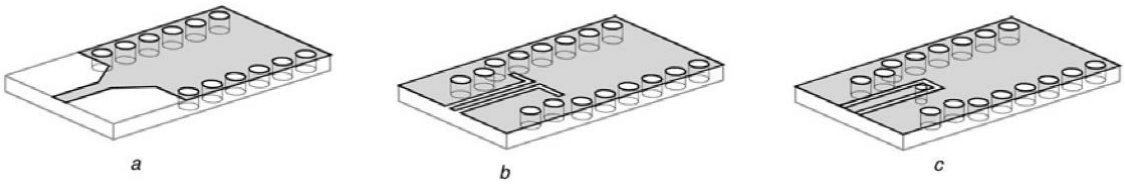

Fig. 2.16. SIW Transitions: (a) microstrip (b) CPW 90° bend (c) CPW with current probe. [2]

There are a variety of SIW components that have been developed; these can be split into passive components, active components and antennas. Passive components include filters [50, 51], couplers [52], diplexers [53](or multiplexers), power dividers [54], phase shifters [55], circulators [56], baluns [57], magic-T connections [58] and six-port circuits [59]. The range of active SIW circuits includes oscillators [5], mixers [60] and amplifiers [61]. Planar SIW antennas will be discussed in chapter 3.

One of the SIW structures that has been directly investigated is the SIW coupler. Generating apertures in the wall between two adjacent waveguides will allow a propagating wave from one to

'couple' into the adjacent waveguide. Controlling the aperture width and position will dictate the amount of coupling that occurs; an outline of the design process follows with a fabricated example and measurements made.

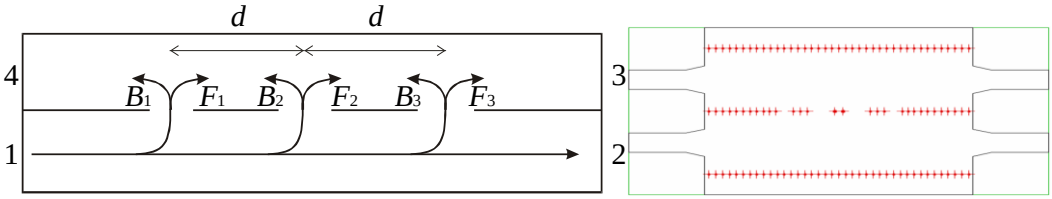

Fig. 2-17. Waveguide coupler schematics.

Fig. 2.17 shows the schematic of a waveguide coupler and comparative layout outline, the coupled components in the forward direction all travel the same distance and combine in phase to produce a coupled signal at port 3. The coupling coefficient is given by [1]:

$$C = -20\log_{10}\left|\sum_{n=0}^{N} F_n\right| \text{ dB} \qquad \text{(Eq.2.39)}$$

where F_n is the forward coupling coefficient of the n^{th} hole and $N + 1$ is the number of coupling holes. The coupled components in the backward direction combine out of phase at port 4 due to the different distances travelled by each component. This gives a directivity of:

$$D = -C - 20\log_{10}\left|\sum_{n=0}^{N} B_n e^{-2j\beta nd}\right| \text{ dB} \qquad \text{(Eq.2.40)}$$

where β is the propagation constant of the guided mode, B_n is the backward coupling coefficient of the n^{th} hole and d is the separation between holes - usually set to $\lambda_g/4$ to ensure that the B_n terms are in antiphase. Conventionally the coupling apertures are circular holes in the broad wall of the waveguide. Due to the single layer implementation of the present device, the coupling holes are in the sidewall of the guide. Furthermore, they form rectangular cross sections with width w and height equal to the waveguide height b. Fig. 2.18 shows the coupling coefficients of a rectangular aperture using the finite element method. The adjoining wall of the two waveguides is an infinitely thin, perfectly conducting plane. This of course differs from the synthesized wall, which uses an array of metallised vias. However it considerably simplifies the simulation and was assumed to be a good approximation.

It is seen from Fig. 2.18 that $B_n \approx F_n$ for $w/a < 0.4$. The functional dependence of F_n and B_n on w/a is approximately quadratic and given by:

$$F_n = B_n = a_1 \frac{w}{a} + a_2 \left(\frac{w}{a} \right)^2 \qquad \text{(Eq.2.41)}$$

$w/a < 0.4$ where a_1 = 0.5769 and a_2 = -0.013. By equating

$$\sum_{n=0}^{N} F_n e^{-2j\beta nd} \qquad \text{(Eq.2.42)}$$

to an appropriate prototype function the width w of each hole can be calculated by specifying the required coupling coefficient and minimum directivity. For a four-hole Chebyshev coupler with coupling C = 20 dB and a minimum directivity of D = 40 dB gives coupling apertures of width $w_0/a = w_3/a$ = 0.165 and $w_1/a = w_2/a$ =0.263.

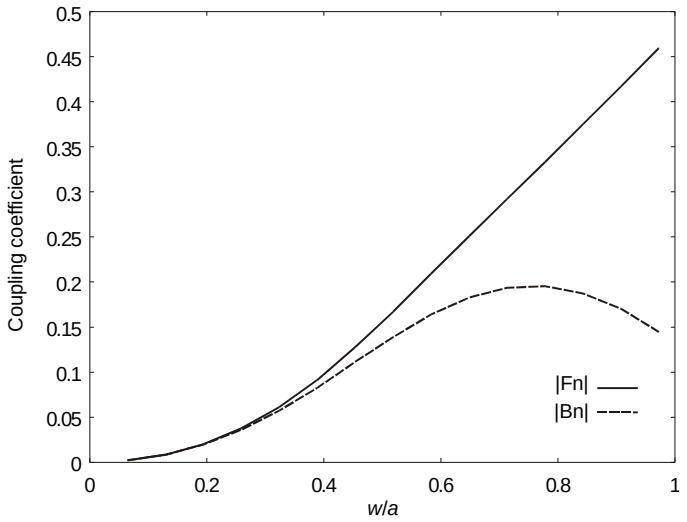

Fig. 2.18. Forward and backward coupling coefficients as a function of normalized aperture width

The cut-off frequency for X band is 6.557 GHz. Using the Rogers RT 5880 substrate with ε_r = 2.2, via diameters of 0.6 mm and a pitch of 1.2 mm gives W = 15.73 mm. The substrate and therefore b is 1.575 mm thick. To reinforce the effectiveness of the short circuit vias, quarter wavelength open circuit parallel plate stubs are placed either side of the sidewalls. Optimized transitions from 50 Ω microstrip feed lines are used to provide a low loss transition to the waveguide.

Fig. 2.19 shows the measured results for the coupler. We see that the S_{11} is generally less than 15 dB across the entire band with S_{21} less than 3 dB. Since the measurements include a transition to SMA the actual return and insertion loss is likely to be better than the measured values. The coupling (S_{31}) is between 17 and 20 dB dropping above 11 GHz. The directivity (S_{41}) falls short of the design value of 40 dB but is generally less than 30 dB up to 10.5 GHz. It is likely that additional coupling through the gaps between the via sidewalls affects the directivity and coupling. A simple technique for overcoming this would be to add a second row of vias. Another factor that

affects the coupling in the present implementation is the proximity of the microstrip feed-lines and waveguide transitions.

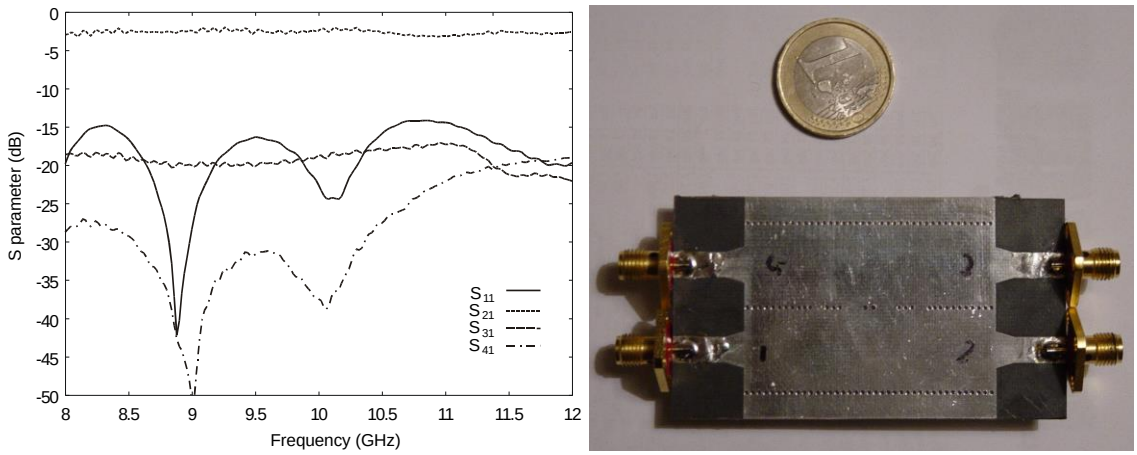

Fig. 2.19. Measured response of coupler and picture of 5880 coupler

Simple SIW filters may use a straight SIW section plus additional isolated vias within the waveguide section to define the filter cavities. The inductive posts may be placed centrally or offset, of the same size or varying. The longitudinal spacing is in the order of half guided wavelength, and the impedance variation may be achieved either by offsetting from the central point or by changing the via diameter. For the inline version, the via diameters vary, and there are issues relating to input matching as well as increasing conductor losses. Hence the offset via filter is generally more preferred, the via diameter is usually kept constant making fabrication easier [21]. Another SIW filter utilises pairs of symmetrically placed vias to form iris windows, similar to filters utilised in box waveguide. Filters may also use cavities (either square or rectangular), these allow a more flexible approach and exhibit a higher flexibility due to the cross-coupling [2, 50, 62]. Recent SIW filter structures of note include; a cavity loaded dielectric resonator bandpass filter [63] offering compact design with high performance, a differential mode bandpass filter [64] and a balanced SIW filter [50] offering high common mode suppression. An example SIW box cavity filter is shown in Fig. 2.20, designed for the K band with a centre frequency of 22 GHz.

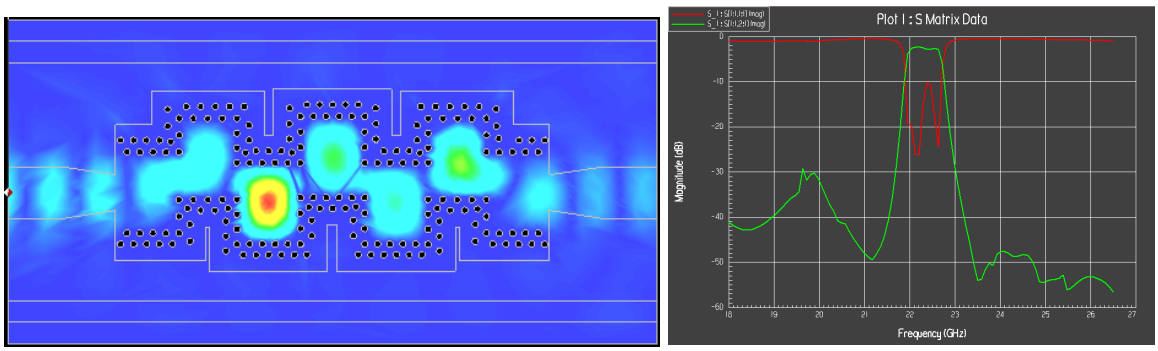

Fig. 2.20. Example K Band SIW 5th order filter, field plot and S-parameters [7]

One of the key advantages of SIW structures is the ease with which other microwave components may be directly integrated, hence the popular use of SIWs with active devices. By directly mounting the microwave component to the SIW the need for complex and lossy interconnections is reduced or completely removed. The connections are normally the microstrip-to-SIW or CPW-to-SIW transitions mentioned in the previous section.

Oscillators are suited to SIW due to the ease of forming resonant cavities with relatively high quality factors. A higher quality factor indicates a lower rate of energy loss relative to the stored energy of the resonator; hence the oscillations die out more slowly. SIW oscillators implemented include the feedback oscillator [65] and the reflector oscillator. The feedback oscillator consists of an amplified circuit with an SIW cavity in the feedback loop, which acts as a frequency selector. The reflector oscillator uses a cavity resonator connected to the gate of a transistor which presents a negative resistance.

2.8 Scattering Parameter Measurement

The equipment used for the measurements was a VNA - Vector Network Analyser, model 37397C manufactured by Anritsu, capable of sweeps from 40MHz to 65GHz. A general PC connected via GPIB to enable screen shot and S-Parameter download, see Fig.4.65. Calibration was completed using the TRL method (Through – Reflect – Line) with dedicated calibration kit.

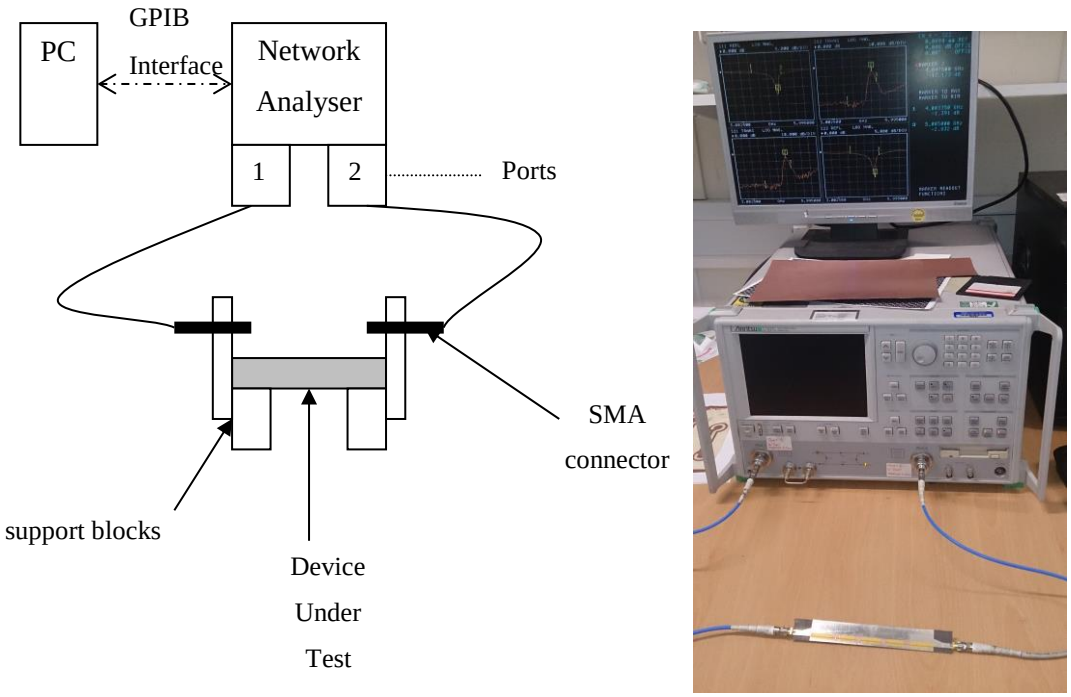

Fig.2.21. VNA Measurement set-up
(Picture shows SSIW filter detailed in chapter 4)

2.9 Comments on SIW design & fabrication

Basic design rules for forming SIWs have been overviewed, and the range of components and structures possible within SIWs has been discussed. A key element however relates to the implementation of the design into fabrication. Dependant on the frequency of interest vias may become too small to form, as there are fabrication limits for drilling and plating. For 1.6 mm laminates, a 0.2 mm drill with an aspect ratio therefore of 1:8 is about the minimum that can be formed. For thicker laminates the via size will have to increase. At higher frequencies, 60-90 GHz , for thinner laminates it may be more pragmatic to form the vias by micro-drilling and using conductive paste, or simply remove the vias altogether and form the wall using a plated (or metallised) slot [46] .

From a design point of view, incorporating fabrication tolerances into the design process is an important step, as is simulating what will actually be fabricated. Exporting the structures that have been simulated into a means of producing a photo-plot for fabrication is not always straightforward. It was found that the best results were obtained when the structures were redrawn in a CAD package for PCBs, this enabled copper areas and planes to be created and the vias controlled more accurately for size and position. The export of the data from a PCB package will require Gerber files for the copper structures and Excellon drill data for the via positions and drill sizes. These may be modified to achieve the required level of accuracy. Important tolerances include; the minimum amount of copper from the edge of a via to the edge of copper, as a certain amount of copper is required to form the via pad on the dielectric surface. The positional accuracy of the drilling process is also important, as is the plating density within the via itself.

As the design complexity for SIW systems grow, so does the PCB design importance to ensure that what is fabricated is that which is required. Gerber manipulation to verify positional data and copper dimensions becomes an important part of design rule checking for design verification prior to fabrication.

2.10 References

[1] D. M. Pozar, *Microwave Engineering.* New York: Wiley, 1998.

[2] M. Bozzi, A. Georgiadis and K. Wu. Review of substrate-integrated waveguide circuits and antennas. *Microwaves, Antennas & Propagation, IET 5(8),* pp. 909-920. 2011.

[3] F. Shigeki, "Waveguide Line," Japanese Patent 06-053 711, 25th Feb, 1994.

[4] D. Deslandes and Ke Wu, "Integrated transition of coplanar to rectangular waveguides," *Microwave Symposium Digest, 2001 IEEE MTT-S International,* vol. 2, pp. 619-622 vol.2, 2001.

[5] Y. Cassivi and K. Wu. Low cost microwave oscillator using substrate integrated waveguide cavity. *Microwave and Wireless Components Letters, IEEE 13(2),* pp. 48-50. 2003.

[6] D. Deslandes and Ke Wu, "Integrated microstrip and rectangular waveguide in planar form," *Microwave and Wireless Components Letters, IEEE,* vol. 11, pp. 68-70, 2001.

[7] A. J. Farrall, "Investigation of substrate integrated rectangular waveguides - University of Kent MSc dissertation," 2003.

[8] K. K. Samanta, D. Stephens and I. D. Robertson, "Design and performance of a 60-GHz multi-chip module receiver employing substrate integrated waveguides," *Microwaves, Antennas & Propagation, IET,* vol. 1, pp. 961-967, 2007.

[9] N. Grigoropoulos, B. Sanz-Izquierdo and P. R. Young. Substrate integrated folded waveguides (SIFW) and filters. *Microwave and Wireless Components Letters, IEEE 15(12),* pp. 829-831. 2005. . DOI: 10.1109/LMWC.2005.860027.

[10] Wei Hong, Bing Liu, Yuanqing Wang, Qinghua Lai, Hongjun Tang, Xiao-Xin Yin, Yuan-Dan Dong, Yan Zhang and Ke Wu. Half mode substrate integrated waveguide: A new guided wave structure for microwave and millimeter wave application. Presented at Infrared Millimeter Waves and 14th International Conference on Teraherz Electronics, 2006. IRMMW-THz 2006. Joint 31st International Conference On. 2006, . DOI: 10.1109/ICIMW.2006.368427.

[11] Qinghua Lai, C. Fumeaux, Wei Hong and R. Vahldieck. Characterization of the propagation properties of the half-mode substrate integrated waveguide. *Microwave Theory and Techniques, IEEE Transactions On 57(8),* pp. 1996-2004. 2009.

[12] W. Che, C. Li, D. Zhang and Y. L. Chow. Investigations on propagation and the band broadening effect of ridged rectangular waveguide integrated in a multilayer dielectric substrate. *Microwaves, Antennas & Propagation, IET 4(6),* pp. 674-684. 2010.

[13] M. Bozzi, S. A. Winkler and K. Wu. Broadband and compact ridge substrate-integrated waveguides. *Microwaves, Antennas & Propagation, IET 4(11),* pp. 1965-1973. 2010.

[14] Ruo Feng Xu, B. S. Izquierdo and P. R. Young, "Switchable Substrate Integrated Waveguide," *Microwave and Wireless Components Letters, IEEE,* vol. 21, pp. 194-196, 2011.

[15] Ruo Feng Xu, A. J. Farrall and P. R. Young, "Analysis of Loaded Substrate Integrated Waveguides and Attenuators," *Microwave and Wireless Components Letters, IEEE,* vol. 24, pp. 62-64, 2014.

[16] S. Ramo, T. Van Duzer, J. R. Whinnery and Theodore Van Duzer, *Fields and Waves in Communication Electronics.* New York: Wiley, 1994.

[17] D. Pozar and D. Schaubert, "The Analysis and Design of Microstrip Antennas and Arrays," *Microstrip Antennas,* 1995.

[18] Y. Cassivi, L. Perregrini, P. Arcioni, M. Bressan, K. Wu and G. Conciauro. Dispersion characteristics of substrate integrated rectangular waveguide. *Microwave and Wireless Components Letters, IEEE 12(9),* pp. 333-335. 2002.

[19] W. Che, K. Deng, D. Wang and Y. L. Chow, "Analytical equivalence between substrate-integrated waveguide and rectangular waveguide," *Microwaves, Antennas & Propagation, IET,* vol. 2, pp. 35-41, 2008.

[20] F. T. Ladani, S. Jam and R. Safian, "Comment on 'Analytical equivalence between substrate-integrated waveguide and rectangular waveguide'," *Microwaves, Antennas & Propagation, IET,* vol. 7, pp. 24-25, 2013.

[21] R. Garg, I. Bahl and M. Bozzi, *Microstrip Lines and Slotlines (Artech House Microwave Library (Hardcover).* Artech House, 2013.

[22] (). *Transmission Lines: Equivalent Circuits, Electromagnetic Theory, and Photons (The Cambridge RF and Microwave Engineering Series)* [The Cambridge RF and Microwave Engineering Series].

[23] Feng Xu and Ke Wu, "Numerical multimode calibration technique for extraction of complex propagation constants of substrate integrated waveguide," in *Microwave Symposium Digest, 2004 IEEE MTT-S International*, 2004, pp. 1229-1232 Vol.2.

[24] L. Yan, W. Hong, K. Wu and T. J. Cui. Investigations on the propagation characteristics of the substrate integrated waveguide based on the method of lines. *Microwaves, Antennas and Propagation, IEE Proceedings 152(1),* pp. 35-42. 2005.

[25] D. Deslandes and Ke Wu. Accurate modeling, wave mechanisms, and design considerations of a substrate integrated waveguide. *Microwave Theory and Techniques, IEEE Transactions On 54(6),* pp. 2516-2526. 2006.

[26] R. E. Collin, *Field Theory of Guided Waves.* Oxford University Press, .

[27] Feng Xu, Ke Wu and Wei Hong, "Domain decomposition FDTD algorithm combined with numerical TL calibration technique and its application in parameter extraction of substrate integrated circuits," *Microwave Theory and Techniques, IEEE Transactions On,* vol. 54, pp. 329-338, 2006.

[28] M. Bozzi, L. Perregrini and Ke Wu. Modeling of losses in substrate integrated waveguide by boundary integral-resonant mode expansion method. Presented at Microwave Symposium Digest, 2008 IEEE MTT-S International. 2008, .

[29] M. Bozzi and L. Perregrini. Numerical modeling and design of substrate integrated waveguide (SIW) components. Presented at Mathematical Methods in Electromagnetic Theory (MMET), 2012 International Conference On. 2012, .

[30] M. Bozzi, L. Perregrini and Ke Wu, "Analysis, design, and sensitivity study of substrate integrated waveguide circuits by using equivalent circuit models," in *General Assembly and Scientific Symposium (URSI GASS), 2014 XXXIth URSI,* 2014, pp. 1-4.

[31] Feng Xu and Ke Wu. Guided-wave and leakage characteristics of substrate integrated waveguide. *Microwave Theory and Techniques, IEEE Transactions On 53(1),* pp. 66-73. 2005.

[32] D. Deslandes and Ke Wu, "Single-substrate integration technique of planar circuits and waveguide filters," *Microwave Theory and Techniques, IEEE Transactions On,* vol. 51, pp. 593-596, 2003.

[33] Li Yan, Wei Hong, Guang Hua, J. Chen, Ke Wu and T. Cui, "Simulation and experiment on SIW slot array antennas," *Microwave and Wireless Components Letters, IEEE,* vol. 14, pp. 446-448, 2004.

[34] A. J. Farrall and P. R. Young, "High frequency postgraduate student colloquium, 2004; substrate integrated rectangular waveguides," in 2004, pp. 133-to 138.

[35] N. Grigoropoulos and P. R. Young, "Compact folded waveguides," in *Microwave Conference, 2004. 34th European,* 2004, pp. 973-976.

[36] N. Grigoropoulos, "Novel substrate integrated waveguides and components. PhD thesis at University of Kent." pp. 179 leaves, 2005.

[37] B. S. Izquierdo, P. R. Young, N. Grigoropoulos, J. C. Batchelor and R. J. Langley, "Slot antenna on C type compact substrate integrated waveguide," in *Microwave Conference, 2005 European,* 2005, pp. 4 pp.

[38] A. O. Lindo, P. M. Anju, C. K. Aanandan, A. J. Farrall and P. R. Young, "Half mode substrate integrated waveguide without via," in *Antennas and Propagation Conference (LAPC), 2013 Loughborough,* 2013, pp. 131-134.

[39] B. Sanz Izqueirdo, N. Grigoropoulos and P. R. Young, "Ultra-wideband multilayer substrate integrated folded waveguides," in *Microwave Symposium Digest, 2006. IEEE MTT-S International,* 2006, pp. 610-612.

[40] H. Uchimura, T. Takenoshita and M. Fujii, "Development of the "laminated waveguide"," in *Microwave Symposium Digest, 1998 IEEE MTT-S International,* 1998, pp. 1811-1814 vol.3.

[41] W. Menzel and J. Kassner, "Millimeter-wave 3D integration techniques using LTCC and related multilayer circuits," in *Microwave Conference, 2000. 30th European,* 2000, pp. 1-4.

[42] M. J. Hill, R. W. Ziolkowski and J. Papapolymerou, "Simulated and measured results from a Duroid-based planar MBG cavity resonator filter," *Microwave and Guided Wave Letters, IEEE,* vol. 10, pp. 528-530, 2000.

[43] M. S. Aftanasar, P. R. Young, I. D. Robertson, J. Minalgiene and S. Lucyszyn, "Photoimageable thick-film millimetre-wave metal-pipe rectangular waveguides," *Electronics Letters,* vol. 37, pp. 1122-1123, 2001.

[44] Chi-Yang Chang and Wei-Chen Hsu, "Photonic bandgap dielectric waveguide filter," *Microwave and Wireless Components Letters, IEEE,* vol. 12, pp. 137-139, 2002.

[45] M. S. Aftanasar, P. R. Young and I. D. Robertson, "Rectangular waveguide filters using photoimageable thick-film processing," in *Microwave Conference, 2002. 32nd European,* 2002, pp. 1-4.

[46] E. Moldovan, R. G. Bosisio and Ke Wu, "W-band multiport substrate-integrated waveguide circuits," *Microwave Theory and Techniques, IEEE Transactions On,* vol. 54, pp. 625-632, 2006.

[47] D. Deslandes, M. Bozzi, P. Arcioni and Ke Wu. Substrate integrated slab waveguide (SISW) for wideband microwave applications. Presented at Microwave Symposium Digest, 2003 IEEE MTT-S International. 2003, . DOI: 10.1109/MWSYM.2003.1212561.

[48] Bao Jun-song, Tong Chuang-ming, Zou Xiong and Yu Ding-wang. Ridged substrate integrated waveguide. Presented at Microwave and Millimeter Wave Technology (ICMMT), 2012 International Conference On. 2012, .

[49] Lin-Sheng Wu, Xi-Lang Zhou, Wen-Yan Yin, Chun-Tian Liu, Liang Zhou, Jun-Fa Mao and Hong-Li Peng, "A New Type of Periodically Loaded Half-Mode Substrate Integrated Waveguide and Its Applications," *Microwave Theory and Techniques, IEEE Transactions On,* vol. 58, pp. 882-893, 2010.

[50] Peng Chu, Wei Hong, Kuangda Wang, Hongjun Tang, Zhangcheng Hao, Jixin Chen and Ke Wu, "Balanced Substrate Integrated Waveguide Filter," *Microwave Theory and Techniques, IEEE Transactions On,* vol. 62, pp. 824-831, 2014.

[51] Peng Chu, Wei Hong, Linlin Dai, Hongjun Tang, Jixin Chen, Zhangcheng Hao, Xicheng Zhu and Ke Wu, "A Planar Bandpass Filter Implemented With a Hybrid Structure of Substrate Integrated Waveguide and Coplanar Waveguide," *Microwave Theory and Techniques, IEEE Transactions On,* vol. 62, pp. 266-274, 2014.

[52] Z. C. Hao, W. Hong, J. X. Chen, H. X. Zhou and K. Wu, "Single-layer substrate integrated waveguide directional couplers," *Microwaves, Antennas and Propagation, IEE Proceedings,* vol. 153, pp. 426-431, 2006.

[53] Z. C. Hao, W. Hong, J. X. Chen, X. P. Chen and K. Wu, "Planar diplexer for microwave integrated circuits," *Microwaves, Antennas and Propagation, IEE Proceedings,* vol. 152, pp. 455-459, 2005.

[54] Kaijun Song, Yong Fan and Yonghong Zhang, "Eight-Way Substrate Integrated Waveguide Power Divider With Low Insertion Loss," *Microwave Theory and Techniques, IEEE Transactions On,* vol. 56, pp. 1473-1477, 2008.

[55] Yu Jian Cheng, Wei Hong and Ke Wu, "Broadband Self-Compensating Phase Shifter Combining Delay Line and Equal-Length Unequal-Width Phaser," *Microwave Theory and Techniques, IEEE Transactions On,* vol. 58, pp. 203-210, 2010.

[56] W. D'Orazio and Ke Wu, "Substrate-Integrated-Waveguide Circulators Suitable for Millimeter-Wave Integration," *Microwave Theory and Techniques, IEEE Transactions On,* vol. 54, pp. 3675-3680, 2006.

[57] Zhen-Yu Zhang and Ke Wu, "A Broadband Substrate Integrated Waveguide (SIW) Planar Balun," *Microwave and Wireless Components Letters, IEEE,* vol. 17, pp. 843-845, 2007.

[58] Fanfan He, Ke Wu, Xiao-Ping Chen, Liang Han and Wei Hong, "A planar magic-T structure using substrate integrated circuits concept," in *Microwave Symposium Digest (MTT), 2010 IEEE MTT-S International,* 2010, pp. 720-723.

[59] Xinyu Xu, R. G. Bosisio and Ke Wu, "A new six-port junction based on substrate integrated waveguide technology," *Microwave Theory and Techniques, IEEE Transactions On,* vol. 53, pp. 2267-2273, 2005.

[60] Ji-Xin Chen, Wei Hong, Zhang-Cheng Hao, Hao Li and Ke Wu, "Development of a low cost microwave mixer using a broad-band substrate integrated waveguide (SIW) coupler," *Microwave and Wireless Components Letters, IEEE,* vol. 16, pp. 84-86, 2006.

[61] M. Abdolhamidi and M. Shahabadi, "X-Band Substrate Integrated Waveguide Amplifier," *Microwave and Wireless Components Letters, IEEE,* vol. 18, pp. 815-817, 2008.

[62] S. S. Sabri, B. H. Ahmad and A. R. B. Othman, "A review of Substrate Integrated Waveguide (SIW) bandpass filter based on different method and design," *Applied Electromagnetics (APACE), 2012 IEEE Asia-Pacific Conference On,* pp. 210-215, 2012.

[63] Ding-Ding Zhang, Liang Zhou, Lin-Sheng Wu, Liang-Feng Qiu, Wen-Yan Yin and Jun-Fa Mao, "Novel Bandpass Filters by Using Cavity-Loaded Dielectric Resonators in a Substrate Integrated Waveguide," *Microwave Theory and Techniques, IEEE Transactions On,* vol. 62, pp. 1173-1182, 2014.

[64] Xin Xu, Jianpeng Wang and Lei Zhu, "A New Approach to Design Differential-Mode Bandpass Filters on SIW Structure," *Microwave and Wireless Components Letters, IEEE,* vol. 23, pp. 635-637, 2013.

[65] Y. Cassivi and K. Wu, "Low cost microwave oscillator using substrate integrated waveguide cavity," *Microwave and Wireless Components Letters, IEEE,* vol. 13, pp. 48-50, 2003.

3 SIW Antennas

An antenna is a specialised transducer that converts RF fields into AC (or vice-versa). It is a transitional structure between free-space and a guiding device [1], the guiding wave structure or transmission line is used to transport electromagnetic energy to or from the antenna. The term ‘integrated antenna’ refers to the antenna and guiding device being combined into a hybrid structure, which in reference to this work is a planar laminate structure.

In this chapter integrated antennas are discussed, focussing on SIW slot antennas with examples of simple single and dual slot antennas, building to a range of SIW switched antennas for two, four and six directional beams.

Planar antennas are referred to as printed structures, in that the design is fabricated using a photoplot and etching process, generally as part of the PCB it is embedded in. This means they benefit from low-cost, low-profile, ease of manufacture and known process tolerances. The negative side of planar antennas is that for certain applications they suffer from narrow bandwidth, poor cross polarisation, unwanted side lobes and low-power capacity. The two main types of planar antennas are printed slot and printed patch, used individually or within an array. Other types of planar antennas available include bowtie antennas [2] (for wideband applications), quasi-Yagi antenna [3-5] (for end-fire launch), SIW horn antenna [6] and reflector antenna. Further information on planar antennas if required is available [1, 7, 8].

A printed slot is, in essence, a dipole element on a dielectric substrate, the key advantages are that it uses less substrate area compared to patch elements (which is useful in array configurations) and it can be used near its first or second resonant frequencies without higher-order modes being excited. Printed patches consist of a thin metallic shape placed above a ground plane, usually separated by a dielectric.

SIW structures may be made to radiate in two key ways; by creating gaps in the via wall by increasing the via spacing allowing leakage to occur, or by creating slots (or apertures) in the top or bottom conductive surfaces. These methods define the SIW leaky-wave antenna and the SIW slot array antenna. Before SIW antennas are discussed some background antenna material is deemed worthwhile.

3.1 Antenna Background

To describe the performance of an antenna, various parameters need to be defined. An *antenna radiation pattern* (or antenna pattern) is a representation of the radiation properties of the antenna as a function of spatial coordinates; this may be mathematical or graphical. For the main part this shows the *far field* response of the antenna. Where the far field is deemed at distances greater than $2A_D^2/\lambda$, where A_D is the overall maximum dimension of the antenna and λ is the wavelength of interest. Associated with the radiation pattern is the *beamwidth*, which is the angular separation between two identical points on opposite sides of the pattern maximum. A common reference point is that of the *half-power beamwidth* (HPBW). The *directivity* of an antenna is the ratio of the radiation intensity in a given direction from the antenna to the radiation intensity averaged over all directions. An ideal antenna will have no associated losses, and radiates all energy supplied to it. The *efficiency* of an antenna is the ratio of radiated power to input power, expressed as a percentage. The *gain* of an antenna (in a given direction) is the ratio of the intensity in a given direction, to the radiation intensity that would be obtained if the power accepted by the antenna were radiated isotropically. Alternatively the gain may be described as the *efficiency* multiplied by the *directivity*.

A key antenna equation that relates the power received to the power transmitted in the far field is the Friss equation and varies with both frequency and distance, here P_R = received power, P_T = transmitted power, r = sphere radius (distance Tx to Rx), and is defined as:

$$P_R = P_T \left(\frac{\lambda}{4\pi r}\right)^2 \qquad \text{(Eq.3.1)}$$

Free space loss dependant only on frequency. Also add A_E effective capture area of receiving antenna, which in turn can be related to the Gain by:

$$G_a = \frac{4\pi A_E}{\lambda^2} \qquad \text{(Eq.3.2)}$$

Equivalent Isotopically Radiated Power (as mentioned in chapter 1) is the apparent power transmitted towards the receiver, if it is assumed that the signal is radiated equally in all directions, such as a spherical wave emanating from a point source; the arithmetic product of the power supplied to an antenna and its gain:

$$EIRP = P_T - L_C + G_a \qquad \text{(Eq.3.3)}$$

where P_T (dBm) power of transmitter, L_C (dB) cable losses, G_a (dBi) antenna gain.

3.2 SIW Leaky-wave Antenna

Leaky-wave SIW antennas are generally straight sections with either uniform or periodic apertures on the top (or bottom) waveguide conducting surfaces or with increased spacing of the vias in the via wall. A leaky-wave is a derivative of the main guided wave. Supposing the guided wave ($e^{-j\beta z}$) is travelling in the $+z$ direction with phase constant β, as in Fig.3.1.

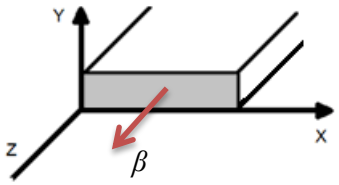

Fig. 3.1 SIW co-ordinate system with propagation in *z* direction.

For a leaky-wave in the y direction (perpendicular to propagation across height of waveguide), then there is the following relationship:

$$k_y^2 = k_0^2 - \beta^2 \qquad \text{(Eq.3.4)}$$

The leaky-wave in *y* direction (vertical) will only start to appear if k_y becomes real, so when $\beta<k_0$. Fig. 3.2 details the leaky wave region between f_c and f_{cl}.

Similarly for a leaky-wave in the *x* direction (across the waveguide width):

$$k_x^2 = \varepsilon_r k_0^2 - \beta^2 \qquad \text{(Eq.3.5)}$$

Here the leaky-wave in *x* direction (horizontal) will only start to appear if k_x becomes real, i.e. when $\beta<\varepsilon_r k_0^2$, which will always be true as shown in Fig.3.2 as $\beta<\varepsilon_r k_0$.

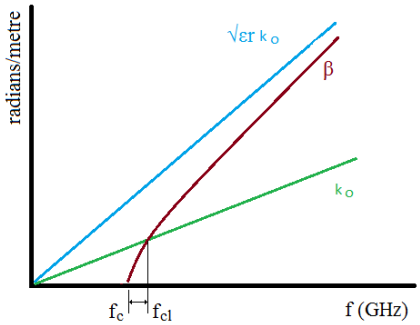

Fig.3.2 Frequency against β and k_o for SIW

To enable leakage in the vertical direction of the SIW, it is possible to create leaky-wave radiation by introducing uniform and periodic apertures onto the top (or bottom) waveguide conducting surfaces. A simple slot [9] with 7 dB gain at 19 GHz as a leaky-wave antenna is an example of a uniform structure, and a set of transvers slots [10], or patches [11] are examples of uniform structures. A combination of uniform and periodic was a 'butterfly' SIW leaky wave antenna [12] which used a period of eight perpendicular slots varying in length for operation around 10 GHz. The leaky wave region is defined from the mode cut-off frequency f_c to the leaky-wave mode cut-off f_{cl} where $\beta=k_0$, as shown in Fig.3.2.

Leaky-wave in the horizontal direction is generally something that is to be avoided, but is obtained by increasing the longitudinal spacing in one row of the via side wall; usually near the dielectric edge of the substrate. The radiation leakage increases if the gaps are large, meaning that the antenna section length may be reduced, however the beamwidth is also reduced. Large gaps may lead to band-gap effects that may alter or stop the propagating mode, an analysis of the via (or post spacing) for SIW leaky-wave antenna design is presented in [13, 14] using a transverse equivalent network.

Half-mode SIWs have also been used to form leaky-wave antennas [15, 16] one by changing positions of the vias in the waveguide wall, the other by the addition of an etched periodic structure to the top conducting surface. Furthermore wave polarization [17] and beam steer [18] have been demonstrated using leaky-wave topography, and a recent summary of leaky-wave structures [19] is available from Professor Wu's group.

3.3 SIW Slot Antenna

Introducing slots into the top or bottom of the SIW waveguide is one way of allowing radiation from the waveguide in a controlled manner. The spacing along the waveguide for the slots is normally near half of the guided target wavelength, and the slots are spaced alternatively just off the centre line. For a collection of slots in an array this allows for full broadside (perpendicular to waveguide face) radiation, at the required frequency and phase [20]. The SIW slot antenna offers reduced weight and cost when compared to conventional slotted-waveguide antennas, in addition to easier integration with planar components; unfortunately, they do suffer from lower gain and antenna efficiency (primarily from dielectric loss).

Since integration and manufacturability is essential in systems design, many applications use planar antennas such as microstrip patches, which are inherently compatible with planar systems. Unfortunately the patch antenna suffers from many disadvantages, including poor polarisation purity, spurious radiation from feeding networks and losses to substrate modes. Several techniques relying on conventional microwave integrated circuit fabrication have been used to realise RWGs. These include multilayer laminates [21], low-temperature co-fired ceramics (LTCC) [22], photoimageable thick films [23] and conventional PCB manufacture [24]. All these techniques have the advantages of easy integration with planar circuitry and comparatively simple and cheap manufacture based on existing microwave fabrication techniques. Furthermore, since the waveguides are dielectric filled, the broadwall dimension is reduced by a factor of $\sqrt{\varepsilon_r}$, where ε_r is the dielectric constant of the material. This allows highly integrated structures to be formed using high dielectric constant substrates.

SIW slot array antennas are similar to the classical slotted-waveguide antennas and may be designed by utilizing a method [25] based on this original concept. As the SIW waveguide height is much less than its width, care must be taken to consider internal coupling for higher order modes. Should circular polarization be required, it may be obtained by alternating the slots at 45°. SIW slot antennas have been designed for a range of frequencies and features, including arrays at 60 GHz [26-29] and with backing cavities [30, 31]. We will initially consider a single and dual slot design at 10 GHz using a PTFE substrate with a dielectric thickness of 1.575 mm and dielectric constant of 2.2.

3.3.1 SIW Slot Antenna Example Design

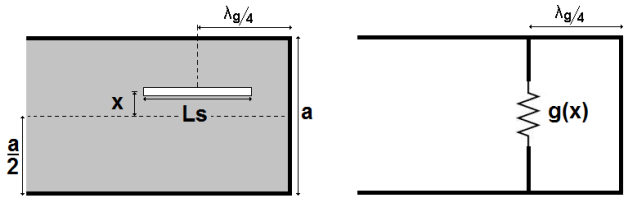

Fig. 3.3. Waveguide resonant slot antenna and equivalent circuit [32].

For a single resonant slot antenna the radiating slot is placed approximately one quarter of a guided wavelength from the short-circuited end of the waveguide. The equivalent circuit of this arrangement is shown in Fig. 3.3 with the slot appearing as a shunt conductance, $g(x)$. If the conductance of the slot is set to the characteristic admittance of the propagating mode then the slot will be perfectly matched to the waveguide and radiate efficiently. The slot conductance is controlled by changing the offset, x, of the slot from the centre of the guide, thereby controlling the coupling.

For a single slot antenna, the equivalent normalized shunt conductance, g, that the slot presents to the waveguide, at resonance, can be calculated by employing the Lorentz reciprocity theorem and ensuring that power flow is conserved [33]. This results in:

$$g(x) = g_0 sin^2(k_x x) \qquad \text{(Eq.3.6)}$$

$$g_0 = \frac{4K^2}{G_r} \qquad \text{(Eq.3.7)}$$

where x is the displacement of the slot from the centre of the waveguide, chosen such that $g(x) = 1$ (for perfect matching); k_x is the transverse phase constant of the TE_{10} mode, $k_x = \pi/a$; a is the waveguide width and G_r is the radiation conductance of the slot. g_0 is a normalised conductance, which is dependent on the slot dimensions, the waveguide ratio b/a and, in this case, the waveguide permittivity.

In the design of resonant slotted arrays the slots are positioned on opposite sides of the waveguide at intervals of half a guided wavelength. The sum of the normalised shunt conductance of all the slots is set to unity to provide a good match. The required value of conductance of each slot is set by x. For a dielectric-filled guide the slot length can be approximated by:

$$L_s = \frac{\lambda_0}{\sqrt{2(\varepsilon_r+1)}} \qquad \text{(Eq.3.8)}$$

Single and dual resonant slot antennas were designed and optimised using the finite-element method at 10 GHz. The guides were fabricated on a Rogers RT 5880 substrate with $\varepsilon_r = 2.2$ and thickness of 1.575 mm. This gives a waveguide width of 15.37 mm for X-band operation. An array of metallised vias of diameter 0.6 mm and pitch 1.2 mm was used to synthesise metallic sidewalls. To reinforce the effectiveness of the vias, quarter-wavelength open-circuit stubs were placed either side of the sidewalls. Optimised transitions from 50 Ω microstrip feed-lines were used to provide a low-loss transition to the waveguide. The spacing between slots was set to $\lambda_g/2$ and the distance from the end of the guide to the middle of the last slot is $\lambda_g/4$. In each case the slot width was 0.4 mm. For the single slot antenna *x=1.64 mm* and *L=12.7 mm*; for the dual slot design *x=1.3 mm* and *L=11.53 mm*. The antennas were fabricated using conventional PCB techniques. A picture of the dual slot antenna is shown in Fig. 3.4.

3.3.2 SIW Slot Antenna Example Results

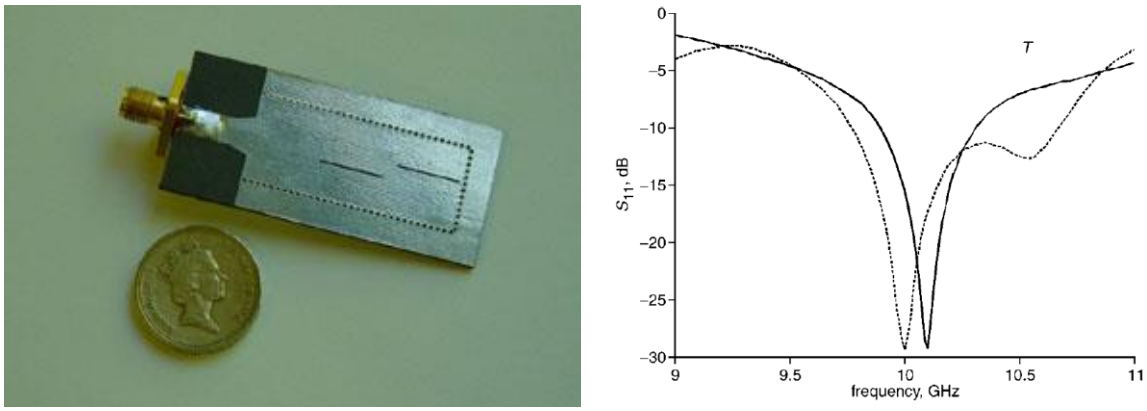

Fig. 3.4. Picture of dual slot antenna, and dual slot antenna and return loss (S_{11}) for single (solid line) and dual (dashed line) slot antenna [34]

Fig. 3.4 shows the measured S_{11} of the single and dual slot antenna. As can be seen both antennas are well matched with resonant frequencies very close to the design value of 10 GHz. The radiation pattern in the array plane is shown in Fig. 3.5 for both the single and dual slot. As can be seen, the dual slot has almost 3 dB gain compared to the single slot. The lack of symmetry in the pattern is due to radiation from the microstrip to waveguide transition. This could be eliminated by feeding the waveguide from the other side of the substrate.

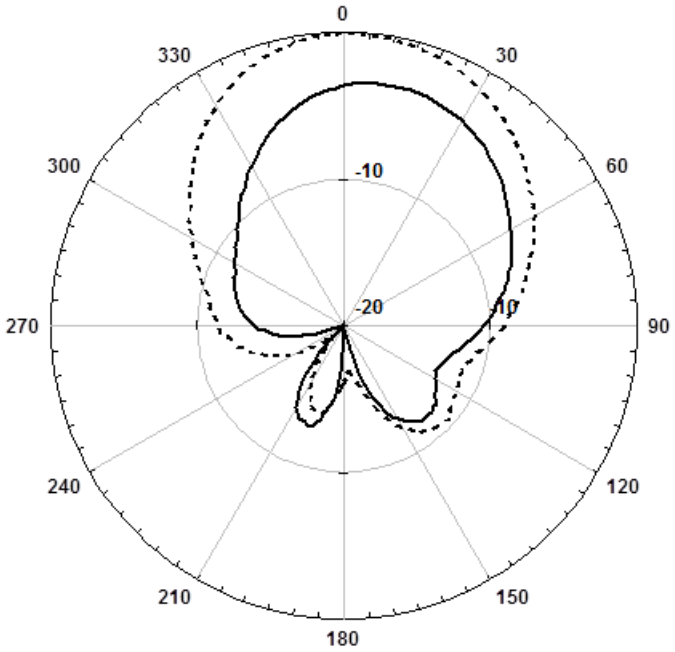

Fig. 3.5. Radiation Pattern in plane of array for single (solid line) and dual (dashed line) slot antenna [34].

In patch antennas the dielectric constant and substrate thickness must be kept small to avoid excitation of unwanted substrate modes, which results in lossy and physically large antennas, particularly troublesome in array design. In contrast, as rectangular waveguides are closed structures, there is no coupling to substrate modes whatever the dielectric constant or thickness.

The only constraint on the thickness is that it is less than one-half the waveguide width to ensure mono-mode propagation. Moreover, the ease with which integrated waveguide slots can be arrayed greatly reduces their size compared to other planar arrays. These integrated rectangular waveguide single and dual slot antennas were a part of previous research [34].

3.4 Switch beam antenna

There has been interest in the use of switched beam antennas with applications ranging from direction finding [35] to angle of arrival detection [36]. In communication systems, switched beam antennas allow spatial diversity which can greatly decrease the problems associated with multipath fading in crowded environments as well as allowing spectral reuse and increasing energy efficiency [37, 38]. In fact for future communication systems, such as 60 GHz WiFi, directional smart antennas are an essential requirement [8].

The classic technique for performing beam steering is the phased array, whereby the phase of each element of an array of antennas is controlled via phase shifters. This has the benefit of a fully controllable beam direction but requires a complicated feed network which not only takes up a large amount of substrate 'real estate' but also proves to be energy inefficient. A simpler technique uses $n \times n$ Butler matrices whereby 90° couplers and fixed phase shifts are used to form a phased array. The input signal is then fed to the nth input port, usually by a switching network, to obtain a beam that can be switched between n different directions. The Butler matrix can be formed in various different technologies with implementations ranging from CMOS [39] to SIW [26]. Although simpler than a phased array the Butler matrix technique is still relatively complicated and physically large.

Other designs have used periodic structures to change the pattern of a simple antenna. For example in [40] a frequency selective surface is used to switch the pattern of a dipole antenna and in [41] a similar technique is used with switchable Electromagnetic Bandgaps (EBG). These methods use a single antenna but since they rely on switching a periodic structure they are physically large and inevitably require a large amount of switches with associated biasing networks.

A simpler technique is to use a switching network to switch between different directional antennas and thereby allow the direction of the beam to be controlled. This has the advantage of reduced size and more control over the individual beams. This technique has been used in [42] with monopole slot antennas whereas in [43] a planar quasi-Yagi-Uda array is used as the directional antenna.
A method to reduce the size of the switched beam still further is to use a single antenna structure where the nature of the structure can be changed by switching radiating elements. This was achieved in [44] where the radiating apertures of a patch antenna were switched on and off by PIN diodes. This can greatly reduce the size of the structure since there is no elaborate switching or feeding network. Unfortunately in [44] the antenna only had two discrete directions.
The concept of a single switchable structure is extended to obtain a pattern that can be switched between either two, four or six discrete directions giving 360° coverage in the four and six direction implementations. The design is based on a SIW slot antenna [34, 45] and is no bigger than a single slot antenna, although in the four and six direction design a perpendicular reflector is also used. The operational frequency of the antenna is chosen to be 2.4-2.5 GHz allowing low cost PIN diodes to be used for the switching elements. However, with appropriate devices, the design could be easily scaled to higher frequencies where the use of SIW is more appropriate.

3.4.1 Main Principle of Switch Beam Design

Three types of switched beam antenna are shown here: a two direction design consisting of a short circuited SIW with longitudinal resonant slots on opposite sides and faces of a SIW (see Fig.3.6); and a four (and six) direction design consisting of an SIW with four slots and a perpendicular reflection plane (see Fig.3.7). In both cases the beam is directed by using PIN diode switches at the centre of each slot. When the diodes are in their on state (forward biased) they present an approximate short circuit to the centre of the slot - effectively eliminating the fundamental resonance. In contrast, if the diode is in its off state (reverse biased) then it presents an approximate open circuit to the slot and therefore has little effect on its resonance or radiation characteristics. As a result only slots with the switch in its open circuit state radiate significantly allowing the beam to be switched in different directions. In the six direction design the structure is optimized to allow slots 1 & 4 or slots 2 & 3 (which are in phase) to radiate simultaneously giving a further two directions perpendicular to the reflector. Note that slots 1 & 2 and slots 4 & 3 are in anti-phase and therefore result in dual patterns which are not considered here.

3.4.2 Loaded Slot Antennas

The single slot antenna design is discussed in section 3.3.1, Fig.3.3 shows the key parameters and equivalent circuit, the slot conductance is given in (Eq.3.6). For the switch antenna, we load the slot with a PIN diode to enable the radiation to be switched on and off. PIN diodes do not work as perfect switches and exhibit a resistance, dependent on the reverse biased voltage, forward biased current and frequency of interest. Typically the resistance is a few ohms, when forward biased, and a few kΩs when reverse biased. It is important to see how this resistance affects the impedance matching of the slot antenna and therefore this section looks at the effective impedance of a single loaded slot antenna. We see that the coupling mechanism from the waveguide to the slot works like an admittance invertor, with the radiation conductance inverted via the factor $2K\sin(k_x x)$. For SIW; K is given by

$$K = \frac{L_s}{a}\left(\sqrt{\frac{2\pi}{ab\eta_0 k_0 \beta}}\right)\left(\frac{\cos(\beta L_s/2)}{\beta^2 {L_s}^2 - \pi^2}\right) \qquad \text{(Eq.3.9)}$$

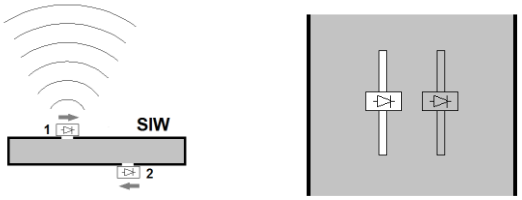

Fig. 3.6. Two direction antenna structure with top PIN diode reverse biased, bottom PIN diode forward biased. Left: transverse plane of waveguide showing top slot radiating; Right: longitudinal plane of waveguide showing slots and diodes [32].

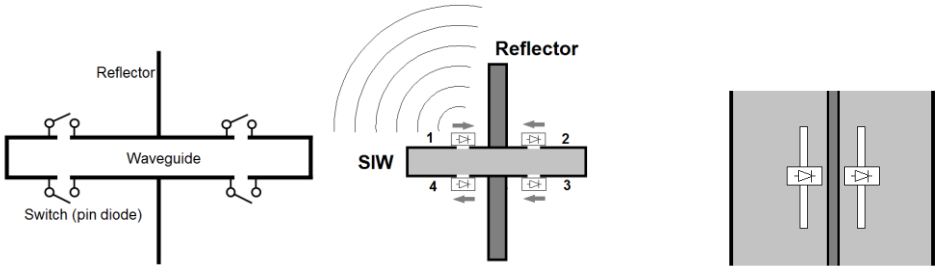

Fig. 3.7. Four direction antenna structure with PIN diode 1 reverse biased and PIN diodes 2, 3 & 4 forward biased. Left: transverse plane of waveguide showing vertical reflector plane and slot 1 radiating; Right: longitudinal plane of waveguide showing slots, diodes and reflector plane [32].

Here L_s is the slot length, b is the waveguide height (the substrate thickness in an SIW implementation), ε_0 is the freespace impedance and k_0 is the freespace wavenumber. The waveguide phase constant β of the TE_{10} mode is given by the well-known expression

$$\beta = \sqrt{\varepsilon_r k_0^2 - k_x^2} \qquad \text{(Eq.3.10)}$$

and is calculated at the resonant frequency of the slot. We note that (Eq.3.11) differs from [33] because the slot length in a SIW is not equal to $\lambda_0/2$. In fact the resonant length is difficult to calculate in practice and is dependent not only on the length and relative permittivity, ε_r, of the substrate but also the displacement, x. A first approximation can be obtained by assuming that the effective permittivity of the standing wave set up in the slot is given by the average of the air and substrate material. This gives an approximate resonant frequency of [46]

$$f_0 = \frac{c}{L_s \sqrt{2(\varepsilon_r + 1)}} \qquad \text{(Eq.3.11)}$$

where c is the speed of light in vacuum.

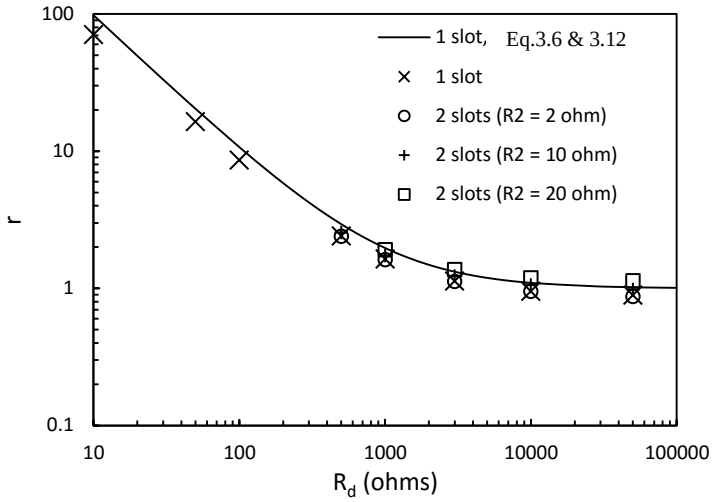

Fig. 3.8. Effective normalized shunt resistance of a waveguide slot antenna as a function of the slot loading resistance R_d. In the case of the 2 slot design, R_2 is the loading resistance of the second slot [32].

When a diode is used to load the slot, the radiation conductance is effectively in parallel with the diode and therefore, if we assume that the diode can be represented by a simple conductance, G_d, then

$$g_0 = \frac{4K^2}{G_r + G_d}. \qquad \text{(Eq.3.12)}$$

It is clear from equation (Eq.3.12) that when $G_d << G_r$ (i.e. when the diode resistance is very large) the impedance presented to the waveguide will be unaffected by the diode and will be given by the normal expression (Eq.3.7). However, when $G_d >> G_r$ (when the resistance is small), g_0 will not depend on the radiation conductance of the slot; in fact it will be very small and therefore present a shunt conductance much smaller than the characteristic admittance of the waveguide. In this case there is little coupling and therefore radiation from the slot. To demonstrate this we consider the normalized shunt resistance, $r = g^{-1}$, of a single slot, at resonance, seen by a waveguide of dimensions a = 52 mm, b = 1.575 mm, and relative permittivity ε_r = 2.2. The slot has length L_s = 52.7 mm, width w = 1.4 mm and is displaced x = *2 mm* from the centre of the guide: resulting in approximately $g(x) = 1$ in the unloaded state. The slot radiation conductance is approximated by a $\lambda_g/2$ slot radiating into half space: $G_r = 2 \times 73.13 \eta_0^{-2}$ [33]. Simulated results use CST microwave studio and model the slot as a two-port device, the slot admittance being extracted from the impedance parameters. Theoretical values use equations (Eq.3.6) and (Eq.3.12). In each case the slot is loaded with a resistance $R_d = G_d^{-1}$. Fig. 3.8 shows the normalized resistance, $r = g^{-1}$ at resonance as a function of R_d. Fig. 3.9 shows the corresponding resonant frequency, calculated

using CST, and determined when the reactance of the slot is zero; equation (Eq.3.11) gives a value of 2.24 GHz.

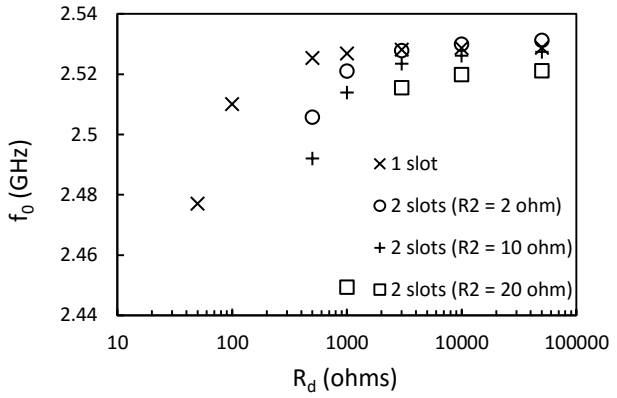

Fig. 3.9. Effect of loading resistance on the slot resonant frequency as a function of the loading resistance, R_d. In the case of the 2 slot design R_2 is the loading resistance of the second slot [32].

Fig. 3.8 shows that the values calculated via equations (Eq.3.6) and (Eq.3.12) are in reasonably good agreement with the normalized shunt resistance calculated using full wave simulation. The graph clearly demonstrates that for loading values greater than 3 kΩ the loading resistor has little effect on the impedance of the slot (seen by the waveguide) and therefore the slots radiation characteristics are unaffected. In contrast, for a loading resistance of 10 Ω or less, the impedance seen by the waveguide is at least 100 times greater than the characteristic impedance and therefore there will be insignificant radiation from the slot.

Although equations (Eq.3.6) and (Eq.3.12) provide a good qualitative explanation of the structure they are not accurate enough for design purposes. In addition, the PIN diode has a reactive component to its impedance which is not accounted for in the above model. The model does however provide a good starting point for a full-wave optimization.

Figures 3.8 and 3.9 also show the effect that loading has when there are two slots present. In this case the structure has identical dimensions as above, but has two slots on opposite sides and faces of the SIW (as in Fig. 3.6). One of the slots is loaded with a nominal short circuit, R_2 (2, 10 and 20 Ω), the other slots loading resistance, R_d, is varied as before. As can be seen there is very little difference in both the resonant frequency and normalized impedance when compared to a single slot as long as R_2 is below 10 Ω. Therefore, as long as the loading impedance on one slot is less than 10 Ω and the impedance on the radiating slot is a few thousand ohms or more, the system operates, from a matching point of view, as a single slot antenna.

It is also interesting to see what effect the loading resistance has on the gain of the antenna. Fig.3.10 shows the simulated gain (using CST) for a single slot loaded with various values of R_d. The structure has the same dimensions as above. Since the radiation resistance and the loading resistance are effectively in parallel with each other, the gain should be of the form:

$$GAIN = GA_u + 10\log_{10}\left(\frac{G_r}{G_r + G_d}\right) \qquad \text{(Eq.3.13)}$$

where GA_u is the unloaded gain of the slot and the second term represents the drop in efficiency due to loading. Using a simulated (CST) unloaded gain of GA_u = 6.5 dBi, equation (Eq.3.13) fits the simulated results almost exactly. It is clear from Fig. 3.10 that acceptable efficiency requires R_d > 3 kΩ.

The efficiency of the antenna is also affected by the forward biased resistance of the diodes used to turn off the radiation in the other slots. Fig. 3.10 also shows the effect of this with a dual slot design (as Fig.3.6) of identical dimensions as above. As can be seen if the resistance, R_2, is 2 Ω then very little change is seen in the gain. However, for values of 10 or 20 Ω the gain drops by 1-2 dB due to dissipation in R_2. It is therefore important to keep the forward biased resistance as low as possible (< 2 Ω) and the open circuit as high as possible (> 3 kΩ).

The radiation patterns were found to be largely independent of variations in the loading impedance from the nominal forward and reverse biased conditions.

3.4.3 Design Procedure

In order to accurately model the loaded slots it is important that a good model for the loading PIN diode is used. In this paper we use the BAR64-02V PIN diode from Infineon. From the manufacturer's data sheet this can be modelled as an inductor of L = 0.6 nH in series with a resistance R_f when forward biased and the same inductor in series with the parallel combination of a 0.17pF capacitor and a resistor R_r when in reverse biased. R_f depends on the forward biased voltage and R_r depends on the reverse biased current. Here we use values of 2 Ω for R_f and 3 kΩ for R_r, corresponding to a forward current of 10 mA and a reverse biased voltage of zero volts. The inductance is not included in the simulation because the coupling capacitors used to couple the diode to the slot are chosen such that they resonate out the inductor at the chosen design

frequency. The reverse biased capacitance, however, is included. The loading elements are simulated using CST's lumped element function.

The procedure starts by simulating the waveguide antenna as a two port device in CST and determining the network's Z-parameters and therefore shunt conductance. Although the practical implementation is in SIW, with conducting vias for the sidewalls, solid walls are used in the design optimization to reduce the complexity of the simulation. One of the slots is loaded with R_f, the others with the parallel combination of 0.17 pF and R_r. Due to the symmetry of the structure the choice of the radiating slot is irrelevant. The length of the slot, L_s, and the displacement, x, are then optimized to give a normalized shunt admittance of unity at the design frequency; 2.45 GHz in this case. Using this value the full structure is then simulated with a terminating short circuit at a distance C_s from the centre of the slot – set to approximately $\lambda_g/4$; a further optimization of C_s is then used with some fine tuning of x and L_s.

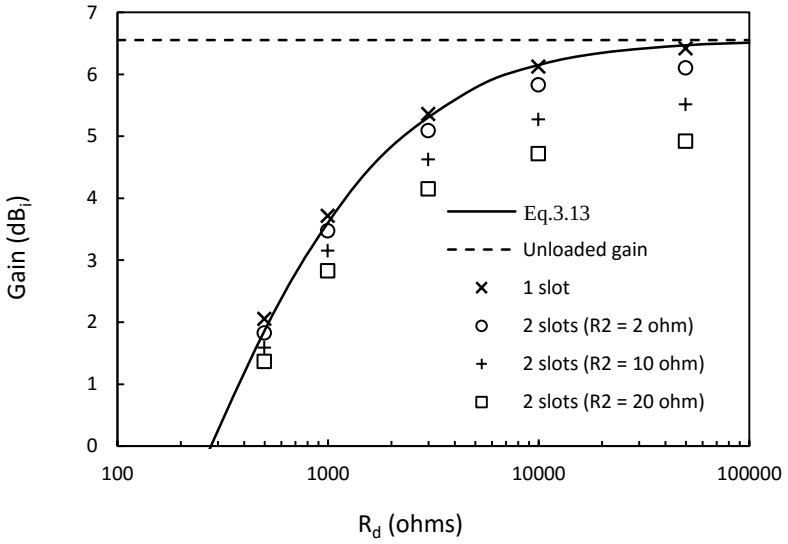

Fig. 3.10. Simulated gain as a function of loading resistance, R_d.
In the case of the 2 slot design R_2 is the loading resistance of the second slot [32].

3.4.4 Practical Implementation

Three designs were fabricated on 1.575 mm thick Rogers RT5880 laminate with $\varepsilon_r = 2.2$, Tan $\delta = 0.0009$ and copper thickness of 70 μm. The designs consisted of: (A) a two slot design (Fig 3.6); (B) a four slot, four direction design and (C) a four slot design optimized for six directions (Fig. 3.7). The designs were simulated and optimized in CST using the method highlighted in section 3.4.3. The reflecting plane, used in the four and six direction designs, was formed from a 1.575 mm FR4 substrate, metallized on both sides. A milled keyway ensured accurate positioning,

and a soldered seam ensured the electrical connectivity. This low frequency laminate was used for cost effectiveness since the wave does not penetrate into the reflector material and therefore the relatively poor dielectric properties of FR4 do not affect the design.

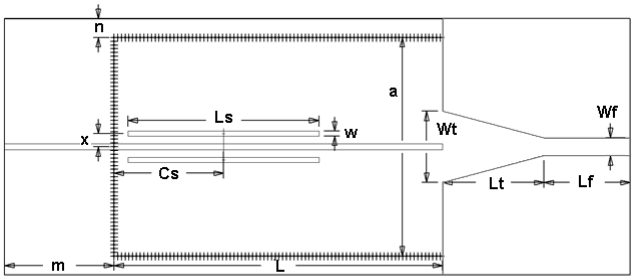

Fig. 3.11. Structure of switched beam antenna [32].

Label	Design			Description
	A*	B	C	
W_{gL} *(L)*	102.7	87.6	75.0	Length of waveguide ($3C_s$)
a	52	58.0	61.0	Waveguide width
L_s	52.7	50.9	48.5	Slot length
C_s	33.6	29.2	25.0	Distance from end of waveguide
n	5.0	5.0	5.0	Distance to edge of substrate
L_t	24	27.0	24.0	Taper length
W_t	13.9	19.0	20.0	Taper width
L_f	22.5	23.0	22.0	Microstrip feed length
w	1.4	1.3	1.3	Slot width
m	33.6	29.2	25.0	Length to end of substrate (C_s)
x	2.0	3.5	3.5	Slot offset

All dimensions in mm.

*Design (A) does not have a reflector and has only one slot on each side – on opposing sides of the center of the waveguide.

TABLE 3.1 Design Dimensions.

PIN diodes have been used in related field of frequency selective surfaces [47, 48] to create switchable states. In this application the concept was extended with the PIN diodes added to flexible circuit design; with controlled copper dimensions to achieve required impedance responses at desired frequencies. A few different connecting topologies were trialled to achieve the best performance using the Mylar overlay, which is a single sided (flexi) laminate with 18μm copper, 12 μm polyester dielectric, $\varepsilon_r = 3.2$, Tan $\delta = 0.003$ (manufacturer reference DuPont Pyralux AC 181200RT).

Fig. 3.12. Structure of overlay showing capacitive pads, PIN diode, inductive chokes and bias wires [32].

Switching is performed by capacitively coupling Infineon BAR64-02V PIN diodes to each of the slots in a similar manner to [46, 49]. This is achieved by etching two pads on a metallized 12 μm thick Mylar overlay. The overlay was then aligned and stuck to the SIW using a 25 μm thick adhesive. A schematic and photo of the overlay is shown in Fig.3.12. The dimensions of the pads are chosen to give approximately 17 pF each which ensures that the two capacitors resonate out the inductance of the PIN diode at the design frequency. The overlay also has two smaller pads used to connect two 1nH inductive chokes and wires for applying the bias to the diodes. The PIN diodes were controlled via a bespoke control box, which switched the four PIN diodes individually between a set forward current bias position and a reverse voltage bias position.

The dimensions of the structures are shown in Fig. 3.11 together with Table 3.1. A photograph of the four direction design is shown in Fig. 3.13. The FR4 reflector has a total height equal to the total width of the waveguide structure and is positioned such that the slot is central. Note that in the case of the two direction design, there is no reflecting plane and only two slots, on opposite sides and faces of the SIW. The antennas have a microstrip to SIW tapered feed which is optimized for each of the three designs and is used to connect an SMA connector for measurement. The microstrip feed line width, W_f, is chosen for 50 Ω; 4.75 mm in this case.

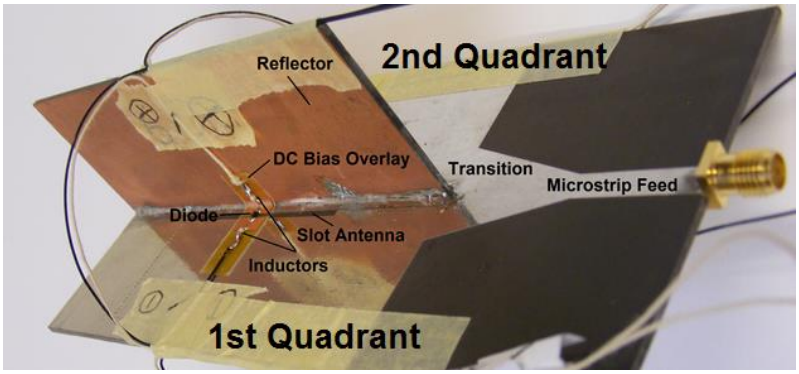

Fig. 3.13. Photograph of four direction switched beam antenna [32].

3.4.5 Measurement Results

The S-parameters were measured using VNA calibrated using a coaxial SOLT method. The SMA connector used to connect the device were not de-embedded and therefore form part of the return loss measurements. A measurement range of ±25% of the antenna design frequency was used, giving a span of 1.8 to 3 GHz. The DC bias to the diodes was supplied via a custom switch box with a 3×9V battery supply. The switch box allowed each diode to be set to either reverse biased (27 V – chosen to maximize the resistance) or forward biased (10 mA), hence enabling each slot to radiate at the target frequency or to be effectively short-circuited and thus not radiate. A current limiting resistor was included in the forward biased switch condition to prevent excessive current in the event of a device failure.

The antenna radiation patterns and gain measurements were made using the department's anechoic chamber, which also required custom mounting jigs to be designed and fabricated.

3.4.6 Two Direction Design Performance

Slot	Simulated				Measured			
	f_0	S_{11}	BW	Gain	f_0	S_{11}	BW	Gain
	GHz	dB	MHz	dBi	GHz	dB	MHz	dBi
1	2.43	-22	60.0	5.4	2.45	-30	80.5	5.2
2	2.43	-22	60.0	5.5	2.45	-27	90.0	4.7

TABLE 3.2. Two Direction Antenna Measured Results
See Fig. 3.6 for slot designation.

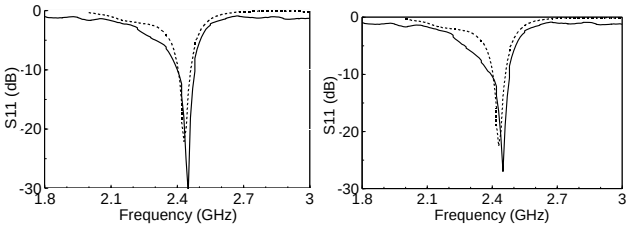

Fig. 3.14. S_{11} of two direction antenna. Left: slot 1 radiating; right: slot 2 radiating.
Solid lines denote measured values, dotted lines denote simulated values.

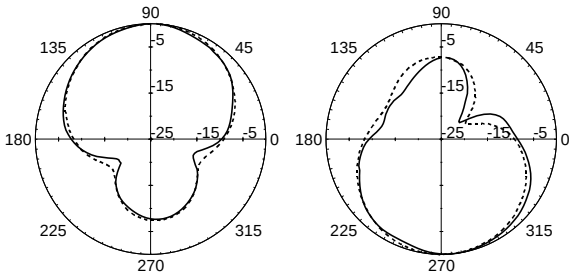

Fig. 3.15. Two direction antenna normalized radiation pattern in dB.
Left: slot 1 radiating; right: slot 2 radiating.
Solid lines denote measured values, dotted lines denote simulated values.

Table 3.2 shows the resonant frequency, f_0, the S_{11} at resonance, the -10 dB return loss bandwidth (BW) and the antenna gain for both simulated (using CST) and measured results. The antenna dimensions are shown in Table 3.1 and Fig. 3.11. We see that the measured and simulated results for all parameters display good agreement. The resonant frequency being slightly higher in the measured results with an increased -10 dB bandwidth. There is a slight degradation in the gain particularly for the second slot which is due to additional losses as well as the bias network.

Fig. 3.14 shows the S_{11} as a function of frequency for both states, again showing very good agreement between simulated and measured results. Fig. 3.15 shows normalized radiation patterns in the plane perpendicular to surfaces of the waveguide. Once again there is excellent agreement between simulated and measured results. The plot clearly shows the two discrete directions of radiation. The backward lobes at approximately -7.5 dB below the main lobe are due to the finite size of the waveguide structure and not radiation from the short-circuited slots. Their level could be decreased by increasing the dimension shown as *n* in Fig 3.11. The slight lack of symmetry between the two states is due to the taper feed which inevitably causes some spurious radiation.

3.4.7 Four Direction Design Performance

Slot	Simulated				Measured			
	f_0	S_{11}	BW	Gain	f_0	S_{11}	BW	Gain
	GHz	dB	MHz	dBi	GHz	dB	MHz	dBi
1	2.43	-42	115	6.5	2.48	-40	68	5.5
2	2.43	-42	115	6.5	2.48	-24	57	4.5
3	2.43	-42	115	6.2	2.47	-22	57	5.4
4	2.43	-42	115	6.2	2.47	-27	68	5.2

TABLE 3.3 Four Direction Antenna Measured Results
See Fig. 3.7 for slot designation.

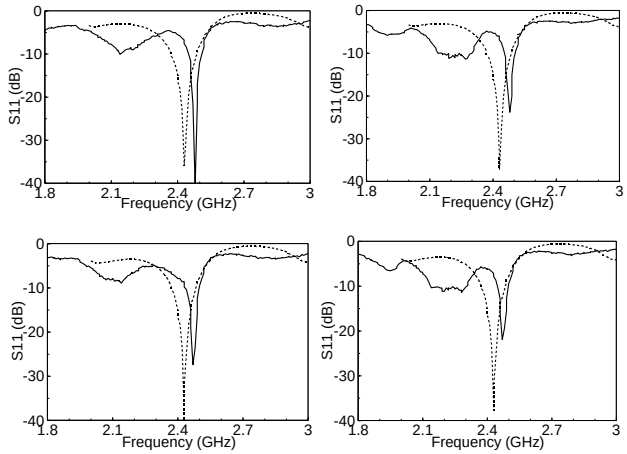

Fig. 3.16. S_{11} of four direction antenna. Top left: slot 1 radiating; Top right: slot 2 radiating; Bottom left: slot 3 radiating; Bottom right: slot 4 radiating.
Solid Lines denote measured values, dotted lines denote simulated values.

Table 3.3 and figures 3.16 and 3.17 show the simulated and measured results for the four direction design, a photograph of which is shown in Fig. 3.13. Once again the results are in good agreement. However, the resonant frequency in this case is 40-50MHz higher than in simulation and has a reduction in the bandwidth – probably due to fabrication tolerance.

The radiation patterns in Fig. 3.17 clearly show the four distinct directions of radiation. The side-lobe size and beamwidth of the main lobe is controlled by the size of the reflector. In this implementation the size was chosen for compactness, resulting in a -3 dB beamwidth of approximately 80°. However, for increased directivity and lower side-lobes a bigger reflector could be used. The dimension shown as *m* in Fig. 3.11 was chosen so that the slot is central in the reflector but could be reduced if required.

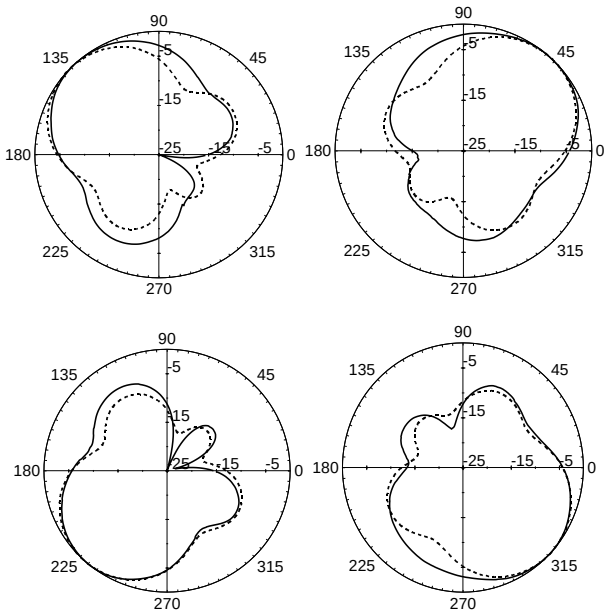

Fig.3.17. Four direction antenna normalized radiation pattern in dB.
Top left: slot 1 radiating; Top right: slot 2 radiating;
Bottom left: slot 3 radiating; Bottom right: slot 4 radiating.
Solid Lines denote measured values, dotted lines denote simulated values.

The measured gain is lower than simulated, particularly for the second quadrant. There are a number of factors that affect the gain, including the increased losses that are present in the practical implementation. However, here, it is more likely that the variation is due to the slot loading impedances. Fig. 3.10 shows how dependent the gain is on the loading resistances of the slots with only a small departure from the nominal design values of 2 Ω (for the diode forward biased resistance) and 3 kΩ for (reverse biased resistance) having a considerable effect on the simulated gain. Since PIN diodes have quite a large natural variability the gain will also be variable. Furthermore, any variation in the bias levels will result in a change in the resistance and therefore the measured gain. Additionally, the reactive loading of the slot will also affect the results with the

rather crude technique of capacitively coupling the diode to the slots inevitably introducing a large degree of variability.

3.4.8 Six Direction Design Performance

Since slots 1 and 4 and slots 2 and 3 radiate in phase with each other, it is possible to provide two additional directions of radiation, perpendicular to the reflector, by allowing two of the slots to radiate at the same time. In order to do this, a slightly different design procedure must be followed, with the design being optimized to provide a good match when one slot is radiating but also when two slots are radiating. This is achieved by noting that two radiating slots effectively half the shunt resistance seen by the waveguide compared to that of a single slot. Therefore, if the slot displacement, *x*, is optimized to give a normalized shunt resistance of $\sqrt{2}$ then for two slots it will be approximately $1/\sqrt{2}$ and therefore a compromise for the S_{11} of both states is achieved with the single and dual slot radiation condition achieving an S_{11} = -15 dB at the resonant frequency. This optimization was performed resulting in the values in Table 3.1.

Slot	Simulated				Measured			
	f_0	S_{11} dB	BW	Gain	f_0	S_{11} dB	BW	Gain
	GHz		MHz	dBi	GHz		MHz	dBi
1	2.46	-15	63	5.6	2.48	-19	70.0	6.0
2	2.46	-15	63	5.6	2.48	-29	80.0	4.6
3	2.46	-15	63	5.6	2.48	-24	80.0	3.8
4	2.46	-15	63	5.6	2.48	-19	70.0	3.0
2&3	2.48	-15	45	4.7	2.50	-17	60.0	5.0
1&4	2.48	-15	45	4.7	2.50	-20	60.0	4.7

TABLE 3.4 Six Direction Antenna Measured Results [32].
See Fig. 3.7 for slot designation.

Table 3.4 gives the measured values of the antenna with the S_{11} shown in Fig. 13.18 and the radiation patterns in Fig. 13.19. We see once again the comparison is very good with only a small difference in the resonant frequency. Fig 13.19 clearly shows the two additional beam directions perpendicular to the reflector.

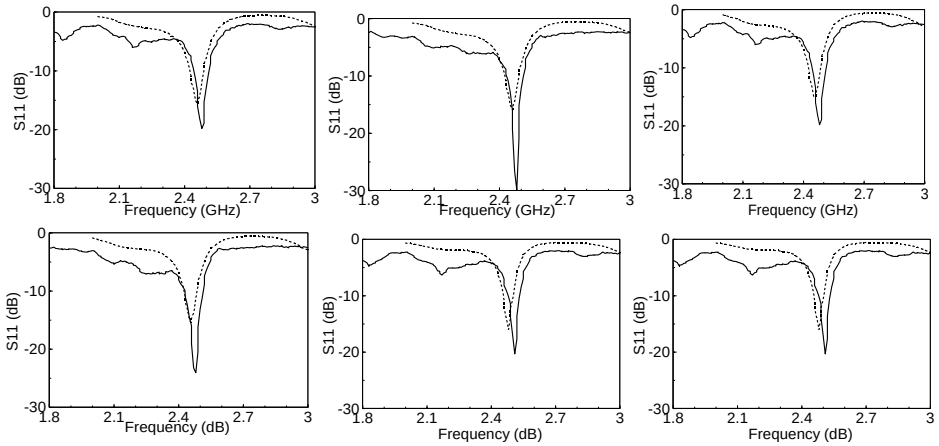

Fig. 13.18. S_{11} of six direction antenna [32].
Top left: slot 1 radiating; Top middle: slot 2 radiating; top right: slot 3 radiating;
Bottom left: slot 4 radiating; Bottom middle: slot 1 & 4 radiating; Bottom right: slot 2 & 3 radiating.
Solid Lines denote measured values, dotted lines denote simulated values.

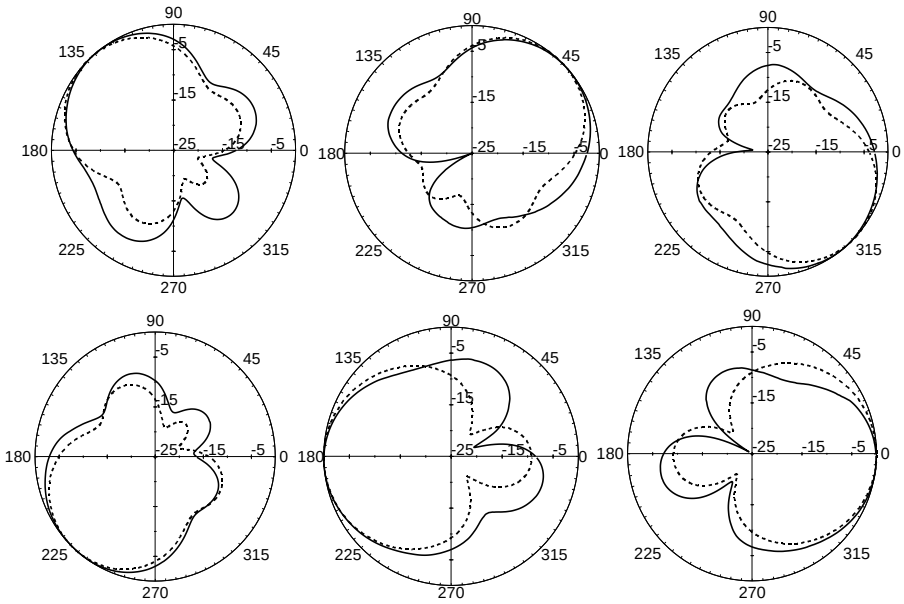

Fig.13.19. Six direction antenna normalized radiation pattern [32].
Top left: slot 1 radiating; Top middle: slot 2 radiating; Top right: slot 3 radiating;
Bottom left: slot 4 radiating; Bottom middle: slot 1 & 4 radiating; Bottom right: slot 2 & 3 radiating.
Solid Lines denote measured values, dotted lines denote simulated values.

3.5 SIW antennas summary

SIW antennas were briefly overviewed, and a single and dual slot antenna design example discussed. The main part of the chapter focussed on a SIW switched beam antenna giving 360°, equally spaced, coverage in up to six discrete directions. The design was shown to be in good agreement with simulated results achieving a measured -10 dB return loss bandwidth of approximately 3% and antenna gains in the range 3 to 6 dBi. Furthermore, the design is no larger than a single SIW slot antenna.

Prototypes were demonstrated at 2.45 GHz; however the design may find greater use at higher frequencies where SIW is a more appropriate host transmission line. The switch beam antenna was a collaborative piece of work between Liang Wu (design simulations in CST), Dr Paul Young, and myself (responsible for the PCB and overlay design, test box design, assembly and fabrication). Measurement, analysis and overall design development was shared and a summary of the work detailing the six direction version has been published [32].

3.6 References

[1] C. A. Balanis, *Antenna Theory: Analysis and Design.* Wiley-Blackwell, 2005.

[2] Fan Zhang, Fu-Shun Zhang, Ya-Bing Yang and Zheng Zhang. Wide band antenna array using bowtie-shaped microstrip patch antenna. Presented at Microwave and Millimeter Wave Technology (ICMMT), 2010 International Conference On. 2010, .

[3] R. A. Alhalabi and G. M. Rebeiz. High-gain yagi-uda antennas for millimeter-wave switched-beam systems. *Antennas and Propagation, IEEE Transactions On 57(11),* pp. 3672-3676. 2009.

[4] P. R. Grajek, B. Schoenlinner and G. M. Rebeiz. A 24-GHz high gain yagi-uda antenna array. *Antennas and Propagation, IEEE Transactions On 52(5),* pp. 1257-1261. 2004.

[5] A. L. Amadjikpe, D. Choudhury, G. E. Ponchak and J. Papapolymerou. High gain quasi-yagi planar antenna evaluation in platform material environment for 60 GHz wireless applications. Presented at Microwave Symposium Digest, 2009. MTT '09. IEEE MTT-S International. 2009, .

[6] M. Esquius-Morote, B. Fuchs, J. -. Zurcher and J. R. Mosig, "Novel Thin and Compact H-Plane SIW Horn Antenna," *Antennas and Propagation, IEEE Transactions On,* vol. 61, pp. 2911-2920, 2013.

[7] H. Nakano and J. Yamauchi, "Printed Slot and Wire Antennas: A Review," *Proceedings of the IEEE,* vol. PP, pp. 1-11, 2012.

[8] K. Huang and D. J. Edwards, *Millimetre Wave Antennas for Gigabit Wireless Communications: A Practical Guide to Design and Analysis in a System Context.* Wiley-Blackwell, 2008.

[9] J. Machac, P. Lorenz, M. Saglam, C. Bui and W. Kraemer. A substrate integrated waveguide leaky wave antenna radiating from a slot in the broad wall. Presented at Microwave Symposium Digest (MTT), 2010 IEEE MTT-S International. 2010, . DOI: 10.1109/MWSYM.2010.5515476.

[10] Juhua Liu, D. R. Jackson and Yunliang Long. Substrate integrated waveguide (SIW) leaky-wave antenna with transverse slots. *Antennas and Propagation, IEEE Transactions On 60(1),* pp. 20-29. 2012.

[11] Feng Xu, Ke Wu and Xiupu Zhang, "Periodic Leaky-Wave Antenna for Millimeter Wave Applications Based on Substrate Integrated Waveguide," *Antennas and Propagation, IEEE Transactions On,* vol. 58, pp. 340-347, 2010.

[12] Y. Mohtashami and J. Rashed-Mohassel, "A Butterfly Substrate Integrated Waveguide Leaky-Wave Antenna," *Antennas and Propagation, IEEE Transactions On*, vol. 62, pp. 3384-3388, 2014.

[13] A. J. Martinez-Ros, J. L. Gomez-Tornero and F. Quesada-Pereira, "Efficient Analysis and Design of Novel SIW Leaky-Wave Antenna," *Antennas and Wireless Propagation Letters, IEEE*, vol. 12, pp. 496-499, 2013.

[14] A. J. Martinez-Ros, J. L. Gomez-Tornero and G. Goussetis. Planar leaky-wave antenna with flexible control of the complex propagation constant. *Antennas and Propagation, IEEE Transactions On 60(3)*, pp. 1625-1630. 2012. . DOI: 10.1109/TAP.2011.2180320.

[15] Aixin Chen, Weiwei Jiang, Jian Fang and Jiaheng Wang. Composite right/left-handed leaky wave antenna with half mode substrate integrated waveguide structure. Presented at Microwave, Antenna, Propagation and EMC Technologies for Wireless Communications (MAPE), 2013 IEEE 5th International Symposium On. 2013, . DOI: 10.1109/MAPE.2013.6689830.

[16] S. A. Razavi and M. H. Neshati. Design investigation of a leaky wave antenna using HMSIW technique. Presented at Telecommunications (IST), 2012 Sixth International Symposium On. 2012, . DOI: 10.1109/ISTEL.2012.6482948.

[17] Yuandan Dong and T. Itoh. Substrate integrated composite right-/left-handed leaky-wave structure for polarization-flexible antenna application. *Antennas and Propagation, IEEE Transactions On 60(2)*, pp. 760-771. 2012.

[18] Yuanxin Li, Quan Xue, E. K. Yung and Yunliang Long, "Dual-Beam Steering Microstrip Leaky Wave Antenna With Fixed Operating Frequency," *Antennas and Propagation, IEEE Transactions On*, vol. 56, pp. 248-252, 2008.

[19] Feng Xu and Ke Wu. Understanding leaky-wave structures: A special form of guided-wave structure. *Microwave Magazine, IEEE 14(5)*, pp. 87-96. 2013. . DOI: 10.1109/MMM.2013.2259400.

[20] Li Yan, Wei Hong, Guang Hua, Jixin Chen, Ke Wu and Tie Jun Cui. Simulation and experiment on SIW slot array antennas. *Microwave and Wireless Components Letters, IEEE 14(9)*, pp. 446-448. 2004.

[21] H. Uchimura, T. Takenoshita and M. Fujii, "Development of the "laminated waveguide"," in *Microwave Symposium Digest, 1998 IEEE MTT-S International*, 1998, pp. 1811-1814 vol.3.

[22] W. Menzel and J. Kassner, "Millimeter-wave 3D integration techniques using LTCC and related multilayer circuits," in *Microwave Conference, 2000. 30th European,* 2000, pp. 1-4.

[23] M. S. Aftanasar, P. R. Young, I. D. Robertson, J. Minalgiene and S. Lucyszyn, "Photoimageable thick-film millimetre-wave metal-pipe rectangular waveguides," *Electronics Letters,* vol. 37, pp. 1122-1123, 2001.

[24] D. Deslandes and Ke Wu, "Integrated microstrip and rectangular waveguide in planar form," *Microwave and Wireless Components Letters, IEEE,* vol. 11, pp. 68-70, 2001.

[25] R. S. Elliott, "An improved design procedure for small arrays of shunt slots," *Antennas and Propagation, IEEE Transactions On,* vol. 31, pp. 48-53, 1983.

[26] Fan Fan He, Ke Wu, Wei Hong, Liang Han and Xiao-Ping Chen. Low-cost 60-GHz smart antenna receiver subsystem based on substrate integrated waveguide technology. *Microwave Theory and Techniques, IEEE Transactions On 60(4),* pp. 1156-1165. 2012.

[27] I. D. Robertson and K. K. Samanta. Multilayer thick-film photoimageable technology for 60 GHz system-in-package. Presented at Microwave Conference, 2008. APMC 2008. Asia-Pacific. 2008, . DOI: 10.1109/APMC.2008.4958263.

[28] K. K. Samanta, D. Stephens and I. D. Robertson, "Design and performance of a 60-GHz multi-chip module receiver employing substrate integrated waveguides," *Microwaves, Antennas & Propagation, IET,* vol. 1, pp. 961-967, 2007.

[29] Xiao-Ping Chen, Ke Wu, Liang Han and Fanfan He. Low-cost high gain planar antenna array for 60-GHz band applications. *Antennas and Propagation, IEEE Transactions On 58(6),* pp. 2126-2129. 2010.

[30] Guo Qing Luo, Zhi Fang Hu, Wen Jun Li, Xiao Hong Zhang, Ling Ling Sun and Jian Feng Zheng. Bandwidth-enhanced low-profile cavity-backed slot antenna by using hybrid SIW cavity modes. *Antennas and Propagation, IEEE Transactions On 60(4),* pp. 1698-1704. 2012.

[31] Guo Qing Luo, Zhi Fang Hu, Lin Xi Dong and Ling Ling Sun, "Planar Slot Antenna Backed by Substrate Integrated Waveguide Cavity," *Antennas and Wireless Propagation Letters, IEEE,* vol. 7, pp. 236-239, 2008.

[32] L. Wu, A. J. Farrall and P. R. Young, "Substrate Integrated Waveguide Switched Beam Antennas," *Antennas and Propagation, IEEE Transactions On,* vol. 63 Issue 5, pp. 2301-2305, 2015.

[33] R. E. Collin and F. J. Zucker, "Antenna theory (part 1)," in *Antenna Theory Part 1*, Volume 7 ed., Inter-University Electronics Series, Ed. New York; London: McGraw Hill, 1969, pp. Chapter 14.

[34] A. J. Farrall and P. R. Young, "Integrated waveguide slot antennas," *Electronics Letters,* vol. 40, pp. 974-975, 2004.

[35] K. A. Gotsis, K. Siakavara and J. N. Sahalos. On the direction of arrival (DoA) estimation for a switched-beam antenna system using neural networks. *Antennas and Propagation, IEEE Transactions On 57(5),* pp. 1399-1411. 2009. . DOI: 10.1109/TAP.2009.2016721.

[36] M. R. Kamarudin, Y. I. Nechayev and P. S. Hall, "Onbody Diversity and Angle-of-Arrival Measurement Using a Pattern Switching Antenna," *Antennas and Propagation, IEEE Transactions On,* vol. 57, pp. 964-971, 2009.

[37] M. Chryssomallis, "Smart antennas," *Antennas and Propagation Magazine, IEEE,* vol. 42, pp. 129-136, 2000.

[38] J. H. Winters, "Smart antennas for wireless systems," *Personal Communications, IEEE,* vol. 5, pp. 23-27, 1998.

[39] B. Cetinoneri, Y. A. Atesal and G. M. Rebeiz, "An 8 8 Butler Matrix in 0.13- CMOS for 5–6-GHz Multibeam Applications," *Microwave Theory and Techniques, IEEE Transactions On,* vol. 59, pp. 295-301, 2011.

[40] A. Edalati and T. A. Denidni, "Frequency Selective Surfaces for Beam-Switching Applications," *Antennas and Propagation, IEEE Transactions On,* vol. 61, pp. 195-200, 2013.

[41] G. Poilasne, P. Pouliguen, K. Mahdjoubi, L. Desclos and C. Terret, "Active metallic photonic band-gap materials (MPBG): experimental results on beam shaper," *Antennas and Propagation, IEEE Transactions On,* vol. 48, pp. 117-119, 2000.

[42] Ming-Iu Lai, Tzung-Yu Wu, Jung-Chin Hsieh, Chun-Hsiung Wang and Shyh-Kang Jeng, "Compact Switched-Beam Antenna Employing a Four-Element Slot Antenna Array for Digital

Home Applications," *Antennas and Propagation, IEEE Transactions On,* vol. 56, pp. 2929-2936, 2008.

[43] R. A. Alhalabi, Yi-Chyun Chiou and G. M. Rebeiz, "Self-Shielded High-Efficiency Yagi-Uda Antennas for 60 GHz Communications," *Antennas and Propagation, IEEE Transactions On,* vol. 59, pp. 742-750, 2011.

[44] P. Ngamjanyaporn and M. Krairiksh, "Switched-beam single patch antenna," *Electronics Letters,* vol. 38, pp. 7-8, 2002.

[45] D. Stephens, P. R. Young and I. D. Robertson, "Millimeter-wave substrate integrated waveguides and filters in photoimageable thick-film technology," *Microwave Theory and Techniques, IEEE Transactions On,* vol. 53, pp. 3832-3838, 2005.

[46] Ruo Feng Xu, A. J. Farrall and P. R. Young, "Analysis of Loaded Substrate Integrated Waveguides and Attenuators," *Microwave and Wireless Components Letters, IEEE,* vol. 24, pp. 62-64, 2014.

[47] B. Sanz-Izquierdo, E. A. Parker, J. -. Robertson and J. C. Batchelor, "Tuning technique for active FSS arrays," *Electronics Letters,* vol. 45, pp. 1107-1109, 2009.

[48] B. Sanz-Izquierdo, E. A. Parker and J. C. Batchelor, "Switchable Frequency Selective Slot Arrays," *Antennas and Propagation, IEEE Transactions On,* vol. 59, pp. 2728-2731, 2011.

[49] Ruo Feng Xu, B. S. Izquierdo and P. R. Young, "Switchable Substrate Integrated Waveguide," *Microwave and Wireless Components Letters, IEEE,* vol. 21, pp. 194-196, 2011.

4 Slot Substrate Integrated Waveguides

Active and discrete devices can be integrated with SIW but usually require transitions to planar transmission lines such as microstrip or coplanar waveguide. These transitions can be relatively large and can suffer from radiation and mismatch losses. To overcome this problem the Slotted SIW (SSIW), which has propagation characteristics similar to half mode SIW [1], offers the advantage of easy integration of lumped element devices across the slot. In this chapter, the SSIW will be introduced and three PCB test coupons will be developed and fabricated. The conditions of the slot unloaded and short circuited will be outlined and then the more complex situation of an intermediate condition will be discussed. By loading the SSIW with impedance discontinuities it is possible to design waveguide devices; in this chapter a travelling wave attenuator using active devices and a passive bandpass filter using a capacitive coupled thin laminate overlay will be considered.

A periodically loaded SSIW is analysed by means of the transverse resonance technique, this method can be used for reactive, resistive or complex valued loading elements. Correctly loading the SSIW periodically leads to demonstrating a variable attenuator using active devices (PIN diodes), which is shown to operate over a relatively large bandwidth. Variable attenuators have applications for use with matching microwave components, limiting power between components and for modulating amplitude; particularly if scaled appropriately to millimetre wave designs. The modulation of amplitude investigated here models passive components and hence produces amplitude attenuation.

Bandpass waveguide filters are designed to demonstrate the use of capacitively coupled overlay circuits. This is an extension to their use described in chapter 3, where it was used as frequency specific DC bias circuit. A *virtual via* has been termed as a short circuit link which crosses the slot of the SSIW, this virtual via is realised in copper on a thin laminate which is placed in close proximity to the SSIW surface, allowing capacitive coupling to occur. To enable the filter design, virtual via configurations are designed and analysed. Bandpass filters are then configured using the characterised virtual via data, fabricated and measured.

4.1 SSIW Introduction

As discussed in chapter 2, an SIW may be split vertically along its longitudinal symmetrical centre line, and the cutting plane may be considered as a magnetic wall (blue line in Fig. 4.1). This enables the half width SIW to maintain the propagation modes of the full SIW, hence the term half mode SIW (HMSIW). The Slot SIW, sometimes referred to as planar HMSIW [2], are similar to standard SIW with the addition of a slot introduced down one side of the top conducting surface. Fig. 4.1 shows a representative diagram of the relative electric field within these three structures. The maximum is denoted by the larger red arrow, and the red line represents the electric field amplitude. The main point is the electric field maximum is located in the centre and is vertical and perpendicular to the direction of propagation (which would be into or out of the page as shown). The top figure is for the fully enclosed standard SIW, the middle is a representation of a half mode SIW (dielectric material not shown), and the bottom is an approximation of the electric field within the SSIW, all three are for the fundamental propagating mode.

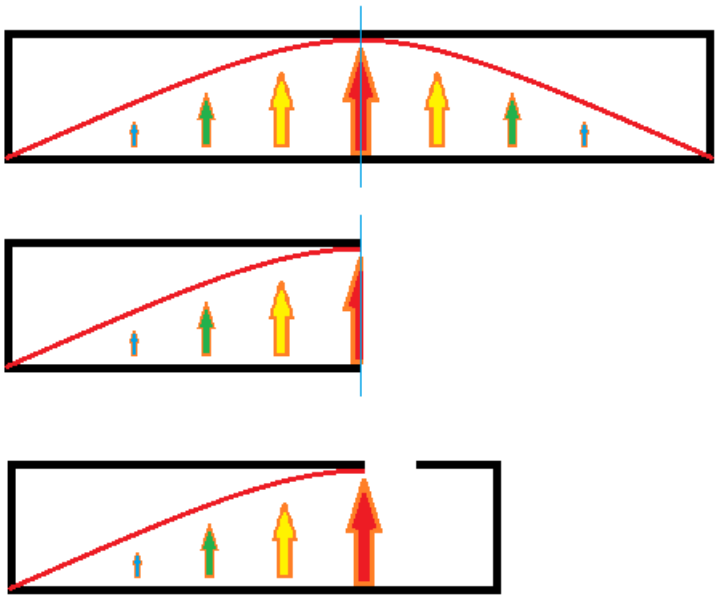

Fig. 4.1 Electric Field representation for Standard SIW (top), HMSIW (middle), SSIW (bottom).

The slot adds a capacitive air gap of width *w*, and the top copper surface is split between the main HMSIW section of length L_1 and a shunt waveguide section is of length L_2 (see Fig.4.3). As with normal SIWs, all sides are conductive, with the side walls again formed by rows of vias. By creating discontinuities across the slot it is possible to modify the propagating characteristics of the waveguide. With the slot fully open it acts as the SSIW in the half mode, with the slot fully closed,

it becomes the standard rectangular SIW, and if the slot is loaded with an impedance then the waveguide propagation becomes more complex, this is summarised in the representation of Fig. 4.2.

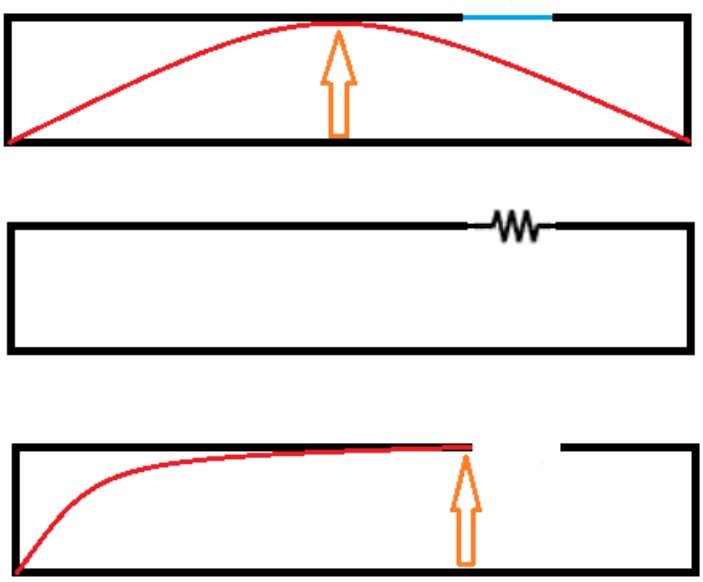

Fig. 4.2 Electric field representation for SSIW; shorted slot (top), loaded impedance (middle), and open slot (bottom)

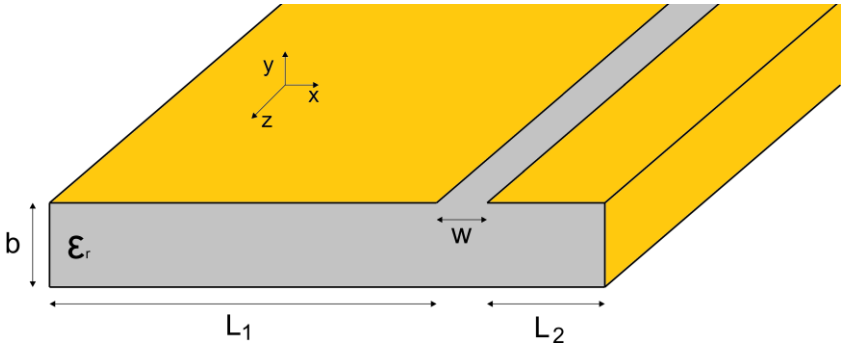

Fig. 4.3 SSIW cross-section (shown with solid side walls)

From section 2.4 for HMSIW with waveguide width $a_{HM}=L_1$, the fundamental TE mode, which strictly should be termed the $TE_{1/2,0}$ cut-off, is defined as:

$$f_{c(1/2,0)} = \frac{c}{4\pi L_1 \sqrt{\varepsilon_r}} \qquad \text{(Eq. 4.1)}$$

This is an approximate cut-off value only, as it does not include the effect of fringing fields, so may only be used as an approximation.

An example with L_1=15mm is shown in Fig. 4.4. This is a vertical view of the electric field simulation (from HFSS) for a SSIW with a slot width w=0.5mm and shunt width L_2=2.5mm using a Rogers 5880 laminate, with ε_r=2.2 (this is referenced as the SSIW01 variant, with full details in section 4.2), this gives $f_{c(1/2,0)}$ ~3.4 GHz well below the frequency shown. The electric field is clearly viewed propagating along the waveguide with the electric field maximum close to the slot, the associated scale to the right of the figure in V/m. The via walls are viewed top and bottom of the plot, and contain the wave within the waveguide, there is a small amount of energy in the shunt waveguide, due to its structure.

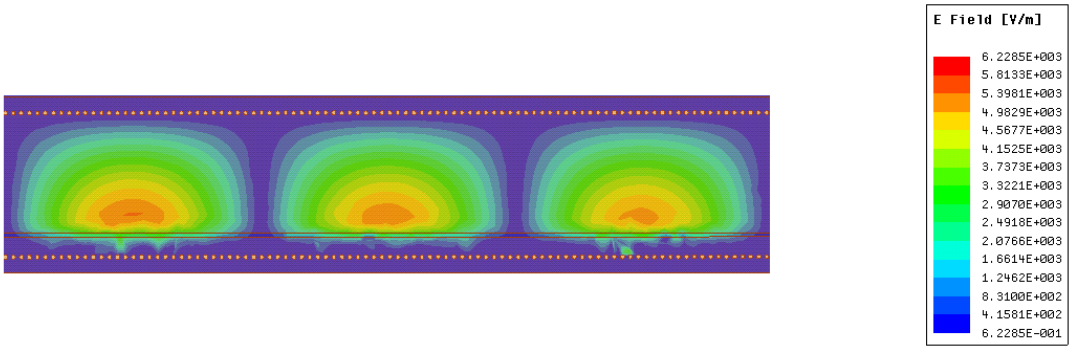

Fig. 4.4 Electric field simulation plot for SSIW01 unloaded slot at 4.5 GHz

However, when the air gap is shorted, the waveguide reverts back to a full SIW so the wave guide width becomes $a=L_1+w+L_2$. The true effective waveguide width a_{eff} may be calculated when the effects of the vias are taken into consideration as in section 2.8.

Thus the waveguide is now full $TE_{1,0}$, and

$$f_{c(1,0)} = \frac{c}{2\pi a_{eff}\sqrt{\varepsilon_r}} \qquad \text{(Eq. 4.2)}$$

The difference between the two cut-off frequencies will depend on the relative values of L_1,w and L_2, if $a_{eff} \approx L_1$ then $f_{c(1,0)} \approx f_{c(1/2,0)}$. Fig. 4.5 shows an electric field plot simulation for the example SSIW discussed, with the slot completely shorted. The $f_{c(1,0)}$ for the filled slot is 5.7 GHz, so an example field plot is show at 6.0 GHz, just above this new cut-off.

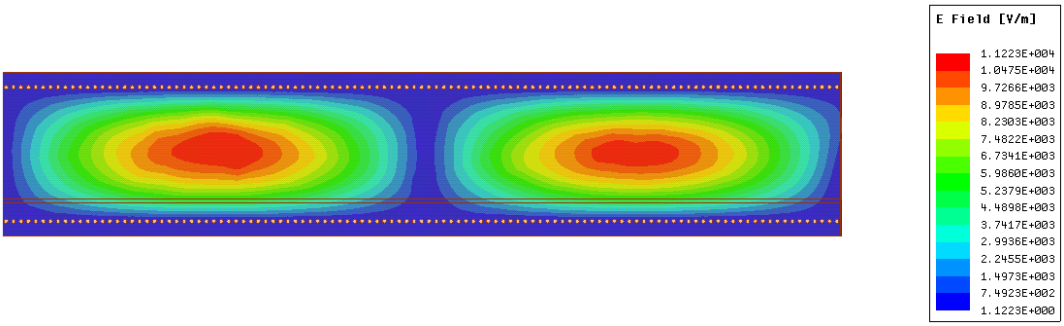

Fig. 4.5 Electric field simulation plot for SSIW01 shorted slot at 6.0 GHz

As mentioned, the SSIW has propagation characteristics similar to the half-mode SIW (HMSIW) but also has the added advantage of easy integration of lumped elements across the slot. The subsequent sections in this chapter will build on this and demonstrate the SSIW use for applications as a wave attenuator and as part of a waveguide filter.

4.2 Waveguide Coupons

Three waveguide coupons were fabricated for analysis and comparison, all for operation between the target frequency range of 3.5 to 5.5 GHz. Each of the coupons had a centre waveguide section of length 135 mm (*WgL*), L_1*=15 mm* with a slot air gap of 0.5 mm. Each coupon had the same microstrip transition in and out of the waveguide, of length 10mm and transition 10mm, optimized to 50Ω (the other dimensions are specified in Fig. 4.6 below), to match to the SMA PCB connector. The PCB material used was Rogers RT5880 (ε_r=2.2, Tan δ=0.0009). The via walls consisted of vias diameter (*D*) 0.5 mm with on a spacing pitch (P_v) of 1mm. This guaranteed low radiation leakage, and as via diameter was relatively small when compared to L_1, a_{eff}~*a*. The variance between the test coupons was for the shunt waveguide length L_2.

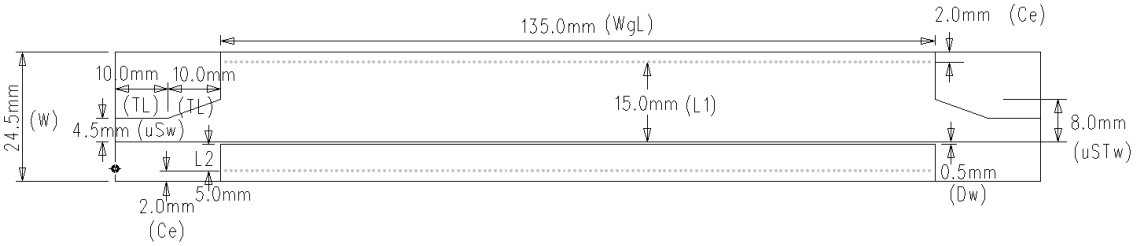

Fig. 4.6 Dimension Details for SSIW02 Coupon

The design criteria and cut-off frequencies are summarised in table 4.1:

SSIW Ref No	**L_1 (mm)**	**L_2 (mm)**	**$TE_{1/2,0}$ f_c (GHz)**	**$a=L_1+w+L_2$**	**$TE_{1,0}$ f_{sct} (GHz)**	**a_{eff} (mm)**	**$TE_{1,0}$ f_{sct} a_{eff} (GHz)**
01	15	2.5	3.37	18.0 mm	5.61	17.74	5.70
02	15	5.0	3.37	20.5 mm	4.93	20.24	4.99
03	15	10.0	3.37	25.5 mm	3.96	25.24	4.00

Table 4.1 SSIW Reference Coupons

Table 4.1 shows that the $TE_{1/2,0}$ cut-off frequency does not change for all coupons, as it is only reliant on L_1. In addition, as the via diameter and pitch used for the via wall is small relative to L_1

and L_2 the $TE_{1,0}$ cut-off frequency for the shorted waveguide, is very similar for the values of a or a_{eff} . As mentioned this is due to relatively small via diameter and pitch used in the via walls, which exceeds the limitation for radiation loss of D / λ_g <0.2. The guided wavelength λ_g [3] for end frequency of 6.0 GHz is ~34 mm (in dielectric) giving a $D / \lambda g$ ~ 0.01. The other criteria for SIW design P_v / λ_{gc} < 0.35 [4] 4.5 GHz is ~45 mm giving P_v / λ_{gc} ~ 0.02. The maximum limits for these design rules would give a via diameter D < 6.8 mm and via pitch P_v < 15.75 mm, however need to maintain P_v / D = 2 [5].

Fig 4.7 Fabricated SSIW Coupons: 01, 02, 03 (top to bottom).

The three test coupons (picture in Fig 4.7) were simulated and measured with the slot unloaded, to assess the waveguide operation and performance. The scattering parameters S_{11} and S_{21} are shown in the following pages, the S_{22} and S_{12} are not shown as the designs are symmetrical, and therefore approximately equal (theoretically identical). In addition the electric field plots within the dielectric are shown, derived from the HFSS simulations to demonstrate the propagation of the wave through the test coupon structures.

For the S_{11} responses shown in Fig. 4.8 and Fig. 4.10 is should be noted that the frequency peaks of simulated and measured results do not align, this is due to the SMA connectors not being included in the simulations. The dielectric within the connectors induces a small phase delay, which will vary depending on the frequency.

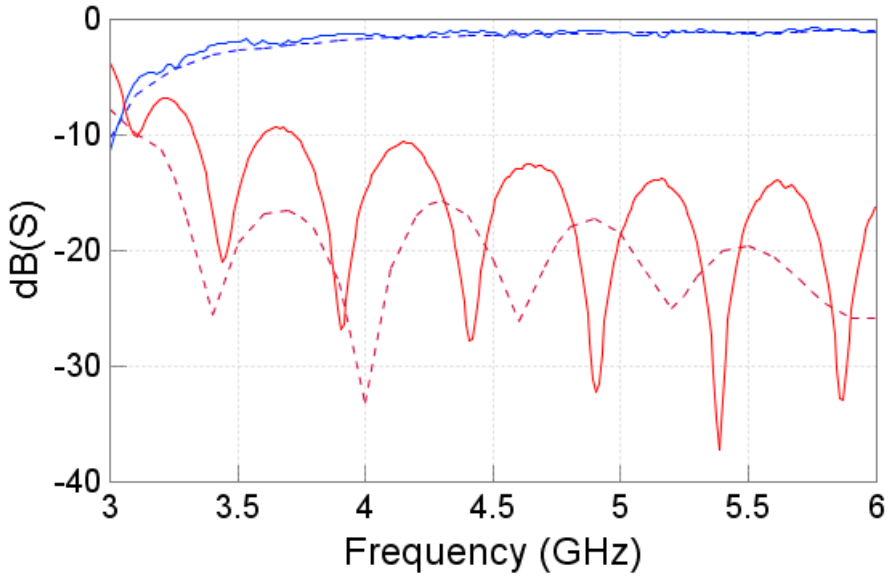

Fig. 4.8 SSIW01 Coupon scattering parameters, slot unloaded (simulated and measured)
(S_{11} red, S_{21} blue, solid measured, dashed simulated)

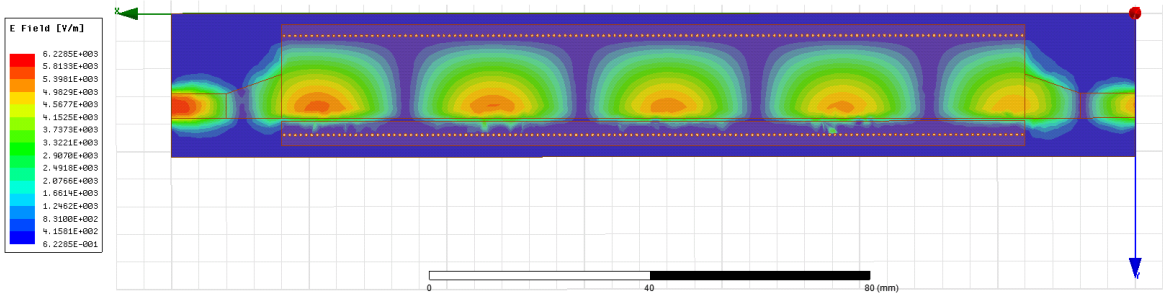

Fig. 4.9 SSIW01 coupon, top view of electric field, slot unloaded at 4.5 GHz

As expected for SSIW01 (Fig. 4.8 and 4.9) and for SSIW02 (Fig. 4.10 and 4.11), with small shunt waveguides (L_2=2.5mm and 5mm respectively) show low conduction loss (<3dB) and low insertion loss (<10dB) across the band of interest (3.5 to 5.5 GHz), indicating that they are useful as a transmission line for this frequency range. The format of representing S_{11} in red, S_{21} in blue, with measured values as solid lines and simulated values as dashed lines will be maintained throughout this thesis. The electric field plots, unless otherwise stated are scalar not logarithmic, which generate a clearer plot for the fields in question.

For SSIW01 and 02, only a small amount of field is within the shunt waveguide, and no field extends beyond the side via walls. As expected the electric field extends beyond the microstrip at either end of the test coupon, but the intensity of the field at both ports is approximately equal, although there is some loss at port 2 due to the conduction, dielectric and radiation losses, as discussed in chapter 2.

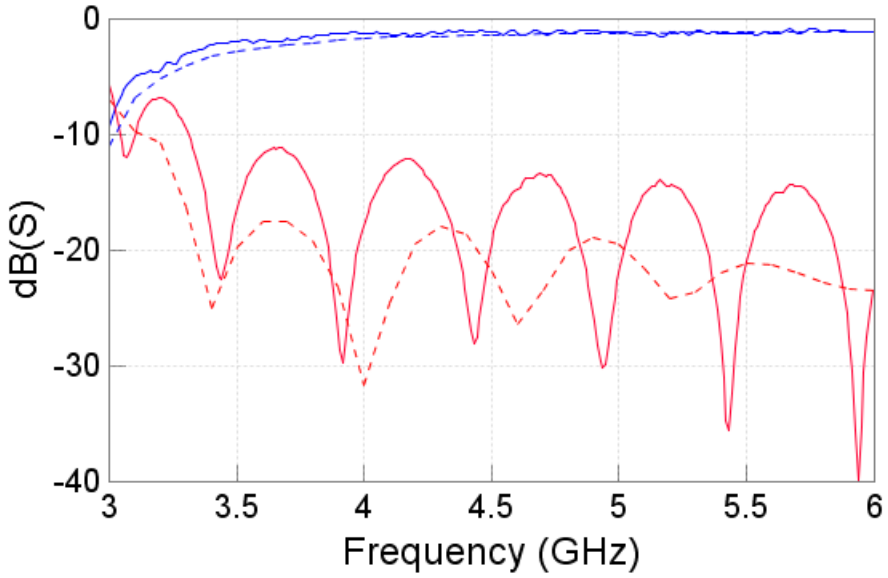

Fig. 4.10 SSIW02 Coupon scattering parameters, slot unloaded (simulated and measured)
(S_{11} red, S_{21} blue, solid measured, dashed simulated)

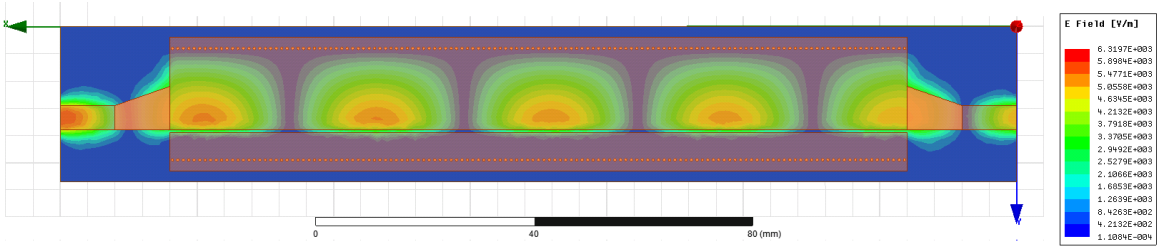

Fig. 4.11 SSIW02 coupon, top view of electric field, slot unloaded at 4.5 GHz

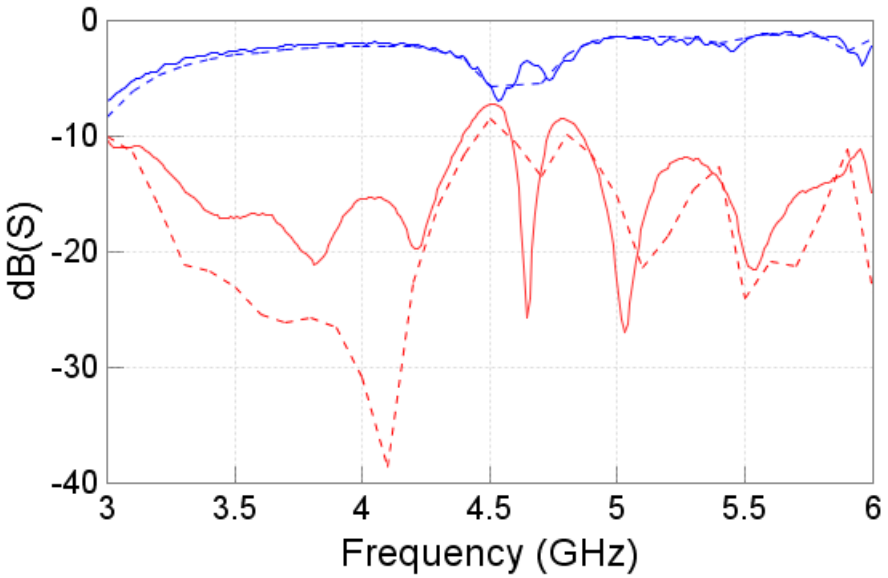

Fig. 4.12. SSIW03 Coupon scattering parameters, slot unloaded (simulated and measured)
(S_{11} red, S_{21} blue, solid measured, dashed simulated)

For SSIW03 with the larger shunt waveguide (L_2=10 mm) the situation is not as straight forward, from Fig 4.12 the S-parameters indicate that more complex wave propagation is occurring. The

$TE_{1/2,0}$ cut-off at 3.4 GHz is visible in the S-parameters for SSIW01, SSIW02 as well as SSIW03, however at 4.5 GHz the S_{11} and S_{21} scattering parameters are almost equal; indicating that the waveguide is failing as a transmission line. Energy is coupling from the main half mode section (the L_1 region) into the shunt waveguide (the L_2 region) resulting in a multi-modal condition occurring. Fig. 4.13 shows three electric field plots for SSIW03 at frequencies of 4.0, 4.5 and 5.0 GHz.

So in summary, the shorter waveguide shunts SSIW01 and SSIW02 are usable over the band of interest, and offer a low loss transmission line to interact with. The SSIW03 has additional propagation modes occurring, which suggests that forming a filter or other microwave devices may not be feasible.

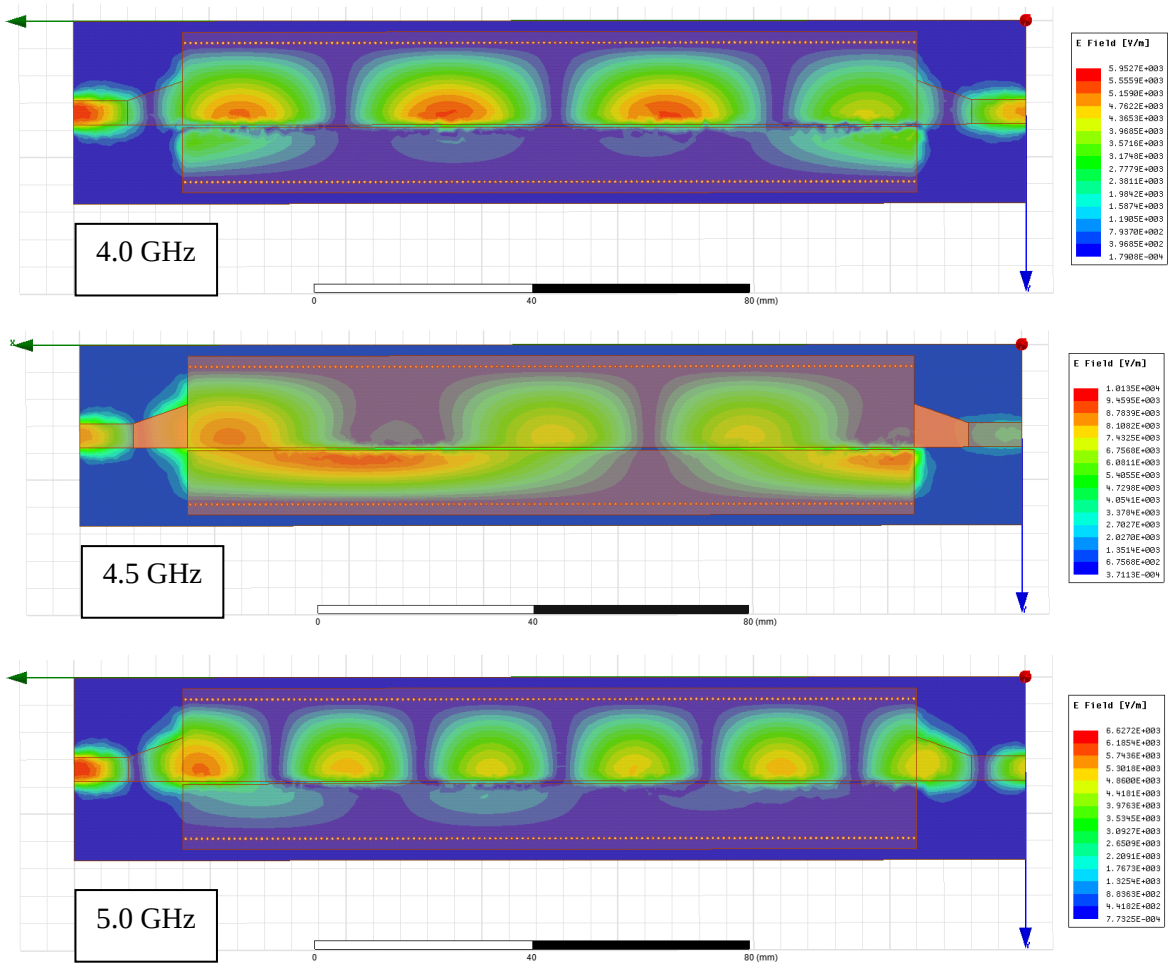

Fig. 4.13 SSIW03 coupon, top view of electric field, slot unloaded at 4.0, 4.5 and 5.0 GHz

4.3 Analysing Loaded SSIW

In section 2.3 different techniques were discussed for analysing integrated waveguides, one of which was the transvers resonance technique, based on the concept of surface impedance calculated from the method of moments. The background to the transvers resonance technique is discussed in section 2.3.3.3, and was developed for SIW by Professor Ke Wu's team originally in 2006 [4]. It is used here to analyse the complex intermediate condition, where the SSIW is loaded not with a perfect short or open, but some pre-determined impedance *Z*. Test coupon SSIW02 was used, with dielectric height b = 1.575 mm, L_1 = 15 mm, L_2 = 5 mm, slot width w = 0.5 mm and relative permittivity ε_r = 2.2.

To produce the impedance *Z*, PIN diodes were used. This enabled the states to be varied between a high impedance state of ~3000Ω when the PIN diodes were reverse biased and a low impedance state ~2Ω forward bias (with 10mA). This is similar to the use of the PIN diode in the previous chapter, where PIN diodes were used to switch slot apertures in a SIW in and out of the required freequency band (Ref section 3.4). If the PIN diodes were not fully forward biased, then the impedance would be dependant on the actual forward current level.

4.3.1 Transverse Resonance Analysis

An SSIW is shown in Fig. 4.14, where the slot is loaded with an impedance *Z*. The impedance *Z* could either be formed by a distributed structure, such as a resistive layer across the slot, or by periodically loaded discrete components, with period much less than a wavelength ($d<<\lambda_g$). Fig. 4.14 also shows the equivalent circuit, in the transverse direction, of one unit cell of the periodically loaded slotted waveguide.

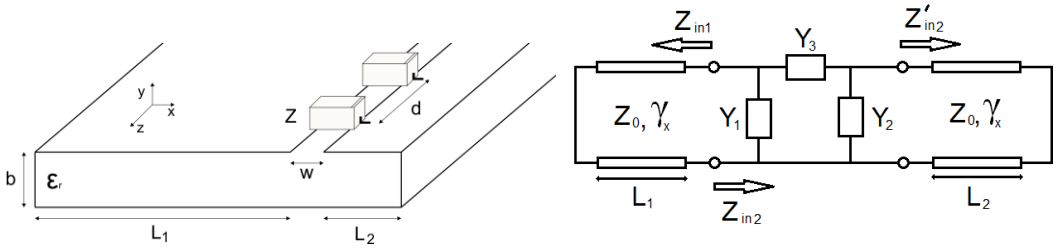

Fig. 4.14 Structure of periodically loaded slotted SIW and transverse resonance equivalent circuit.

The loaded slot was modelled using a pi-network where Y_1 and Y_2 take account of the effective shunt capacitances C_f of the fringing fields at the slot, and Y_3 is the parallel combination of the loading element *Z* and slot capacitance C_s. At resonance the condition $Z_{in1} = -Z_{in2}$ must be met,

where Z_{in1} is the impedance seen looking towards the left from the left hand side of the slot and Z_{in2} is the impedance at the same point looking towards the right. By expressing the pi-network in terms of its ABCD parameters, the transverse resonance condition yields:

$$\frac{AZ'_{in2} + B}{CZ'_{in2} + D} = -Z_0 \tanh \gamma_x L_1 \qquad \text{(Eq. 4.3)}$$

where the impedance seen looking to the right, from the right hand side of the slot, is $Z'_{in2} = Z_0 \tanh \gamma_x L_2$. The unknown transverse propagation constant is $\gamma_x = \alpha_x + jk_x$ where α_x and β_x are the transverse attenuation and phase constants, respectively. *A*, *B*, *C* and *D* are the ABCD parameters of the pi-network and are related to Y_1, Y_2 and Y_3, see [6] for example.
Equation (Eq. 4.3) is transcendental but can be solved for γ_x using common root solving algorithms such as Gauss-Newton or Levenberg-Marquardt. Once γ_x is determined the longitudinal propagation constant can be calculated from $\gamma = \alpha + j\beta = (\gamma_0^2 - \gamma_x^2)^{1/2}$, where α is the longitudinal attenuation constant, β is the phase constant and γ_0 is the propagation constant of the substrate material, $\gamma_0 = j\omega\sqrt{\mu\varepsilon}$. If the loading element has a resistive element then γ_x is complex and equation (Eq. 4.3) becomes a coupled non-linear equation in α_x and β_x. This may be difficult to solve without an initial estimated value for the root solving algorithm. In order to do this, it is useful to first solve a reduced form of equation (Eq. 4.3) by assuming that the shunt capacitances can be neglected, such that $A = D = 1$, $C = 0$ and $B = Y_3^{-1}$. Equation (Eq. 4.3) then reduces to

$$Z_0 \tanh \gamma_x L_1 + Z_0 \tanh \gamma_x L_2 + Z_3 = 0 \qquad \text{(Eq. 4.4)}$$

where $Z_3 = Y_3^{-1}$. This equation is more straightforward to solve than equation (Eq. 4.3) since the poles of the tanh functions are known, allowing the range of values between which the solution γ_x lies to be easily determined. It is usual, that either the real or imaginary part of *Z* is more significant and consequently γ_x will be approximately real or imaginary. In this case a simple bisection technique can be used to calculate the roots of (Eq. 4.4). This value can then be used as an initial estimate for equation (Eq. 4.3).

The stubs in the equivalent transverse circuit are effectively parallel plate waveguides of height *b* and cell width, *d*. The characteristic impedance is therefore $Z_0 = (b/d)(\mu/\varepsilon)^{1/2}$.

4.3.2 Analysis Results

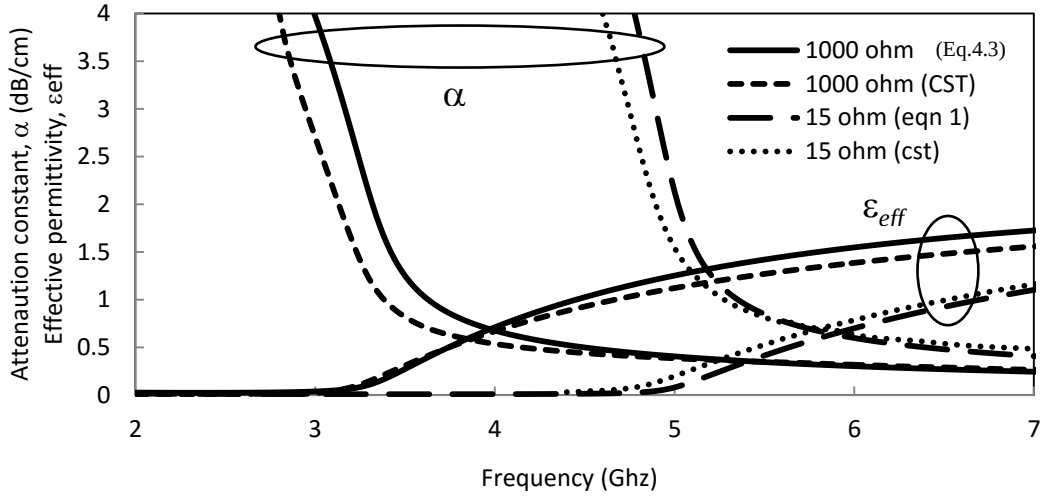

Fig. 4.15. Comparison between full-wave (CST) and transverse resonance values.

Fig. 4.15 shows comparisons between the transverse resonance technique and full wave solutions using CST Microwave Studio. Both the effective permittivity, $\varepsilon_{eff} = (\beta/k_0)^2$, and attenuation constant, in dB cm^{-1}, of the fundamental mode are compared for a resistively loaded SSIW, where $k_0 = \mathrm{Re}\{\gamma_0\}$. Solutions are shown for resistive loading elements of 1000 Ω and 15 Ω separated by 5 mm. For accuracy, the values of C_f and C_s are obtained from full-wave simulation yielding values of C_f = 0.014 pF and C_s = 0.109 pF for a 5 mm length. This compares well with the approximate expression in [7] of C_s = 0.113 pF, at 3 GHz. The reference [7] does not provide approximate expressions for C_f but numerical results demonstrate that for narrow slots C_f is at least an order of magnitude smaller than C_s. As can be seen from Fig. 4.15 there is good agreement between the full-wave solutions and values computed from equation Eq.4.3. When the resistance is large, the waveguide operates like a $TE_{1/2,0}$ type mode of a half mode waveguide of width L_1, with a small loss due to the resistance. When the resistance is small the loading element acts like a short circuit and the mode is of a TE_{10} type mode of a (L_1 + w + L_2) wide un-slotted waveguide.

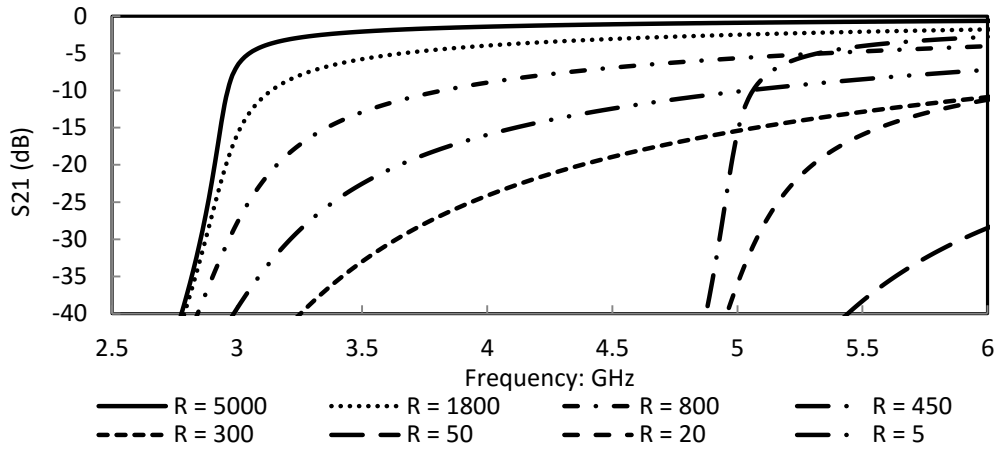

Fig. 4.16. The fundamental mode of a slotted waveguide loaded with
a resistance of varying values using the transverse resonance technqiue.

4.4 Travelling wave Attenuator

A variable attenuator operating over the 3-5 GHz range was designed using the transverse resonance method previously discussed. The cut-off frequency of the waveguide is predominantly set by the L_1 dimension and, for L_1 = 15 mm, gives a cut-off frequency of 3.0 GHz using equation (Eq.4.3). Which differs from the $f_{c1/2,0}$ value of 3.4 GHz calculated from equation Eq.4.1 which as mentioned is only approximate (fringing fields not included).

The test coupons have a waveguide section length W_{gL} = 135 mm, adequate section length for attenuation. Fig. 4.16 shows the forward voltage wave transmission coefficient, $S_{21} = \exp(-\gamma W_{gL})$, that this length of waveguide produces, for varying values of loading resistance using equation (Eq.4.3) with all other dimensions the same as previous section. The loading impedances are spaced at 5 mm intervals and range in value from 5000 to 5 Ω. It is seen that by varying the loading resistance over the 5000-300 Ω range the propagation remains as a $TE_{1/2,0}$ type mode with variable attenuation.

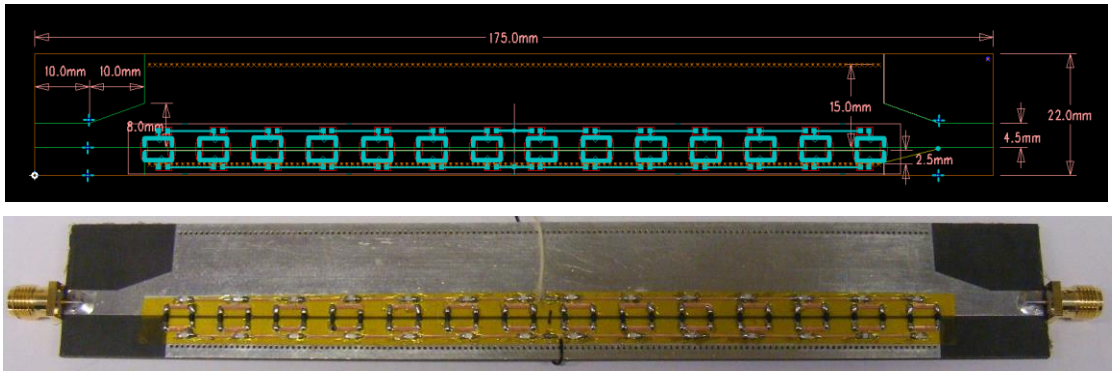

Fig. 4.17. Structure of travelling wave attenuator CAD Data and SSIW02 with Mylar overlay.

The design was verified, using the test coupon SSIW01 (shown in Fig. 4.17 and Fig.4.18), and a 12 μm thick Mylar overlay with 25 μm thick adhesive placed over the waveguide to allow an array of twenty-eight Infineon BAR64-02 silicon PIN diodes to be capacitively coupled to the waveguide slot in a similar manner to [8], which was a development from previous work [9] within the research group. The diodes provided a controllable resistance ranging from a few 1000 ohms for a reverse bias voltage down to a few ohms for 10 mA forward current. Each diode was separated by 5 mm with the bias applied across two thin tracks on the overlay. Surface mount inductors were soldered directly to the top and bottom copper feed tracks to limit coupling of the RF signal to the bias network. The diodes are connected to thick tracks that provide an approximate 2.5 pF capacitance between the PIN diodes and each side of the slot.

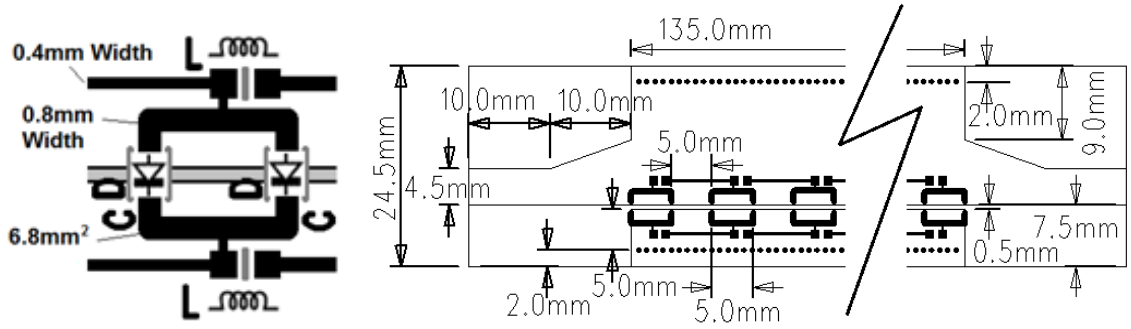

Fig. 4.18. Schematic of travelling wave attenuator (SSIW02 with Mylar overlay)

Fig. 4.19 shows measured results for the S-parameters of the structure obtained using a VNA. A coax SOLT calibration was performed and as such the SMA connectors are not de-embedded from the measurements. Measurements were performed for a range of forward bias currents by adjusting the DC supply voltage on a PSU; a reverse bias condition of 30V (no DC current) was also considered. The forward current shown in the Fig. 4.19 are the individual diode forward bias currents of 1.8, 7.1, 14.3 and 21.4 μA, these values were obtained by applying 50, 200, 400 and 600 μA, respectively, to the bias structure - the current being divided equally amongst the 28 diodes. To obtain the corresponding resistance values for these bias conditions, the PIN diode resistance was measured by performing a coaxial SOLT calibration and connecting a diode directly to an SMA connector. After de-embedding the connector it was found that the resistance of an individual PIN diode, over the 2-5GHz range, was approximately 300 Ω for a 21.4 μA forward current, 450 Ω for a 14.3 μA, 800 Ω for 7.1 μA, 1800 Ω for 1.8 μA bias and greater than 3000 Ω when a 30 V reverse bias voltage was applied. These values are shown in brackets on Fig. 4.19.

It is seen from Fig. 4.19 that the structure provides a variable attenuation from 2 dB to 25 dB over the waveguide band, the results follow the general trend of Fig.4.16; however it does not accurately predict the values of attenuation - the cut-off frequency shifting to 2.7 GHz and the attenuation

displaying a more constant response with frequency in Fig. 4.19 which also shows an increase in attenuation above 4.5 GHz. It is believed that both the change in cut-off frequency and the other differences in attenuation are due to the parasitic components of the diode and biasing network which load the slot in a complicated manner.

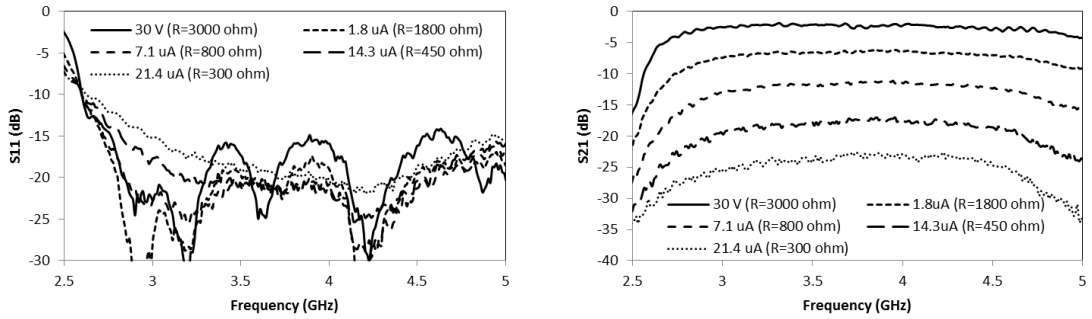

Fig. 4.19. Measured S-parameters of the variable attenuator structure given in Fig. 4.18 for various values of forward current and reverse bias voltage.

4.4.1 Travelling Wave Attenuator Summary

A TWA was designed and demonstrated constant attenuation over a relatively wide bandwidth, utilising one of the developed SSIW test coupons and by using a modelled impedance peridocially applied to the SSIW using a bespoke capacitvely copuled overlay. A summary of this work was published as an IEEE Microwave and Wireless letter in 2014 [10].

4.5 Waveguide Filters

In this section SSIW filters are investigated, the design, fabrication and measurement of bandpass filters for the SSIW coupons using a capacitively coupled thin laminate overlay. Different overlay configurations are analysed based on the concept of using a *virtual via* as a shunt conductance between the two parts of the SSIW. As previously mentioned the virtual via is a fixed dimension of copper that crosses the waveguide gap width *w*. The filters have a centre frequency of 4.5 GHz, and will be designed as a 3rd order Chebyshev.

The filters are based on shunt inductive reactances which create half wave resonators between them; they are modelled using a parallel network. A background to how the required shunt conductances and cavity lengths are calculated is overviewed; these are ‘point’ impedances as represented in a circuit schematic. A means of calculating how long the virtual via will have to be, to meet these conductances is hence required, and this is also introduced along with the adjustment

formulae required to account for the physical dimension of the shunt conductance in the waveguide.

To determine the length of virtual via required for the specific conductance required, the virtual via configuration needs to be characterised. The analysis will begin with the simplest virtual via design, a symmetrical pad (or strip) directly over the waveguide gap, but will develop into more involved designs. The characterisation of the virtual vias required separate simulations sweeps with the S-parameters de-embedded to the model centre. The exported S-parameter data is collated and analysed, with the output being a relationship between the virtual via length and the resultant shunt conductance and the associated phase offset for that virtual via length.

When the filter characteristics are known, a full EM wave simulation of the complete SSIW coupon and filter overlay was run to verify the filter performance. Due to the physical size and complexity of the structure, perfect electric boundaries instead of the via walls are utilised to simplify the simulation model. The overlay design is then re-created in CAD software, fabricated and assembled onto the test coupon using double sided adhesive. Two thicknesses of adhesive are considered 25 and 90 μm, both of which are included in the full EM simulation. A reference filter design without the overlay, where the waveguide gap is filled directly on the copper layer is simulated for direct comparison.

4.5.1 Waveguide Filter Theory

There a number of different methods for designing waveguide bandpass filters [11] based on set lengths of waveguide loaded with shunt discontinuities, the gaps between discontinuities create half wave resonators. An example in rectangular waveguide would be introducing a pattern of posts across the waveguide wall, the number of posts and positioning depending on the characteristics of the filter required. In section 2.3.2.1 two port network representations were mentioned, one of those was the ABCD transfer matrix [T], which relates the input voltage and current vector to the output voltage and current vector (shown here in Fig. 4.20).

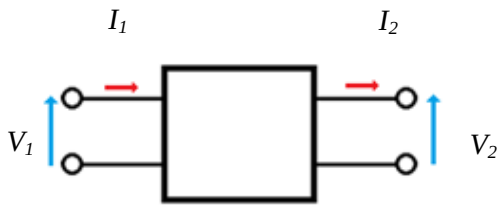

Fig.4.20 Two port network schematic

The network may be described using the matrix equation:

$$\begin{bmatrix} V_1 \\ I_1 \end{bmatrix} = \begin{bmatrix} A & B \\ C & D \end{bmatrix} \begin{bmatrix} V_2 \\ I_2 \end{bmatrix}, where\ [T] = \begin{bmatrix} A & B \\ C & D \end{bmatrix} \quad \text{(Eq.4.5)}$$

One of the main uses of the transfer matrix is for analysis of cascaded networks, e.g. $[T_{TOT}]=[T_1][T_2][T_3]$

For a lossless rectangular waveguide, with a distance (or delay) between discontinuities of θ, and normalising the elements in the filter with respect to terminating impedances equivalent to an infinite waveguide, the transfer matrix for a length of guide will be:

$$[T] = \begin{bmatrix} cos\theta & jsin\theta \\ jsin\theta & cos\theta \end{bmatrix}, where\ \theta = \beta L = \frac{2\pi L}{\lambda_g}\ or\ \theta = \frac{\pi \lambda_{g0}}{\lambda_g} \quad \text{(Eq.4.6)}$$

and when resonances are chosen to be half wave, then $L = \lambda_{go}/2$.

For the loading of the waveguide, a single sided Mylar laminate with a thin dielectric was chosen. However, microwave filter design and fabrication is complex and it is difficult to obtain the exact results required. For frequencies below ~3 GHz, when using lumped components to accommodate variances in material properties and component values, a component value may be selected 'on test' as part of the assembly process. For higher frequencies, lumped components are not used due to the physical dimensions of the devices becoming comparative to the wavelengths in use. For construction of the overlay microwave filters, it will not be possible to adjust the overlay itself once fabricated, but it is relatively simple to modify the design and fabricate and fit a new overlay. This enables re-use of the waveguide test coupon, and a relatively low cost and quick fabrication method for filter trial.

Standard filter characterization includes start and stop frequencies, plus some level of acceptance of amount of ripple allowed. The higher the order of the filter, the larger the number of discontinuities, but the more defined the filter performance (cut-off) will be, in addition the lower the order of filter the lower the associated losses. Due to practical limitations of the available waveguide length and the frequency under consideration (and hence the wavelength involved) the filter design considered will be limited to a 3rd order filter, thus giving four discontinuities with three resonant cavities.

The filter characteristics are the order number, the start and stop frequencies and the ripple allowance; these produce the filter design parameters which are the values of the shunt conductances and the spacing between them. This is derived from the theory of a direct-coupled resonator filter [12], and considering a Chebychev filter response. This equates to a ladder network with series inductances and parallel capacitances represented by conductances.

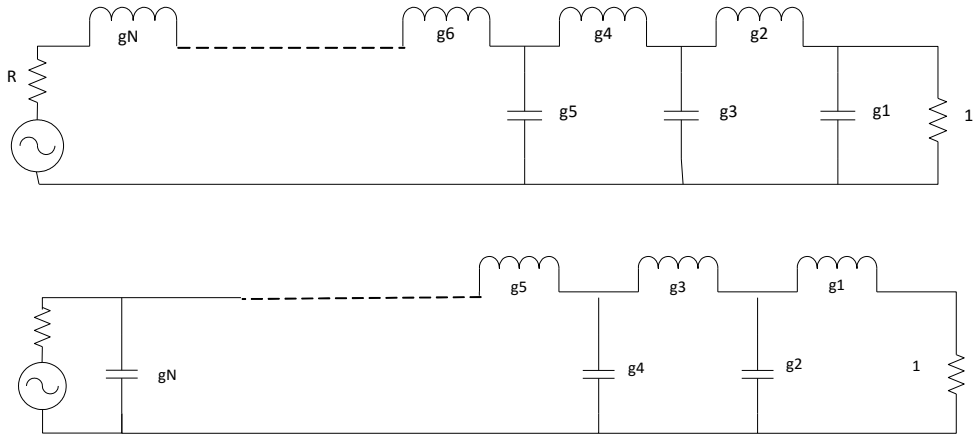

Fig. 4.21 Ladder Networks for low-pass filter [13] (Top N odd, bottom N even)

Starting with a Chebyshev low-pass-filter (Fig.4.21) with Z_L=1 Ω ,

$$for\ N\ odd, g_{N+1} = 1, and\ N\ even\ g_{N+1} = 2k^2 + 1 - 2k\sqrt{1+k^2} \qquad \text{(Eq.4.7)}$$

When g_N is a capacitor then g_{N+1}=R, and when g_N is an inductor then g_{N+1}=1/R

The other elements in the ladder network are given by:

$$g_k = \frac{4a_{k-1}a_k}{b_{k-1}b_k}\ , where\ a_k = sin\left(\frac{2k-1}{2N}\pi\right), and\ b_k = sinh^2\left(\frac{\beta_k}{2N}\right) + sin^2\left(\frac{k\pi}{N}\right)$$

$$and, \beta_k = ln\left(\frac{\sqrt{1+k^2}+1}{\sqrt{1+k^2}-1}\right)\ where\ g_1 = \frac{2a_1}{sinh\left(\frac{\beta}{2N}\right)}$$

Parameter *N* is the number of reactive elements in the network, and *k* is the order of the elements from 1 to N.

There is a need to characterise the waveguide section, to obtain the propagation values for the frequencies considered and the β values for the waveguide (with overlay) for the centre frequency plus the start and stop values for the filter frequency points. With these parameters, and the above equations, it is then possible to calculate the required shunt conductance values. This was performed using Matlab code which would return an array for G [g_1 g_2 g_3 g_4] for the required 3rd order filter. Also, due to symmetry, g_1=g_4 and g_2=g_3.

The filter may be represented by a parallel shunt network (as in Fig. 4.22), with the design equations from Cohn [12], defined as follows:

$$B_1 = \frac{1-\omega/g_1}{\sqrt{\omega/g_1}}, B_2 = \frac{1}{\omega}\left(1 - \frac{\omega^2}{g_1 g_2}\right)\sqrt{g_1 g_2} \quad , \qquad where\ \omega = \frac{\pi}{2}\frac{\beta_2 - \beta_1}{\beta_0}$$

and β_0 is the value at the centre frequency of the filter, β_1 value at the frequency start of the filter, β_2 value at the frequency end of the filter.

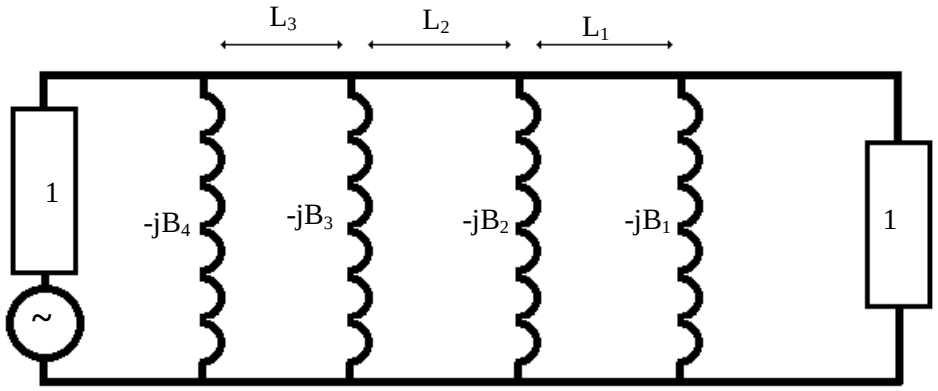

Fig. 4.22 Schematic representation of 3rd order parallel shunt network

The general k^{th} term and the N^{th} term are defined here for completeness:

$$B_k = \frac{1}{\omega}\left(1 - \frac{\omega^2}{g_k g_{k-1}}\right)\sqrt{g_k g_{k-1}}$$

$$B_N = \frac{1 - \omega R/g_{N-1}}{\sqrt{\omega R/g_{N-1}}}$$

From [12] the shunt inductive reactances with short sections of waveguide either side are modelled as quarter wave impedance inverters (in Fig.4.23). The k^{th} unit cell shunt reactance is termed $-B_k$ with a waveguide length either side of θ_{lk}

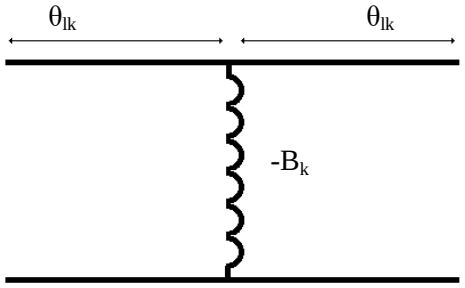

Fig. 4.23 Shunt conductance equivalent circuit for waveguide cavity

$$Where\ \theta_{lk} = -\frac{1}{2}arctan\left(\frac{2}{B_k}\right),\ and\ B_k = \frac{1-K^2}{K} \qquad \text{(Eq.4.8)}$$

And K is the characteristic impedance of the quarter wave impedance inverter.

These expressions are accurate for ~20% bandwidth when frequency is near the reference frequency (so $\omega=\omega_0$ and $\theta_k=\pi$). The reactance X is then given by:

$$X = sin\theta_k = -\frac{\pi}{2}\left(\frac{\beta_k}{\beta_0} - \frac{\beta_0}{\beta_k}\right), and\ l_k = \frac{\lambda_{g0}}{2} + \frac{\lambda_{g0}}{2\pi}(\theta_{lk} + \theta_{lk+1}) \qquad \text{(Eq.4.9)}$$

The negative lengths of the impedance inverters are hence included in the cavity lengths. Finally the length of the k[th] cavity is: $l_k = \frac{\lambda_{g0}}{2} - \frac{\lambda_{g0}}{4\pi}\left(arctan\left[\frac{2}{B_{k+1}}\right] + arctan\left[\frac{2}{B_k}\right]\right)$ (Eq.4.10)
But still need to deduct negative lengths from equation Eq.4.8.

By parameterising a single shunt design and analysing the S-parameters, it is possible to derive a relationship equating the shunt conductance with the virtual via length. The virtual via is defined by its width (*VW*) across the waveguide slot, and its length (*VL*) along the waveguide slot (see Fig. 4.24). It is then possible to calculate the value of virtual via length which will give the required shunt impedance. A Chebyshev filter response in the pass band is symmetrical around the centre point, so for the third order filter with three resonant cavities, $B_1=B_4$ and $B_2=B_3$, and $L_1=L_3$

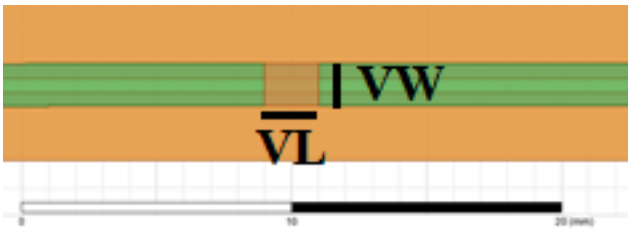

Fig. 4.24 Representation of overlay virtual via

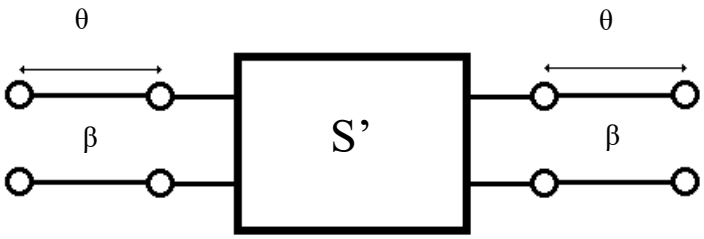

Fig. 4.25 Two port network representation of virtual via characterisation

If we consider the virtual via shunt as a two port network, with the beta values of the waveguide and the associated lengths (*L*) equating to the phase delay, may be represented by the scattering matrix S' (Fig.4.25).

$$where\ S' = Se^{2j\beta L} = \begin{bmatrix} S_{11} & S_{12} \\ S_{21} & S_{22} \end{bmatrix} e^{2j\beta L} \qquad \text{(Eq.4.11)}$$

Assuming the admittance matrix is a shunt inductor, with phase offset of theta either side, then normalising the impedance gives:

$$S' = \begin{bmatrix} S_{11} & S_{12} \\ S_{21} & S_{22} \end{bmatrix} = \begin{bmatrix} \frac{-Y}{2+Y} & \frac{2}{2+Y} \\ \frac{2}{2+Y} & \frac{-Y}{2+Y} \end{bmatrix} e^{-j2\theta} \qquad \text{(Eq.4.12)}$$

with Y=-jB, then it is possible to derive the shunt conductance from the s-parameter amplitudes:

$$S_{11} = \frac{jB}{2-jB} e^{-2j\theta}, and\ S_{21} = \frac{2}{2-jB} e^{-2j\theta} \qquad \text{(Eq.4.13)}$$

then

$$|S_{11}| = \frac{B}{\sqrt{4+B^2}}\ , and\ |S_{21}| = \frac{2}{\sqrt{4+B^2}}$$

Which leads to: $$B = 2\frac{|S_{11}|}{|S_{21}|} \qquad \text{(Eq.4.14)}$$

Where the magnitude of the S-parameters are found from the square root of the sum of the squared real and imaginary parts from the electromagnetic full wave simulation (Ansoft HFSS). With the value of B now known it is possible to calculate the phase offset theta. Where the phase of the scattering parameters may be calculated from arctan (im S_{n1} / re S_{n1}), where n= 1 or 2.

$$\frac{jB}{2-jB} = \frac{Be^{j\pi/2}}{\sqrt{4+B^2} \times e^{-j\varphi}}\ , where\ \varphi = arctan\left(\frac{B}{2}\right)$$

Hence for the S_{11} phase,

$$\angle S_{11} = \frac{\pi}{2} + \varphi - 2\theta, leading\ to\ \theta_{11} = \frac{\pi}{4} + \frac{1}{2} arctan\left(\frac{B}{2}\right) - \frac{1}{2}\angle S_{11} \qquad \text{(Eq.4.15)}$$

Similarly;

$$\angle S_{21} = \frac{\pi}{2} + \varphi - 2\theta, leading\ to\ \ \theta_{21} = \frac{\pi}{4} + \frac{1}{2} arctan\left(\frac{B}{2}\right) - \frac{1}{2}\angle S_{21} \qquad \text{(Eq.4.16)}$$

Care needs to be taken using these formulae, as the phase for the S_{11} and S_{21} is not reliable if the associated magnitude is small. However, if the phase offset θ for S_{11} and S_{21} are approximately equal, then a further accuracy may be obtained from averaging them, hence:

$$\theta = \frac{\theta_{11}+\theta_{21}}{2} \qquad \text{(Eq.4.17)}$$

Note: formulae calculations are in radians, HFSS results are in degrees, therefore a conversion was required for analysis.

Also we need to determine that the virtual via characterisation shunt conductance is actually inductive and not capacitive at the frequency of interest. To verify this, we consider the virtual via

as a ‘T-network’ model [6], and concentrate on Z_{21} (as structure is symmetrical equals Z_{12}), then the virtual via may be expressed as Fig. 4.26.

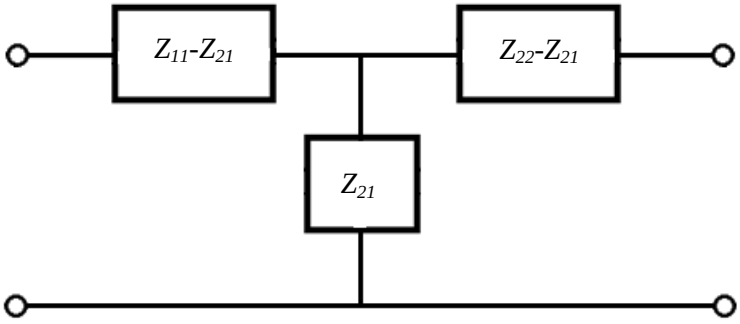

Fig. 4.26. T-equivalent of virtual via

The impedances Z_{11} and Z_{22} will be approximately equal and should cancel, leaving the required impedance Z_{21}. Which if the imaginary part of Z_{21} is positive will mean that the shunt conductance is indeed inductive as required. Calculations of $Im(Z_{21})$ are possible directly from the S-parameters, but are complex, however it may be exported directly from HFSS simulations.

4.5.2 SSIW01 Filter Direct on Copper Layer

For comparison, using only simulation, a filter for SSIW01 without an overlay laminate is designed and simulated. This equates to forming the discontinuities directly in the top copper layer of the test coupon (see Fig 4.27). This fixes the virtual via width to the gap of the slot, so *VW*=0.5mm, *VL* may then be varied to obtain the required characterisation.

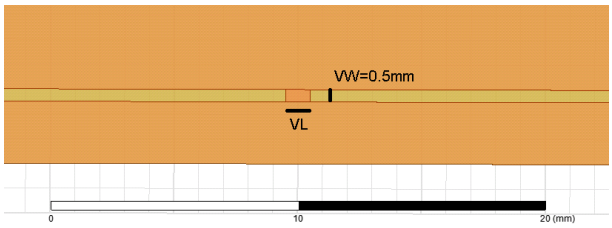

Fig. 4.27 Virtual Via direct in copper layer on test coupon

The parameter *VL* was varied from 0.5 mm to 6.0 mm in steps of 0.5 mm, and between 0.1 and 0.5 mm in steps of 0.1 mm. At the small lengths the change is more of a significant factor, thus smaller steps improved accuracy. The characterisation graphs are shown in Fig. 4.28, varying *VL* produced a range of shunt conductance from 1.5 to 4.5S (Siemens), and an associated phase offset between 7.5° and 1.5°. The equations are generated from 4th order polynomial trend lines, but it is clear that both relationships for conductance and phase are approximately linear. This is ideal, meaning that there is a strong direct correlation to the virtual via length and its shunt conductance.

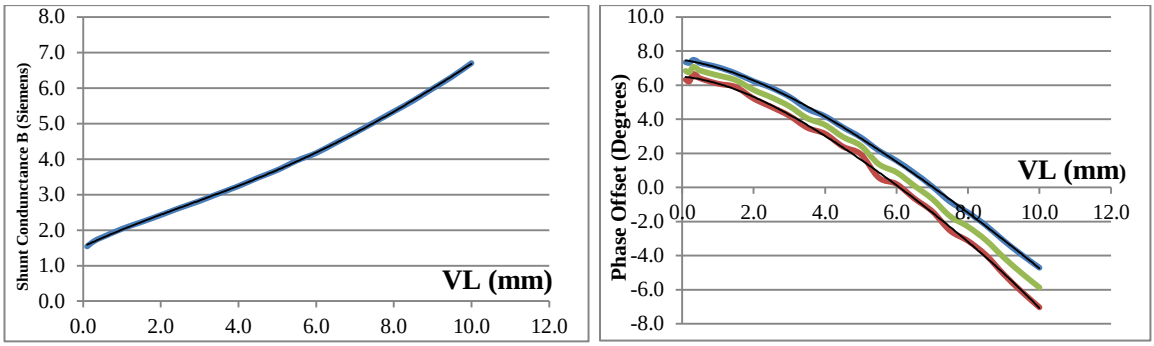

Fig. 4.28 Characterisation graphs for Virtual Via formed Directly in Top Copper Surface of Laminate (phase offset blue S_{21}, red S_{11}, green theta average)

From Fig. 4.29 shows a plot for Im(Z_{21}) against the virtual via length parameter *VL*, this indicates that for all values Im(Z_{21}) is positive and therefore inductive. The trend is declining as *VL* increases and the phase offset changes from positive to negative. This would limit the range of *VL* using this configuration to less than 6 mm.

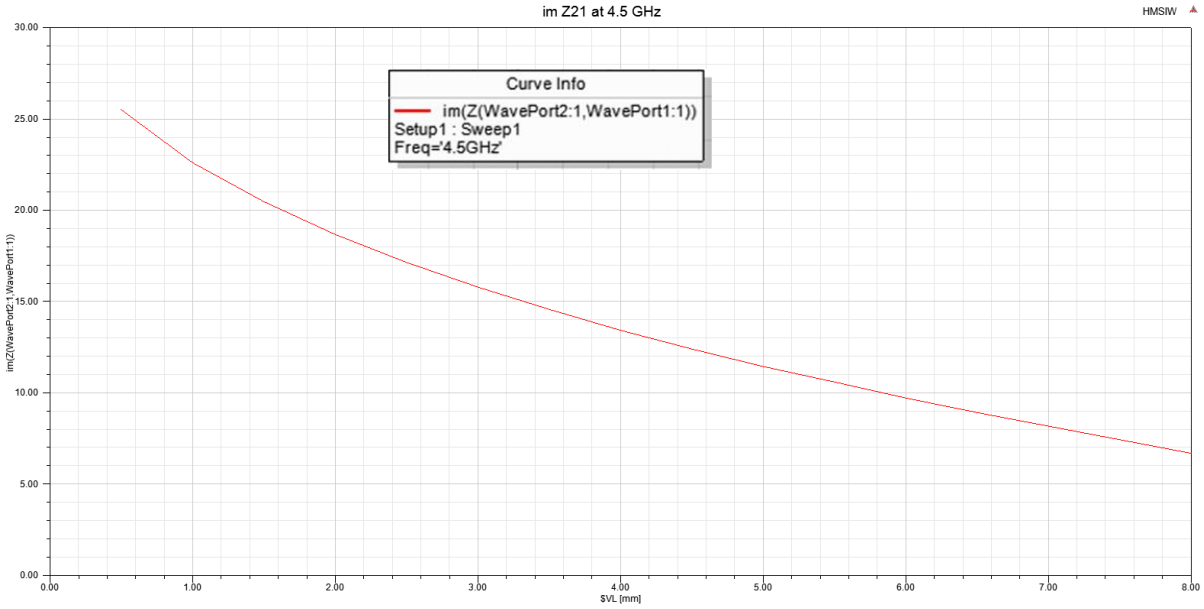

Fig. 4.29 Plot of im(Z_{21}) against virtual via length *VL* (extended range)

With the virtual via characterised, the filter parameters may be calculated. Table 4.2 shows four sets of parameters for filters with 0.2 and 0.4 GHz bandwidth and a passband ripple of 0.1 and 0.5dB. The 0.4 GHz bandwidth means that with a centre frequency f_0=4.5 GHz, the filter start frequency is f_1=4.3 GHz and stop frequency f_2=4.7 GHz. From the characterisation simulation the β values for these frequencies also need to be exported to be included in the analysis.

BW (GHz)	Ripple (dB)	B1 (s)	B2 (s)	B3 (s)	B4 (s)	L1 (mm)	L2 (mm)	L3 (mm)
0.2	0.1	2.274	7.278	7.278	2.274	29.4	31.9	29.4
0.2	0.5	2.995	8.904	8.904	2.995	30.4	32.4	30.4
0.4	0.1	1.333	3.411	3.411	1.333	26.6	29.1	26.6
0.4	0.5	1.894	4.255	4.255	1.894	28.8	30.1	28.8

Table 4.2. 3rd Order Filter Parameters for direct copper variant

Due to the high values of B for the 0.2 GHz bandwidth filter, no value of *VL* was able to match this requirement, and there is no value of *VL* which will form a value of *B*<1.5S. Meaning that only the 3rd order filter with 0.5dB ripple, 400 MHz bandwidth, centred at 4.5 GHz is realisable. From the Matlab code, the following results were obtained:

- Calculated B Values: B_1=1.8941 S, B_2=4.2548 S, B_3=4.2548 S, B_4=1.8941 S
- Calculated Cavity Lengths: L_1=28.8 mm, L_2=30.1 mm, L_3=28.8 mm
- Derived virtual via widths: 0.6945 mm, 6.0979 mm, 6.0979 mm, 0.6945 mm
- Adjusted cavity lengths: 26.37 mm, 29.58 mm, 26.37 mm

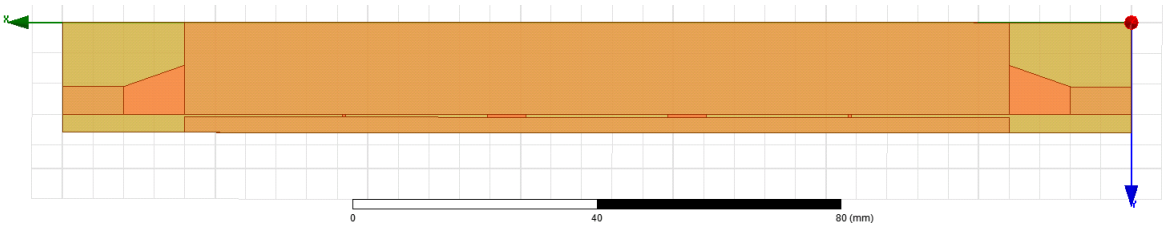

Fig. 4.30. Top Copper Surface Simulated SSIW with Virtual Vias

The full wave EM simulation for the direct copper virtual via was then run in Ansoft HFSS. The top view of the structure is shown in Fig. 4.30 and the simulated S-parameters are shown in Fig. 4.31. The S-parameter response it worth noting for several reasons, the first is that there is a passband filter response occurring in the SSIW01 simulation (compare this to the unloaded plot in Fig.4.8). However, it is not symmetrical, and it is not centred on 4.5 GHz. The tail off above the filter, is a limit of the order of the filter, a higher order filter would have produced a steeper curve. So there is indication that there is a small error in the modelling analysis process, and a limitation as to what may actually be achieved.

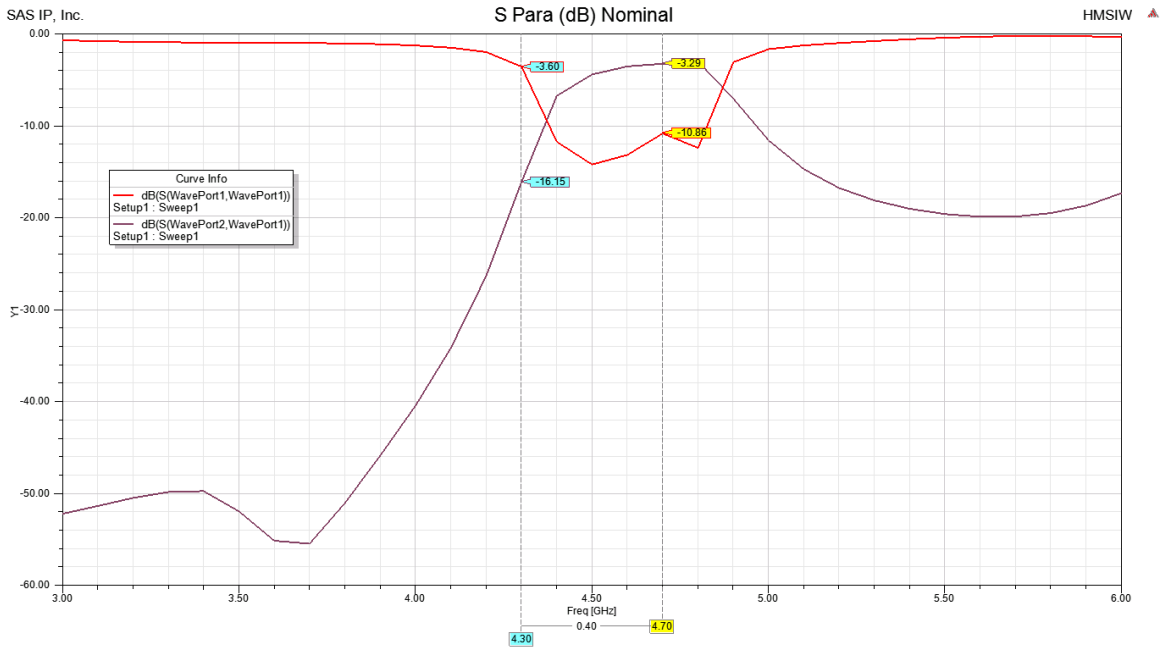

Fig. 4.31. S-parameters for direct copper formed pass-band filter – **calculated values**

Consideration was given to the through loss (S_{21}) at the lower cut-off of the filter (4.3 GHz), and that there could be increased losses due to potential radiation from the microstrip, the transition or from radiation across the waveguide slot. To check this, a simulation was run with 'lossless' materials, the Tan δ for the dielectric was set to zero and the copper was changed to being a perfect conductor. The results for the lossless model S-parameters are shown in Fig. 4.32, it is very similar to the original simulation. Radiation plots did not show any excessive radiation loss over the filter frequencies.

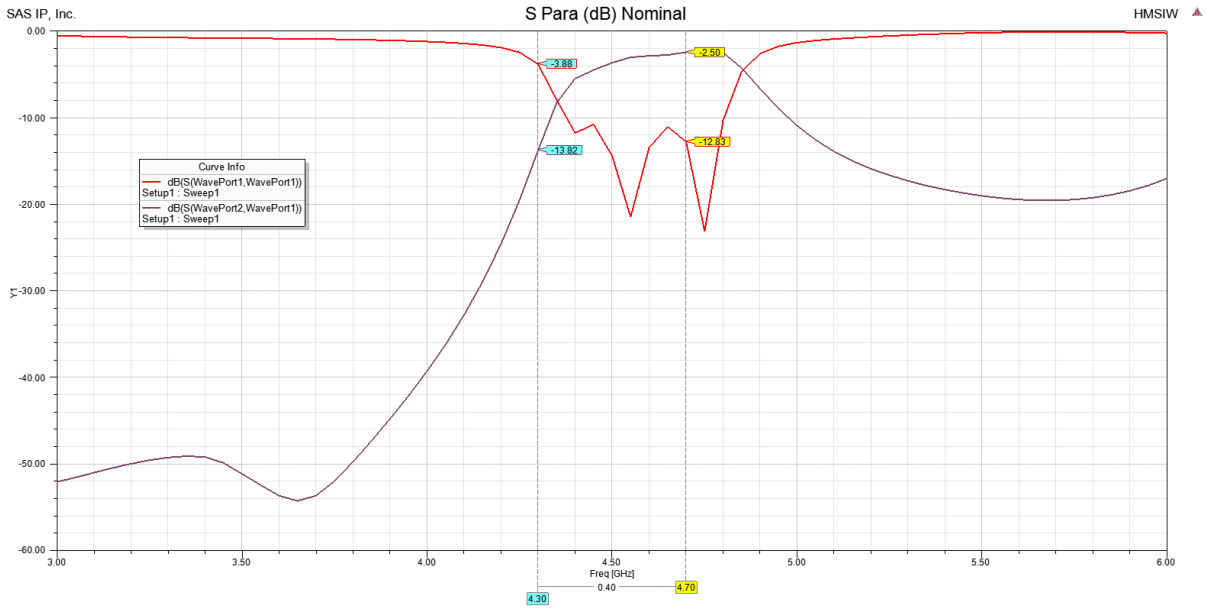

Fig. 4.32. S-parameters for direct copper formed pass-band filter – **lossless**

One further design iteration undertaken was the use of the HFSS optimization algorithms. Using the Quasi Newton optimizer, with key targets to achieve performance of S-parameters at the three key frequencies of the filter (lower cut-off, centre and upper cut-off), additional lower priorities were set outside the filter range to improve the filter response. The optimization process required significant processing time, but resulted in the S-parameters shown in Fig. 4.33. These have managed to remove the frequency offset and centre the filter back to 4.5 GHz. However the result is still asymmetric. The optimized values are shown below, with the original offset:

- Original derived virtual via widths: 0.6945 mm, 6.0979 mm, 6.0979 mm, 0.6945 mm
- Original adjusted cavity lengths: 26.37 mm, 29.58 mm, 26.37 mm
- Optimised virtual via widths: 0.810 mm, 7.379 mm, 7.379 mm, 0.810 mm
- Optimised cavity lengths: 26.974 mm, 30.808 mm, 26.974 mm

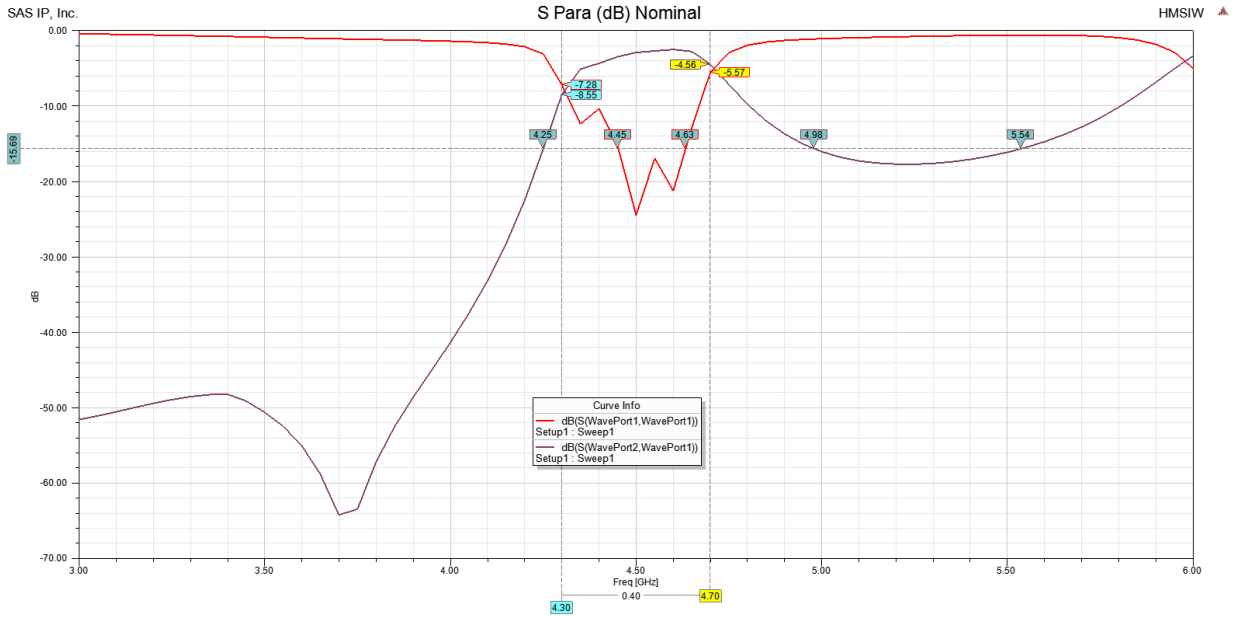

Fig. 4.33 S-parameters for direct copper formed pass-band filter – **optimized**

4.6 Virtual Via Configuration SSIW01

As mentioned, the PCB test coupons are fabricated from Rogers RT duroid 5880 18 µm copper base copper over plated predominantly with tin an additional ~17 µm, dielectric thickness 1.575 mm, $\varepsilon_r = 2.2$, Tan $\delta = 0.0009$. The overlay is a single sided (flexi) Mylar laminate with 18µm copper, 12 µm polyester dielectric, $\varepsilon_r = 3.2$, Tan $\delta = 0.003$ (manufacturer reference DuPont Pyralux AC 181200RT). Two types of adhesive were investigated with thicknesses of 90µm and 25um. The 90 µm adhesive, consisted of polyimide dielectric, $\varepsilon_r = 3.5$, Tan $\delta = 0.008$ and acrylic adhesive (manufacturer reference Pro-Power PPC226). The 25 µm adhesive was a polyester film with acrylic adhesive: dielectric $\varepsilon_r = 3.2$, Tan $\delta = 0.003$, (manufacturer reference Fosseway R600).

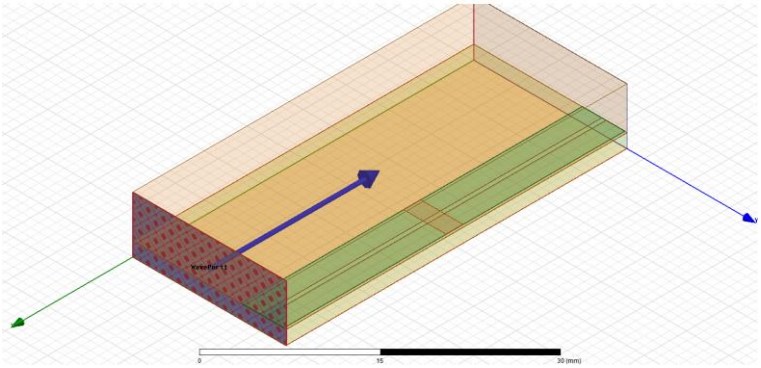

Fig. 4.34. Virtual Via Characterisation simulation cell (showing *VW*=5mm and *VL*=2mm) SSIW01

The simulation cells (Fig.4.34) utilised PMLs on the top and sides of the air section above the SSIW, and the walls of the SSIW were set to perfect electrical boundaries. To obtain the direct effect of the virtual via alone the S-parameters were de-embedded to the centre of the virtual via.

An additional factor considered was the capacitive reactance of the virtual via at the value of *VL* at the centre frequency of 4.5 GHz. To calculate this reactance, the standard equations were used:

$$X_c = \frac{1}{2\pi f_0 C}, where\ C = \frac{\varepsilon_0 \varepsilon_r A_T}{\Delta d} \qquad \text{(Eq.4.18)}$$

Where A_T is the total area of copper of the virtual via configuration for the set value of *VL*, Δd is the total separation distance between the bottom of the copper layer of the overlay and the top copper surface of the SSIW (Mylar dielectric plus adhesive thickness), f_0 is the centre frequency of the filter. The target being to keep the reactance as low as feasible (a few ohms) and as linear as possible across the range of *VL*.

4.6.1 Central Strip

The simplest virtual via shunt to form is a central symmetric strip (Fig. 4.35) with parameters *VL* and *VW* for virtual via width and length (along waveguide). Initially a range of widths was considered between 0.5 and 4 mm, the width needed to provide sufficient area to allow coupling on either side of the slot to couple to the waveguide. The virtual via length was varied between 0.5 and 3.0 mm, as an initial starting point to assess the virtual vias effect.

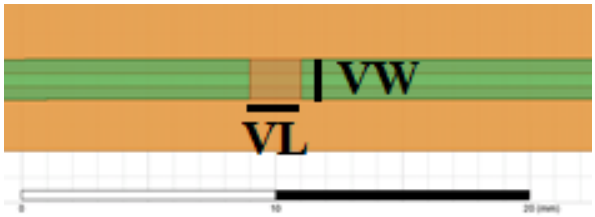

Fig. 4.35. Virtual Via central strip

Plotting the magnitude of the capacitive reactance for the ranges of *VW* and *VL*, with the two adhesive thicknesses (Fig. 4.36) highlights the immediate problem of using a central strip. Significant changes of reactance for small changes of *VL*, especially when *VW* is also small, effectively need a sufficient area of copper to allow capacitive coupling to occur, and for small *VL* the reactance remains large (greater than tens of ohms).

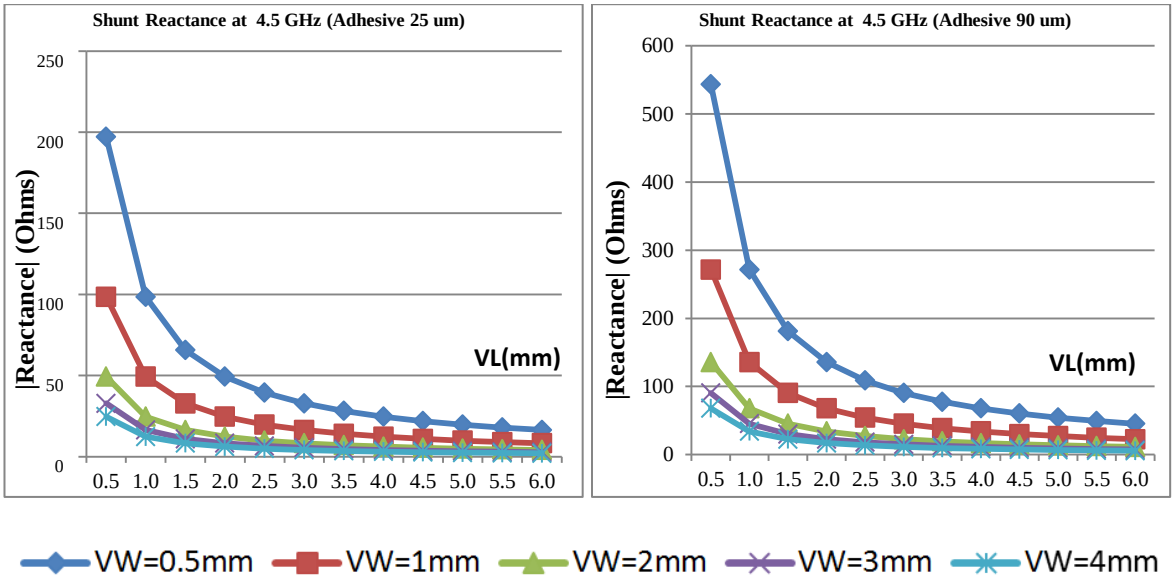

Fig. 4.36. Reactance magnitude variation of virtual via with 25 µm and 90 µm adhesive

This would then lead to problems of the virtual via characterisation, which is shown in Fig. 4.37 for *VW* = 3mm, where for close coupling (25 µm) the conductance is approximately exponential with regard to *VL* and the phase offset approaches 90°. For the thicker adhesive, the relationships are more linear, however there is still a relatively large phase offset for only a small variance in conductance.

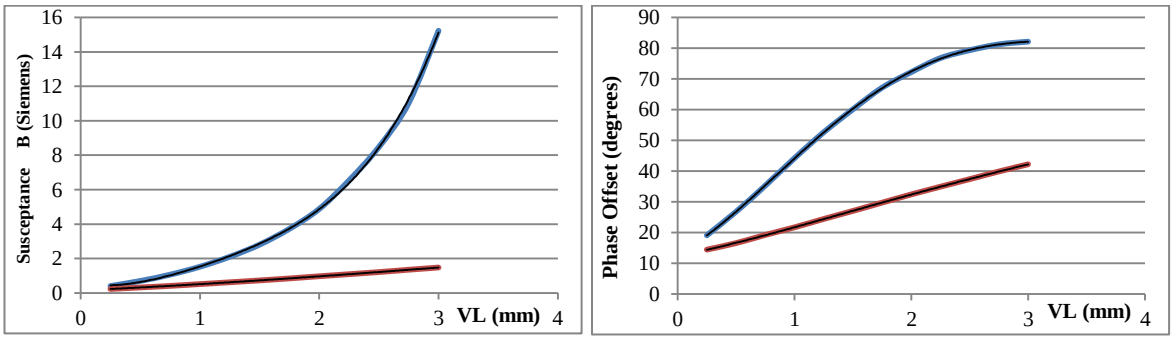

Fig. 4.37 Characterisation with 25 µm (blue) and 90 µm (red) adhesive VW=3.0mm

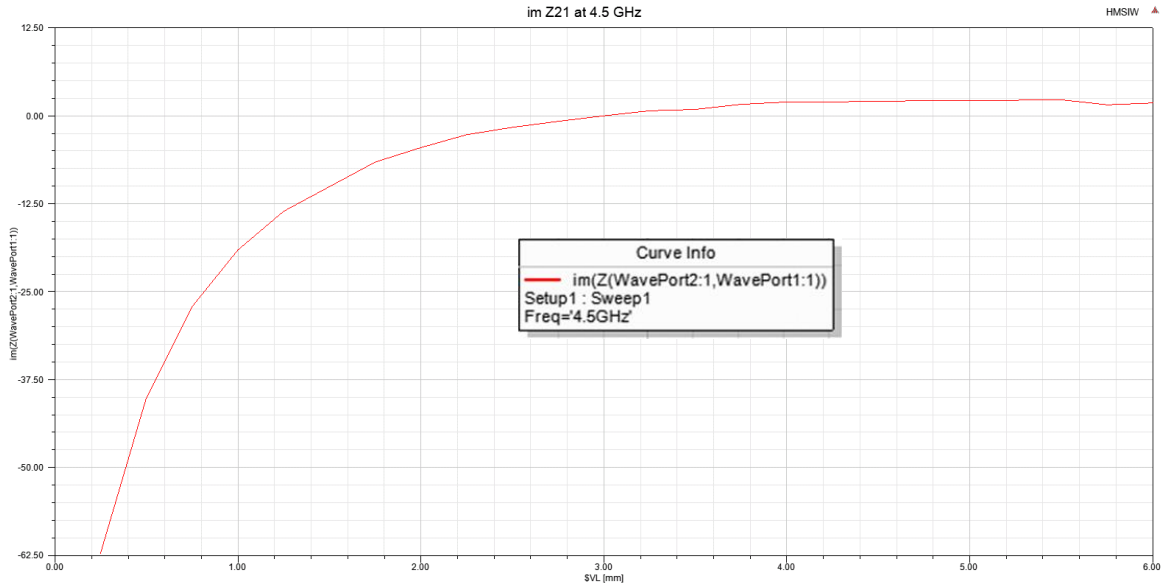

Fig. 4.38 Im(Z_{21}) at 4.5 GHz for VW=3mm, adhesive 25µm

The plot of the Im(Z_{21}) (Fig. 4.38) only becomes positive when *VL* exceeds 3mm, but only by a few Ohms. The value of *VW* was chosen as the first detailed value to analyse. Calculating the filter parameters for the 3rd order Chebyshev, with 0.5dB ripple, 400 MHz bandwidth, and centred at 4.5 GHz.

- Calculated B Values: B_1 = 1.9182 S, B_2 = 4.3372 S, B_3 = 4.3372 S, B_4 = 1.9182 S
- Calculated Cavity Lengths: L_1 = 27.7 mm, L_2 = 29.8 mm, L_3 = 27.7 mm
- Derived virtual via widths: 1.16 mm, 1.89 mm, 1.89 mm, 1.16 mm
- Adjusted cavity lengths: 4.88 mm, 3.01 mm, 4.88 mm

It was possible to calculate variants of 0.1 dB ripple and 200 MHz bandwidth, but not form within the waveguide due to adjusted cavity lengths causing the virtual vias to overlap. The phase offsets are too large (for both adhesives) causing the adjusted cavity lengths to be less than the half wave resonators they needed to be. The reactance of the virtual via at 4.5 GHz varies considerably for both thicknesses of adhesive, and is only inductive when *VL* exceeds 3.0 mm. Increasing the width of *VW* will increase the area of copper and hence the capacitive coupling and improve the virtual vias performance. A central symmetric virtual via with width (*VW*) equal to 5mm, improves the capacitive reactance with the range of *VL* , as shown in Fig. 4.39 . The values of Im(Z_{21}) for the range of *VL* are positive and hence inductive, but low in magnitude (less than 10Ω) – plot not shown.

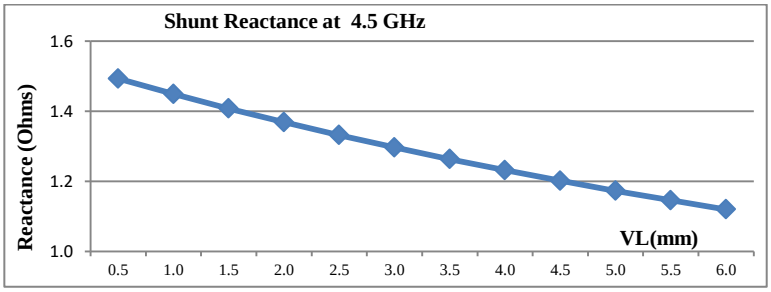

Fig.4.39 Shunt reactance for VW=5mm (25µm adhesive)

Unfortunately, characterising the symetric virtual via with *VW*=5.0mm shows that now only a minimum conductance value of 8S may be obtainined when *VL*=4.0 mm and the phase offsets are still significant (Fig. 4.40).

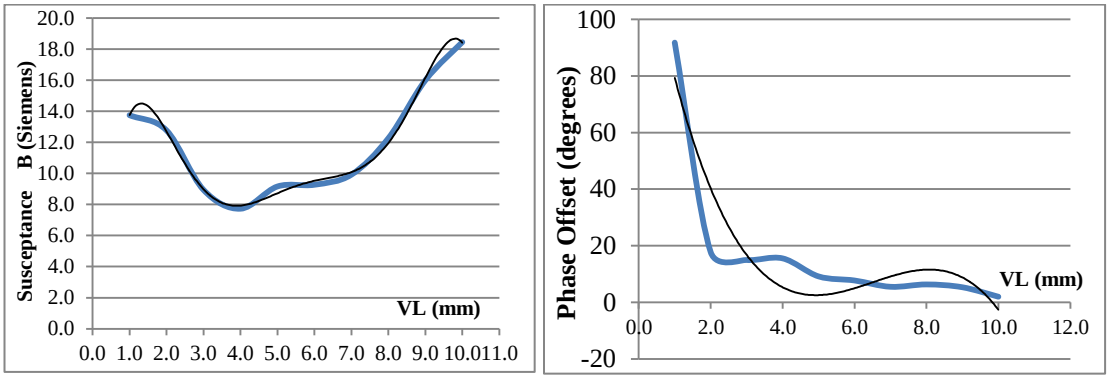

Fig.4.40 Susceptance and phase offset for VW=5mm at 4.5 GHz (25µm adhesive)

With phase offset still large (>60°) for small *VL* (less than 2mm), and for larger *VL* reducing but not linear, although inductive across the range of *VL* the limitation of minimum susceptance and non-linear characterisation means that the central symmetric strip is not suitable to use as a virtual via to load the SSIW. In addition the thicker adhesive does not allow sufficient coupling, and will not be considered further.

4.6.2 Offset Strip

By using an offset strip (Fig. 4.41), copper could be added over the main SSIW section and the amount of copper coupling across the slot controlled. The concept was to add sufficient capacitance to ensure a low reactance at the centre frequency and a more linear response as *VL* varied.

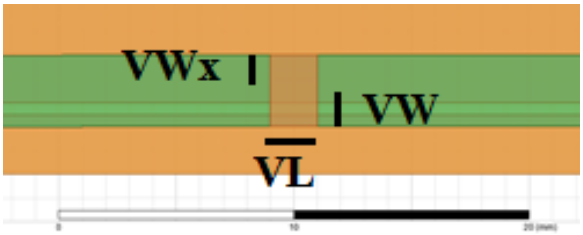

Fig. 4.41 Virtual Via offset strip

With the offset pad, a new variable was added *VWx*, so the total virtual via width was the addition of *VW and VWx*. With the adhesive thickness fixed at 25 µm, initial values of *VW*=1.5 mm and *VWx* = 1.5 mm , the shunt reactance (Fig. 4.42) is still large for small *VL*. Im(Z_{21}) is negative for all *VL* and although susceptance is more linear the phase offset is still too large.

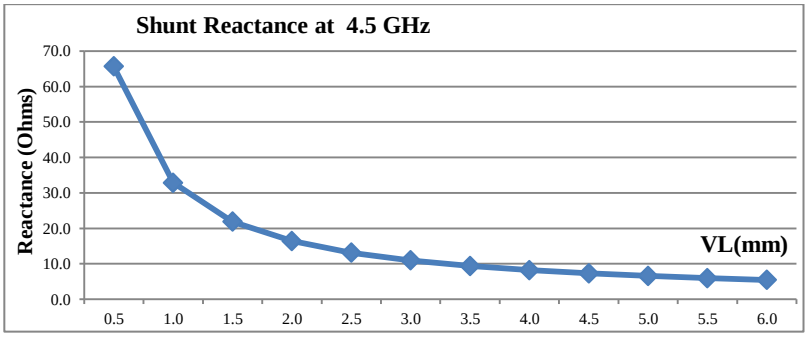

Fig.4.42. Shunt reactance for VW=1.5mm VWx=1.5mm (25µm adhesive)

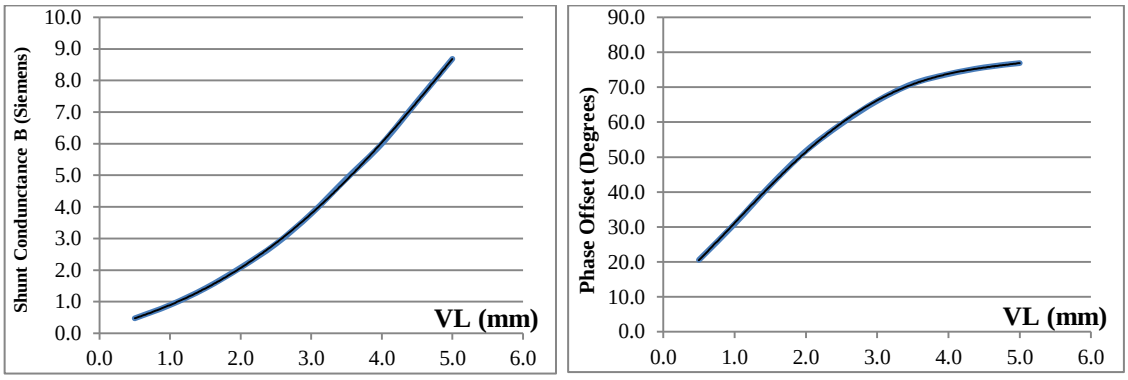

Fig.4.43 Susceptance and phase offset for offset strip at 4.5 GHz (25µm adhesive)

Hence the offset strip does produce a more linear characterisation, but it is not inductive and the phase offset still remains too large.

4.6.3 Symmetric I Strip

Introducing pads to both sides of the virtual via increased the copper area, improving the capacitance coupling, was intended to meet all of the problems highlighted so far, that of; linear characterisation yielding a good range for shunt conductance, low phase offset with approximately linear response, low and linear capacitive reactance across range of *VL*, Im(Z_{21}) positive and therefore shunt is inductive. This configuration was deemed symmetric 'I' virtual via and is shown in Fig. 4.44.

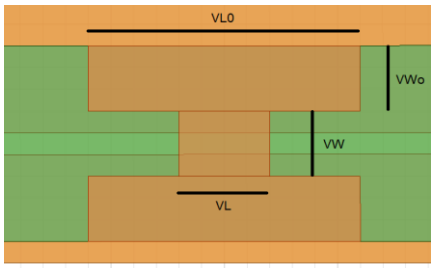

Fig. 4.44. Virtual Via Symmetric I strip

Two new parameters are introduced to define the size of the pads, *VLo* defines the length of the pad along the waveguide, and *VWo* the width of the pad across the waveguide width. The analysis with *VW* = 1.5 mm, *VWo* = 1.5 mm, *VLo* = 6.0 mm and varying *VL* between 0.1 and 6.0 mm, produced an approximate linear characterisation, a phase offset of less than 10° (approximately linear), a capacitive reactance at 4.5 GHz varied from 2.7 Ω to 1.8 Ω, and positive Im(Z_{21}).

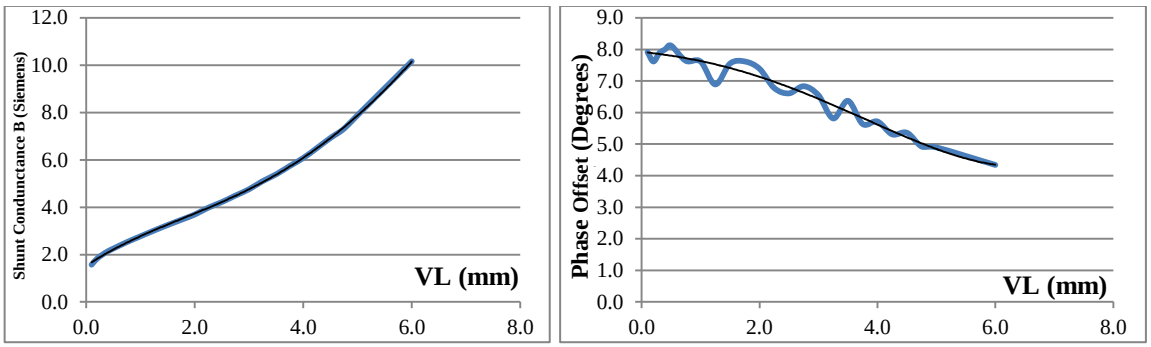

Fig.4.45 Susceptance and phase offset for symetric I strip at 4.5 GHz (25μm adhesive)

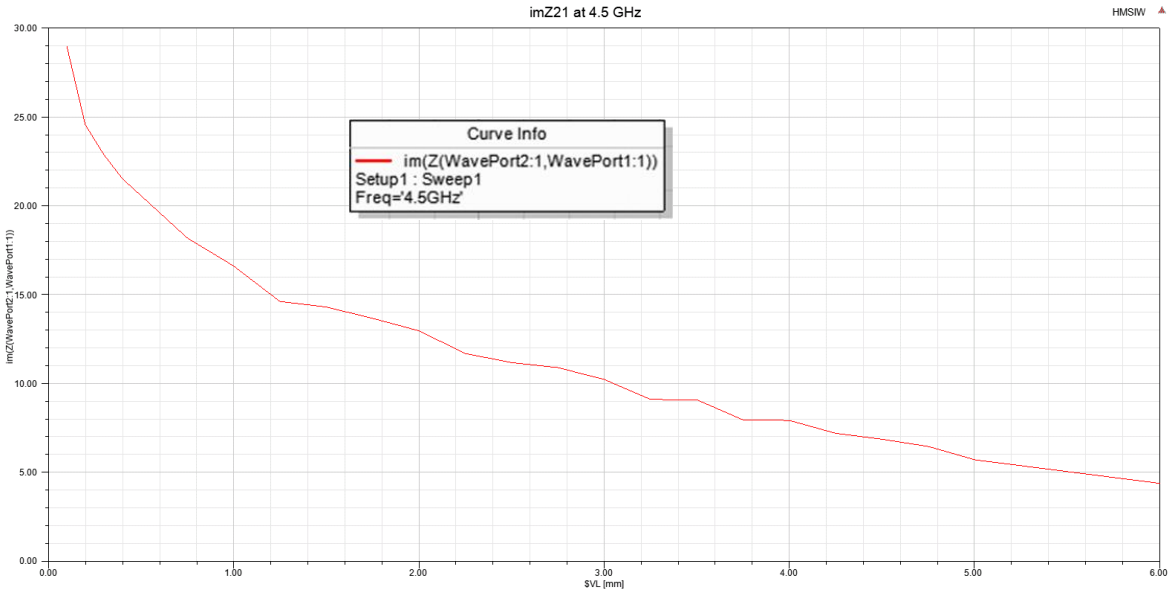

Fig.4.46 Im(Z_{21}) for symetric I strip at 4.5 GHz (25µm adhesive)

4.6.4 Asymmetric I Strip

The symmetric I strip met all the criteria, but only minimally. A small amount of simulation error was evident on the phase offset characterisation and the Im(Z_{21}) (Fig. 4.45 and 4.46), a possible indication that additional refinement was required within the simulation model. Several different iterations were trialled, but a more stable solution was obtained, giving the final configuration as the Asymmetric 'I' virtual via (Fig.4.47), a combination of several of the previous versions.

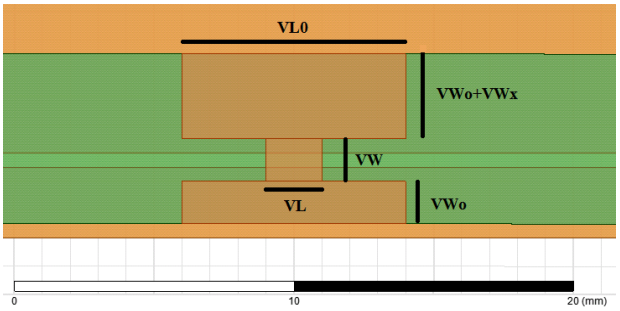

Fig. 4.47. Virtual Via asymmetric I strip

The total number of parameters required to define the virtual via are shown in Table 4.3. From the characterisation plots (Fig.4.48) it can be seen that approximately linear responses are obtained, a low variance on the capacitive shunt reactance (Fig.4.49) is achieved, and Im(Z_{21}) (Fig.4.50) is positive across range of *VL*. The phase offset characterisation is stabilised, with S_{11} phase offset and theta average offset plots also included, as the phase of S_{11} and S_{21} are approximately equal the theta average may be used for a more accurate characterisation (see Fig.4.48).

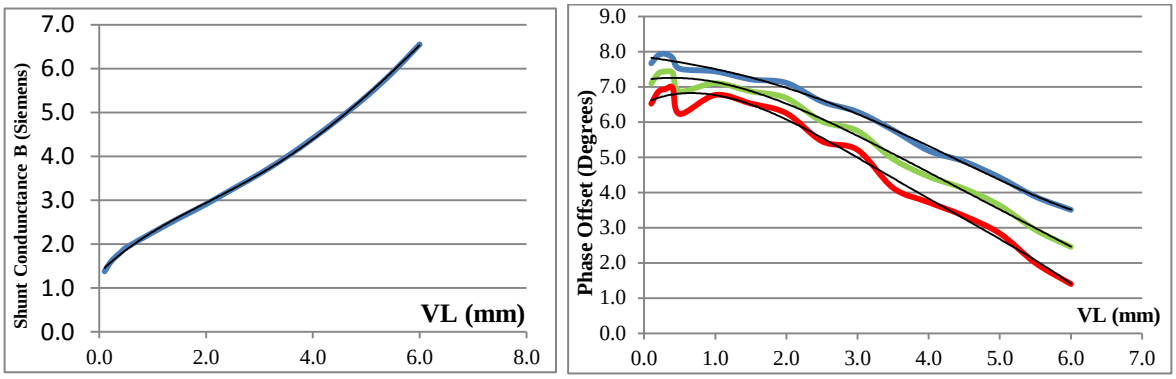

Fig.4.48 Susceptance and phase offset for asymetric I strip at 4.5 GHz (25um adhesive)
(Phase offset Blue-S_{21}, Red-S_{11}, Green – average)

Parameter	*VL*	*VW*	*VWo*	*VLo*	*VWx*
Description	virtual via length	Virtual via width	Pad base width	Pad base length	Pad width extension
Value (mm)	0.1 to 6.0	1.5	1.5	8.0	1.5

Table 4.3. Asymmetric 'I' Configuration Virtual Via Parameters

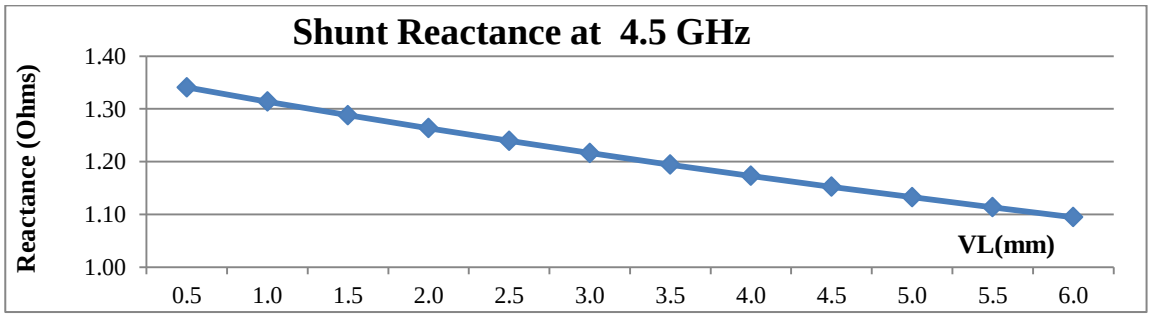

Fig. 4.49 Capacitive Reactance at 4.5 GHz

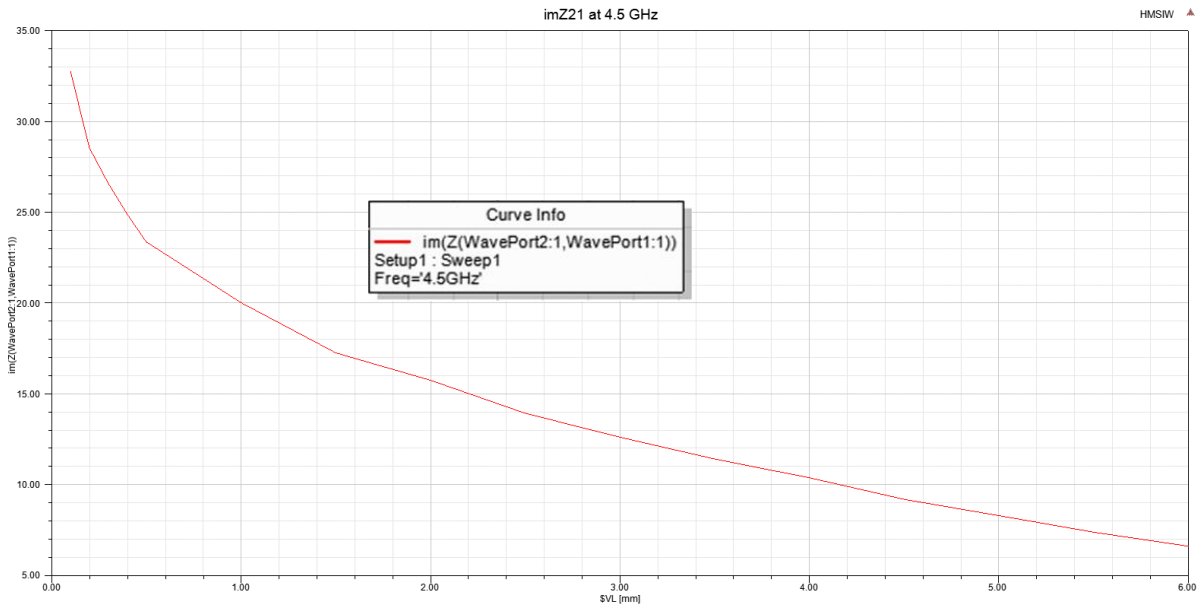

Fig. 4.50 Im(Z_{21}) for asymetric I strip at 4.5 GHz (25µm adhesive)

4.7 SSIW01 Filters

With the virtual via now fully defined it is possible to complete the filter design stage. As mentioned the adhesive used was the thinner option, which gave a total separation between SSIW and overlay copper of ~40µm. The SSIW01 used the asymmetrical I virtual via configuration based on the parameters: *VW* = 1.5 mm, *VWo* = 1.5 mm, *VWx* = 1.5mm, *VLo* = 8.0 mm. The overlays were drawn in Mentor Graphics PADs PCB design CAD software, as an additional layer to the original PCB coupons. The Gerber files were exported and inverted to produce the negative image photo-plots required to etch the Mylar laminate, which was completed in-house. Alignment marks were added to the layout (see Fig 4.52) to aid in assembly.

4.7.1 SSIW01 Filter 1

The first filter using the overlay implemented was a 3rd Chebyshev order pass-band filter with 0.5 dB ripple, 400 MHz bandwidth, centred at 4.5 GHz. From the Matlab code, the following results were obtained:

- Calculated B Values: B_1=1.904 S, B_2=4.2887 S, B_3=4.2887 S, B_4=1.904 S
- Calculated Cavity Lengths: L_1=27.7 mm, L_2=29.8 mm, L_3=27.7 mm
- Derived virtual via widths: 0.5434 mm, 3.8899 mm, 3.8899 mm, 0.5434 mm
- Adjusted cavity lengths: 25.241 mm, 27.73 mm, 25.241 mm

These parameters were then implemented in the CAD drawing (Fig.4.51), where the dimensional check confirmed the required spacing and copper sizes.

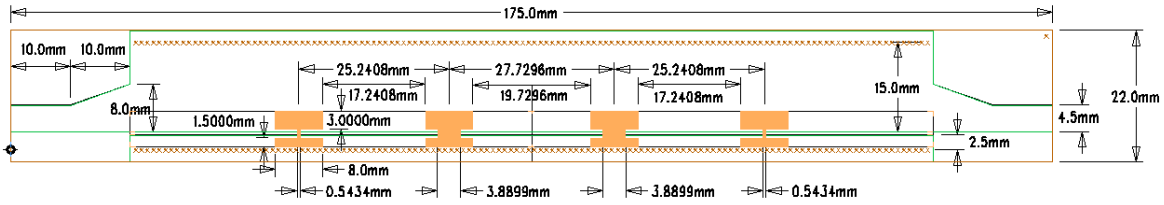

Fig. 4.51 CAD design of SSIW01 filter 1

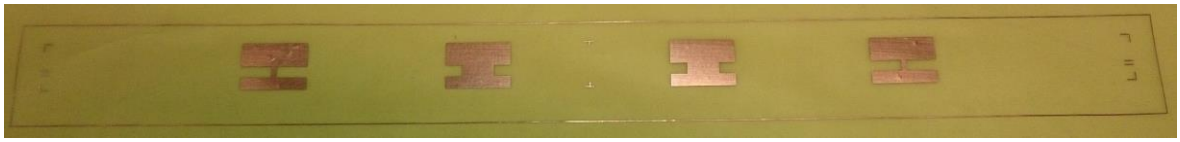

Fig. 4.52 fabricated SSIW01 filter 1 (showing alignment marks)

After assembly, the waveguide was measured and the results combined with the initial simulation S-parameters, see Fig. 4.53. A reasonable correlation between the simulated and measured was obtained; but a frequency offset was evident, as with the direct copper filter simulation. However, the S_{11} response was stronger than simulated.

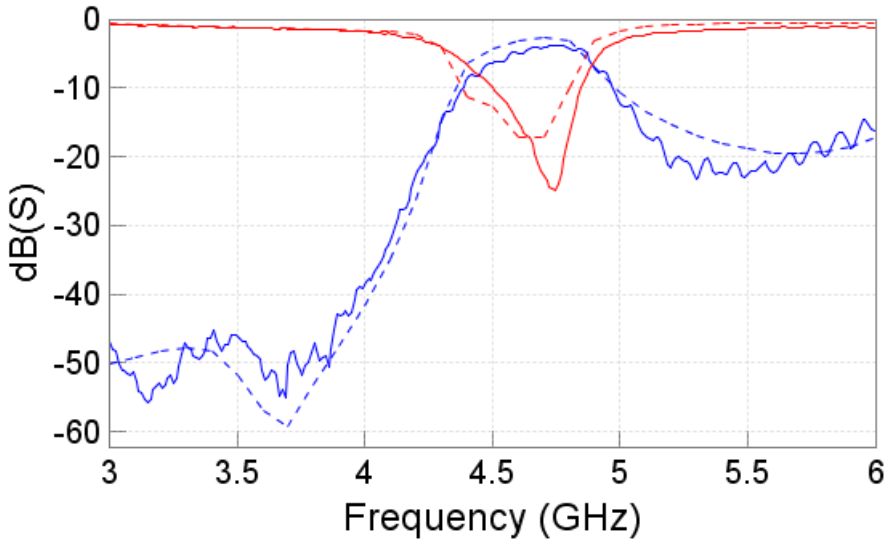

Fig. 4.53. SSIW01 Filter 1 S-Parameters (simulated and measured)
(S_{11} red, S_{21} blue, solid measured, dashed simulated)

Alignment of the overlay was challenging, a number of attempts were made to position the filter exactly as required. Position errors for horizontal, vertical and rotational occurred, and due to the thin nature of the overlay linearity along the waveguide had to be maintained.

4.7.2 SSIW01 Filter 2

The second filter iteration used optimization of the simulation data to achieve

- optimized Virtual Via Widths: 0.438 mm, 4.05 mm, 4.05 mm, 0.438 mm
- optimized cavity lengths: 25.291 mm, 27.521 mm, 25.291 mm

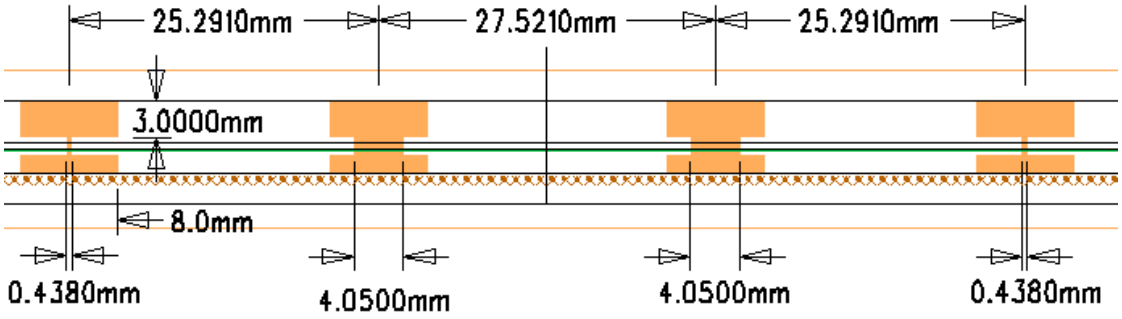

Fig. 4.54 CAD design of SSIW01 filter 2 (optimised values)

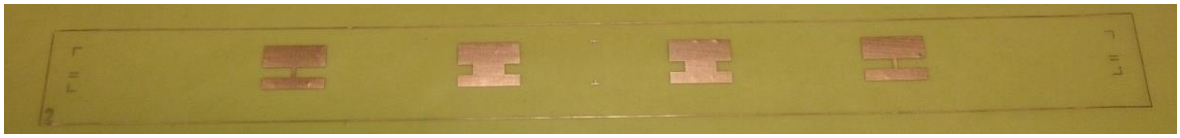

Fig. 4.55 fabricated SSIW01 filter 2 (showing alignment marks)

Fig. 4.56 assembled SSIW01 filter 2

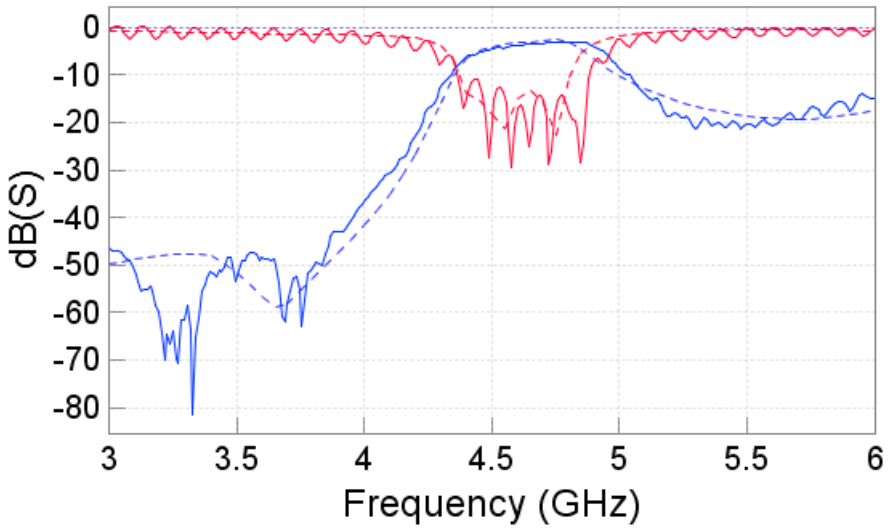

Fig. 4.57. SSIW01 Filter 2 S-Parameters (simulated and measured)
(S_{11} red, S_{21} blue, solid measured, dashed simulated)

The measured S_{11} result in Fig. 4.57 shows a ripples along the frequency span, indicative of a longer electrical length; which is incorrect and is probably due to a calibration error.

4.7.3 SSIW01 Filter 3

To compensate for the error in modelling, a design was offset by 0.1 GHz, to produce a 3rd order filter with 0.5 dB ripple, 400 MHz bandwidth, centred at 4.4 GHz. From the Matlab code, the following results were obtained:

- Calculated B Values: B_1 = 1.8042 S, B_2 = 3.9536 S, B_3 = 3.9536 S, B_4 = 1.8042 S
- Calculated Cavity Lengths: L_1 = 28.8 mm, L_2 = 30.9 mm, L_3 = 28.8 mm
- Derived virtual via widths: 0.4355 mm, 3.4861 mm, 3.4861 mm, 0.4355 mm
- Adjusted cavity lengths: 26.089 mm, 28.605 mm, 26.089 mm

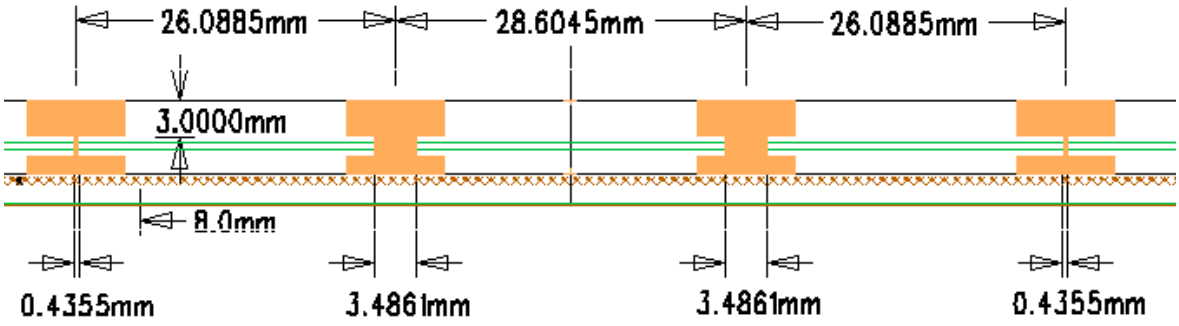

Fig. 4.58. CAD design of SSIW01 filter 3 (offset centre frequency)

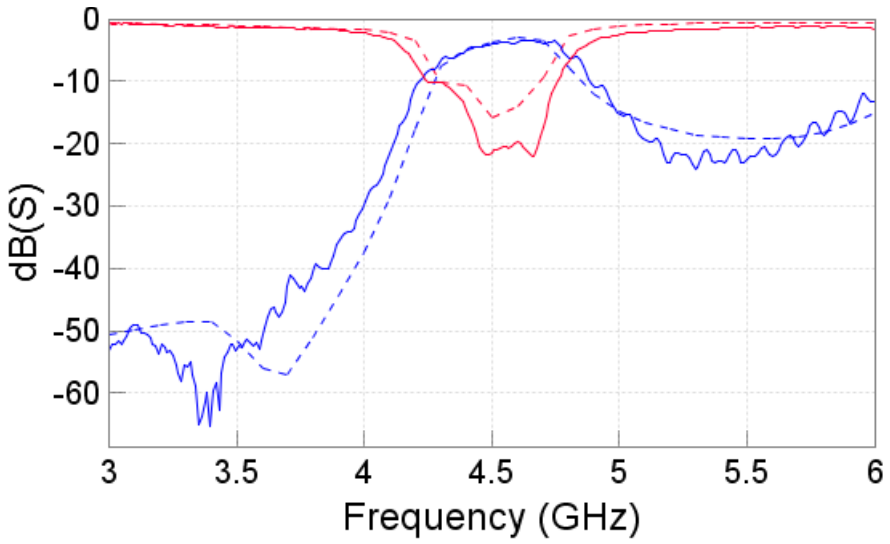

Fig. 4.59. SSIW01 Filter 3 S-Parameters (simulated and measured)
(S_{11} red, S_{21} blue, solid measured, dashed simulated)

The filter is centred on 4.5 GHz with a reasonable correlation between the simulated and measured.

4.8 Virtual Via Configuration SSIW02

Re-characterising the asymmetrical I virtual via for the increased shunt waveguide width of 5mm, but maintaining the parameters established of: *VW*=1.5mm, *VWo*=1.5mm, *VWx*=1.5 mm *VLo*=8 mm

The characterisation between the SSIW01 and 02 coupons are close but not exactly equal due to the increased loading form the larger shunt waveguide. The values of Im(Z_{21}) for the asymetric I strip was positive as previously for all values of *VL*, ranging from ~ 25 Ω for *VL* = 1mm to ~5 Ω when *VL* = 8mm.

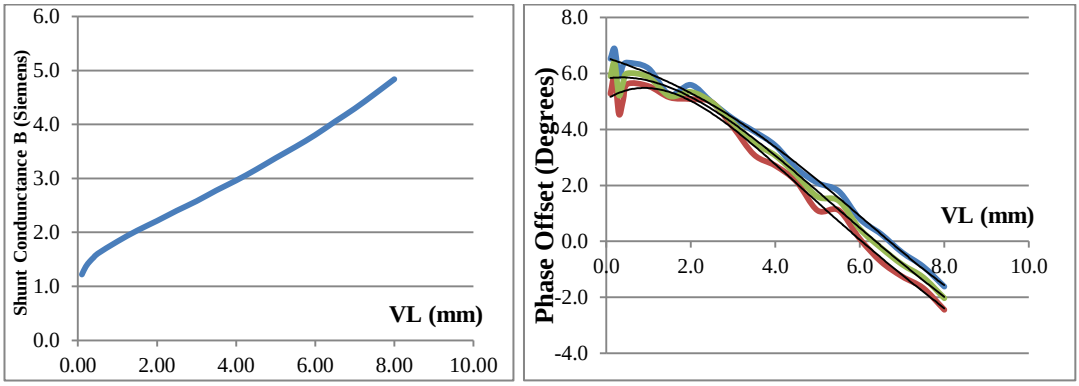

Fig.4.60. Susceptance and phase offset for asymetric I strip at 4.5 GHz (SSIW02)
(Phase offset Blue-S_{21}, Red-S_{11}, Green – average)

4.9 SSIW02 Filter

SSIW02 design 3rd order filter with 0.5dB ripple, 400 MHz bandwidth, centred at 4.5 GHz. From the Matlab code, the following results were obtained:

- Calculated B Values: B_1 = 1.9325 S, B_2 = 4.3867 S, B_3 = 4.3864 S, B_4 = 1.9325 S
- Calculated Cavity Lengths: L_1 = 27.4 mm, L_2 = 29.4 mm, L_3 = 27.4 mm
- Derived virtual via widths: 1.2427 mm, 7.0199 mm, 7.0199 mm, 1.2427 mm
- Adjusted cavity lengths: 26.368 mm, 29.587 mm, 26.368 mm
- Optimized Virtual Via Widths: 0.8095 mm, 7.3789, 7.3789 mm, 0.8095 mm
- Optimized cavity lengths: 26.974 mm, 30.808 mm, 26.974 mm

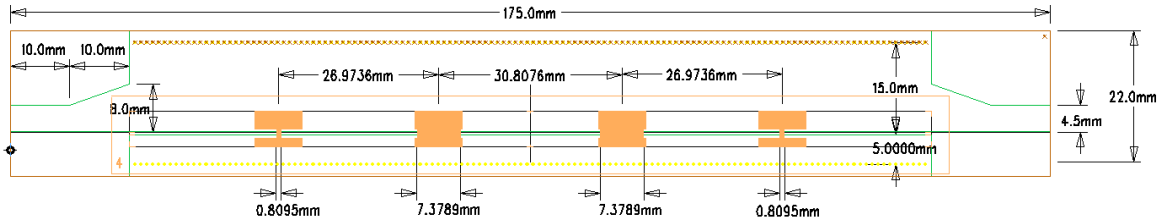

Fig. 4.61. CAD design of SSIW02 filter 4 (optimised)

Fig. 4.62. assembled SSIW02 filter 4

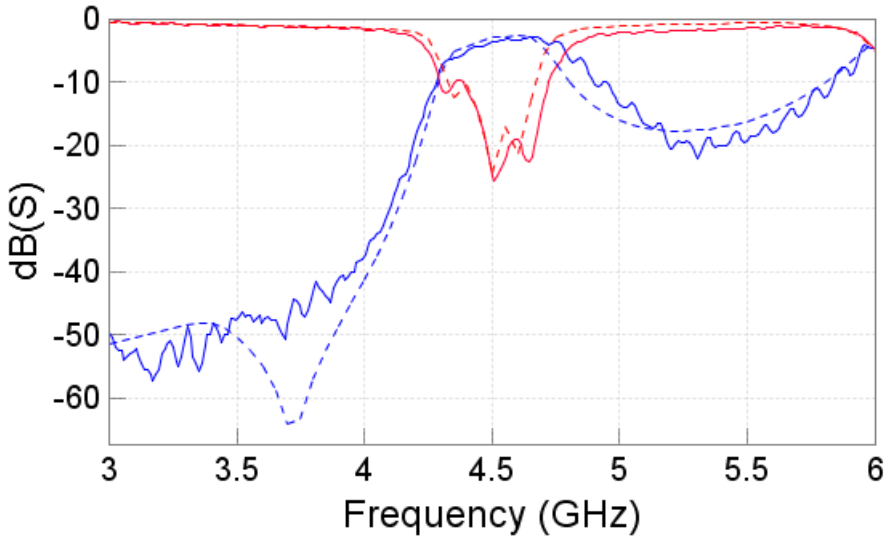

Fig. 4.63. SSIW02 Filter 4 S-Parameters (simulated and measured)
(S_{11} red, S_{21} blue, solid measured, dashed simulated)

4.10 Virtual Via Configuration SSIW03

Re-characterising the asymmetrical I virtual via for the increased shunt waveguide width of 10mm, but maintaining the parameters established as before: *VW* = 1.5mm, *VWo* = 1.5mm, *VWx* = 1.5 mm *VLo* = 8 mm. Shunt capacitive reactance remains unchanged, but for SSIW03 the larger shunt waveguide preloads the SSIW. As mentioned in section 4.2, the SSIW03 coupon has mode coupling at 4.5 GHz when the slot is unloaded. The characterisation of the asymmetrical I virtual via (as shown in figure Fig. 4.64), shows that the shunt conductance is not varying significantly with *VL*, hence neither is the phase offset, values for Im(Z_{21}) are negative for range of *VL* (0.1 to 6.0mm), meaning that the virtual via is capacitive and not acting as a shunt shorting the SSIW.

Other values and configurations for virtual vias were investigated, but as expected SSIW03 due to its mode coupling at 4.5 GHz is not usable for the filter range proposed. In addition to the developed asymmetrical I virtual via developed is not usable with the SSIW03. Further investigation is required to determine if an alternative virtual via configuration at a different frequency may be feasible.

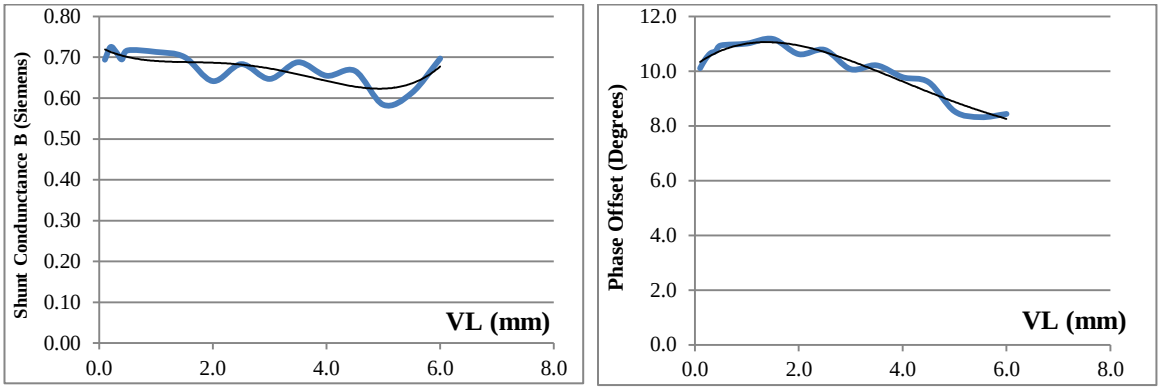

Fig.4.64 Susceptance and phase offset for asymetric I strip at 4.5 GHz (SSIW03)
(Phase offset Blue-S_{21})

4.11 Measurement Comment

Small variations in position of the overlay resulted in significant performance changes for the filter. As can be seen from Fig. 4.65, maintain an even spacing in both horizontal and vertical alignment, as well as avoiding rotational error was difficult. Multiple attempts were made to obtain the results achieve, but these will not have been as exactly simulated. Hence, positional error is probably the main reason for inaccuracy between the measured and simulated results.

Fig. 4.65 assembled SSIW02 filter 4 (close up)

Some further simulations were undertaken investigating the variations in the dielectric value of the adhesive (polyimide ε_r=3.5) and Mylar (polyester ε_r=3.2), which were estimated from data showed little change in the filter performance. Small positional variations in the overlay as expected altered the performance significantly, as found during assembly and measurement. In addition varying the adhesive thickness also had a significant impact, as this directly effects the coupling element of the filter. As previously stated the thinnest adhesive would achieve the greatest coupling effect, but it would also result in the greatest variation of thickness due to surface imperfections. The effects of planarity and stretch in overlay, along with fabrication tolerances are areas were further work could be focussed.

4.12 SSIW Summary

In this chapter Slot SIWs were introduced as a possible means of easily integrating both passive and active microwave devices. Three test coupons were analysed with varying shunt waveguide sizes (2.5, 5.0 and 10.0 mm), the largest of which exhibited coupling within the fundamental mode at the target centre frequency; meaning it was not usable.

One of the SSIW coupons were analysed using the transvers resonance technique to investigate when the SSIW is loaded not with a perfect short or open, but some pre-determined impedance *Z.* An array of PIN diodes, on a capacitively coupled overlay, were used to load the slot with impedances controlled by the biasing current to form a travelling wave attenuator. Measured results showed the degree of attenuation was related to the biasing current supplied to the PIN diode array, variable attenuation from 2 dB to 25 dB over the 3-5 GHz waveguide range was demonstrated.

The use of the capacitively coupled overlay was then developed as a waveguide filter, requiring the characterisation of the *virtual via*, a capacitive element which loads the SSIW slot with a controlled impedance and position to create resonant cavities. Third order pass-band filters were developed, fabricated and measured utilising the *asymmetrical 'I' shaped virtual via*. The modelling method was only approximate and the initial design parameters required optimising to achieve the required results. It was noted, that exact positioning of the overlay onto the SSIW was problematic, with small deviations significantly effecting the filters performance.

In summary, the use of the capacitively coupled overlay as a means of allowing integration of both active and passive elements with the Slot SIW was demonstrated. Low-cost waveguide bandpass filters, with centre frequency of 4.5 GHz, using capacitively coupling overlays were verified on a reusable SSIW test coupon. The positional requirements for the placement of the overlay filter onto the SSIW could be improved with additional alignment marks, alternatively a direct implementation of the filter directly in copper would be straight forward, but would not then be reusable.

4.13 References

[1] Ruo Feng Xu, B. S. Izquierdo and P. R. Young, "Switchable Substrate Integrated Waveguide," *Microwave and Wireless Components Letters, IEEE,* vol. 21, pp. 194-196, 2011.

[2] R. F. Xu, "Miniaturized guided wave structures and applications. PhD Thesis. Univeristy of Kent," 2010.

[3] Feng Xu and Ke Wu. Guided-wave and leakage characteristics of substrate integrated waveguide. *Microwave Theory and Techniques, IEEE Transactions On 53(1),* pp. 66-73. 2005.

[4] D. Deslandes and Ke Wu. Accurate modeling, wave mechanisms, and design considerations of a substrate integrated waveguide. *Microwave Theory and Techniques, IEEE Transactions On 54(6),* pp. 2516-2526. 2006.

[5] M. Bozzi, A. Georgiadis and K. Wu. Review of substrate-integrated waveguide circuits and antennas. *Microwaves, Antennas & Propagation, IET 5(8),* pp. 909-920. 2011.

[6] D. M. Pozar, *Microwave Engineering.* New York: Wiley, 1998.

[7] Young Ki Cho, "On the equivalent circuit representation of the slitted parallel-plate waveguide filled with a dielectric," *Antennas and Propagation, IEEE Transactions On,* vol. 37, pp. 1193-1200, 1989.

[8] B. Sanz-Izquierdo, E. A. Parker and J. C. Batchelor, "Switchable Frequency Selective Slot Arrays," *Antennas and Propagation, IEEE Transactions On,* vol. 59, pp. 2728-2731, 2011.

[9] B. Sanz-Izquierdo, E. A. Parker, J. -. Robertson and J. C. Batchelor, "Tuning technique for active FSS arrays," *Electronics Letters,* vol. 45, pp. 1107-1109, 2009.

[10] Ruo Feng Xu, A. J. Farrall and P. R. Young, "Analysis of Loaded Substrate Integrated Waveguides and Attenuators," *Microwave and Wireless Components Letters, IEEE,* vol. 24, pp. 62-64, 2014.

[11] I. Hunter, *Theory and Design of Microwave Filters.* London: Institution of Electrical Engineers, 2001.

[12] S. B. Cohn, "Direct-Coupled-Resonator Filters," *Proceedings of the IRE,* vol. 45, pp. 187-196, 1957.

[13] N. Grigoropoulos, "Novel substrate integrated waveguides and components. PhD thesis at University of Kent." pp. 179 leaves, 2005.

5 Rotated Waveguide

In this chapter a new variant to the SIW structures is introduced and analysed, its characteristics with different dielectric constants and laminate thicknesses is investigated. Modifying the parameters of the waveguide structure changes the cut-off frequency of the fundamental mode, this is discussed and new formulae that more accurately defines the cut-off frequency for this new waveguide are developed. Test coupons are designed, along with a novel microwave transition and measurements made to assess the performance of the new waveguide.

5.1 Overview

Standard SIWs enable propagation along the longitudinal axis with the electric field vertically aligned across the dielectric between the top and bottom metal surfaces. The rotated half-mode substrate integrated waveguide (rHMSIW) allows the electric field to be concentrated on the top dielectric surface, which enables direct interaction with the field at its maximum [1].

To form impedance discontinuities within SIW structures - to create devices such as filters, couplers, and antennas [2-5]. Vias (or the absence of) are often used to create impedance discontinuities; meaning that the resultant performance is reliant on the accuracy of the drilling process and the reliability of the through hole plating process. With the rHMSIW, however, impedance structures may be formed directly on (or as part of) the top metal surface, using the more accurate etching processes, with the option of direct integration of microwave components.

In the previous, chapter Slot SIWs (SSIWs) were used with capacitive overlays to create a travelling wave attenuator [6] and pass-band waveguide filters. The majority of the field in the SSIW is concentrated within the dielectric, and the shunt waveguide loads the complete waveguide. The amount of field in the SSIW slot limits the capability for any device or structure to interact with that field, thus for the example of the SSIW filter in chapter 4 it limits the value of shunt conductance obtainable for the virtual vias. For the rHMSIW, the electric field maximum is located on the top dielectric surface and it is possible to directly interact with it at that point. In addition, it is possible to control the gap width of the waveguide as required. A loss comparison between the rHMSIW and regular HMSIW is expected to be similar, but was not investigated in detail.

The concept to be explored was to develop a test coupon with high bandwidth (ideally equal to an existing frequency band), capable of placing the electric field maximum directly on the top

dielectric surface to allow direct interaction. Capacitor coupled overlays would then be used to introduce discontinuities into the wave path to form filters and other structures, such as leaky-wave antennas.

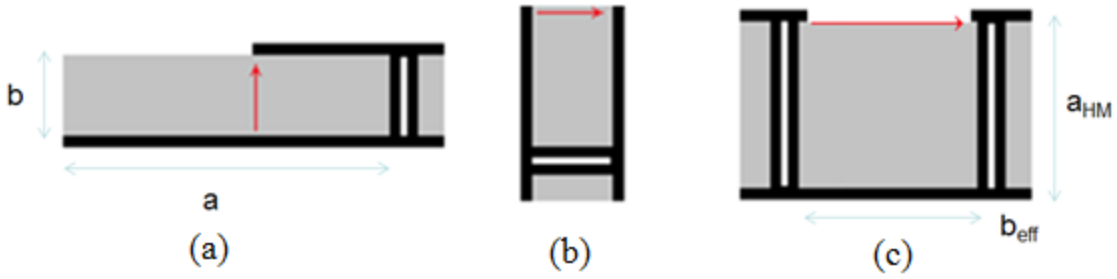

Fig. 5.1 Rotation of waveguide from HMSIW to rHMSIW

Fig. 5.1a shows the basic concept: a standard HMSIW waveguide is shown with the electric field maximum centred in the dielectric, *a* and *b* dimensions showing the waveguide width and height respectively. Fig. 5.1b represents the rotated HMSIW, with the electric field maximum now on the dielectric surface, finally Fig. 5.1c the rHMSIW is re-constructed in planar form, with the vias now forming the waveguides top and bottom giving b_{eff} and the waveguide width defined as twice a_{HM} (the half mode width of the waveguide which is the dielectric thickness).

The objective was to investigate the properties of the rotated HMSIW and its performance, with the goal of producing a test coupon which could be used across a complete frequency band.

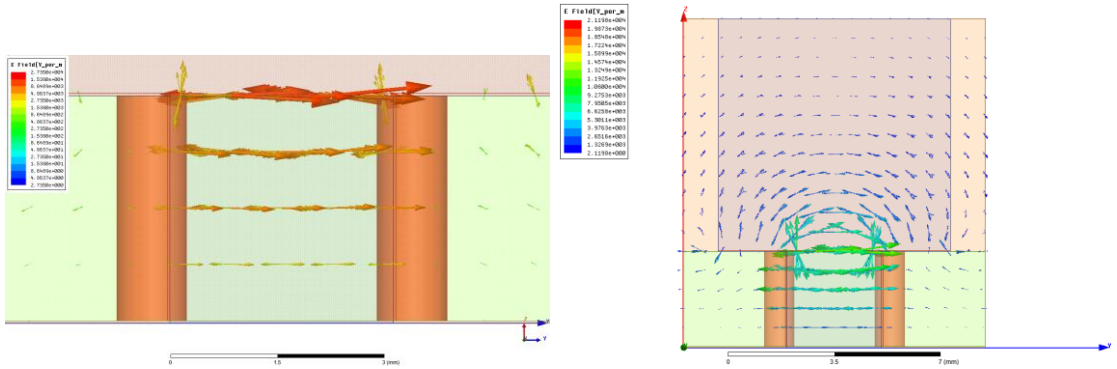

Fig. 5.2 Segment views of rHMSIW, with vector plots of the electric

Fig. 5.2 shows two cross sections from the HFSS simulations, showing the electric field in vector form for the fundamental propagating mode. The E-field is shown concentrated on the top dielectric surface, with a close coupled field in the air space just above. These are end views looking directly into the waveguide structures, therefore the vectors point in both directions.

Initial investigation focussed at K band (18 to 26 GHz), requiring an rHMSIW with a cut off frequency below this and a bandwidth of 8 GHz, utilizing Rogers 5880 material with a dielectric

thickness of 3.175 mm gave a cut-off frequency of ~16 GHz. However, focus then moved to using Rogers 6010 material with a dielectric thickness of 1.91 mm and a rHMSIW cut off frequency of 12.3 GHz, which was just within the Ku band (12 to 18 GHz) a bandwidth of ~6 GHz (See section 5.2.2 for further details).

The Rogers duroid materials utilised are high frequency laminates filled with PTFE (Polytetrafluoroethylene) they are designed for low electrical loss and stable dielectric constant value over a wide frequency range. The 5880 material is reinforced with glass microfibers, and the 6010 with ceramic.

The 5880 material has a Dielectric Constant (ε_r) of 2.2 (specified tolerance of ±0.02) and Dissipation Factor (or Loss Tangent or Tan δ) of 0.0009. Copper thicknesses of 9 μm, 17 μm, 35 μm and 70 μm (equating to ¼, ½, 1 and 2 ounce copper densities), either in rolled copper foil or electrodeposited form. The standard dielectric thicknesses available from Rogers are:

- 0.127 mm (or 5') [Note: Symbol ' denotes thousandth of an inch = 25.4 μm)
- 0.254 mm (or 10')
- 0.381 mm (or 15')
- 0.508 mm (or 20')
- 0.787 mm (or 31')
- 1.575 mm (or 62')
- 3.175 mm (or 125')

The RT/duroid 5880 materials are targeted at exacting stripline and microstrip circuit applications.

The 6010 material has a Dielectric Constant (ε_r) of 10.2 (specified tolerance of ± 0.25) and Dissipation Factor (or Loss Tangent or Tan δ) of 0.0023. Copper thicknesses of 18 μm, 35 μm and 70 μm (equating to ½, 1 and 2 ounce copper densities) in electrodeposited form. The standard dielectric thicknesses available from Rogers are:

- 0.127 mm (or 5')
- 0.254 mm (or 10')
- 0.635 mm (or 25')
- 1.270 mm (or 50')
- 1.900 mm (or 75')
- 2.500 mm (or 100')

The RT/duroid 6010 materials is targeted at high dielectric constant circuit applications.

The design and structure of the waveguides were to be based on SIW technology using metallised vias to form the waveguide floor and ceiling; previously they had formed the waveguide walls. Traditional box waveguides maintained a width *a* to height *b* ratio of typically 2:1 sometimes 2.5:1 (Fig. 5.3 shows a number of standard waveguide *a/b* ratios). With traditional SIW design and fabrication the height of the waveguide has been fixed with the laminate thickness, bit for the rHMSIW the laminate thickness fixes the half-mode height a_{HM} meaning that the waveguide width b_{eff} may be adjusted.

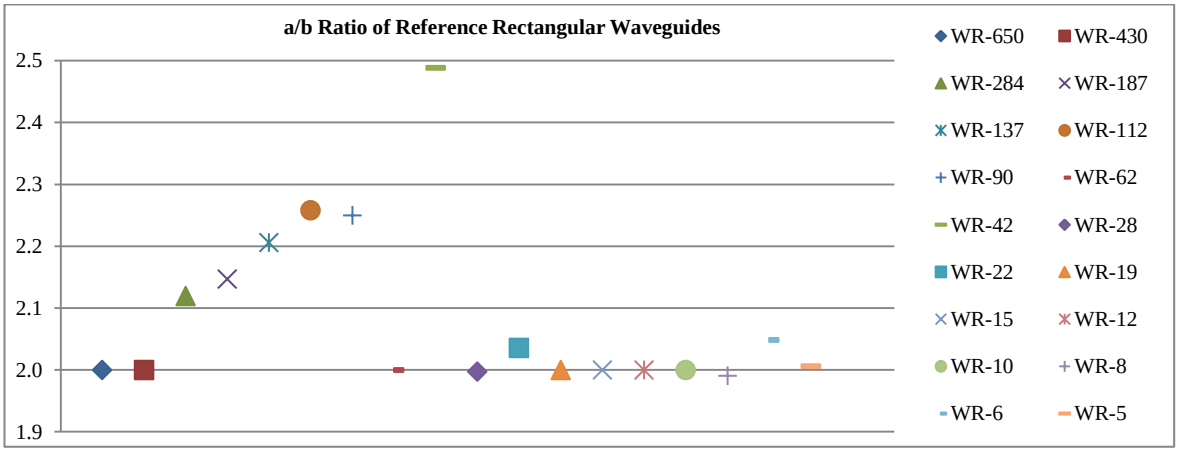

Fig. 5.3 a/b ratio for reference waveguides.

5.1.1 Parameters

There are a number of key parameters required to define the rHMSIW, these are initially defined and described below:

- a_{HM} is the dielectric thickness, which gives the effective waveguide width $a_{eff} = 2a_{HM}$
- b_{eff} is the effective waveguide height which takes into account the via diameter and pitch, and gives the 'b' dimension for the waveguide height.
- C_w is the copper width of the top surfaces and is intially defined as ¼ of the wavelength in the substrate at the centre frequency considered, then optimised for performance of the waveguide.
- D_w is the exposed 'Dielectric Width' of the waveguide on the top surface of the laminate.
- b_{eff}/a_{HM} is the normalised value for comparison and will nominally be 1 to give a standard *a/b* ration of 2:1, but a variation will be considered.
- D_w/a_{HM} is the normalised value for comparison and will vary between 0 and 1, conidered in steps of 0.1.

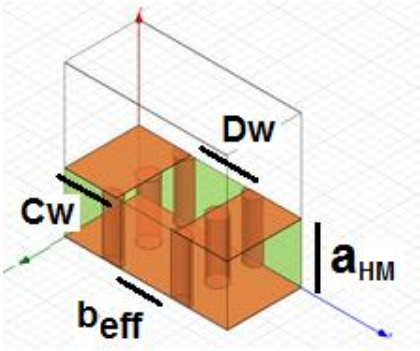

Fig. 5.4 rHMSIW segment

Fig. 5.4 shows a single via segment of the rHMSIW, detailing a_{HM} and b_{eff}, but also two other important parameters D_w the exposed dielectric width and C_w the top waveguide copper width. The more dielectric that is exposed on the top surface the greater the amount of energy for interaction, but also the larger D_w increases radiation losses. The top copper width C_w is there to help stabilise the required waveguide half-mode ($TE_{1/2,0}$). C_e (not shown in Fig.5.4) is the minimum copper clearance from the via hole to the inside top copper edge required for PCB fabrication, which will hence limit the range of D_w.

Varying D_w/a_{HM} allows a comparison of the performance of the waveguide for various degrees of gap width, which is shown in Fig.5.5 below.

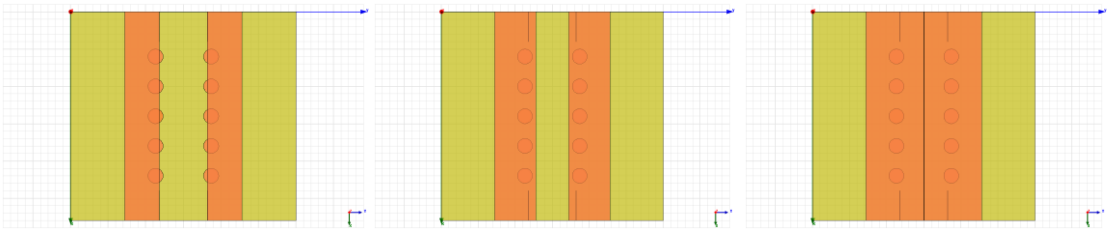

$D_w/a_{HM}=1$ $D_w/a_{HM}=0.7$ $D_w/a_{HM}=0$

Fig. 5.5 rHMSIW sections showing range of values for D_w.

When D_w/a_{HM} is equal to '1' the copper inside edge extends only as far as the effective waveguide height b_{eff} , which exposes the tops of the vias, casing a fabrication problem, the minimum copper required from the via edge to the inside copper edge is defined as C_e and will be defined as a process tolerance from the PCB fabricator. In addition when D_w/a_{HM} becomes '0', the waveguide becomes fully enclosed and is no longer a rHMSIW but reverts to an enclosed SIW but with dimensions b_{eff}/a_{HM} . Effectively this is a square waveguide if b_{eff}/a_{HM} , and the mode will change to a full $TE_{1,0}$ with the cut-off frequency set by a_{HM}, being square the propagation mode could switch between horizontal and vertical as both waveguide dimensions are equal. This mode is not

investigated in detail, but is discussed at several points. Radiation loss is also a factor, the larger D_w/a_{HM} is the more exposed dielectric is presented and the more energy is available to interact with, but also the greater the loss of energy due to radiation. The cut-off frequency for leaky wave energy is considered in relation to the operating band, as this will impact at what frequencies antennas and filters may be formed. A number of simulations investigating D_w/a_{HM} and b_{eff}/a_{HM} are undertaken and discussed in subsequent sections. A summary of key parameters and values for rHMSIW is shown in Table 5.1.

Description	**Parameter**	**Initial Calculation**	**5880 Values**	**6010 Values**
Waveguide Width (half mode)	a_{HM}	Dielectric Thickness	3.175 mm	1.91 mm
Effective Waveguide Width	a_{eff}	$=2*a_{HM}$	6.35 mm	3.82 mm
Effective Waveguide Height	b_{eff}	$= a_{HM}$ (for a/b=2)	3.175 mm	1.91 mm
Via Diameter	D	Design choice	0.5 mm	1.0 mm
Pitch of Vias (in wall)	P_v	Design choice	1.0 mm	2.0 mm
Via wall Pitch (Waveguide height)	W	$W = b_{eff} + D^2/(0.95*P_v)$	3.4 mm	2.4 mm
Top Dielectric width	D_w	$(D_w / a_{HM}) * a_{HM}$	Varied	Varied
Top copper width	C_w	$\sim \lambda g/4$	2.3 mm	3.1 mm
Top Copper Edge	C_e	Fabrication limit	~0.5 mm	~0.5 mm
Start Frequency	f_s	Design choice	18.0 GHz	12.0 GHz
End Frequency	f_e	Design choice	26.0 GHz	18.0 GHz
Centre Frequency	f_{ce}	$=(f_s+f_e)/2$	22.0 GHz	15.0 GHz

Table 5.1 Summary of key parameters and values for rHMSIW

5.2 Waveguide Modes

Half-mode SIWs were introduced by Professor Ke Wu's group in 2006 [7], highlighting that with reduced size compared to a full SIW, lower attenuation was also achieved. By removing one of the via walls and half of the top copper surface, in the dominant (or fundamental mode) an equivalence to a magnetic wall is created at the centre symmetrical line (in direction of propagation). Research on the propagation properties of HMSIW [8] showed that they were a viable means of high frequency propagation for above 40 GHz. The fundamental mode for rectangular waveguides, and for full SIWs (as previously mentioned) is $TE_{1,0}$, its equivalence in HMSIW structures is termed $TE_{½,0}$. To demonstrate the modes being considered, a plot from the HFSS cell simulations are shown in Fig. 5.6.

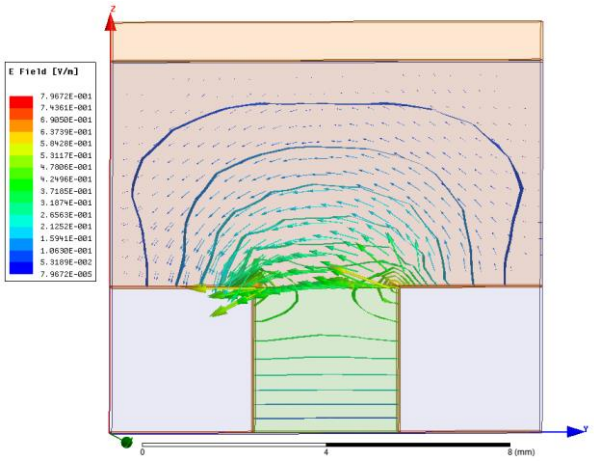

Fundamental Mode $TE_{½,0}$

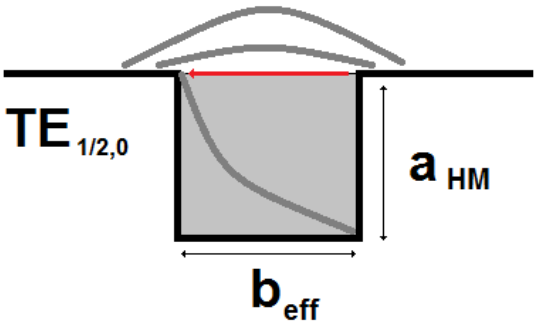

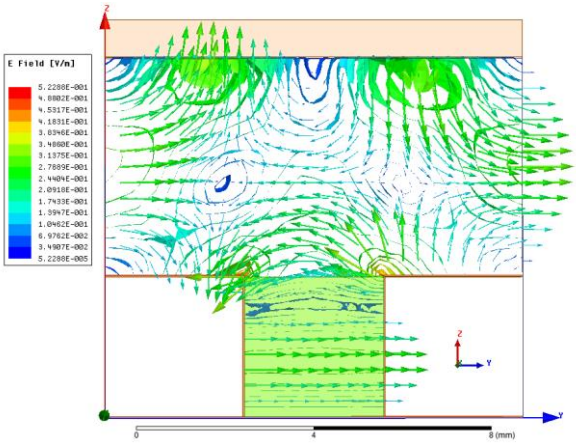

$TE_{3/2,0}$ (3x $TE_{½,0}$)

Next highest propagation mode

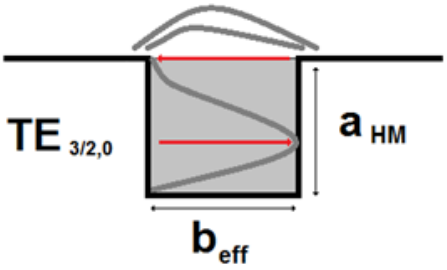

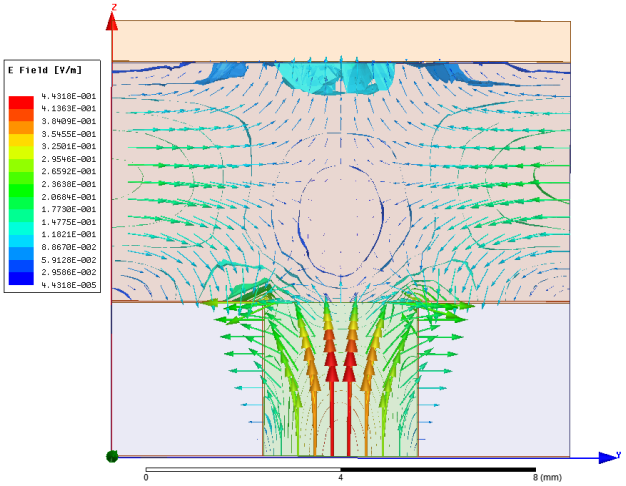

$TE_{1/2,1}$

propagation mode

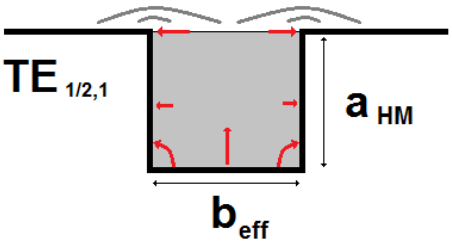

Fig. 5.6 rHMSIW propagation modes.

5.2.1 Cut off frequencies

From established microwave theory for standard rectangular waveguides, the $TE_{m,n}$ mode cut-off frequency is defined as:

$$fc_{m,n} = \frac{1}{2\pi\sqrt{\mu_0\mu_r\varepsilon_0\varepsilon_r}}\sqrt{\left(\frac{m\pi}{a}\right)^2 + \left(\frac{n\pi}{b}\right)^2} \qquad \text{[see section 2.2] (Eq.5.1)}$$

Where the fundamental mode is defined when *m=1* and *n=0*, giving:

$$fc_{1,0} = \frac{1}{2a\sqrt{\mu_0\mu_r\varepsilon_0\varepsilon_r}} \qquad \text{(Eq.5.2)}$$

but for the half-mode variant this simplifies to:

$$fc_{1/2,0} = \frac{c}{4a_{eff}\sqrt{\varepsilon_r}} \qquad \text{(Eq.5.3)}$$

Where a_{eff} is the effective width of the waveguide.

For the *m=1*,*n=1* mode:

$$fc_{1,1} = \frac{1}{2\pi\sqrt{\mu_0\mu_r\varepsilon_0\varepsilon_r}}\sqrt{\left(\frac{\pi}{a}\right)^2 + \left(\frac{\pi}{b}\right)^2} = \frac{1}{2\pi\sqrt{\mu_0\mu_r\varepsilon_0\varepsilon_r}}\sqrt{\left(\frac{\pi}{a}\right)^2 + \left(\frac{\pi}{a}\right)^2 \times \left(\frac{a}{b}\right)^2} = \frac{1}{2a\sqrt{\mu_0\mu_r\varepsilon_0\varepsilon_r}}\sqrt{1 + \left(\frac{a}{b}\right)^2}$$

Then by substitution:

$fc_{1,1} = fc_{1,0}\sqrt{1 + \left(\frac{a}{b}\right)^2}$, for half-mode equates to $fc_{1/2,1} = fc_{1/2,0}\sqrt{1 + \left(\frac{a}{b}\right)^2}$ (Eq.5.4)

Finally for *m=3*,*n=0*, this gives:

$fc_{3,0} = \frac{1}{2\pi\sqrt{\mu_0\mu_r\varepsilon_0\varepsilon_r}}\sqrt{\left(\frac{3\pi}{a}\right)^2} = 3 \times fc_{1,0}$ for Half-Mode equates to $fc_{3/2,0} = 3 \times fc_{1/2,0}$ (Eq.5.5)

Using the leaky wave radiation cut of frequency formulae derivation from Chapter 2,

$$\beta = \sqrt{(k)^2 - (k_c)^2} \qquad \text{(Eq.5.6)}$$

Where *k* is the wave number and k_0 is the free-space wave number,
and $k = k_0\sqrt{\varepsilon_r}$, and $k_0 = \frac{\omega}{c} = \frac{2\pi f}{c}$.

For $TE_{1,0}$ main waveguide mode, $k_c = \left(\frac{\pi}{a}\right)^2$, substituting into above gives:

$\beta = \sqrt{(k_0\sqrt{\varepsilon_r})^2 - \left(\frac{\pi}{2a}\right)^2}$ which then gives: $\beta^2 = \varepsilon_r k_0^2 - \left(\frac{\pi}{a}\right)^2$ (Eq.5.7)

At leaky wave cut-off frequency $\beta = k_0$ [9], and for leaky wave radiation to occur $\beta < k_0$, otherwise all radiation is along the longitudinal propagation direction. With β along longitudinal (z) axis and a leaking wave k_x perpendicular in the waveguide width direction, then the resultant wave k_0 will be the resultant of the two. $k_0^2 = k_x^2 + \beta^2$, and at point of leaky wave cut-off k_x will equal zero.

Giving, $k_0^2 = \varepsilon_r k_0^2 - \left(\frac{\pi}{a}\right)^2$ and rearranging produces $(\varepsilon_r - 1)k_0^2 = \left(\frac{\pi}{a}\right)^2$

Then $k_0 = \frac{\pi}{a} \times \frac{1}{\sqrt{\varepsilon_r - 1}}$ using $k_0 = \frac{2\pi f}{c}$ finally $f = \frac{c}{2a\sqrt{\varepsilon_r - 1}}$

But a is the effective waveguide width and $a_{eff} = 2 \times a_{HM}$ which leads to:

$$f_{cl} = \frac{c}{4a_{HM}\sqrt{\varepsilon_r - 1}} \quad \text{(Eq.5.8)}$$

As mentioned previously two main high frequency laminates are investigated, these materials are now considered with regard to the cut-off frequencies relating to the dielectric thicknesses and the different dielectric constants. The first is a relatively low dielectric constant material and the other is ~5 times greater.

5880 Material

RT/duroid® 5880 is a glass microfiber reinforced PTFE composite designed for stripline and microstrip circuit applications. The laminate has glass reinforcing microfibers are randomly oriented to maximize the benefits of fibre reinforcement in the direction required for the end application. The dielectric constant of $\varepsilon_r = 2.2$ is uniform from and constant over a wide frequency range. Its low dissipation factor (Tan δ=0.0009) aids in frequency use to the Ku-band and above.

From the range of dielectric thicknesses available, the values considered are: 0.254 mm, 0.381 mm, 0.508 mm, 0.787 mm, 1.575 mm, 3.175 mm. The various cut-off frequencies are shown in Table 5.2, where a_{eff} is equal to the dielectric thickness, a_{eff} / b_{eff} fixed at 1. *h* is the dielectric thickness *fc* is the $TE_{1/2,0}$ waveguide cut-off (multiples also shown), *fcl* is the leaky waveguide cut-off, and when the dielectric gap is reduced to zero, and the waveguide the reverts to a square waveguide of a_{eff}, which is 2 f_c.

h (mm)	fc (GHz)	fcl (GHz)	3*fc (GHz)	fc for D_w/a_{HM} =0 (GHz)
0.254	198.9	269.4	596.8	397.9
0.381	132.6	179.6	397.9	265.2
0.508	99.5	134.7	298.4	198.9
0.787	64.2	86.9	192.6	128.4
1.575	32.1	43.4	96.2	64.2
3.175	**15.9**	**21.5**	**47.7**	**31.8**

Table. 5.2. Cut-Off frequencies for 5880 dielectric thicknesses

With the K band running between 18 and 26 GHz, a laminate thickness giving an *fc* below the start frequency is required, in addition the *2fc* value needs to be above the end frequency to cover the entire band. The cut-off values are more easily viewed when the values are plotted, as in Fig. 5.7.

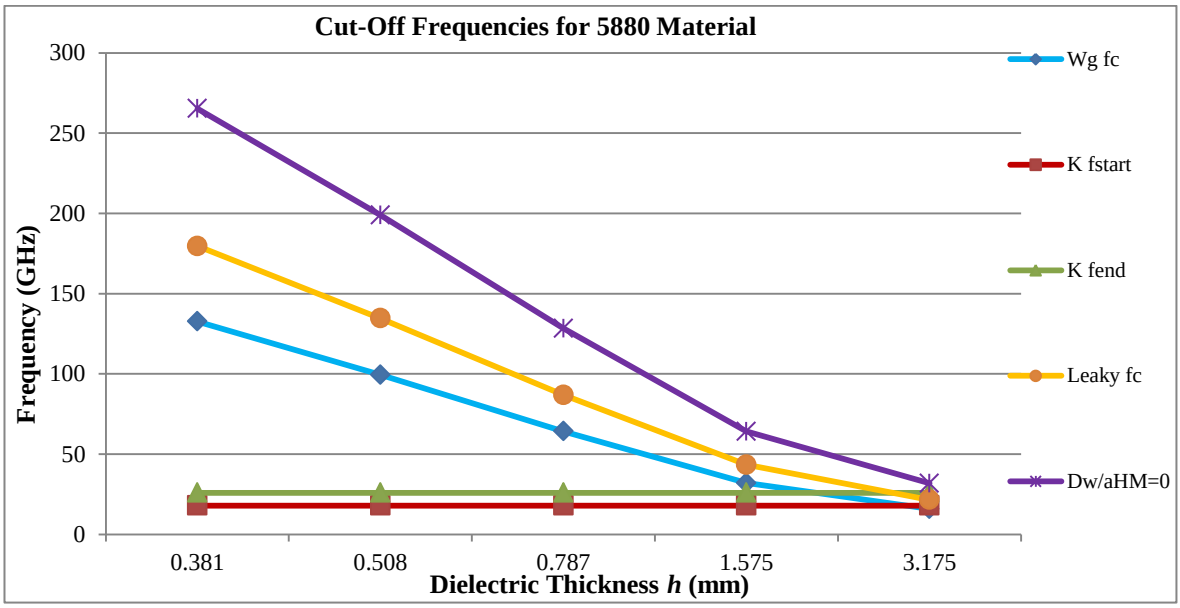

Fig. 5.7 Cut-Off frequencies for 5880 dielectric thicknesses

Hence the dielectric thickness of 3.175 mm gives a cut-off frequency for base mode below the start of the K band (18 GHz), however the leaky cut-off frequency (21.5 GHz) falls within the centre of the frequency band. Meaning that there will be a restriction for forming leaky wave antennas below *fcl* and forming waveguide filters above this frequency.

6010 Material

RT/duroid® 6010LM microwave laminate is a ceramic-PTFE composite designed for electronic and microwave circuit applications requiring a high dielectric constant (10.2), ease of fabrication and stability in use; tight dielectric constant and thickness control, low moisture absorption, and good thermal mechanical stability. Dissipation factor of 0.0023, meaning it is ~2.5 times lossier than the 5880 material. However the higher dielectric constant, allows dimension scaling and the resultant planar constructions to be larger by a factor of $\sqrt{\varepsilon_{6010}}/\sqrt{\varepsilon_{5880}} \approx 2.2$

h (mm)	fc (GHz)	fcl (GHz)	3*fc (GHz)	fc for D_w/a_{HM} =0 (GHz)
0.127	184.8	194.6	554.3	369.6
0.254	92.4	97.3	277.2	184.8
0.635	37.0	38.9	110.9	73.9
1.270	18.5	19.5	55.4	37.0
1.900	**12.4**	**13.0**	**37.1**	**24.7**
2.500	9.4	9.9	28.2	18.8

Table. 5.3 Cut-Off frequencies for 6010 dielectric thicknesses

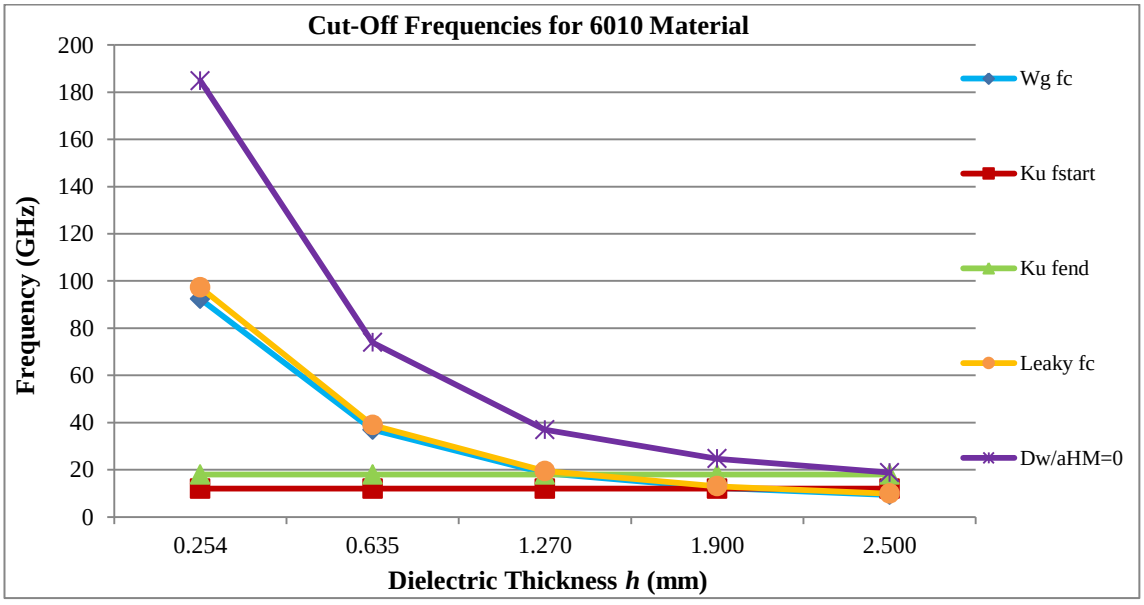

Fig. 5.8 Cut-Off frequencies for 6010 dielectric thicknesses

For 6010 material with ε_r=10.2, the dielectric thickness of 1.9 mm gives a cut-off frequency for base mode below the start of the Ku band, plus the leaky cut-off frequency is of a similar value, also below the start of the Ku band.

In summary, the 5880 material with dielectric thickness 3.175 mm is more suitable for the higher frequency band, and offers the possibility of forming leaky wave structures below ~21 GHz and filters above it. Whilst the 6010 material perhaps is more suitable for developing filters as the waveguide cut-off and leaky wave cut-offs are approximately equal for the 1.9mm thick laminate.

The rotated half-mode substrate integrated waveguide (rHMSIW) structure, will now be investigated for these two materials.

5.2.2 5880 Material rHMSIW

Simulations were run initially for variations of the rHMSIW using the 5880 dielectric. In general all simulations were run using 'real' values for dimensions and included conduction, dielectric and radiation losses. Certain simulations were run with solid walls and lossless properties for comparison and specific simplification.

Reference simulations for 5880 rHMSIW sections with dielectric thickness of 3.175 mm are shown in Fig 5.9 and Fig. 5.11. one with a single row via wall the other with a double row via wall. The S-parameters for both structures (Fig. 5.10 and 5.12) show low insertion loss for S_{11} (<-20dB) and low transmission loss of S_{21} (>-3dB). Both are consistent across the frequency band of interest.

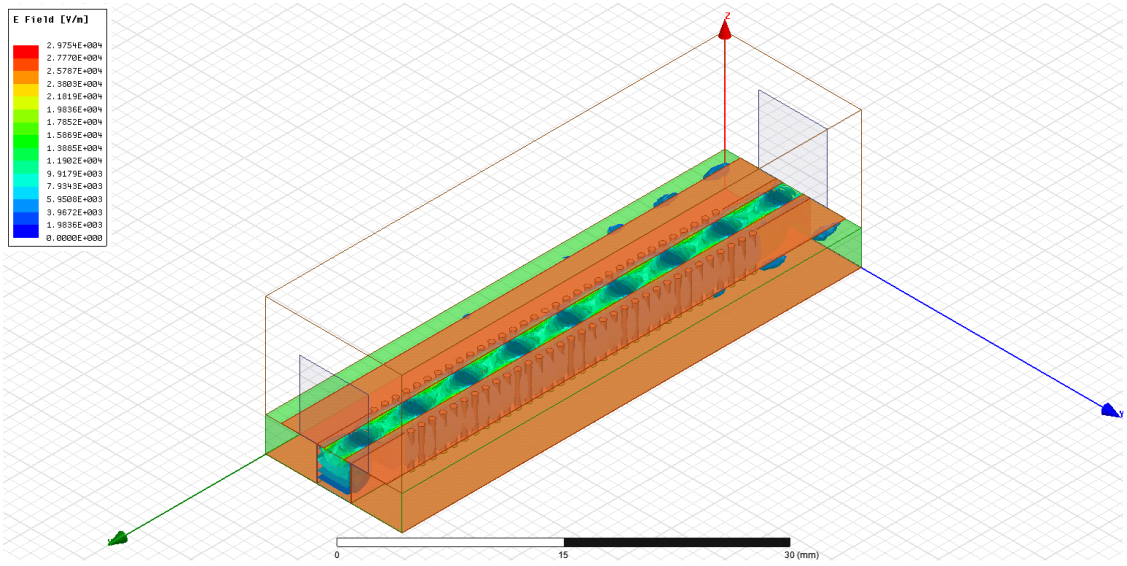

Fig. 5.9 5880 rHMSIW waveguide section, showing electric field in dielectric at 26 GHz, single row via wall

The designs include copper thicknesses for 1oz copper (35µm), and an *a/b* ratio equal to 2, hence $b_{eff} = a_{HM} = 3.175\ mm$. With via walls formed by 0.5 mm diameter vias on a 1 mm pitch, the via

wall pitch is given by $b_{eff} + \frac{D^2}{0.95 \times P_v}$, which is therefore 3.44 mm. With the minimum copper edge of ~0.5 mm, we have a value for D_w/a_{HM} = *0.6, TL = 5 mm, Wg_L = 33 mm,* b/a_{HM} = *1,* C_w = *3.2 mm.*

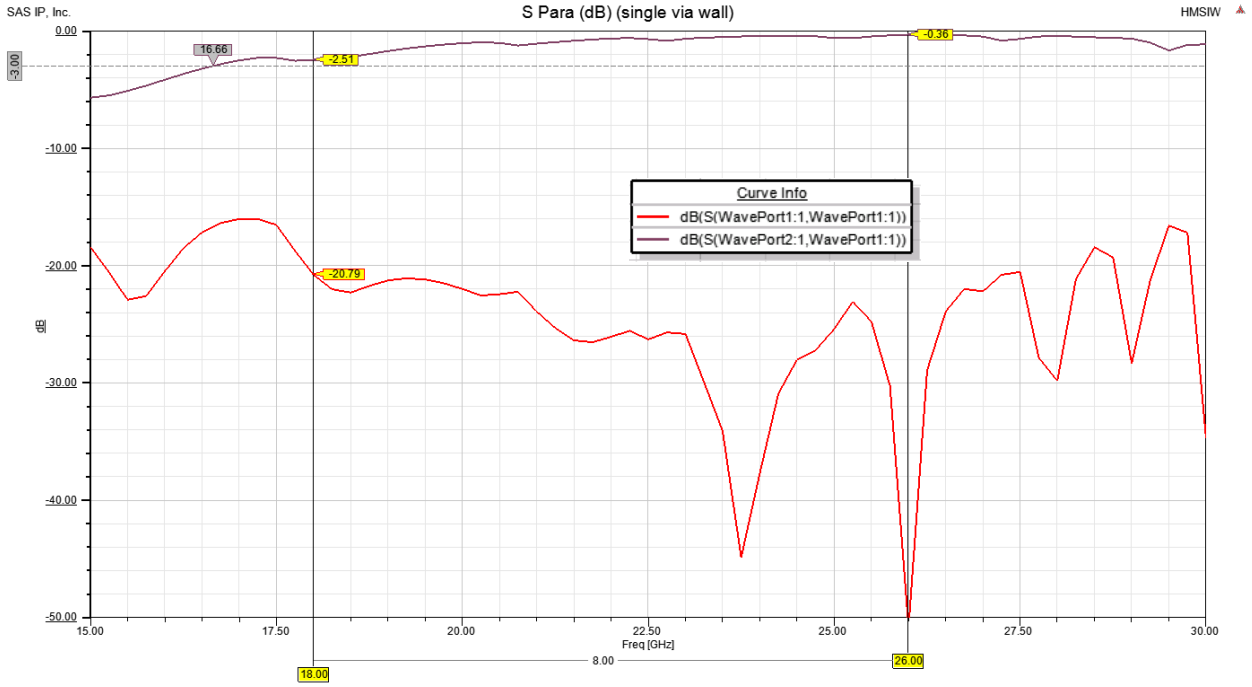

Fig. 5.10 S-parameters for 5880 rHMSIW waveguide section, single row via wall

The theoretical cut-off frequency is ~16 GHz, however the through loss and insertion loss from Fig 5.10 would indicate that the cut-off is lower than this as the usual sudden change close to cut-off is not seen. The fundamental mode also extends beyond 30 GHz, so interestingly from these S-parameters no direct cut-off between 15 and 30 GHz is observable.

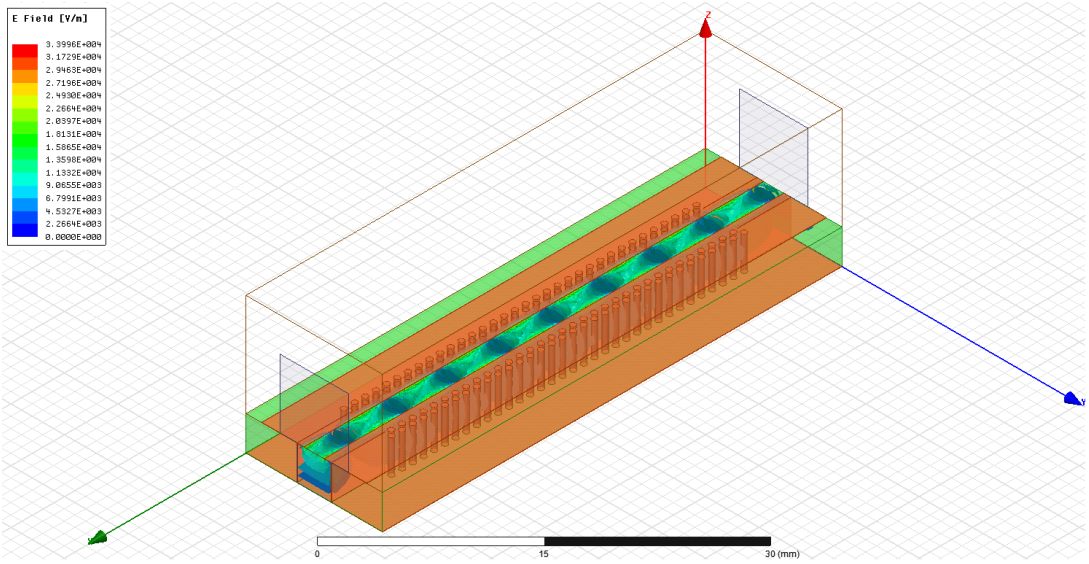

Fig. 5.11 5880 rHMSIW waveguide section, showing electric field in dielectric at 26 GHz, double row via wall

The S-parameter frequency span for the double via 5880 section is extended, and now the fundamental mode cut-off and next higher mode cut-off may be seen. The extra row of vias does not significantly alter the performance of the waveguide as the via pitch was chosen to minimize any leakage radiation. The 3 dB bandwidth of the waveguide is shown at ~14 GHz, with a central lower loss region. The cut-off modes would be estimated at just over 10 GHz and just over 30 GHz, which matches the f_c and $3f_c$ range derived earlier.

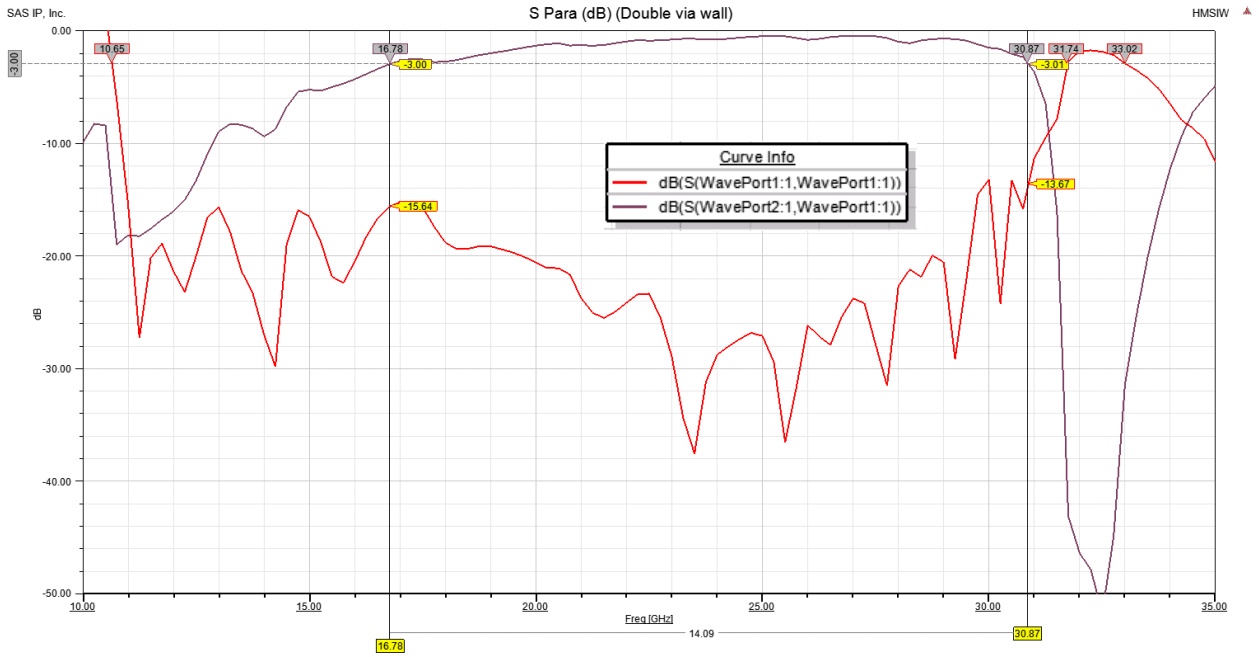

Fig. 5.12 S-parameters for 5880 rHMSIW waveguide section, double row via wall

A more accurate means of determining the cut-off frequency is to plot the propagation constant for all of the modes simulated as in Fig. 5.14. This is a complex plot, showing the real and imaginary parts of the gamma (the propagation constant), and 10 modes were simulated. The modes in question are mode 1 (the fundamental $TE_{1/2,0}$) and mode 8 ($TE_{3/2,0}$), which can only be determined by viewing the port mode field plots and the wave plots at the relevant frequencies.

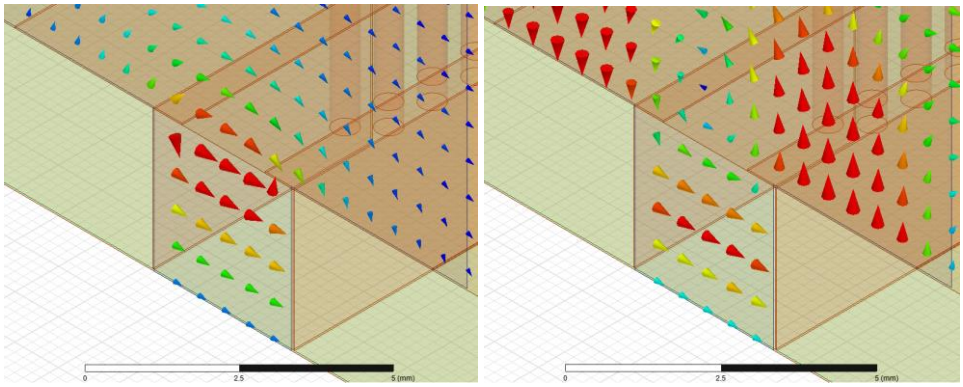

Fig. 5.13 Wave port electric field vector plot for 5880 rHMSIW waveguide section, double row via wall mode 1 $TE_{1/2,0}$ (left) and mode 8 $TE_{3/2,0}$ (right)

Fig 5.13 shows the two modes discussed, for the $TE_{1/2,0}$ the field maximum is on the dielectric surface and for the $TE_{3/2,0}$ there is a maximum in the centre, similar to the mode plots shown previously. The real part of the gamma plot represents the attenuation constant α, and this is a small value when compare to the imaginary part, β the phase constant, hence the α plots overlap close to the horizontal axis. Adjacent gamma mode plots in HFSS appear to 'swap' values, this is a simulation error, as the β curves should be continuous.

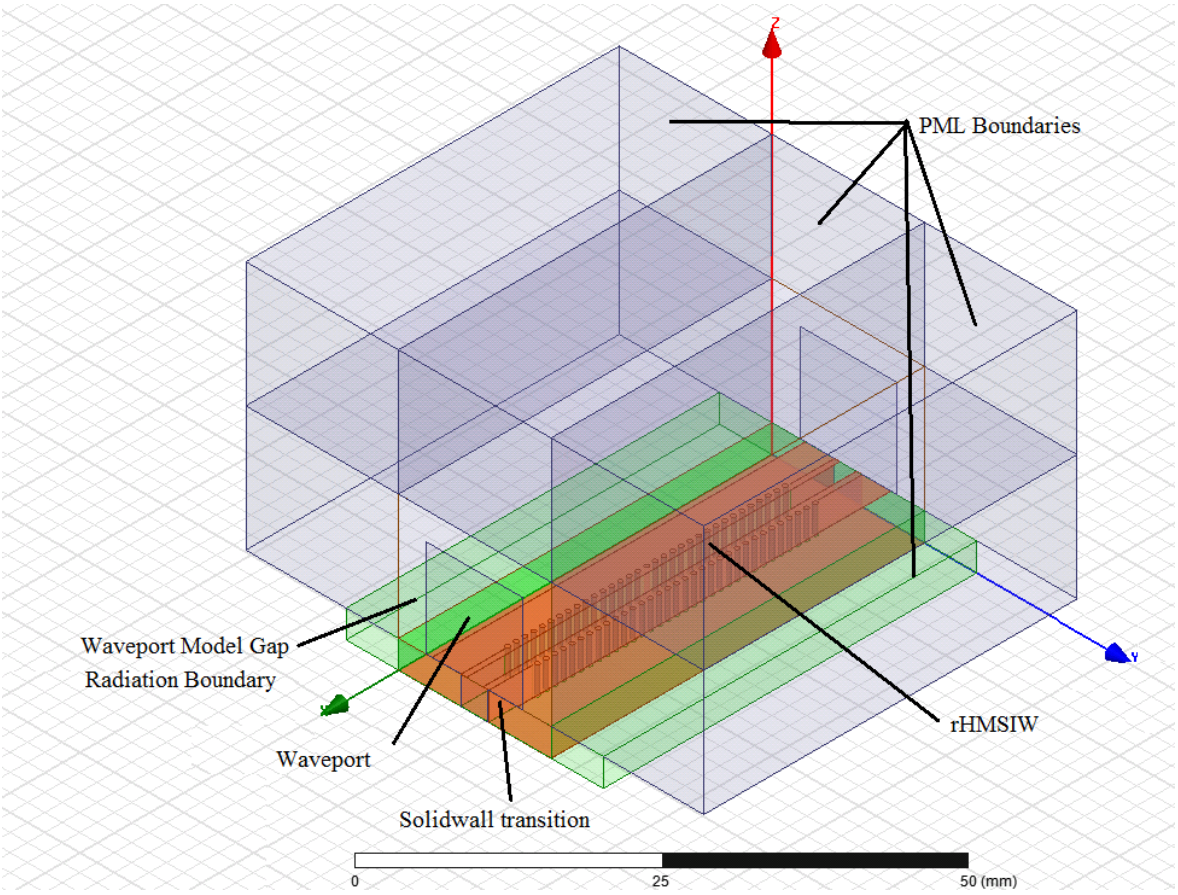

Fig. 5.14 HFSS Simulation set-up.

A short comment of the HFSS model setup is worth noting, as shown in Fig. 5.14. The simulation model is surrounded by PML boundaries, with radiation boundaries at the waveport ends, at which there is a gap between the waveport edge and the model edge. This waveport gap was optimised to achieve constant results and maintained for all simulations, but is a scaling factor linked to the width of the waveguide being simulated. Care needs to be given to setting up the model elements to ensure correct simulations are achieved [10, 11].

The $TE_{1/2,0}$ cut-off from the simulations for both of these sections is ~10.7 GHz, and from Fig 5.12 for $TE_{3/2,0}$ is ~30 GHz, and as mentioned the theoretical cut-off was ~14.0 GHz. The cut-off

frequency (when $\beta = 0$) for the wave-guide section has been effected by the solid wall transition in the simulation, which is used to stabilise the wave prior to entering the rHMSIW section. Even though the S-parameters de-embedded the solid wall section, the cut-off is offset, the mode bandwidth of ~3*fc* is still valid. A different method was required to determine the exact cut-off of the waveguide without the solid wall transition and investigate the effect on varying the amount of dielectric exposed and the height of the waveguide.

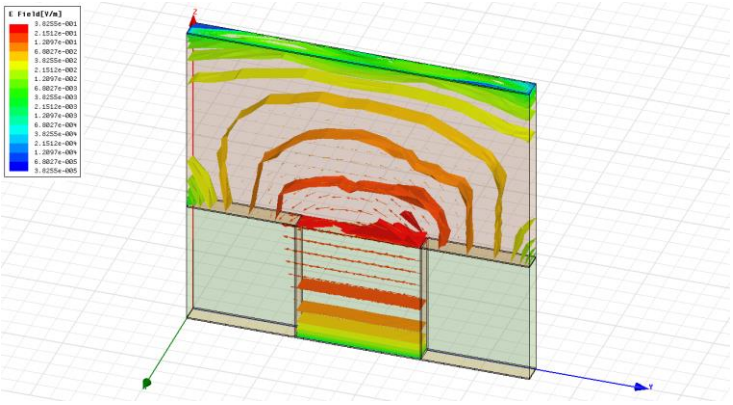

Fig. 5.15 Eigen solver cell for 5880 solid wall model

The Eigen solver cells (Fig. 5.15) utilised a master and slave impedance boundary and calculated the phase difference φ between them, with the physical distance between the two boundaries (i.e. the cells depth) defined as the via pitch P_v, then the phase difference will be given by: $\varphi = \beta P_v$ (in radians). By solving the Eigen solutions for φ it is possible to obtain the cut-off frequency of the resonant mode for the structure, i.e. when $\varphi=0$.

Running these Eigenvalue solvers for a range of rHMSIW cell structures, for both solid and via walls, with different dielectric thicknesses, and varying D_w/a_{HM} and b_{eff}/a_{HM} comparative plots were generated. Each data point is calculated from the cut-off frequency determined from the propagation constant where $\beta = 0$. Also displayed is the *fc* value predicted from the theoretical equation Eq.5.3 for each relevant dielectric thickness.

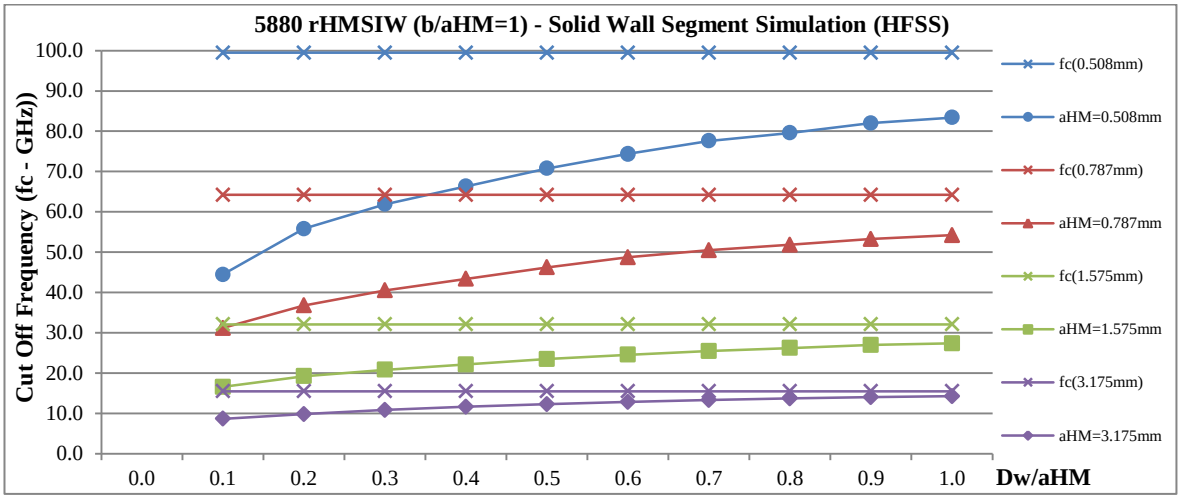

Fig. 5.16 5880 rHMSIW Solid Wall Cut-Off Frequencies for variations in D_w/a_{HM}

The plot in Fig. 5.16 compares different dielectric thicknesses with variations of D_w/a_{HM}, the comparison is interesting as when the waveguide is fully open (D_w/a_{HM}) , the cut-off frequency (when $\beta = 0$) simulated is close but not equal to the general theoretical value (Eq. 5.3) for that particular dielectric thickness. As D_w/a_{HM} decreases the cut-off frequency moves further away from the theoretical value. This is due to the capacitive effect of the waveguide central slot and as the dielectric gap reduces, the capacitive effect increases. There are fringing fields at the edges of the slot, and the effects of these are not included in the approximate theoretical equation Eq.5.3 which is for lossless waveguide, as the gap reduces, these fringing fields will have a more significant impact on the cut-off frequency, hence the divergence from the approximate answer.

For the 3.175 mm dielectric thickness, a comparison was made between using solid walls and via walls, whilst also varying b_{eff}/a_{HM} . As expected small variance between the simulations was noted as the results for the solid wall simulations were a simplification. The data was plotted for both D_w/a_{HM} against f_c, *and* b_{eff}/a_{HM} against f_c these plots are shown in Figs. 5.18 and 5.19. The difference between these ratios is summarised in Fig. 5.17 to demonstrate where a waveguide is open or nearly closed, and if the waveguide is narrow or maintains the *a/b=1* ratio.

$D_w/a_{HM}=0$	$D_w/a_{HM}=0.1$	$D_w/a_{HM}=0.1$
$b_{eff}/a_{HM}=1$	$b_{eff}/a_{HM}=1$	$b_{eff}/a_{HM}=0.1$

Fig.5.17 rHMSIW example configurations

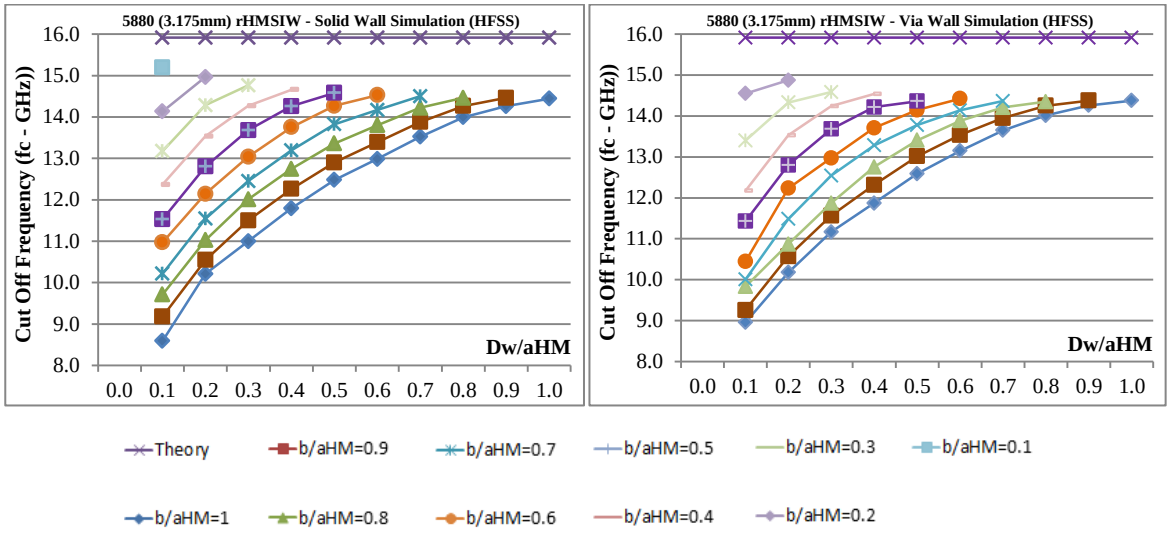

Fig. 5.18 5880 3.175mm rHMSIW solid wall and via wall
cut-off Frequencies for variations in D_w/a_{HM} and b/a_{HM}

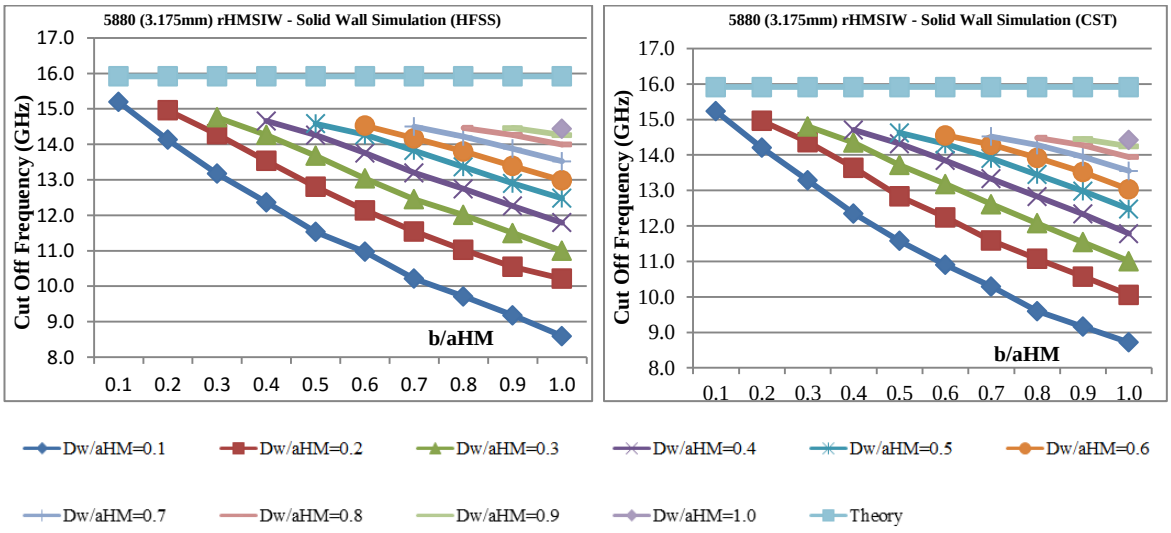

Fig. 5.19 5880 3.175mm rHMSIW solid wall cut-off frequencies
For HFSS and CST, with variations in b/a_{HM} and D_w/a_{HM} .

For the normalisation ratios, it is not possible to have $D_w/a_{HM} > b_{eff}/a_{HM}$, and for the via model for $b/a_{HM}=0.1$ is not possible as the vias overlap. The plots of b_{eff}/a_{HM} against f_c show a more linear relationship than D_w/a_{HM} against f_c.

The plots of Fig. 5.18 and 5.19 were all run both in CST and HFSS full EM wave simulators, however not all of the plots are shown, as there was a good correlation between the two solvers. A summary comparison is shown in Fig. 5.20 where the values are compared for cut-off frequencies against D_w/b_{eff} . The minor differences were believed to be caused by discrepancies between the solver solutions. A comparison between commercial EM solvers is available for further consideration if required [10].

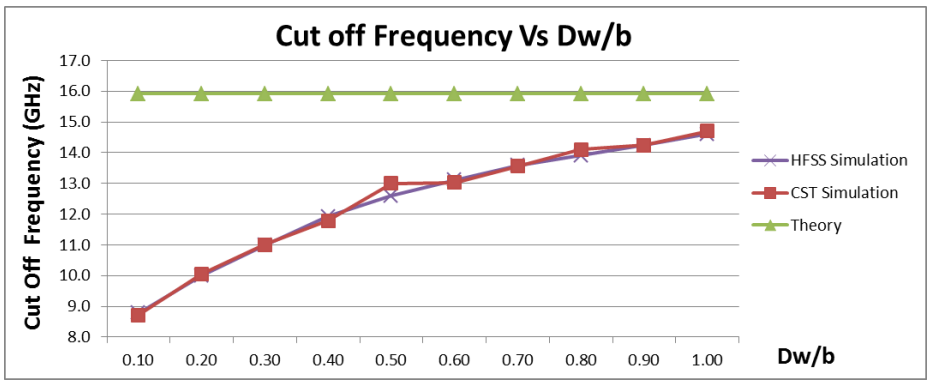

Fig. 5.20 Comparison between EM solvers

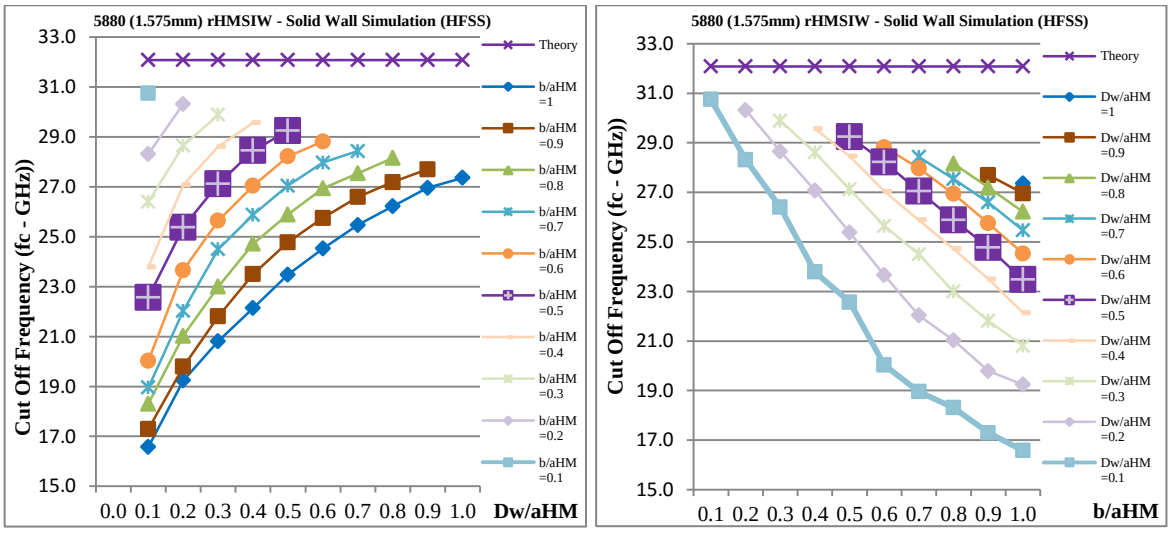

Fig. 5.21. 5880 1.575 mm rHMSIW solid wall cut-off frequencies for variations in D_w/a_{HM} and b/a_{HM}

The characterisation was repeated for dielectric thickness of 1.575 mm, with similar results obtained, but at a higher frequency due to the thinner dielectric. In a later section the cut-off frequencies for the solid wall 3.175 mm variant will be analysed further, along with the equivalent model for the 6010 material.

5.2.3 6010 Material rHMSIW

A similar process was undertaken for the 6010 material, focussing primarily on the 1.9 mm thick laminate, a full waveguide section simulation is shown then a solid wall segment simulation plot for variations of D_w/a_{HM} for a range of dielectric thicknesses. Then a variation plot for D_w/a_{HM} and b_{eff}/a_{HM} for the 1.9 mm and 2.5 mm dielectric thicknesses is shown.

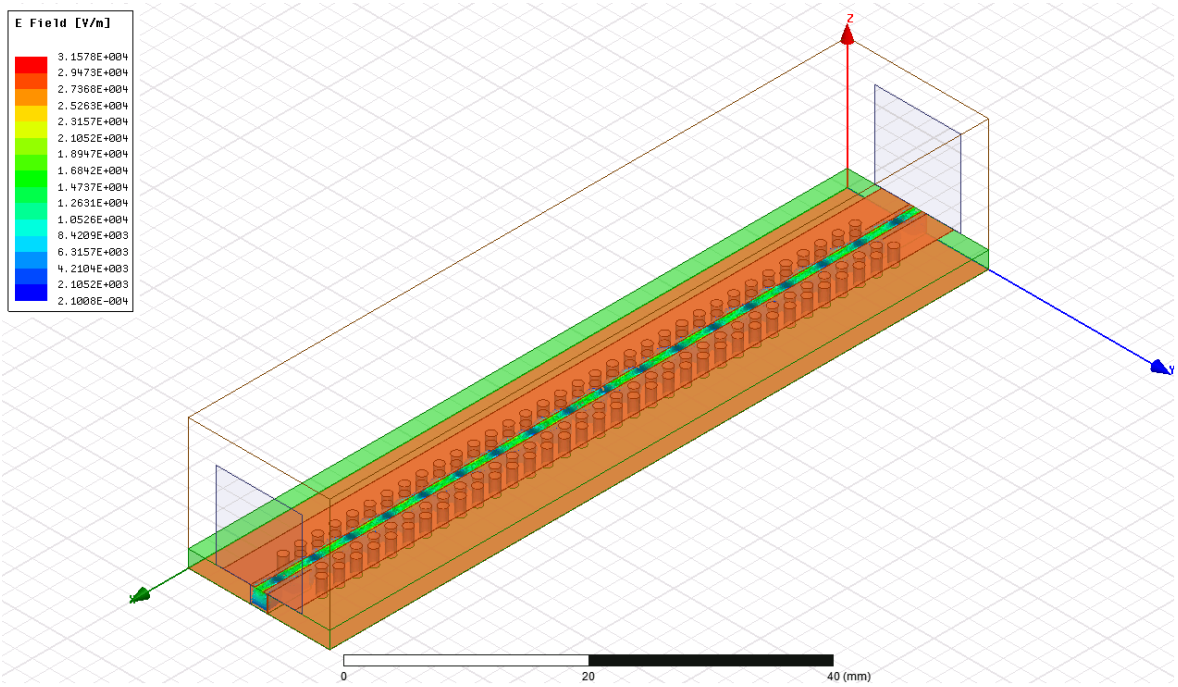

Fig. 5.22 6010 rHMSIW waveguide section, showing electric field in dielectric at 18 GHz, for 1.9 mm laminate.

D_w/a_{HM} = 0.5, TL=5mm, Wg_L=66mm, b/a_{HM}=1, C_w=3.2mm, P_v=2mm

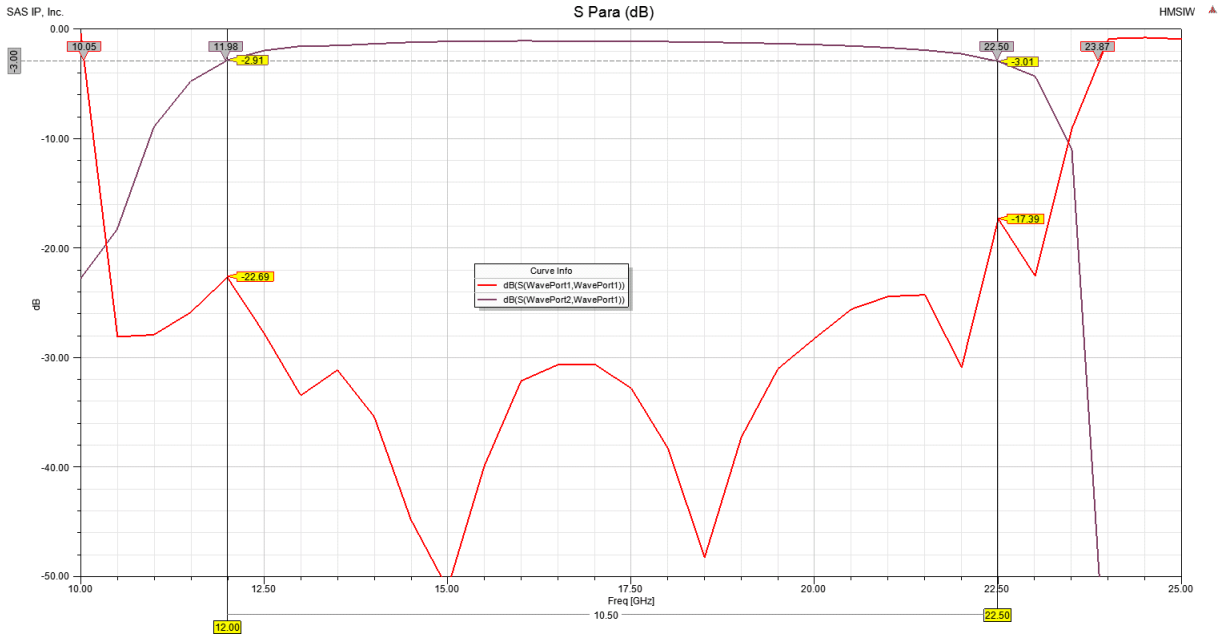

Fig. 5.23 S-Parameters for 6010 rHMSIW waveguide section defined in Fig. 5.22

The S-parameters show a low through loss across the majority of the Ku band, with an increase of loss at 12 GHz caused by the cut-off frequency. From the solid wall model for 1.9 mm, with D_w/a_{HM}=0.5 *mm* an f_c~11.2 *GHz* is indicated, and the approximate theoretical cut-off is 12.3 GHz. It is difficult to determine the exact cut-off frequency from the S_{11} and S_{21} plots, a more accurate answer is again required. One definition of cut-off sometimes used is when $S_{11} = S_{21}$, which can be seen in Fig. 5.23 occurs at ~ 10.2 GHz and 23.5 GHz but at different levels -20 dB and -10 dB respectively. The difference in loss is due to the increased

radiation losses at the fundamental mode cut-off frequency. The 3dB bandwidth is 10.5 GHz (from 12 to 22.5 GHz), this for the same number of vias as for the 5880 section, but with the larger via pitch equates to a larger waveguide section of 66 mm.

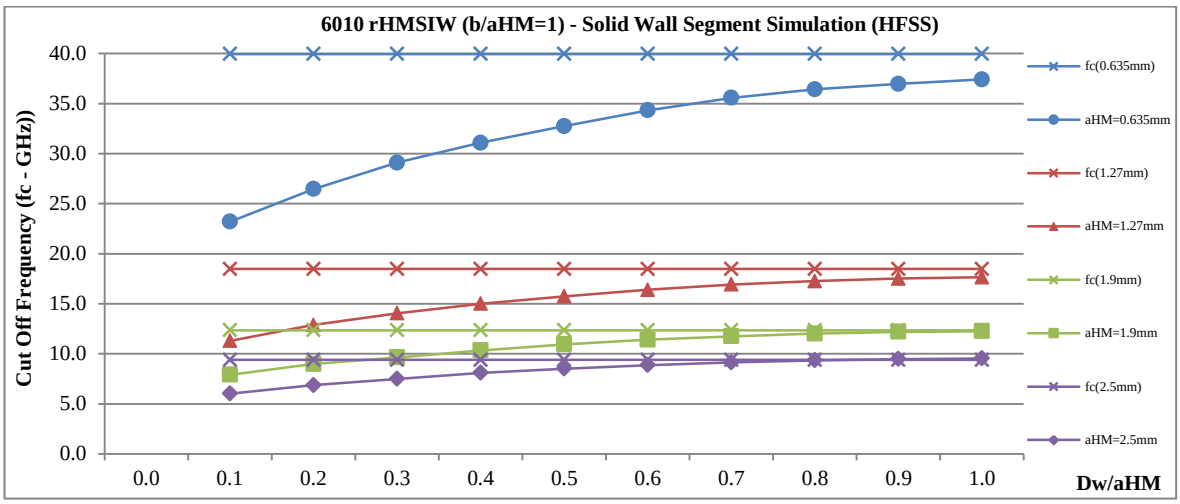

Fig. 5.24 6010 rHMSIW solid wall cut-off Frequencies for variations in D_w/a_{HM}

The cut-off frequency values for the 6010 material (Fig.5.24) repeated the trend of the 5880 material, with the difference between theoretical and simulated cut-off frequency increasing as D_w/a_{HM} decreases. Closer agreement was however, noted when D_w/a_{HM} increases and equals 1. When, b/a_{HM} plots were run, it became apparent that *fc* is exceeding the predicted value. With the higher dielectric constant, the 6010 material holds more of the wave field within the dielectric, reducing the fringing fields. The thinner the laminates the less dielectric material and, hence, the decrease in volume to contain the fields, the fringing element again causes divergence from the theoretical (or approximate) value. For the normalisation ratios, it is not possible to have $D_w/a_{HM} > b_{eff}/a_{HM}$.

Fig. 5.25 show plots of the 6010 material with solid walls for laminate thicknesses of 1.9 mm and 2.5 mm. With the Ku band running from 12 to 18 GHz, and the cut-off frequencies for the 1.9 mm laminate being approximately 12.3 GHz there will be an associated loss at the start of the frequency band. However, the 1.9 mm is the best available matching choice to the frequency band, as the end frequency of 18 GHz is a limitation of the SMA connectors.

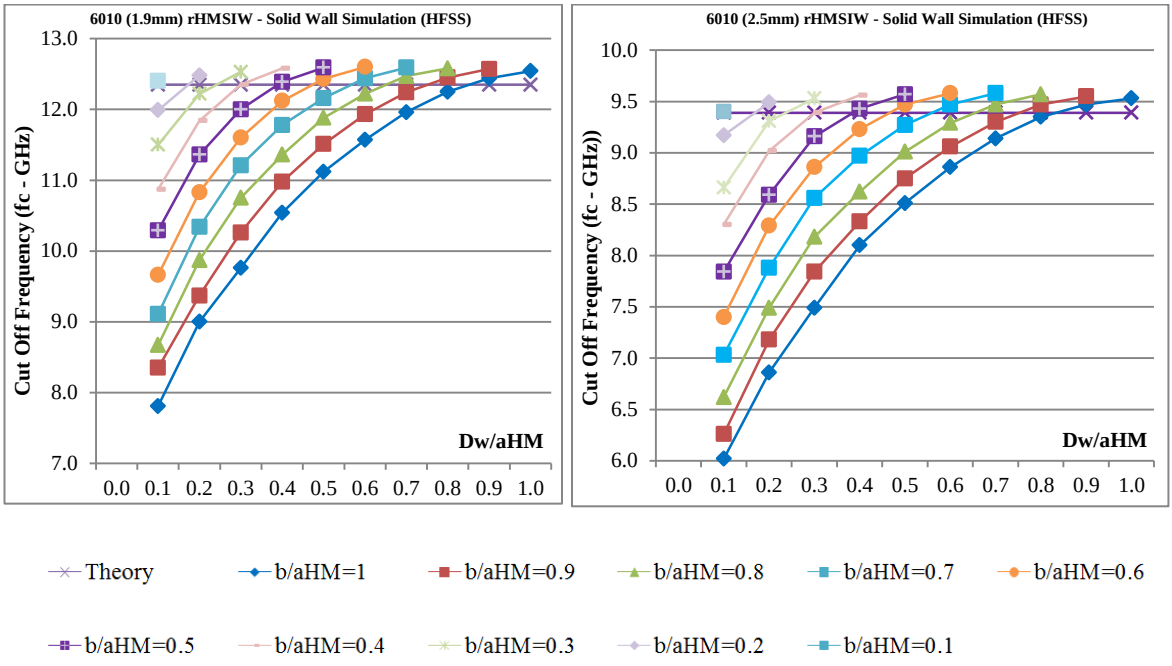

Fig. 5.25. 6010 rHMSIW solid wall cut-off frequencies
for variations in D_w/a_{HM} , dielectric thicknesses 1.9 mm and 2.5 mm

A number of simulations were run considering single and double row via walls, via pitch and diameter for the via wall, and optimizing the width of the copper (C_w). A reference waveguide section is shown in Fig. 5.22, there is a solid wall transition at the start and end of the waveguide to allow the correct waveguide mode to form prior to entering the rHMSIW via section.

5.3 Waveguide Characterisation

In section 2.2 equations are defined for calculating β, k_0 *and* k_c , these calculated values are plotted in Fig. 5.26 for the 3.175 mm dielectric 5880 material and 1.9 mm dielectric 6010 material. It can be seen that when $k_0=\beta$, defines the leaky wave cut-off, which is 21.5 GHz for 5880 and 13.0 GHz for 6010 material, these values are marked with the dashed line. k_c is constant as it is related to the waveguide width. k_0 is a linear scaling of the frequency. The value of β falls rapidly as it approaches the cut-off frequency, and the 6010 material starts at 12.3 GHz the closest value to cut-off possible to calculate. The guided wavelength is a function of β and will vary with frequency.

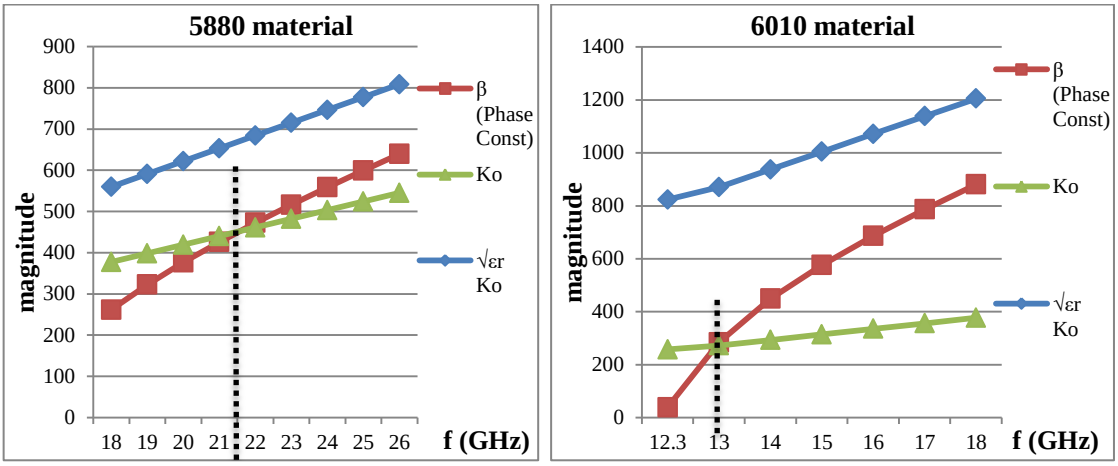

Fig. 5.26 Calculated waveguide characteristics.

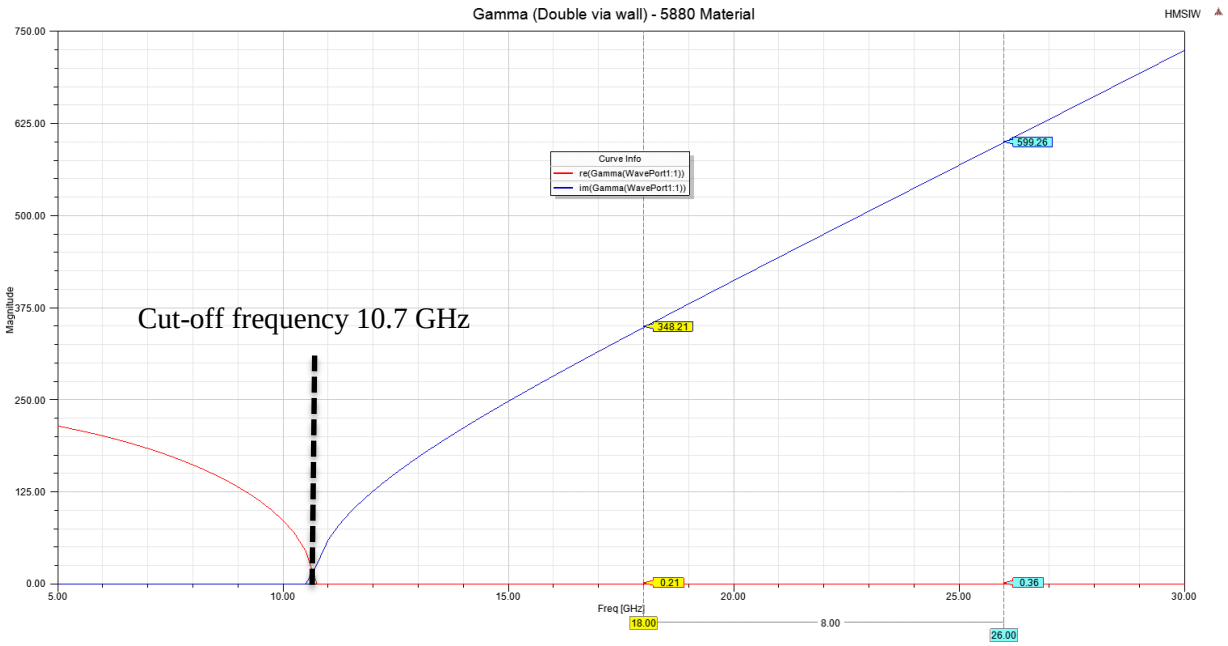

Fig. 5.27a. Simulated waveguide β characteristics 5880 material.

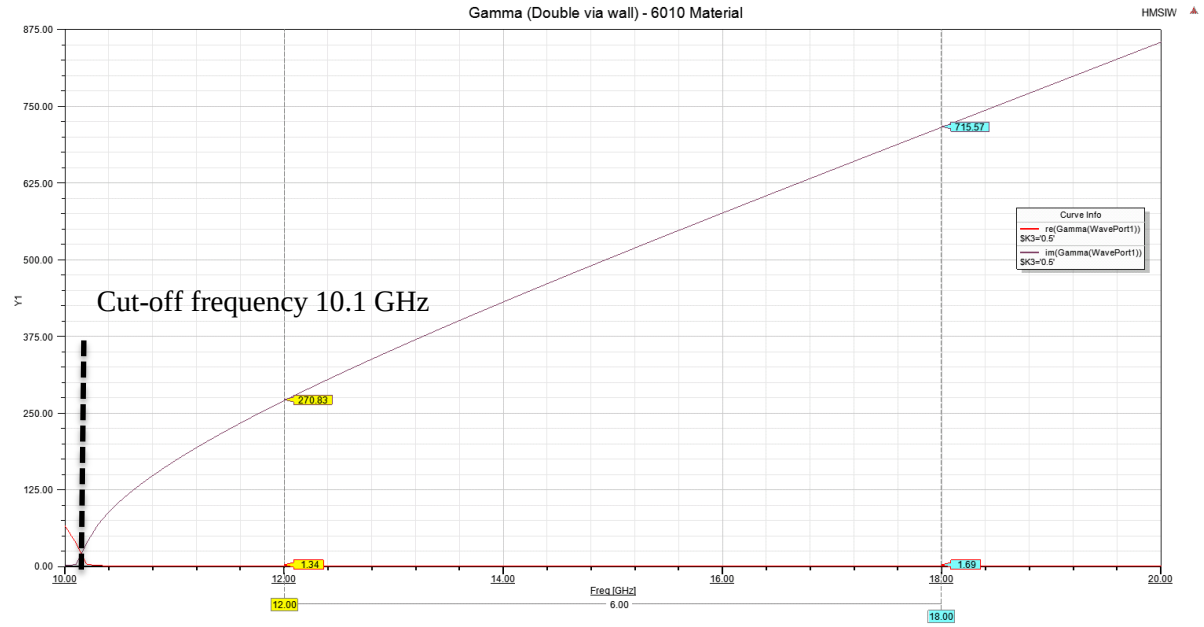

Fig. 5.27b. Simulated waveguide β characteristics 6010 material.

Fig. 5.28 shows the difference in wavelength between the guided wavelength ($\lambda_g=2\pi/\beta$) and the wavelength in the dielectric medium ($\lambda_m= v_m/f$). As the frequency increases the two wavelengths become equal, as the waveguide has a reduced effect on the wave. For the 6010 material, the guided wavelength rapidly increases as the frequency drops to the cut-off frequency as a consequence of β reducing.

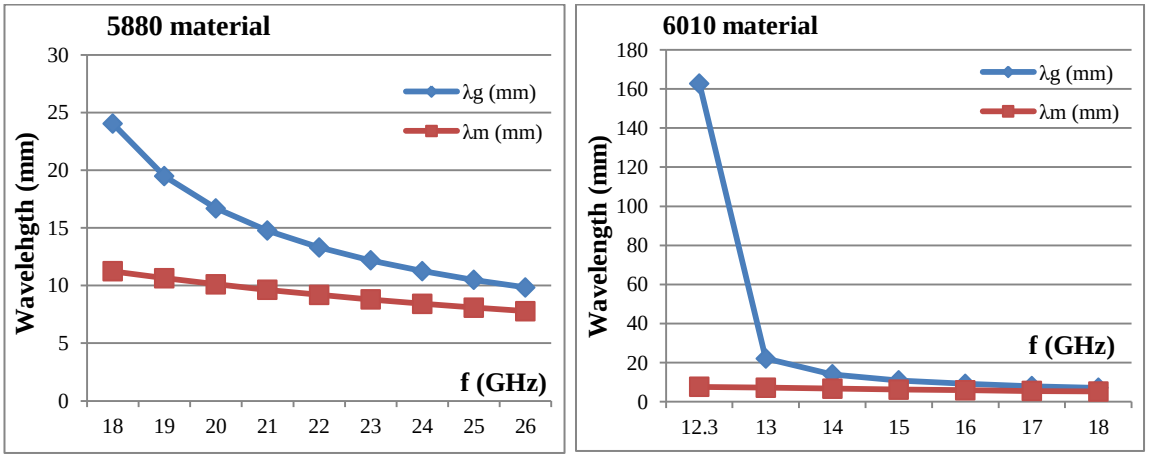

Fig. 5.28 Wavelengths in the dielectric material

It was perceived that a formula connecting the ratios b_{eff}/a_{HM} and D_w/a_{HM} to calculate the waveguide cut-off frequencies for the rHMSIW structure would be useful. The derived theoretical value is not sufficiently accurate for this model (Eq. 5.3). Thus considering the solid wall cut-off cells for the 3.175 mm 5880 material and the 1.9 mm 6010 material (Figs. 5.18 and 5.21). The b_{eff}/a_{HM} curves may be approximated by a logarithmic function of the form:

$$f_c = b_1 \times ln(D_w/a_{HM}) + c_1$$, where b_1 and c_1 are scaling constants (Eq.5.9)

By approximating all of the curves it is possible to obtain the range of coefficients for the b_{eff}/a_{HM} values, which were then in turn plotted in Fig. 5.29.

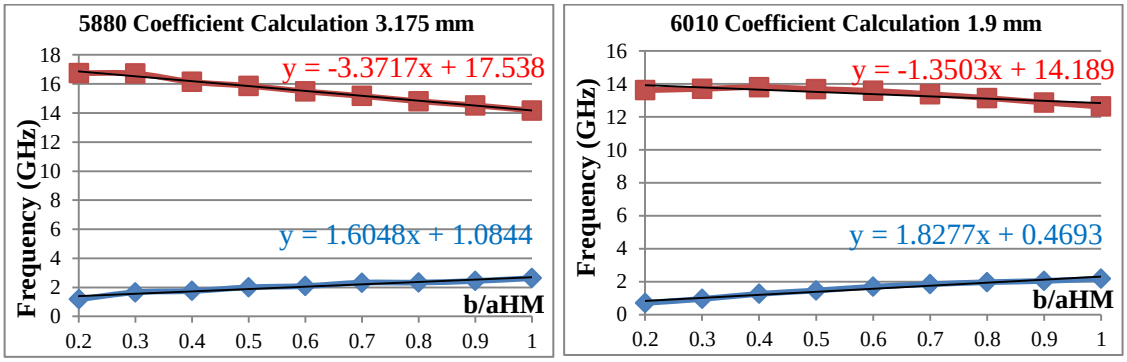

Fig. 5.29 Scaling coefficients for solid wall rHMSIW structures (red c_1, blue b_1)

These then enable the following equations to be derived:

$$f_{c\,(5880\_3.175mm)} = \left(0.1604 \times \frac{b_{eff}}{a_{HM}} + 1.0844\right) \times ln(D_w/a_{HM}) + \left(17.538 - 3.3717 \times \frac{b_{eff}}{a_{HM}}\right)$$

(Eq.5.10)

$$f_{c\,(6010\_1.9mm)} = \left(1.8277 \times \frac{b_{eff}}{a_{HM}} + 0.4693\right) \times ln(D_w/a_{HM}) + \left(14.189 - 1.3503 \times \frac{b_{eff}}{a_{HM}}\right)$$

(Eq.5.11)

However, main consideration is for when b_{eff}/a_{HM}=1, which reduces equations to:

$$f_{c\,(5880\_3.175mm)} = (2.6884) \times ln(D_w/a_{HM}) + (14.1663) \quad \text{(Eq.5.12)}$$

$$f_{c\,(6010\_1.9mm)} = (2.297) \times ln(D_w/a_{HM}) + (12.8387) \quad \text{(Eq.5.13)}$$

However for this special case of b_{eff}/a_{HM} = 1, a more accurate polynomial may be used, due to the larger number of data points. 3rd order polynomials valid only for b_{eff}/a_{HM} = 1 are:

$$f_{c(5880\_3.175mm)} = 2.0785(D_w/a_{HM})^3 - 9.1265(D_w/a_{HM})^2 + 14.151(D_w/a_{HM}) + 7.1677$$

(Eq.5.14)

$$f_{c(6010\_1.9mm)} = 2.7059(D_w/a_{HM})^3 - 10.256(D_w/a_{HM})^2 + 13.509(D_w/a_{HM}) + 6.599$$

(Eq.5.15)

Fig. 5.30 shows a plot of the simulated cut-off frequencies as shown in Fig. 5.18 for the 5880 material and Fig. 5.25 for the 6010 material when $b_{eff}/a_{HM} = 1$, along with the calculated values using the logarithmic approximation and the 3rd order polynomial.

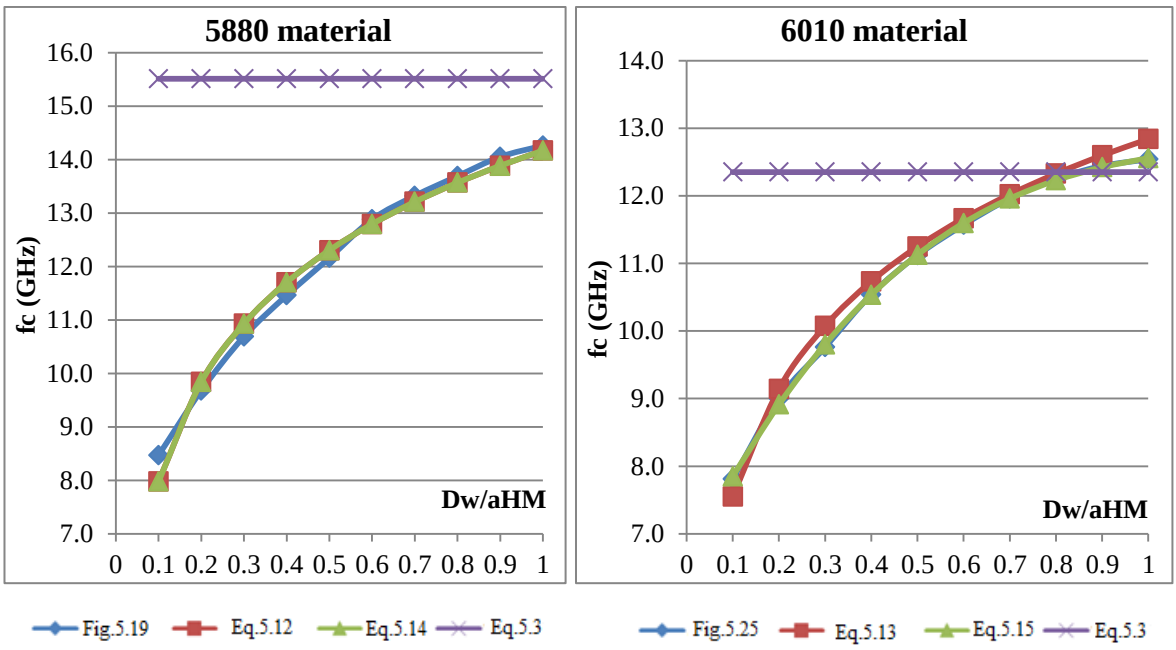

Fig.5.30 Cut-off frequency formulae comparison

For the rHMSIW the wave travels partly within the dielectric and partly within the air. The 5880 material has a relative permittivity of $\varepsilon_r=2.2$, and for the 6010 material $\varepsilon_r=10.2$. As the relative permittivity of air is equal to 1, a more effective value would be useful. An approximate value may be obtained by averaging the two, thus $\sim\varepsilon_{reff} = \frac{\varepsilon_r+1}{2}$. This works out as 1.6 for the 5880 material and 5.6 for the 6010 material. A more accurate relative permittivity may be calculated from $\varepsilon_{reff} = \left(\frac{\beta}{k_0}\right)^2$ which will vary with frequency. A comparison of these values is shown in Fig. 5.31. Note how the calculated tends to the approximate value at the end of the relative frequency bands.

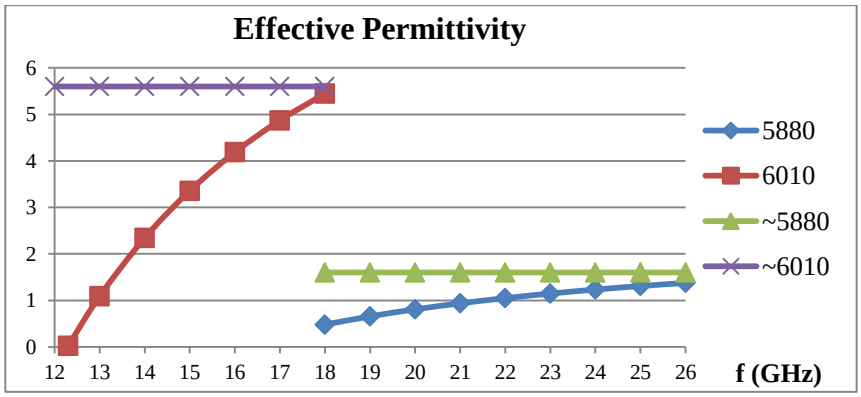

Fig. 5.31 effective permittivity for 5880 and 6010 materials
(calculated and approximate values shown)

5.4 Wave Impedance

Using solid wall models for simulation, the waveguide impedance was calculated from the port impedance (S_{11}) measured at the centre frequency of each band, as this was a solid wall model and symmetrical the impedance seen at the port is the same as within the waveguide itself. The main dielectric thicknesses of 3.175 mm was analysed and D_w/a_{HM} was varied as previously.

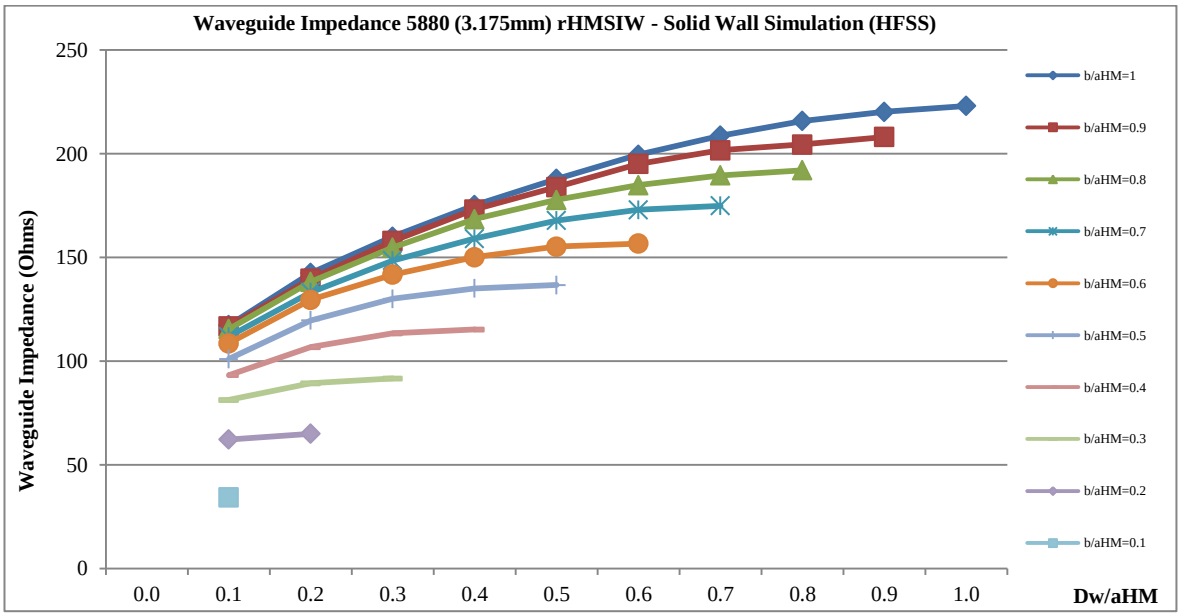

Fig. 5.32. 5880 3.175 mm rHMSIW waveguide impedance at 22 GHz (centre frequency) for variations in D_w/a_{HM}

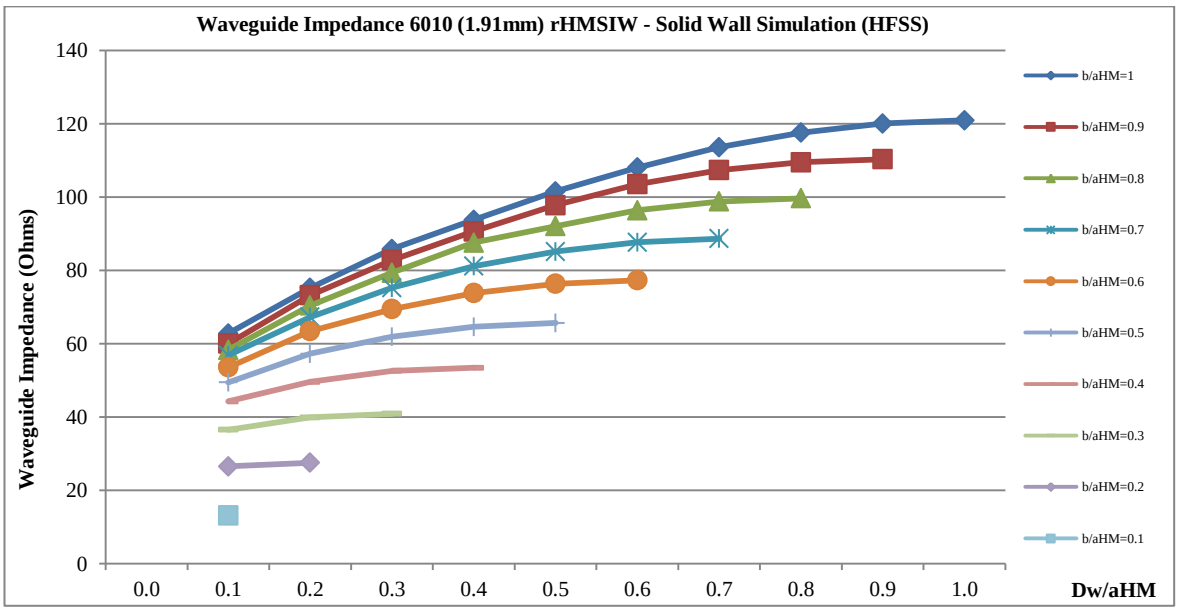

Fig. 5.33. 6010 1.9 mm rHMSIW waveguide impedance at 15 (centre frequency) GHz for variations in D_w/a_{HM}

Impedance varies due to capacitive coupling effect of top copper edges, and due to the volume of dielectric material within the waveguide. As $D_w/a_{HM} \rightarrow 0.1$ the dielectric gap narrows and the impedance reduces. Also, as $b_{eff}/a_{HM} \rightarrow 0.1$ the waveguide narrows, again leading to a reduction of waveguide impedance. The cross sectional area for the 5880 material 3.175 mm laminate with b_{eff}/a_{HM} =1 is ~10.1 mm^2 (equating to ~220 Ω), and for the 6010 material 1.9 mm laminate with b_{eff}/a_{HM} =1 is ~3.6 mm^2 (equating to ~120 Ω).

5.5 Waveguide Radiation Loss

To compare the radiation loss of the two materials, a short section of waveguide was modelled, (10 mm) with a range of via pitches. The dielectric material properties were modified so that the dielectric loss was set to zero, to offer a lossless material comparison. As per the SIW rules the via pitch and via diameter (V_p/D) was maintained at 2. Larger via pitches of 3 mm and 4 mm were considered, however due to the symmetry and dimensions of the waveguide structure they were not applicable.

The normalised power flow values were determined using the formula:

$$Rad_{loss} = 1 - [S_{11}]^2 - [S_{21}]^2 \qquad \text{(Eq.5.16)}$$

The S_{11} and S_{21} values were averaged across the frequency bands of interest, 12 to 18 GHz for the 6010 material and 18 to 26 GHz for the 5880 material.

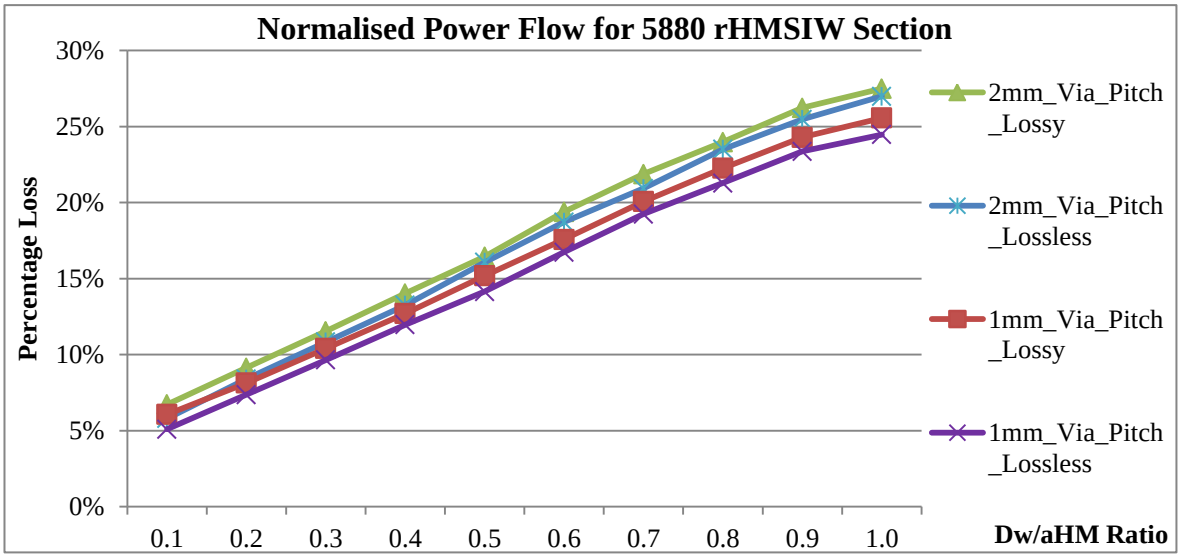

Fig. 5.34. 5880 rHMSIW normalised power flow for variations in D_w/a_{HM}

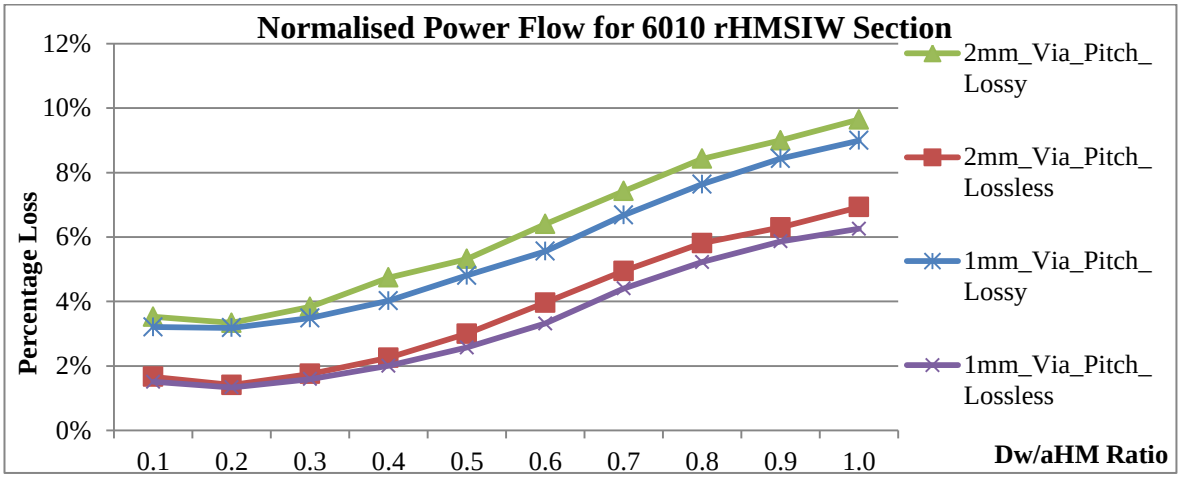

Fig. 5.35. 6010 rHMSIW normalised power flow for variations in D_w/a_{HM}

Interesting points arising from Fig. 5.34 and 5.35 are that it is fundamentally the structure that is responsible for the radiation loss. There is little difference for the 5880 energy loss, as the lossless and lossy variants, with the pitch variation are all relatively close. For D_w/a_{HM} equal to '1', when the waveguide is fully open, the rHMSIW has a radiation loss of ~25%, but as D_w/a_{HM} reduces the radiation loss also reduces to 5% when D_w/a_{HM} = 0.1. The relationship between radiation loss and D_w/a_{HM} can be seen as approximately linear.

The 6010 material, suffers less from radiation loss, due to the higher dielectric constant the field is contained more within the material. This is aided by the leaky wave cut-off *fcl* being below the band of interest. There is also a distinct difference between the lossy and lossless variants.

The width of the HMSIW may be calculated by simply reducing the standard SIW width calculation by half. It should be noted that a more accurate design should take into account the effect of the fringing fields will effect the waveguide width and alter the cut-off frequency. Losses in HMSIW are comparable to SIW, apart from a small frequency band just above cut-off, here the open side of the HMSIW behaves like a slot with uniform field distribution and radiation loss is significant. [8].

5.6 Transition Development

Previous sections have outlined that the simulations of rHMSIW waveguides showed usable performance for the purpose of energy transmission and interaction. The next stage required is to provide a means of injecting the energy into the waveguide structures. A number of transitions for SIW were discussed in chapter 2, the microstrip-to-SIW and CPW-to-SIW being the main two that

have been utilised. A number of different options were investigated and trialled for the rHMSIW, including: slot waveguide, RF probe (a version of CPW) and SMA microstrip. The main target was to produce a means of transition from a VNA that did not limit the performance of the waveguide itself.

5.6.1 Transition 5880 Material - Slotline

The Rogers material was chosen for the higher frequency band considered 18 to 26 GHz (K band). The simplest transition into the rHMSIW is using the standard slotline, which was the first transition analysed. The impedance match is defined by the slotline gap width and is, therefore, resonant. In addition there are fabrication tolerances that need to be considered.

One of the limitations was the standard SMA PCB connector has a top frequency limit of 16 GHz, due to its dielectric and structure. An alternative SMA PCB connector was sourced which used a CPW connection with a top limit of 26 GHz. This high frequency variant was utilised with some modification on the slot line transition shown in Fig 5.36.

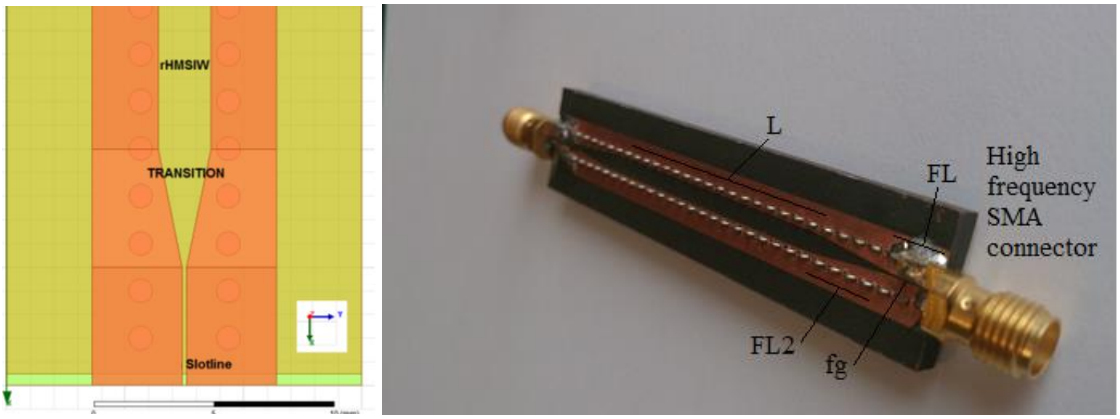

Fig. 5.36. 6010 rHMSIW slot line transition and test coupon

Test coupons using the Rogers RT5880 material were fabricated, using the following parameters: $D_w/a_{HM} = 0.7$, $b/a_{HM} = 1.0$, *b = 3.175mm, FL = 5mm, FL2 = 10mm,* P_v *= 1mm, D = 0.5mm, W = 3.44mm, Cw = 2.3mm, Ce = 0.48mm, (Cw+Ce=2.78mm).* There were two slotline feed gap widths, 0.1 and 0.2 mm. The prototypes were fabricated in-house, with limitations on the etching process and forming plated through holes. As a compromise, to form the via walls, a 0.5 mm metal wire was fed through the vias and soldered on the underside. This was not ideal, as irregularities were introduced, both within the via wall structure and onto the surface of the rHMSIW.

The summary of the test coupons were as follows:

1. W_{gL} (L) =64mm, f_g=0.2mm — Fabrication Problem
2. W_{gL} (L) =64mm, f_g=0.1mm — Fabrication Problem
3. W_{gL} (L) =65mm, f_g=0.2mm — Assembled and Measured
4. W_{gL} (L) =65mm, f_g=0.1mm — Assembled and Measured

The intention was to use the difference in lengths to extract the beta value by comparative measurement. Coupons 1 and 2 had fabrication problems caused by the etching process and from positional inaccuracy when aligning the photoplot, for the first attempt all four coupons were lost. The in-house etching tolerance is for a minimum gap of 0.2 mm, ideally 0.3 mm, therefore we were aware that we were pushing the limits of what could be achieved.

After the full EM wave HFSS simulation was completed, the structure was redrawn in CAD software (PADs PCB), then the variants Gerber plots were exported and collated in CAM software (Gerbtool) to produce the fabrication panel photoplots. The via holes were drilled prior to the etching process, after which the vias were assembled and the connectors added.

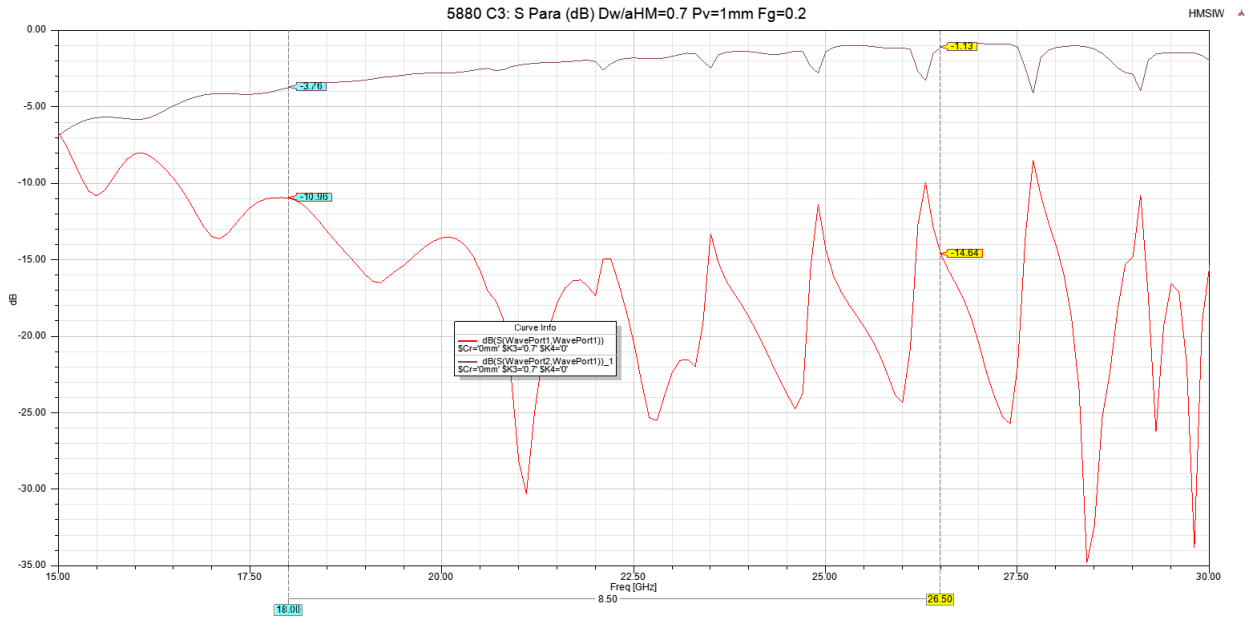

Fig. 5.37. 5880 test coupon 3 simulation.

The initial simulations for the complete test coupons were promising but were not ideal: the S_{21} is not linear and ~-4 dB at start of band improving towards the end of band, the S_{11} is below 10 dB across the complete band. Fig. 5.37 shows the simulated S-parameters, the peaks in the S_{11} (and associated S_{21} especially when insertion loss >-10 dB) indicate a mismatch in the transition causing

standing waves to resonate, the resonances will also increase radiation and hence overall loss. On the basis of the simulations the first prototypes were fabricated.

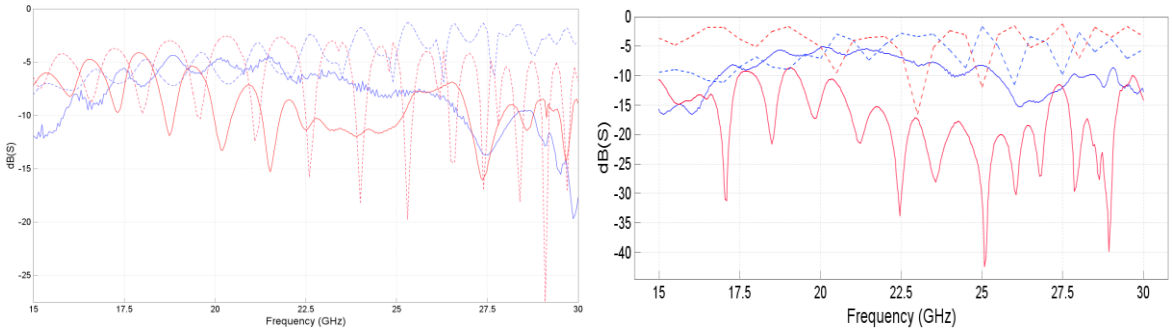

Fig. 5.38. 5880 test coupon 3 (left side) & 4 (right side), 50Ω normalized simulation and measured results.
(S_{11} red, S_{21} blue, solid measured, dashed simulated)

Fig. 5.38 shows the simulated and measured results for the 5880 test coupons. They are very poor, in part this is due to the fabrication process and creating the vias with wire. At the frequencies investigated in this material 1/10th of a wavelength is ~ 1 mm. However, a basic error was made, in that the simulations for the 5880 test coupons (Fig. 5.37) were not normalised to 50 Ω, an impedance mismatch causes the insertion loss to rise. The slotline is not a suitable transition as the PCB laminate is too thick to achieve a 50 Ω match with a gap that was possible to fabricate, Fig. 5.39 below shows that a gap of 0.01 mm is required to achieve the required impedance match. This was an error that should have been spotted prior to fabrication.

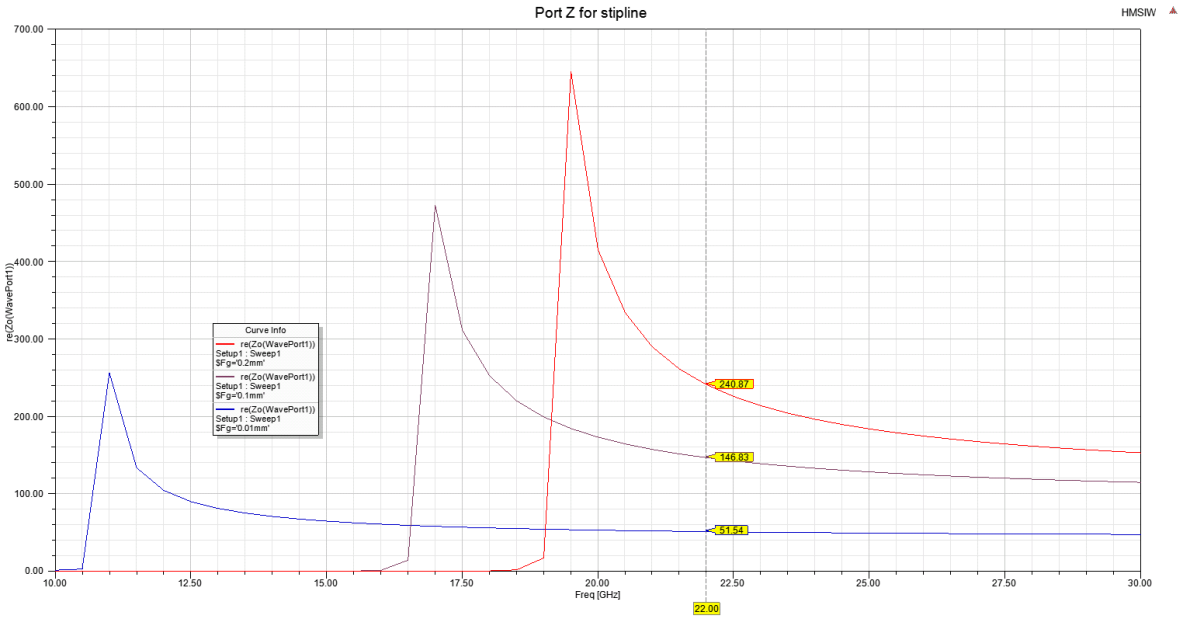

Fig. 5.39 Slotline Port Impedance for 3.175mm 5880 material

5.6.2 Transition 5880 Material – RF Probe

To overcome the matching limitation for the slotline-to-SMA issue, there was the option of using an RF probe on the VNA to measure the test coupon. This was not ideal due to the added complexity of using the probe station, however if a transition could be developed it would mean that a test coupon within the K band could be developed.

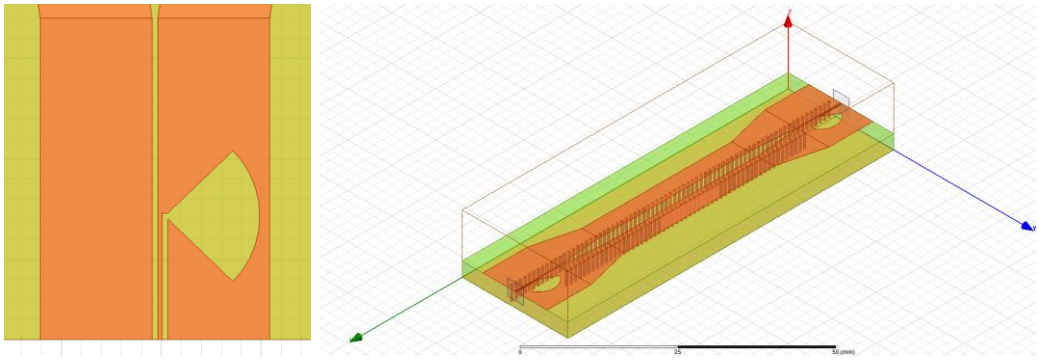

Fig. 5.40 6010 rHMSIW RF probe transition and test coupon structure

Utilising a known CPW-to-slotline transition [12], a 90° radial slotline stub is added to improve the transisition bandwidth. The dimensions of the CPW are fixed by the RF probe contacts which reqired a central conductor width of 0.1 mm with a gap of 0.15 mm to match the 0.2 mm spacing for the RF probes.

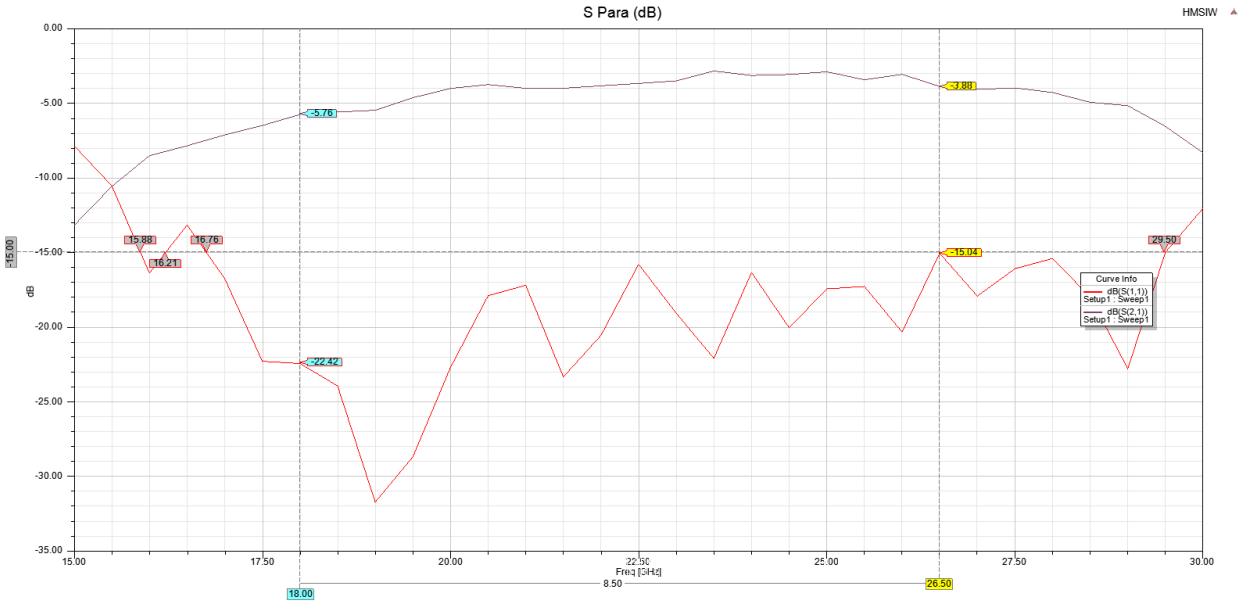

Fig. 5.41 6010 rHMSIW RF probe full test coupon simulation

The full EM simulation shown above (Fig. 5.41) uses real material values and thus includes loss. It shows a reasonable insertion loss (S_{11}) across the K band, of less than 15 dB, however the through loss (S_{21}) is nearly 6 dB at the start of the band and only rises to 3 dB at the end. Although an

improvement in overall performance and stability, the loss across the entire band was too great, the target was to achieve an S_{21} greater than -3 dB across the entire band.

5.6.3 Transition 6010 Material

The problem for the required transition is that the electric field needed to be rotated from the more common vertical to the horizontal direction to feed into the rHMSIW. CPW and slotline transitions, with horizontal electric field orientation at the feed, as discussed did not demonstrate sufficient bandwidth, plus due to the dielectric thickness very thin slots were required to match 50 Ω impedance. By changing to a higher dielectric material (the 6010) the frequency would be reduced hence the frequency of interest was switched to the Ku band (12 to 18 GHz).

Initially a solid wall lossless model was used to develop a solution which incorporated a microstrip input, feeding into a SSIW with a further transition into the rHMSIW. The microstrip feed has a vertical electric field between the strip and ground plane, with the majority of energy travelling within the dielectric. The next stage transitions the wave energy into the Slot SIW, where again most of the energy travels within the dielectric. The SSIW supports a $TE_{1/2,0}$ fundamental mode, similar to that of an HMSIW, near the slot the electric field begins to rotate from vertical to horizontal, with some energy moving into the air region above the dielectric [13]. A longer gradual transition then reduces the width of the SSIW until it forms a symmetrical waveguide where the electric field is horizontal with a maximum on the dielectric surface, the rHMSIW.

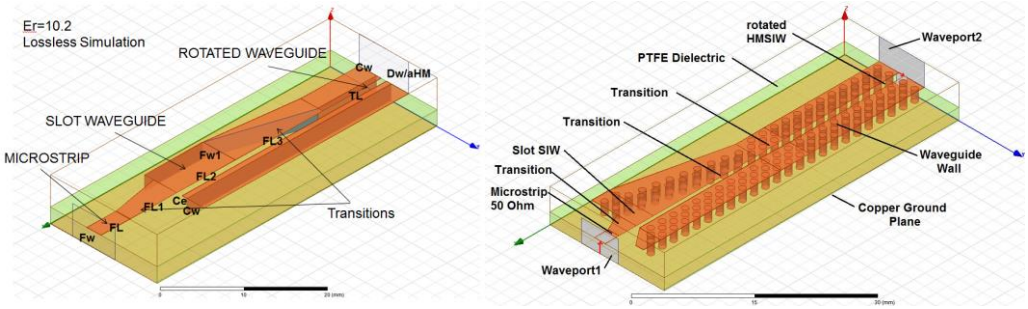

Fig 5.42. Overview of transition with SIW elements.
(red lines indicate electric field orientation at waveports).

A second transition was added between the SSIW and rHMSIW to allow for different D_w/a_{HM} ratios. The SSIW (see Fig. 5.43 for top view) has a cut off frequency fixed by the length F_{w1}, the rHMSIW fundamental mode is fixed by 'a_{HM}' (the dielectric thickness) and the microstrip is matched to 50 Ω.

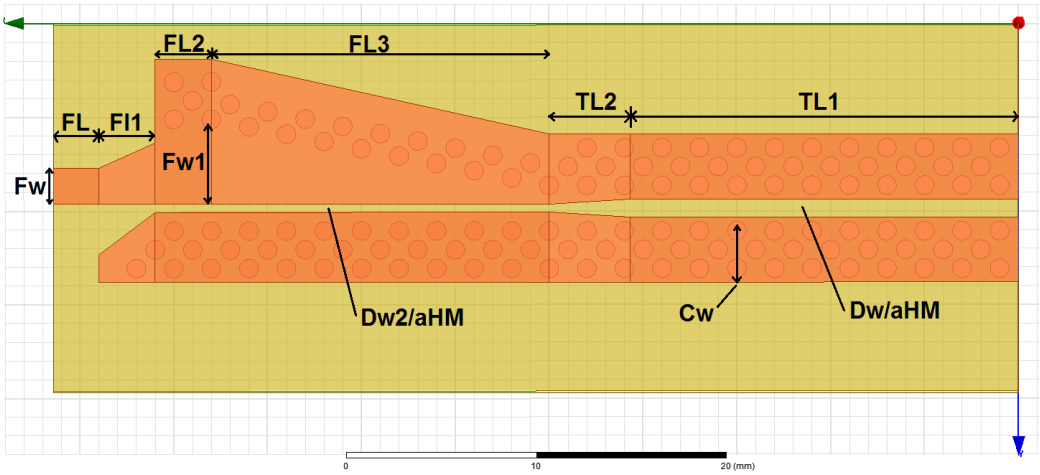

Fig. 5.43. Top view of transition showing design parameters.

The rHMSIW transition was optimized with Ansoft HFSS for a number of parameters (Table 5.4); initially as a simplified lossless model, then subsequently using real material values and full SIW elements.

Parameter	**Transition Parameters**		
	Description	***Value***	***Comment***
Fw	Microstrip Feed Width	2.0 mm	for 50Ω
FL	Microstrip Feed Length	2.4 mm	optimized
FL1	Microstrip to SSIW length	3.4 mm	optimized [a]
D_{w2}/a_{HM}	Dielectric Width in Transition	0.23	set value
Fw1 (L_1)	SSIW width (L1 parameter)	4.1 mm	optimized
FL2	SSIW section length	3.3 mm	optimized [a]
FL3	main transition length	18.0 mm	optimized [a]
TL2	minor transition length	4.8 mm	optimized
TL1	rHMSIW section length	20.2 mm	set value
D_w/a_{HM}	dielectric width in waveguide	0.5	set value
C_w	copper width	3.0 mm	set value
D	SIW via diameter	1.0 mm	set value
Pv	SIW via wall pitch	2.0 mm	set value
a_{HM}	Dielectric Thickness	2.1 mm	set value

Table 5.4 6010 rHMSIW Transition parameters

[a] *Value is proportional to Pv*

To maintain fabrication tolerances a minimum of 0.2 mm from the edge of the via to the edge of the copper structures had to be maintained. This restricted the range of D_w/a_{HM} as a value of 1 would mean that part of the via would be exposed due to the effective value of the waveguide width. The two different ratios of D_w/a_{HM} meant that radiation of energy could be reduced in the transition and utilized in the rHMSIW section where required.

Initially a 2.54 mm thick substrate was used, however results showed a loss at the top end of the frequency band. On investigation, it was determined that it was a dielectric waveguide effect, relating to the mode cut-off frequencies, that was causing the loss, reducing the dielectric thickness shifted the cut-off frequency. The dielectric thickness dictates a_{HM} (the waveguide half mode width) and hence the waveguide cut-off frequency. Fig.5.44 shows the variation of cut-off frequency for the effective $TE_{1/2,0}$ mode we are using in the rHMSIW, $fc_{2.54}$ = 9.3 GHz and $fc_{2.10}$ = 11.2 GHz.

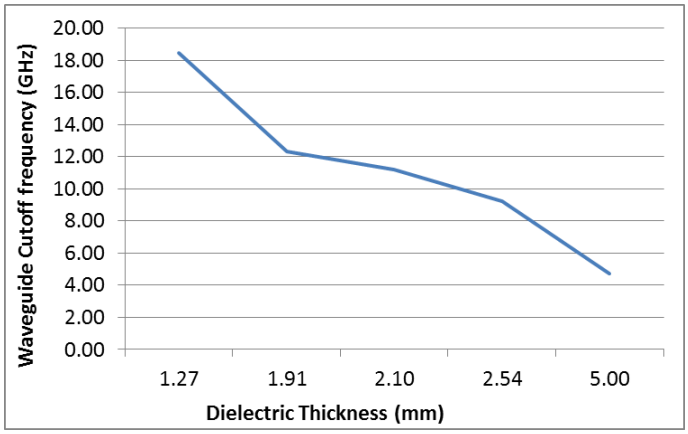

Fig. 5.44. Waveguide cut-off frequency versus dielectric thickness.

However it is the $TE_{3/2,0}$ cut-off that caused the loss for the 2.54 mm dielectric near 18 GHz , as $2fc_{2.54}$ = 18.6 GHz and at this frequency near cut-off a dielectric mode started to occur, resulting in the dispersion of wave energy. But with $fc_{2.10}$ = 11.2 GHz there was an improved balance between the start and end frequencies of the waveguide bandwidth compared to the $TE_{1/2,0}$ and $TE_{3/2,0}$ mode cut-off frequencies. Due to the loading of the waveguides by the SIW structures the actual cut-off frequencies vary slightly from the predicted theoretical values. Unfortunately 2.10 mm dielectric thickness is not a standard laminate thickness (nearest being 2.54 mm and 1.91 mm).

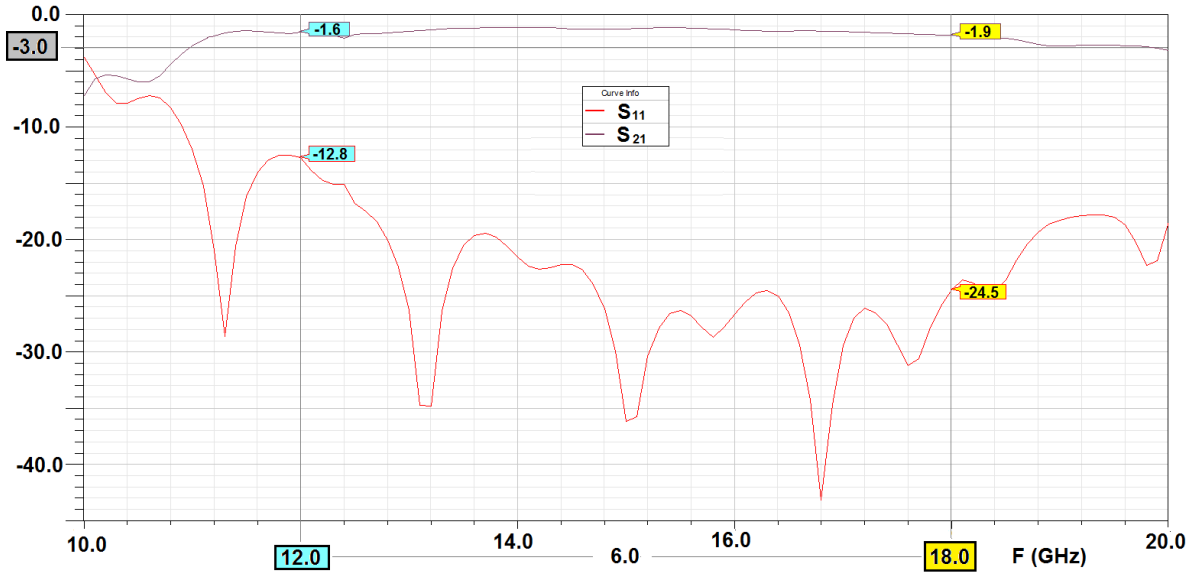

Fig. 5.45. Scattering Parameters for SIW transition (from HFSS simulation).

The scattering parameters for the transition across the target bandwidth is shown in Fig.5.45 the S_{21} averages better than -2 dB, indicating a reasonable passage of energy between the two ports. Fig. 5.48 is a plot of the normalized power flow as a percentage, showing the complete transition and with the rHMSIW section in isolation. The complete transition has a normalized power flow (Eq.5.19) of ~28% across the frequency band, and the rHMSIW section ~8%.

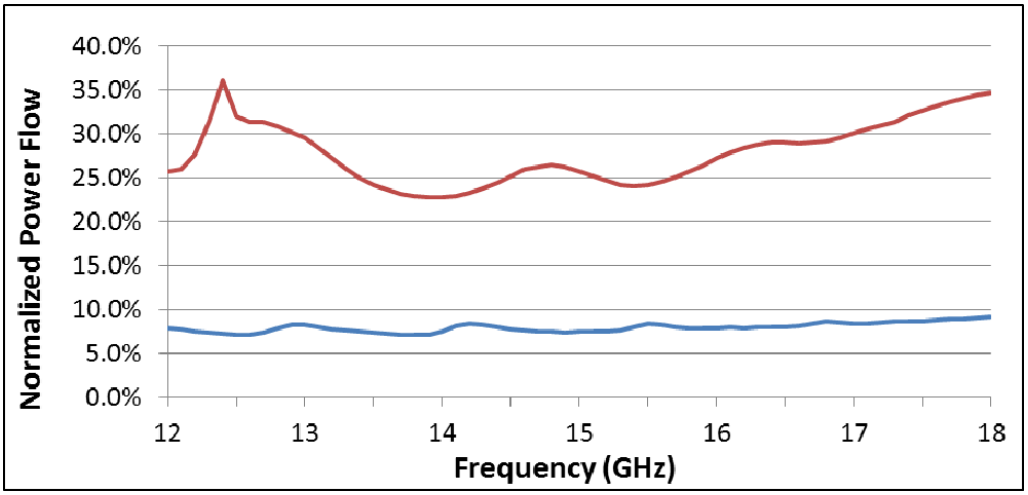

Fig 5.46. Plot of normalized power flow, bottom blue line is for rHMSIW section, top red line complete structure (transitions and rHMSIW).

The return loss although better than 10 dB at the start of the freqency band, is not ideal. This is due to the compromise of the dielectric thickness and the frequency cut off mode at ~11 GHz. Restricting the frequency band of use from 12-18 GHz is one option, as is changing the dielectric

thickness dependant on the exact requirement. For this particular application this compromise was deamed the most effective solution.

In addittion to the electric field rotation through the transition, the amount of wave energy that is travelling in the air proprotional to the energy in the dielectric increases through the transition, until it stabilizes in the rHMSIW section. This increases radiation losses, but does place the center of the electric field on the top dielectric surface, as originally intended. Fig. 5.47 is a two dimensional plot of the transition structure, showing the energy travelling in the dielectric. Fig. 5.48 is a top view of the structure, with a linear electric field vector plot through the dielectric. The small dots on the left indicate vertical vectors (coming out of the page), and the shortended vectors in the SSIW are at an angle. The vector magnitude in the long transition is larger than that in the rHMSIW as the dielectric exposed gap is smaller, concentrating the field slightly more.

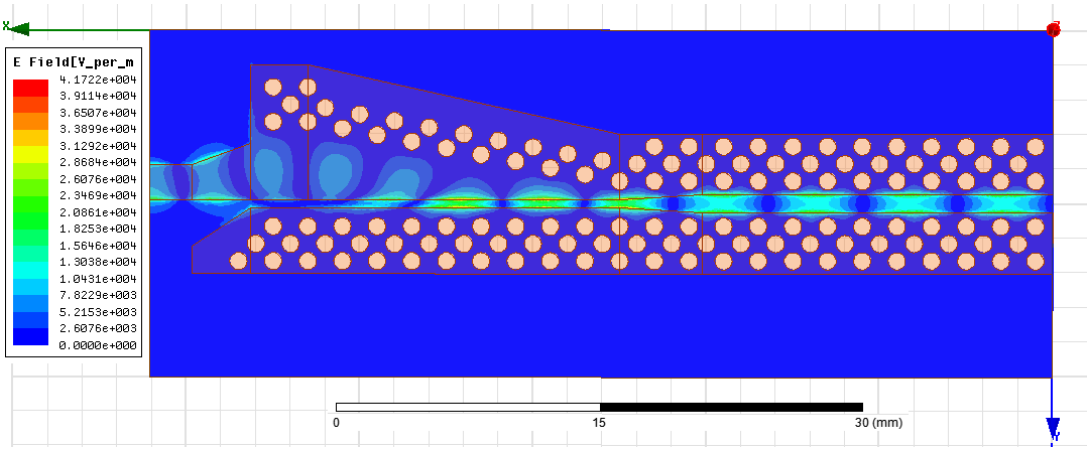

Fig. 5.47. 2D view of linear magnitude plot of electric field in dielectric at centre frequency of 15 GHz.

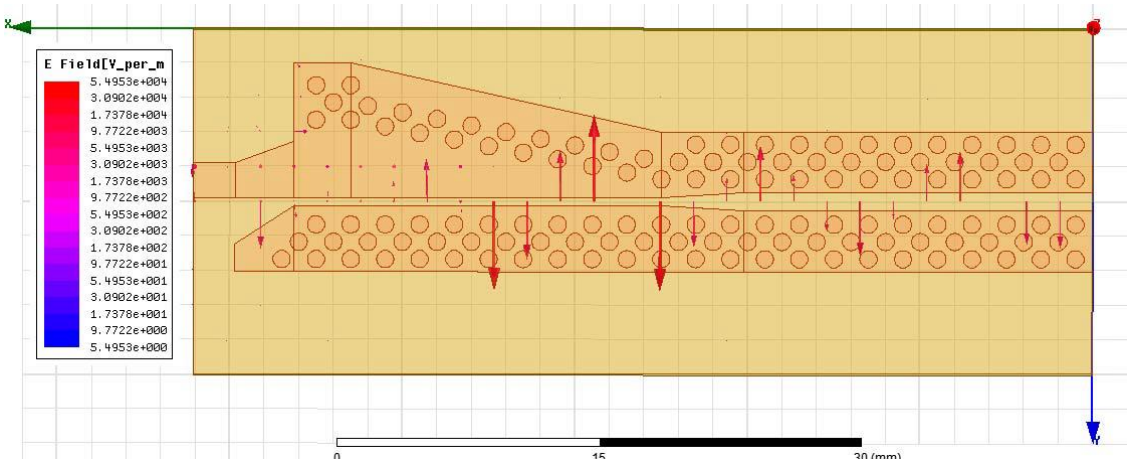

Fig. 5.48. Top view of linear vector plot of Electric Field in dielectric material. Point vectors on left indicate vertical polaization, and shows transition of orientation to horizontal field parrallel to top surface on right hand side.

A SIW transition which enables a connection from a 50Ω microstrip to a rotated half-mode substrate integrated waveguide (rHMSIW) was developed. By adding this transition to either end of an rHMSIW, direct connection to standard connectors using microstrip becomes possible. An operational bandwidth across the complete Ku band (12 to 18 GHz) was simulated with a relatively low through loss (<3dB) and insertion loss of less than 10dB. CPW and Slotline transitions [14] investigated could not achieve the 6 GHz bandwidth required, as by their nature, are more resonant. By combining different SIW structures together a hybrid transition was developed and was presented at LAPC [15].

5.7 6010 Test Coupon

By adding the 6010 transition onto a waveguide section of rHMSIW, a PCB test coupon was developed to enable full EM simulations to be conducted. Once the simulations were completed the designs were fabricated and measurements made. Four 6010 test coupons were fabricated with the 6010 material using the 1.9 mm thick dielectric. Three ~111mm long x 23mm wide with D_w/a_{HM} values 0.2 (smallest) , 0.3 (optimal) 0.5 (maximum), one ~113mm long x 23mm wide with D_w/a_{HM} 0.3 (optimal). The additional length was intended to compare S-parameters for β characterisation.

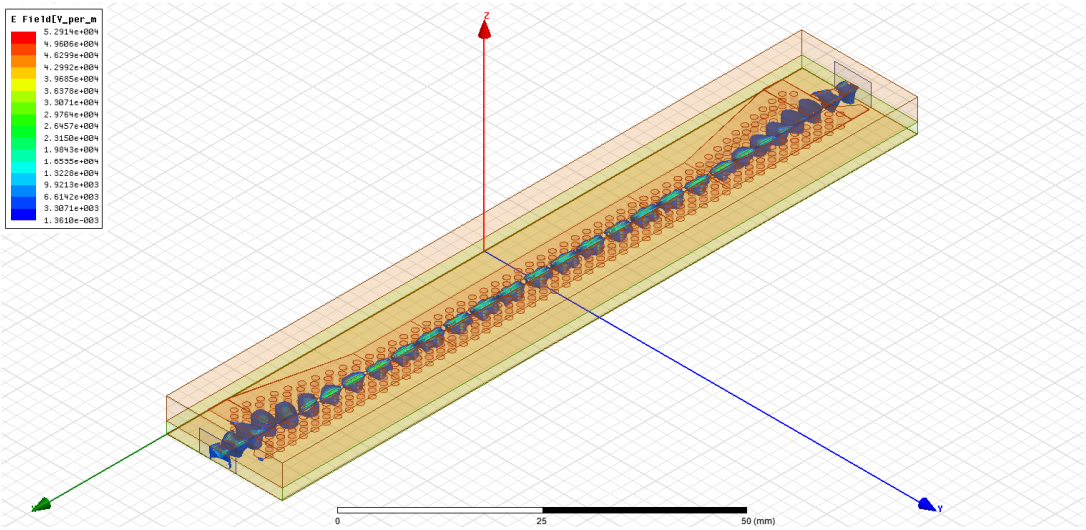

Fig. 5.49. 6010 Test coupon simulated electric field in dielectric at 18 GHz

A double via wall was used to assist in the adjustment from one SIW structure to the next. Due to the change of via pitch, a single row allowed gaps to occurr and hence leakage. As discussed in the transition section, the parameters were optimized to achieve the best response, but once set were maintained between the four coupons. Only the waveguide section lengths (*WgL*) and the D_w/a_{HM}

ratio were varied. The S-parameters for the simulation of the C1 coupon is shown in Fig. 5.50. (the other simulated results are included in Fig. 5.54 They show a through loss of ~-3dB across the Ku band, and am imnsertion loss of less than -10dB.

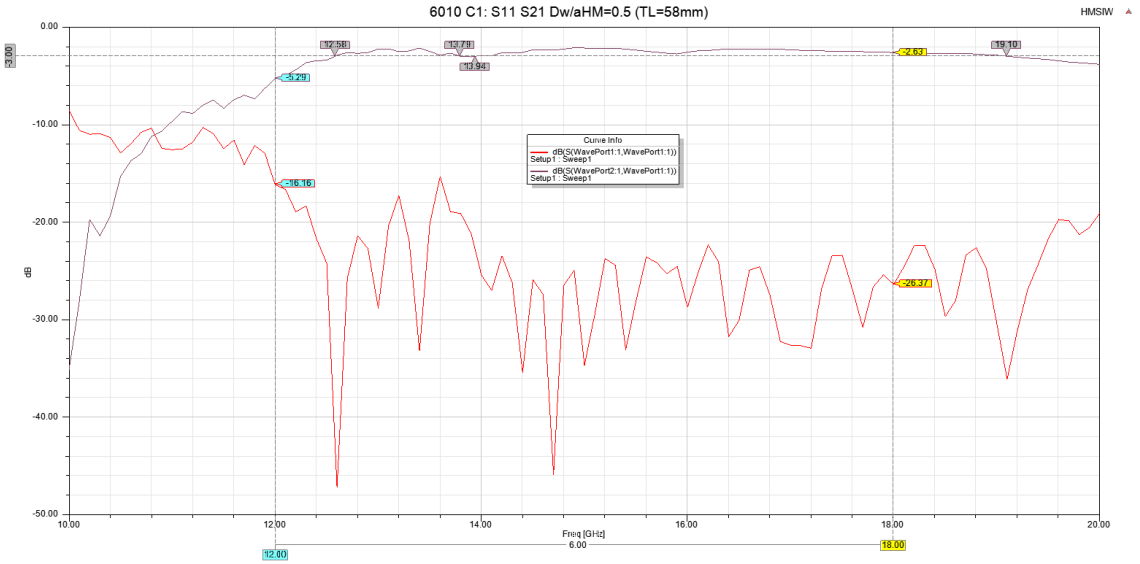

Fig. 5.50. 6010 C1 coupon simulated result
(S_{11} red, S_{21} blue, solid measured, dashed simulated)

The Rogers 6010 sample panel was 5" x 5", giving and effective working area 119 mm by 104 mm. The transition and waveguide section for all four coupons were designed to fit within this working area, a limitation imposed by the by the Rogers Corporation sample request program. A CAD representation is shown in Fig. 5.53 for the fabrication panel containing all four 6010 test coupons.

1. *WgL*=58mm, D_w=0.955mm Assembled and Measured
2. *WgL*=58mm, D_w=0.573mm Assembled and Measured
3. *WgL*=58mm, D_w=0.382mm Assembled and Measured
4. *WgL*=60mm, D_w=0.573mm Assembled and Measured

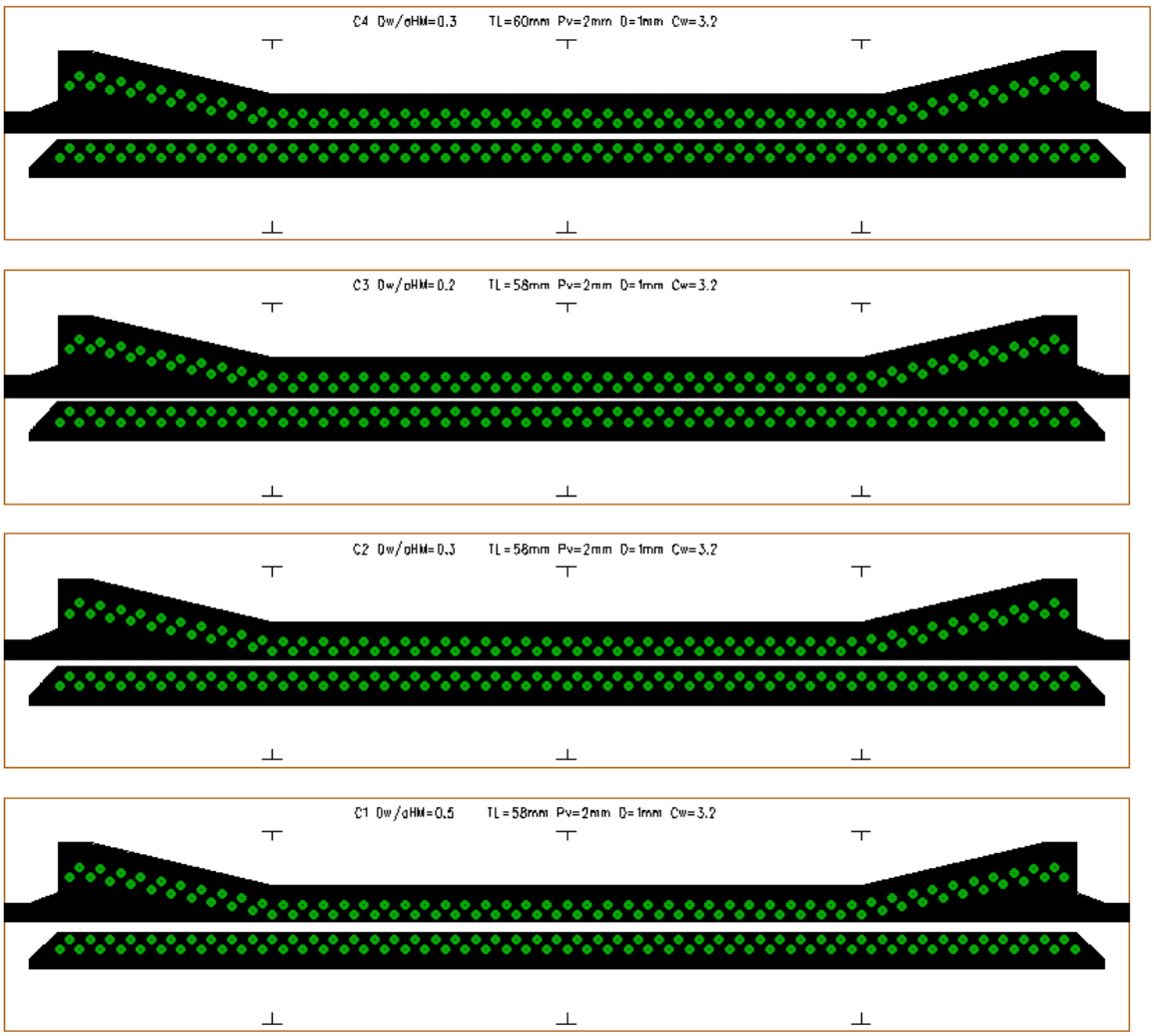

Fig. 5.51. CAD plot of 6010 fabrication panel.

The prototypes were fabricated externally to achieve the plated through hole connctions for the via walls. Unfortunately there was a minor problem with the PCB surface finish, although gold plating was ordered (ENIG – electroless nickel imersion gold), air leveled tin was received (HASL– hot air solder level). The gold was requested for surface linearity, the HASL finish by its nature is not as flat. This can be seen in Fig. 5.52, were the uneven solder is unevenly distibuted.

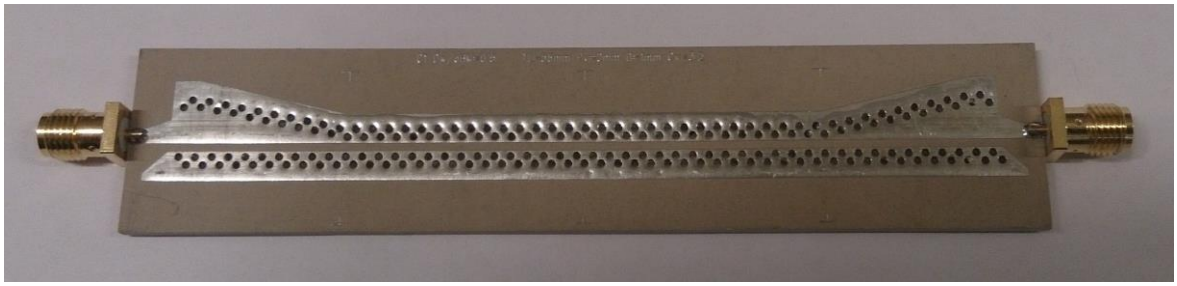

Fig. 5.52. PCB 6010 Test Coupon 01

5.8 Comparison of Simulated and Measured Results

As with the SSIW a VNA was used to for measurements, calibration was completed using the TRL method (Through – Reflect – Line) with a dedicated calibration kit. The combined simulated and measured results for the 6010 test coupons are shown in Fig. 5.54. The measured results show a disappointing correlation with the expected simulated results. All four showed a greater loss than expected by the simulations for both through loss and insertion loss. The prototypes were all dimensionally checked to verify design values with fabricated values, and found to be accurate.

One consideration was the SMA connectors used, as the top frequency limit from the component data sheet was 18 GHz. A measurement was made of two connectors back-to-back to create an approximate through line. The measurements revealed that there was a low insertion loss and low through loss, which was maintained to over 20 GHz where the connector dielectric limitation started to show. Therefore the connectors were not a limiting factor.

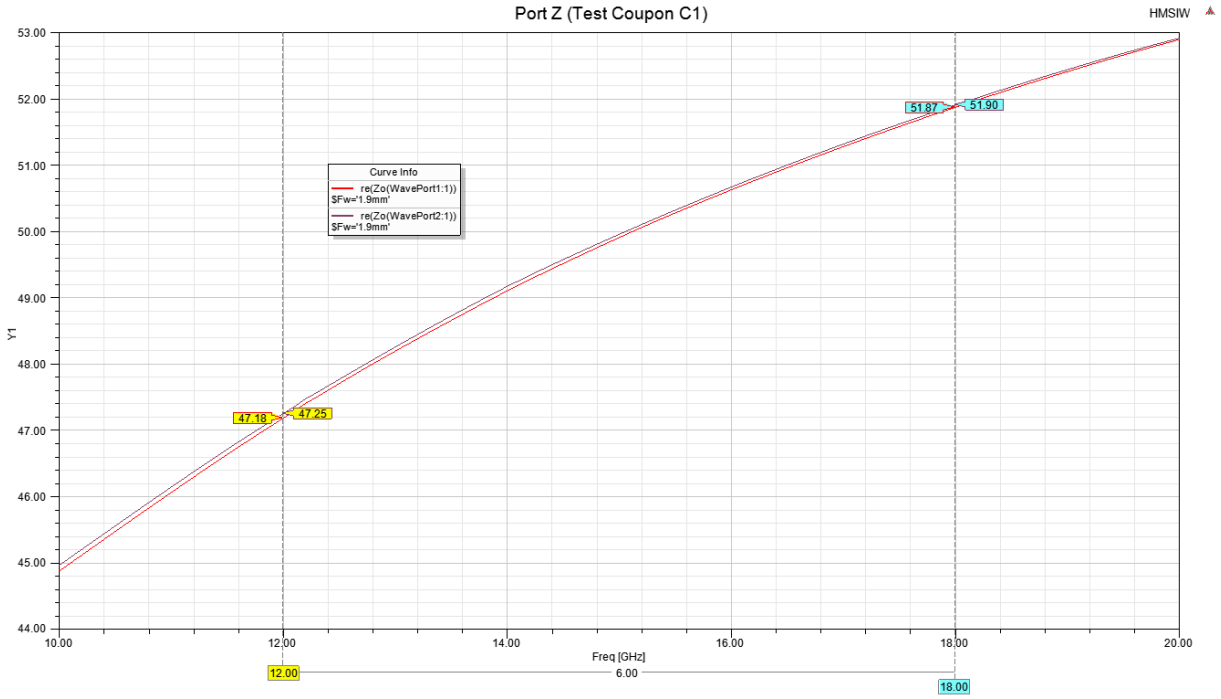

Fig. 5.53. Port Impedance of test coupon C1 across Ku band

The higher losses may have been an indication that the match of the microstrip was not exactly 50 Ω, a plot of the port impedance is shown in Fig. 5.53 indicating that there was a reasonable match, the impedance only varying between 47 and 52 Ω. The simulations were completed for the entire test coupon with the ports normalised and non-normalised. The coupon simulations used lossy

materials and included all vias as copper. Simplifications made included modelling the vias as solid copper and not cylinders, and the conductors as only copper and not layers of copper and tin.

Variations in surface roughness were considered as the skin depth within copper is less than 0.6 μm across the Ku band, and for tin less than 1.5 μm. The surface roughness of the copper laminate for the top side was specified as 0.4 μm and for the underside as 1.7 μm. The main problem for surface roughness is that the solder finish ranges from 70 to 200 μm, (the surface roughness is measured as the RMS roughness calculated over the profiled area).

By shorting the waveguide section to create a resonant cavity, it is possible to obtain a value for β by measuring the order of resonance (by counting S_{11} resonances separated by half wavelengths), based on [16]. This method was attempted; unfortunately the test coupons were too lossy to obtain a reliable result.

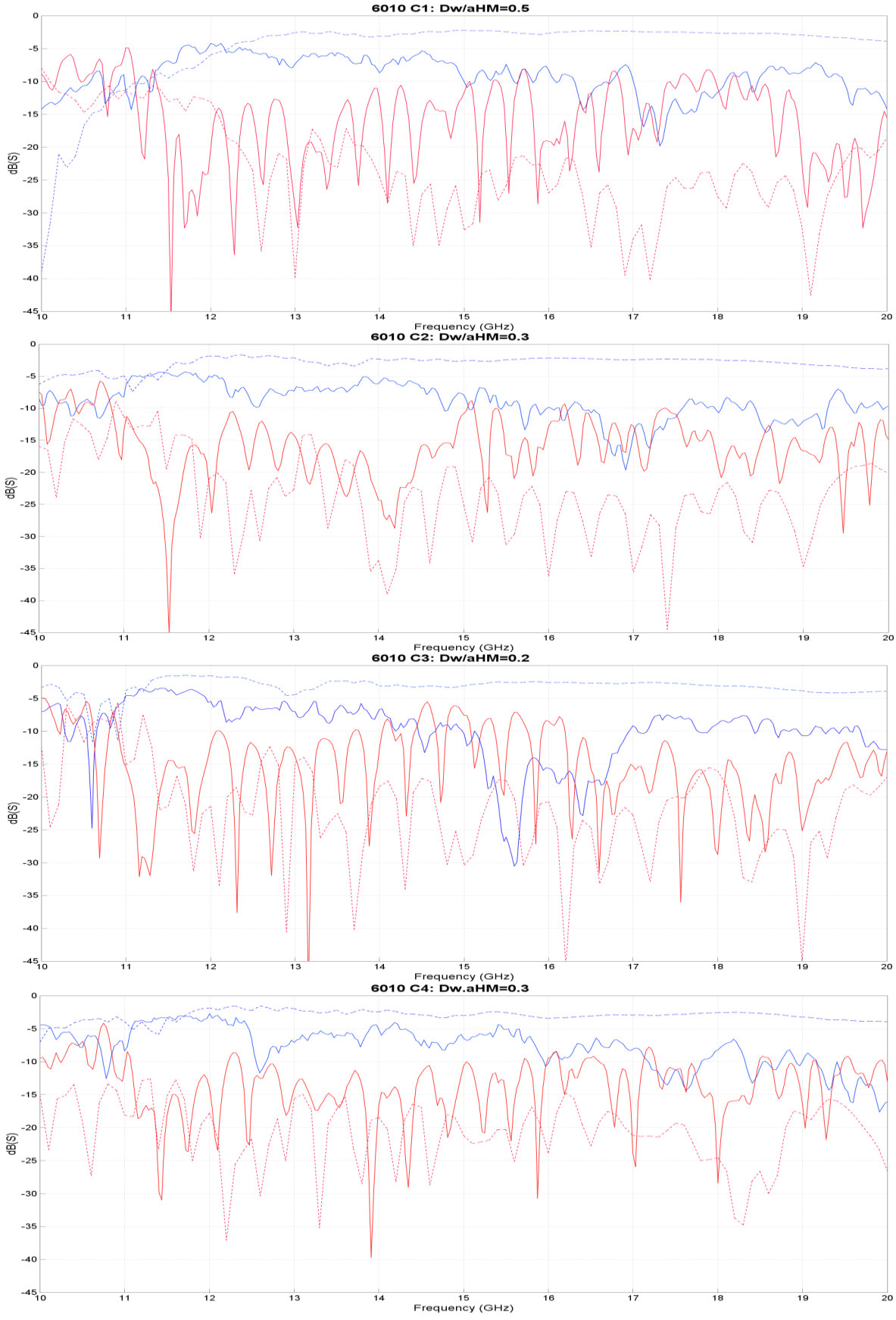

Fig. 5.54. 6010 coupons simulated and measured results
(S_{11} red, S_{21} blue, solid measured, dashed simulated)

Additional simulations were run to investigate the divergence between the simulated and measured results, including using hollow vias (instead of solid) with correct plated thickness, varying the surface roughness of copper on all relevant surfaces, over-plating of tin on copper (creating multiple layers of conductor) and varying the dielectric loss value.

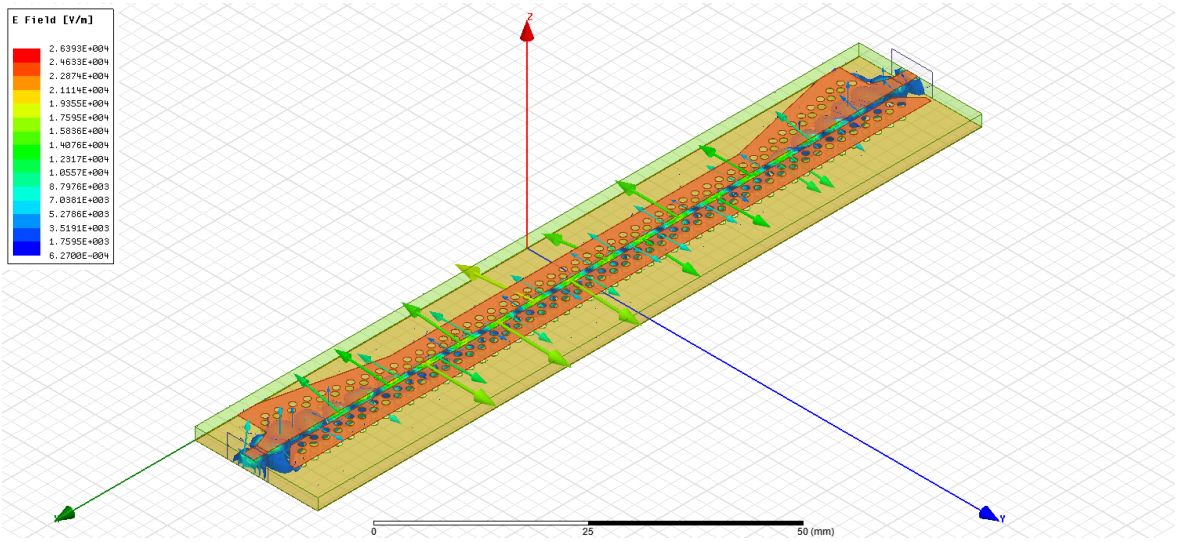

Fig. 5.55. 6010 C1 coupon at 15 GHz Mode1 , Mag E in dielectric Vector E on top surface
Hollow vias with surface roughness

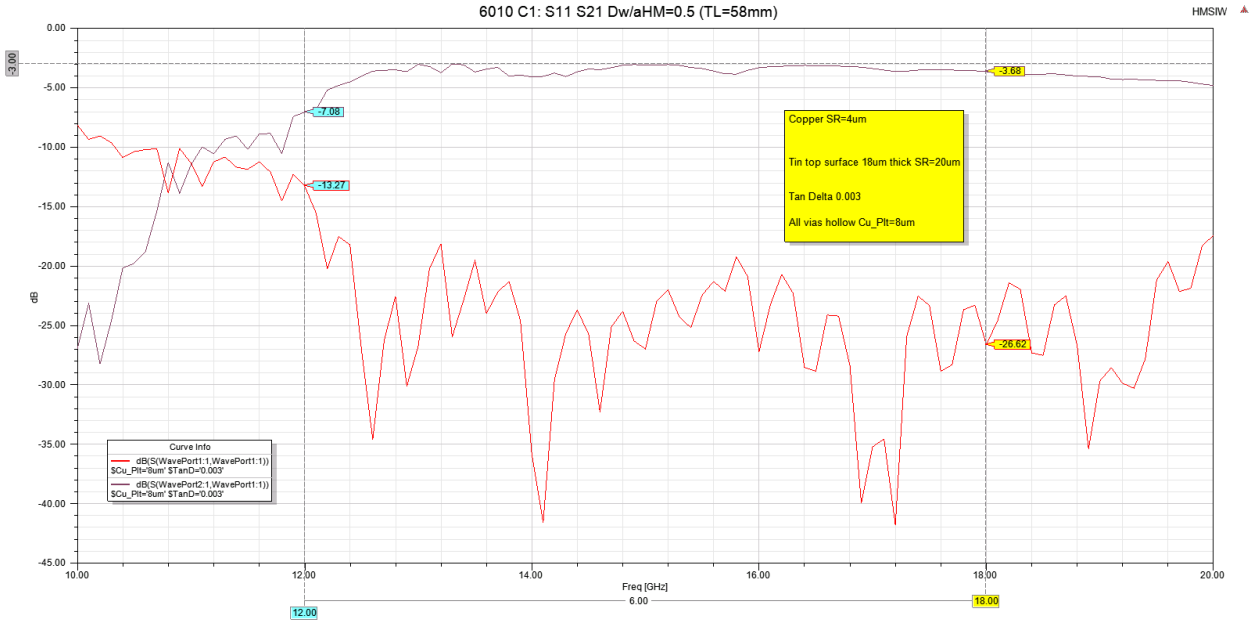

Fig. 5.56. S-parameters of 6010 C1 coupon with hollow vias and surface roughness correction.

Figs. 5.55 and 5.56 show the revised full coupon model and S-parameters, with hollow vias (8µm copper thickness to represent plating), tin layer on surface (18µm) with surface roughness for

solder finish, surface roughness on internal edge of copper surfaces. The loss has increased but it is still a poor comparison with the measured values, as Fig. 5.57 shows with a replot.

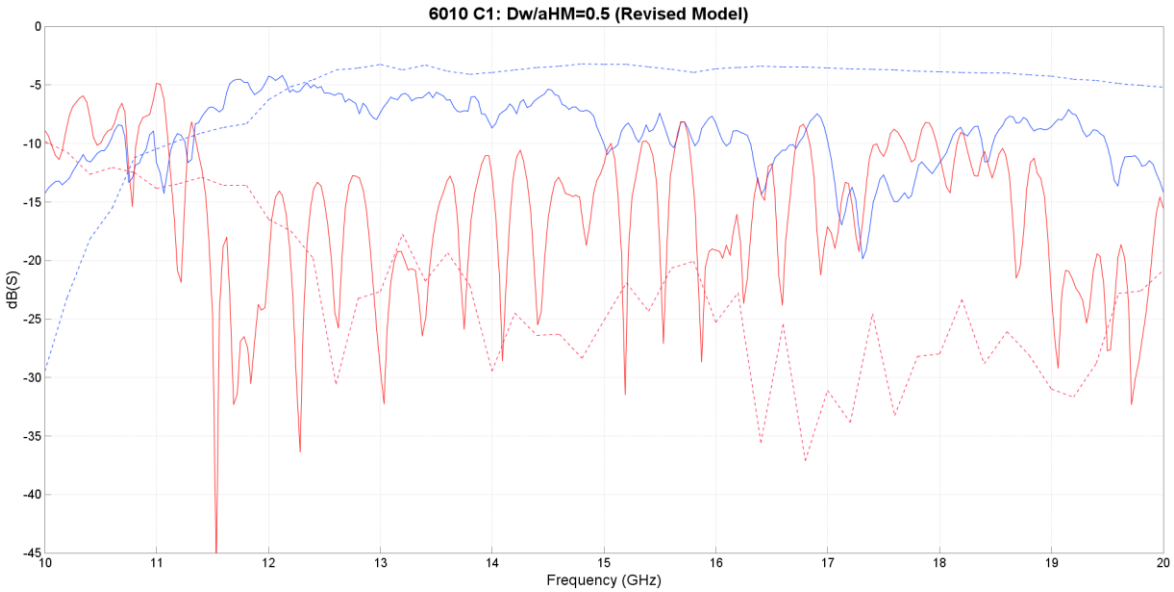

Fig. 5.57. 6010 C1 Coupon revised simulated with measured results
(S_{11} red, S_{21} blue, solid measured, dashed simulated)

5.9 Summary

The rotated half-mode SIW (rHMSIW) was introduced as a means of placing the electric field maximum directly on the top dielectric surface allowing easy and direct access. The waveguide structure was assessed with two different PTFE laminates from the Rogers Corporation (5880 and 6010) and a range of dielectric thicknesses were considered. The nature of the waveguide uses the dielectric thickness as its half-mode waveguide thickness (a_{HM}), thus equating the separation of the via walls to its waveguide height (b_{eff}). The open structure of the waveguide allows the amount of exposed dielectric width (D_w) to be controlled. All of these parameters effect the waveguide cut-off frequency for the fundamental mode $TE_{1/2,0}$. The ratios of b_{eff}/a_{HM} and D_w/a_{HM} were analysed and a new formulae (Eq.5.10 and Eq.5.11) was derived to describe the rHMSIW cut-off frequency for each of the materials:

$$f_{c\,(5880\_3.175mm)} = \left(0.1604 \times \frac{b_{eff}}{a_{HM}} + 1.0844\right) \times ln(D_w/a_{HM}) + \left(17.538 - 3.3717 \times \frac{b_{eff}}{a_{HM}}\right)$$

$$f_{c\,(6010\_1.9mm)} = \left(1.8277 \times \frac{b_{eff}}{a_{HM}} + 0.4693\right) \times ln(D_w/a_{HM}) + \left(14.189 - 1.3503 \times \frac{b_{eff}}{a_{HM}}\right)$$

Where f_c is in GHz, and D_w/a_{HM} and b_{eff}/a_{HM} vary between 0.1 and 1.

The developed rHMSIW was aimed at spanning the Ku band (12 to 18 GHz) and the K band (18 to 26 GHz), and the simulations indicated that this was possible for the K band with the 5880 material and for the Ku band using the 6010 material. The original aim was to use the capacitive coupled overlay concept used in previous chapters to form filters and other structures such as leaky-wave guides, initial simulations showed potential to achieve this. However the measured performance of the prototype coupons were a poor match to the simulations and the overlays were not developed.

Using a full wave simulation tool (Ansoft HFSS) to model the rHMSIW provided an accurate means of accounting for the effect of the fringing fields that directly effect the waveguide cut-off frequency. Significant time and effort was invested in the development of the characterisation of the waveguide, the modal performance and the rHMSIW transition. The measured response of the 6010 test coupons were poor, for which a variety of causes for the difference between the measured and simulated results were investigated. There was not a fabrication error as the fabricated samples were dimensionally checked against the CAD data and the original simulation structures. Dimensional changes (to assess fabrication tolerances) within the simulation did not yield significantly different results. Surface roughness was considered, and a range of simulations were run, but it was not found to be the cause. The simulation model was developed to include hollow

vias, more as a means of completeness than belief in actual cause. Finally the complete test coupons with all variations were run, which was complex and required a great deal of processing time. No simulation results obtained, matched the measure response found. The possibility of sheet resistivity between the copper and tin layers has been suggested, which would explain the loss increase with frequency, however this is felt to be unlikely as the fabrication process between the copper and HASL finish is well defined and there was no visible evidence to suggest a poor intermetallic bond.

During simulations, single and multi-modes were considered. For SIW structures (especially with apertures) cross coupling between higher order modes may be an issue. The plots of the propagation constant showed that the simulation would swap between modes, but each mode was calculated separately. Simulations of the complete coupon with no set mode, to allow the dominant mode at each frequency to manifest did not yield a different result, which is not surprising as the structure is essentially designed for monomode operation.

It is perceived that there is a cross coupling condition occurring within the waveguide structure, which was not directly simulated or observed. Another possibility is that there was a fault with the PTFE material and the dielectric loss was not as specified, this was not ruled out, but is felt to be unlikely. It is noted that a 6 GHz bandwidth from 12 to 18 GHz was an ambitious target to achieve, and that a reduced bandwidth target may have been more practical to implement on a planar structure.

5.10 References

[1] A. J. Farrall and P. R. Young, "Rotated half-mode substrate integrated waveguide," in *Antennas and Propagation Conference (LAPC), 2013 Loughborough,* 2013, pp. 514-517.

[2] A. J. Farrall and P. R. Young, "Integrated waveguide slot antennas," *Electronics Letters,* vol. 40, pp. 974-975, 2004.

[3] B. S. Izquierdo, P. R. Young, N. Grigoropoulos, J. C. Batchelor and R. J. Langley, "Slot antenna on C type compact substrate integrated waveguide," in *Microwave Conference, 2005 European,* 2005, pp. 4 pp.

[4] Liang Wu, B. S. Izquierdo and P. R. Young, "Half mode substrate integrated waveguide slot antenna," in *Antennas and Propagation Society International Symposium, 2009. APSURSI '09. IEEE,* 2009, pp. 1-4.

[5] M. Bozzi, A. Georgiadis and K. Wu. Review of substrate-integrated waveguide circuits and antennas. *Microwaves, Antennas & Propagation, IET 5(8),* pp. 909-920. 2011.

[6] Ruo Feng Xu, A. J. Farrall and P. R. Young, "Analysis of Loaded Substrate Integrated Waveguides and Attenuators," *Microwave and Wireless Components Letters, IEEE,* vol. 24, pp. 62-64, 2014.

[7] Wei Hong, Bing Liu, Yuanqing Wang, Qinghua Lai, Hongjun Tang, Xiao-Xin Yin, Yuan-Dan Dong, Yan Zhang and Ke Wu. Half mode substrate integrated waveguide: A new guided wave structure for microwave and millimeter wave application. Presented at Infrared Millimeter Waves and 14th International Conference on Teraherz Electronics, 2006. IRMMW-THz 2006. Joint 31st International Conference On. 2006, . DOI: 10.1109/ICIMW.2006.368427.

[8] Qinghua Lai, C. Fumeaux, Wei Hong and R. Vahldieck. Characterization of the propagation properties of the half-mode substrate integrated waveguide. *Microwave Theory and Techniques, IEEE Transactions On 57(8),* pp. 1996-2004. 2009.

[9] Feng Xu and Ke Wu. Understanding leaky-wave structures: A special form of guided-wave structure. *Microwave Magazine, IEEE 14(5),* pp. 87-96. 2013. . DOI: 10.1109/MMM.2013.2259400.

[10] E. Episkopou, S. Papantonis, W. J. Otter and S. Lucyszyn. Defining material parameters in commercial EM solvers for arbitrary metal-based THz structures. *Terahertz Science and Technology, IEEE Transactions On 2(5),* pp. 513-524. 2012. . DOI: 10.1109/TTHZ.2012.2208456.

[11] Joo-Young Choi and S. Lucyszyn. HFSS™ modelling anomalies with electrically thin-walled metal-pipe rectangular waveguide simulations. Presented at High Frequency Postgraduate Student Colloquium, 2005. 2005, . DOI: 10.1109/HFPSC.2005.1566372.

[12] R. Garg, I. Bahl and M. Bozzi, *Microstrip Lines and Slotlines (Artech House Microwave Library (Hardcover).* Artech House, 2013.

[13] Ruo Feng Xu, B. S. Izquierdo and P. R. Young, "Switchable Substrate Integrated Waveguide," *Microwave and Wireless Components Letters, IEEE,* vol. 21, pp. 194-196, 2011.

[14] K. Gupta, *Microstrip Lines and Slotlines.* Boston: Artech House, 1996.

[15] A. J. Farrall and P. R. Young. Microstrip to rotated half-mode substrate integrate waveguide planar transition. Presented at Antennas and Propagation Conference (LAPC), 2014 Loughborough. 2014, . DOI: 10.1109/LAPC.2014.6996332.

[16] C. H. Chandler, "An Investigation of Dielectric Rod as Wave Guide," *J. Appl. Phys.,* vol. 20, pp. 1188, 1949.

6 Conclusion

SIWs are one of the options available to microwave engineers when considering planar transmission lines. In addition to creating point-to-point links, other operations will be required on the signals (or waves), such as splitting into separate channels, altering amplitude (boosting weak signals, damping strong ones), filtering out noise and integrating with other components (to name a few). Some of these operations are directly realisable with SIW structures and components.

As the size of SIWs architectures are directly related to the frequency of operation, the associated wavelength means that SIWs are an important transmission option for high frequency (60 GHz) and mm-waves; due to their low loss, low radiation, and ease of integration with discrete components. Directly developing SIW structures and components at mm-wave frequencies is complex and costly, as SIW structures are frequency scalable, a pragmatic approach has been to use lower frequencies to demonstrate new approaches.

6.1 SIW Antenna

A detailed review of a novel switch beam antenna (with variants for 2, 4 and 6 direction) developed for use within the current WiFi band at 2.4 GHz was presented. The switched beam antenna utilised a flexible circuit overlay to capacitively couple the switched impedance of PIN diodes to the radiating slots in the waveguide. Effectively shorting the slot in two, and shifting the radiating frequency above the 2.4 GHz of interest.

The switched beam antenna was shown to be in good agreement with simulated results achieving a measured -10 dB return loss bandwidth of approximately 3% and antenna gains in the range 3 to 6 dBi. Furthermore, the design is no larger than a single SIW slot antenna. Prototypes were demonstrated at 2.45 GHz, however the design may find greater use at higher frequencies where SIW is a more appropriate host transmission line. The switch beam antenna was a collaborative research project, however the work included in this document has not been previously published in its entirety, a summary of the work focussed on the six direction variant was published in May 2015.

One area of future work being considered includes the varying of the PIN diode bias current. As shown in chapter 4 with the travelling wave attenuator, the PIN diode impedance may then be varied, and instead of short circuiting the slot aperture it may be loaded sufficiently to steer the beam. This is somewhat problematic as the currents involved are small (in the region of micro amps) and maintaining current levels and variations of PIN diode responses require significant research to develop this further.

Also being considered is utilising the overlay design to form leaky-wave antennas on the rHMSIW structures, which will necessitate the coupon design being revised. An alternative being discussed is to fabricate a normal RSIW with the top conducting layer replaced with an overlay. This will then allow the RSIW top layer to be either a capacitively coupled solid conductor or enable slots or periodic shapes to be introduced to form leaky-wave structures.

6.2 Slot SIW

To demonstrate the ease of interaction with SIW structures, two applications were developed and demonstrated using the Slot SIW. The SSIW has a small longitudinal gap along one of the main conducting surfaces, forcing the fundamental propagating mode away from the traditional full SIW mode into a half-mode. The slot allows easy integration of lumped elements or active devices, enabling the waveguide to be loaded with impedances or to be shorted. When the slot is shorted, the waveguide reverts back to the full SIW mode, and when partially loaded an intermediate state results. Test coupons were designed and fabricated with a range of shunt waveguide widths. One of which was analysed with the transverse resonance technique, to model this intermediate state and lead to the development and demonstration of a travelling wave attenuator. With the SSIW periodically loaded using PIN diodes, variable attenuation from 2 dB to 25 dB over the 3-5 GHz waveguide range was verified. A summary of this work was published in January 2014.

The use of the capacitively coupled overlay was then developed further to form a waveguide filter. Using controlled elements created directly in copper; termed *virtual vias,* an inductive shunt element loads the SSIW slot with a controlled impedance at defined positions within the waveguide to create resonant cavities. Third order pass-band filters were developed centred on 4.5 GHz, fabricated and measured utilising the *asymmetrical 'I' shaped virtual via*.

The use of the capacitively coupled overlay as a means of allowing integration of both active and passive elements with the slot SIW was demonstrated. Although the positional requirements for placements of the overlay filter onto the SSIW make this problematic, a direct implementation of the filter in copper would be straight forward. The coupon waveguide length limited the order of band-pass filter that was implemented, a longer waveguide section would have allowed for higher order filters to have been developed; which will be considered for future research. A problematic limitation of the SSIW overlay filter design was the physical alignment between overlay and filter. Although alignment marks were added to the overlay, no alignment marks were added directly to the SSIW top copper layer. Alignment marks directly on the test coupon, ideally on the copper layer for accuracy, but possibly on a silk screen layer should be strongly considered.

An extension of this work was briefly investigated using the SSIW02 diode overlay array to assesses if a filter could be formed by switching between the two states for each diode. Fig 6.1 shows the overlay array and Fig. 6.2 the S-parameters for the two cut-off frequencies for the diodes being all-off and all-on.

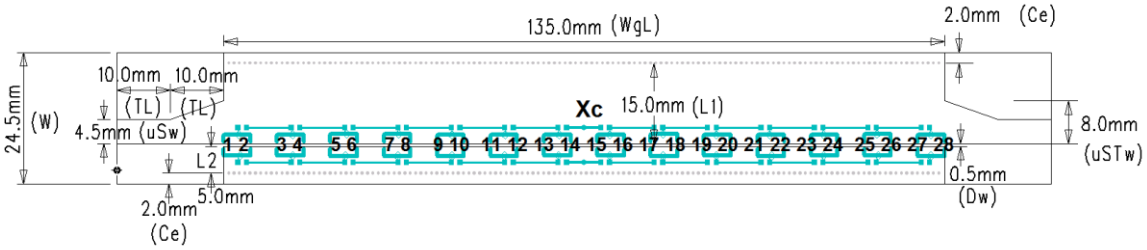

Fig. 6.1 SSIW02 with diode array overlay

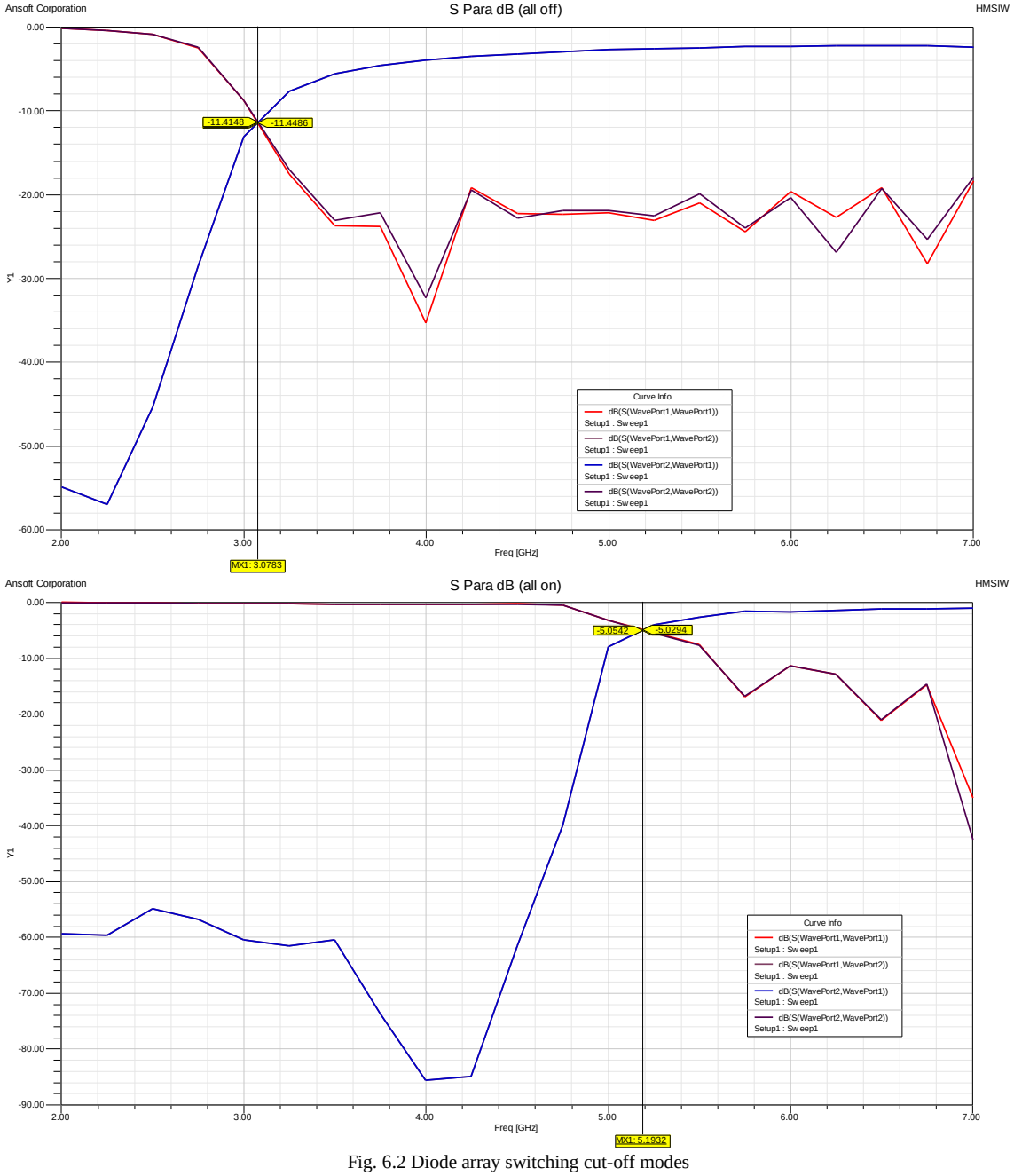

Fig. 6.2 Diode array switching cut-off modes

Switching combinations of diodes produced a very limited filter response, as the cavity lengths were fixed as multiples of 5 mm (the original diode pitch), a smaller pitch array of diodes would no doubt have been an improvement. This did lead to the consideration of developing a switched filter, combining the previous overlay designs for travelling wave attenuator and band-pass filter.

A few initial simulations were run, using four pairs of PIN-diodes (Fig. 6.3) to form a 3rd order band-pass filter, with an inner cavity dimension (P_d) and outer cavity dimension (P_{d2}), the impedance loads of the switched diodes could be positioned accordingly. The diode separation pitches for the inner pairs (F_{vp}) and outer pairs (F_{vp2}) added an additional means of response control. To Minimize the effect of the transition on the filter, a 'keep out' distance of $\lambda_g/4$ ~17.0 mm was maintained.

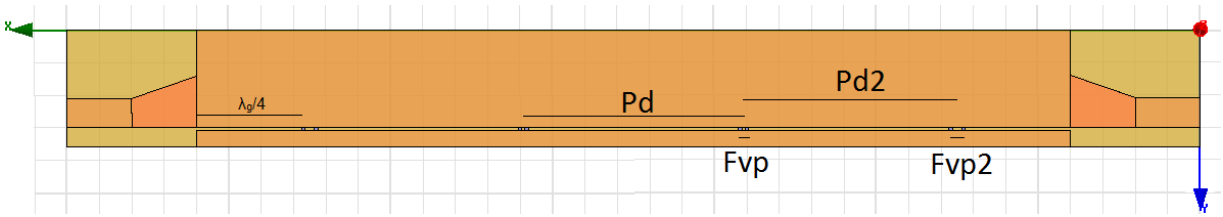

Fig. 6.3 direct switch diode band-pass filter

The response was poor as the diode impedances are fixed at 2 Ω when forward biased, a significant improvement is required to generate the required filter response. Fig. 6.4 shows a combination of the virtual via used in chapter 4, with two PIN diodes spaced a distance *VL* apart, on the coupling overlay.

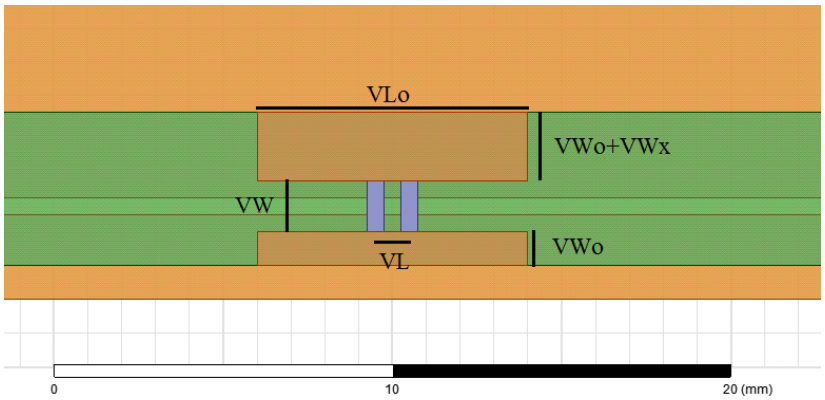

Fig. 6.4 Diode pair virtual via on overlay configuration

With *VW* maintained at 1.5mm, *VWx = VWo = 1mm* and *VLo* = 8.0mm the diode pair virtual via configuration was characterised, the results are shown in Fig 6.5. The shunt conductance response for varying the diode separation is approximately linear, but has a minimum value of ~2.5 S. The theta offset values are also relatively small, plus the range of VL (0.5 to 6.0 mm) Im(Z_{21}) was

positive (17.50 to ~6.0 Ω respectively). So the configuration looks promising although the minimum value of *B* will be a limitation.

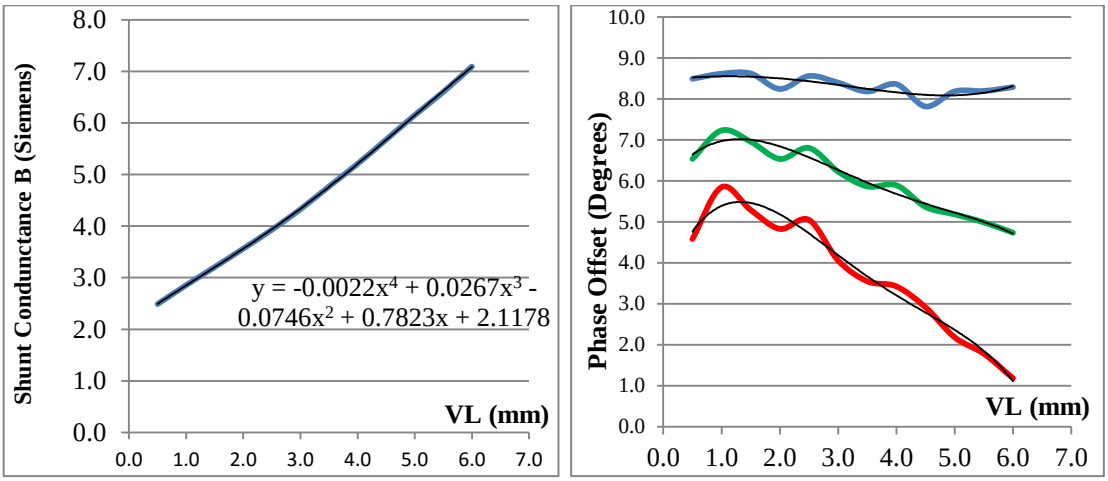

Fig.6.5 Susceptance and phase offset for diode pair virtual via at 4.5 GHz (25um adhesive)
(Phase offset Blue-S_{21}, Red-S_{11}, Green – average)

Repeating the 3rd Chebyshev order pass-band filter with 0.5dB ripple, 400 MHz bandwidth, centred at 4.5 GHz parameters, the results were:

- Calculated *B* Values: B_1 = 1.9168 S, B_2 = 4.3325 S, B_3 = 4.3325 S, B_4 = 1.9168 S
- Calculated Cavity Lengths: L_1 = 27.6 mm, L_2 = 29.7 mm, L_3 = 27.6 mm
- Derived diode separations: -0.25 mm, ~3.0 mm, ~3.0 mm, -0.25 mm
- Adjusted cavity lengths: 25.3 mm, 26.9 mm, 25.3 mm

The negative lengths meant that the diodes would overlap, so a single diode was used to form the shunt conductances B_1 and B_4. The structure is shown in Fig. 6.x which was simulated as a test coupon and then optimised as previously.

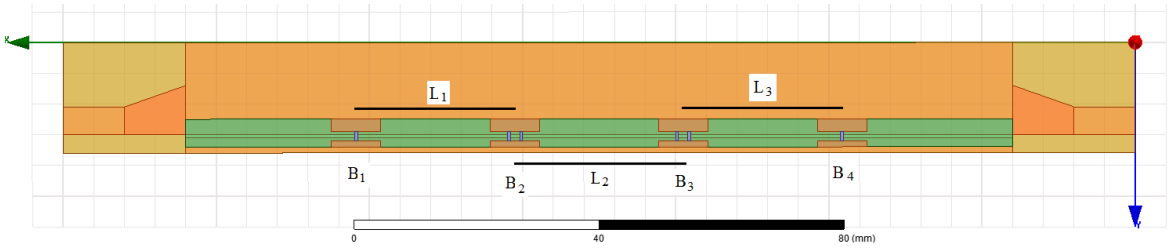

Fig. 6.6. Diode pair virtual via filter structure

This work is ongoing, and requires further study to improve the simulations before fabricating the design. The virtual via configuration is not ideal, consideration needs to be given to varying the copper dimensions with the diode spacing, possibly a ‘half bow tie’ shape.

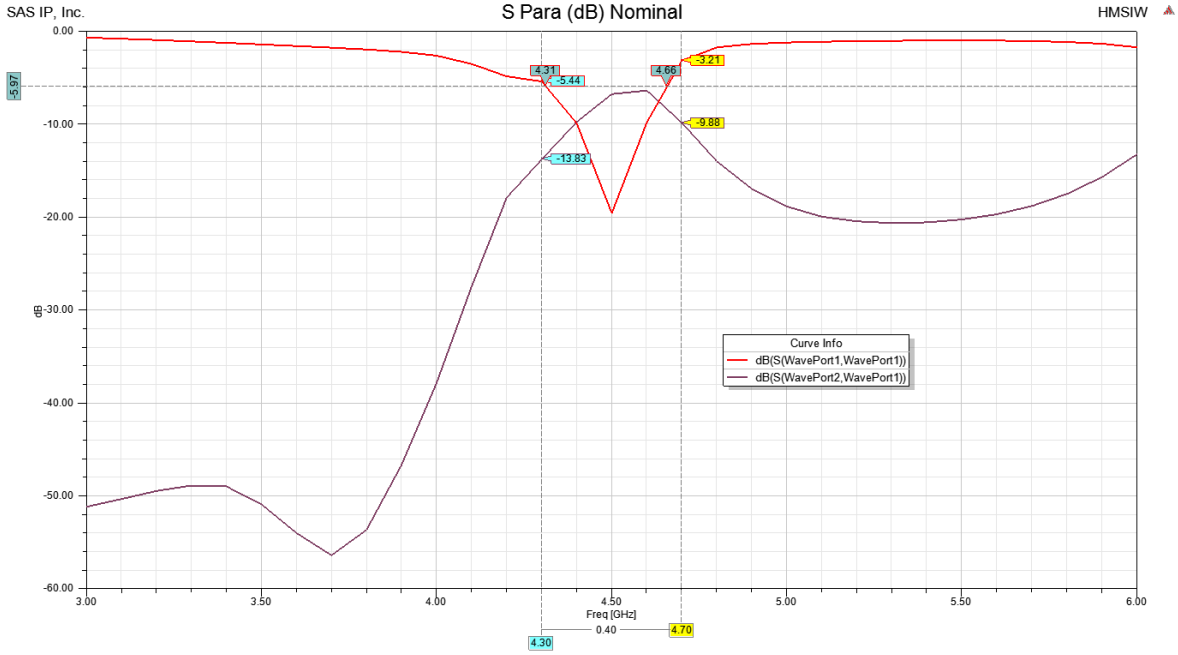

Fig. 6.7. Diode pair virtual via filter simulated S-parameters – **diodes turned 'on'**

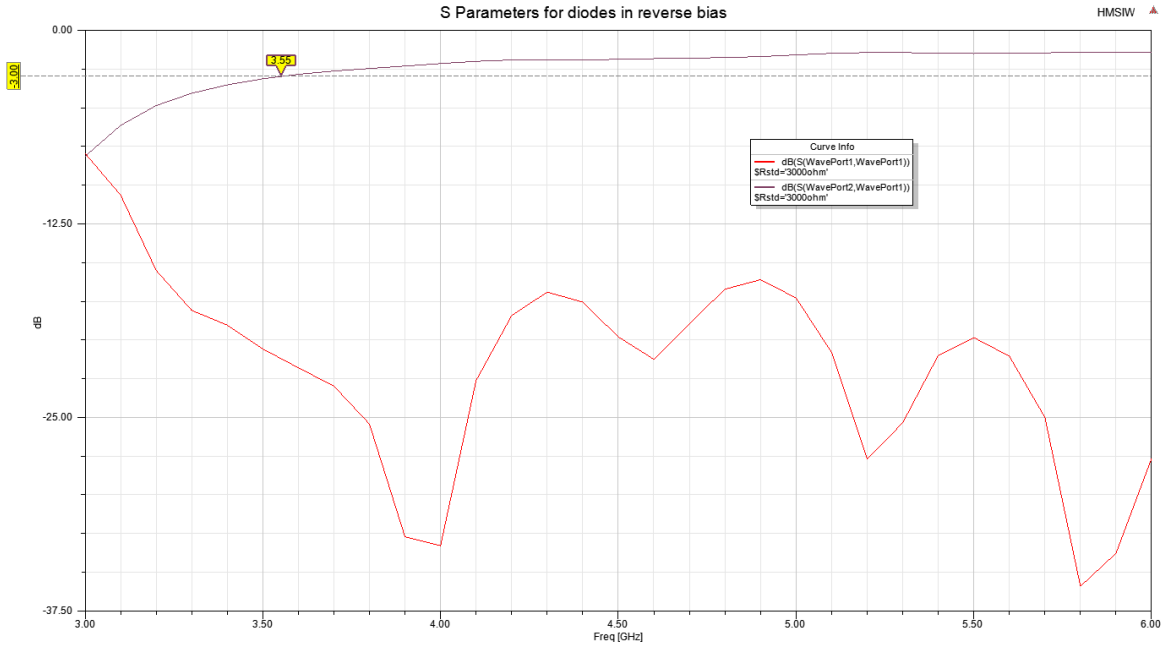

Fig. 6.8. S-parameters with diodes in reverse bias condition **- diodes turned 'off'**

The response of the filter is not ideal and is included as a 'work-in-progress', a more effective design will use the full eight diodes (giving four pairs) with a revised virtual via configuration. The S-parameters in Fig. 6.7 show the waveguide response with the diodes forward biased (in the 'on' position), a bandpass response is evident; but not ideal. Fig. 6.8 is a plot of the S-parameters with the diodes reverse biased (in the 'off' position), and the response reverts back to that of a waveguide. The S_{21} (thru loss) is similar to that shown for the unloaded waveguides in chapter 4. The simulations indicate that a switchable bandpass filter for SSIW is feasible, however further work is required to improve the filter response prior to fabrication and measurement. One means of

which is to utilise a thinner adhesive, to that end a new material has been sourced from Japan - Nitto 5600, which is only 5 μm thick.

6.3 Rotated Half Mode Substrate Integrated Waveguide

The rHMSIW, a new variant of the SIW family, places the maximum of the electric field directly on the top dielectric surface, allowing for direct interaction, an improvement over the SSIW where the majority of the field remains within the dielectric. The waveguide width *a* is now defined by the dielectric thickness, meaning that the waveguide height *b* adjustable. The rHMSIW is characterised with regard to the height and width ratios *b/a,* and the dielectric exposed width. These parameters effect the modal cut-off frequency, this was investigated and new equations describing the fundamental mode cut-off frequency were empirically derived for both of the laminates investigated. A detailed loss comparison between rHMSIW and regular HMSIW is an area of future work that is deemed worthwhile and is being considered. Papers relating to the rHMSIW were presented at Loughborough Antenna and Propagation Conference in 2013, and relating to the developed waveguide transition in 2014.

The developed rHMSIW was aimed at spanning the Ku band and the K band, and simulations indicated that this was possible for the K band with the 5880 material and for the Ku band using the 6010 material. The goal was to use capacitive coupled overlays to form filters and other structures such as leaky-wave guides, which initial simulations showed potential to achieve. However the measured performance of the 6010 prototype coupons were a poor match to the simulations and the overlays were not developed. The improvement of the test coupon response for the rHMSIW is an initial focus for future work, as the simulations indicate that the waveguide does have potential as discussed, hence, a transition for the 5880 material in the K band is also required.

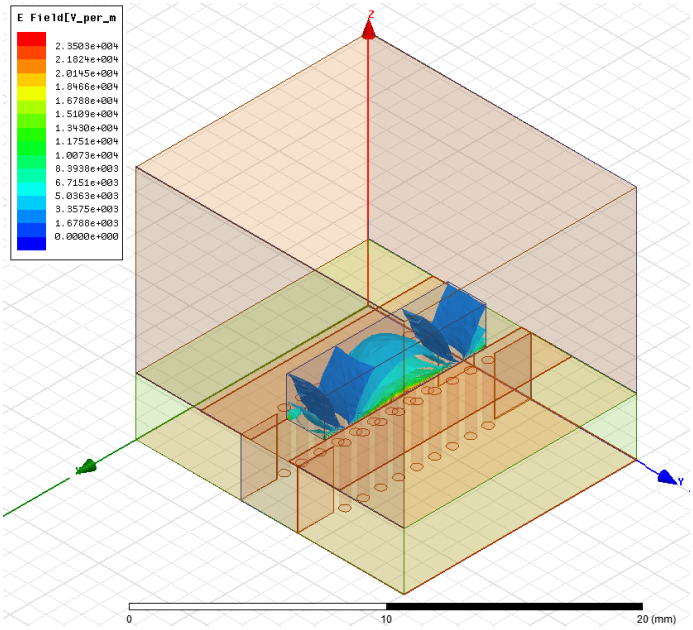

Fig. 6.9. Permittivity simulations with rHMSIW (5880 material)

One application that was considered was the use of the rHMSIW as potential fluid sensor. Simulations showed that the rHMSIW S_{11} (insertion loss) was directly effected by changes in the permittivity directly above the dielectric surface (Fig. 6.9), whilst the S_{21} remained relatively constant. Considerable more research is required to investigate this area, however, it is deemed a significant area of interest for future work.